UNIVERSIDAD AUTÓNOMA DE MADRID

Superconducting proximity effect and nonlocal transport in graphene and carbon nanotubes

by

Pablo Burset Atienza

A thesis submitted in partial fulfillment for the degree of

Doctor of Philosophy

in the subject of

Physics

in the
Facultad de Ciencias
Departamento de Física Teórica de la Materia Condensada

under the supervision of

Prof. Alfredo Levy Yeyati

April 2012

"Flying is learning how to throw yourself at the ground and miss."

Douglas Adams

Abstract/Resumen

Facultad de Ciencias

Departamento de Física Teórica de la Materia Condensada

Doctor of Philosophy in the subject of Physics

by Pablo Burset Atienza

This thesis is devoted to the study of superconducting effects on carbon based systems. On the first part, the induced superconducting proximity effect is studied in graphene-superconductor (GS) hybrid structures. On the second, nonlocal transport is studied in graphene and carbon nanotubes. On the one hand, a theoretical analysis of the graphene-superconductor interface is presented at the microscopic level. Two different models for the interface are proposed: one in which the superconductor induces a finite pairing in the graphene regions underneath, thus maintaining the honeycomb structure at the interface and one that assumes that the graphene layer is directly coupled to a bulk superconducting electrode. The Andreev reflection probability and its channel decomposition critically depend on the model used to describe the interface. The proximity effect on the local density of states on the graphene layer has also been studied for semi-infinite and finite layers, armchair and zigzag edges and different transparencies. Additionally, the induced minigap at finite layers and how it is reduced when the length of the layer increases has been analyzed. Subsequently, the formation of Andreev bound states at isolated graphene-superconductor junctions has been demonstrated. These states are sensitive to a supercurrent flowing on the superconducting electrode and are robust against moderate disorder. They also provide long-range superconducting correlations on the graphene layer, which may be exploited for the detection of crossed Andreev processes. On the other hand, a graphene pnp junction with a central superconducting electrode has been demonstrated to act as a Veselago lens for incoming electrons by focusing them and their phase-conjugated counterpart (holes) into different points of the optical axis. This property can be useful for the detection of entangled electron pairs. Finally, a Cooper pair splitter device based on carbon nanotubes has been analyzed microscopically. It has been demonstrated that the splitting efficiency can be raised to $\sim 100\%$ in the nonlinear regime. As a result, recent experiments in this regime have been analyzed.

Abstract/Resumen

Facultad de Ciencias
Departamento de Física Teórica de la Materia Condensada

Doctor of Philosophy in the subject of Physics

by Pablo Burset Atienza

Esta tesis está dedicada al estudio de los efectos de la superconductividad en sistemas basados en carbono. En la primera parte, se ha estudiado el efecto de proximidad superconductor inducido en estructuras híbridas grafeno-superconductor. En la segunda, se ha estudiado el transporte no local en grafeno y en nanotubos de carbono. Por un lado, se ha analizado la juntura grafeno-superconductor a nivel microscópico. Para este fin, se han propuesto dos modelos para la interfase: uno en el que el acoplo con el superconductor induce un potencial de pares en el grafeno, manteniéndose la estructura hexagonal del grafeno en la interfase, y otro en el que se asume que la lámina de grafeno está conectada directamente a un electrodo superconductor. La probabilidad de reflexión Andreev y su descomposición en canales dependen críticamente de las características de la interfase. También se ha estudiado el efecto de proximidad en la densidad local de estados del grafeno para láminas semi-infinitas y finitas, así como para bordes armchair y zigzag con distintas transparencias. Además, se ha estudiado el minigap inducido en láminas finitas y su dependencia con la longitud de la lámina. Seguidamente, se ha demostrado la aparición de estados de Andreev ligados en uniones grafeno-superconductor aisladas. Estos estados son sensibles a una supercorriente en el electrodo superconductor y su formación es robusta frente a la presencia de un desorden moderado. Adicionalmente, los estados producen correlaciones superconductoras de largo alcance en la lámina de grafeno que pueden ser explotadas para la detección de reflexiones de Andreev cruzadas. Por otro lado, se ha demostrado que una unión *pnp* de grafeno con un electrodo central superconductor actúa como una lente de Veselago, focalizando los electrones provenientes de una de las partes normales y los huecos que estos generan en el superconductor en distintos puntos de la otra parte normal. Esta propiedad puede resultar útil en la detección de pares de electrones entrelazados. Finalmente, se ha analizado microscópicamente un dispositivo divisor de pares de Cooper basado en nanotubos de carbono. Se ha demostrado que la eficiencia de separado de pares se puede incrementar hasta $\sim 100\%$ en el régimen no lineal. Como consecuencia, estos resultados se han usado para analizar experimentos recientes en este régimen.

Acknowledgements

I would like to thank my supervisor Prof. Alfredo Levy Yeyati. The work presented in this thesis has been done in collaboration with Prof. Álvaro Martín-Rodero from the Universidad Autónoma de Madrid, Prof. William Javier Herrera and Dr. Shirley Gómez from the Universidad Nacional de Colombia, Prof. Luis Brey from CSIC and Prof. Herbert Fertig from Indiana University. I thank Prof. Takis Kontos and Henning Söller for their help in my actual line of work. I also thank the members of my research group, present and past, Prof. Juan Carlos Cuevas, Dr. Sebastian Bergeret, Dr. Rèmi Avriller, Dr. Linda Zotti, Stefan Bilan and Dr. Michael Häfner.

Contents

List of Figures

Abbreviations

N	**N**ormal metal
G	**G**raphene
S	**S**uperconductor
I	**I**nsulator
BCS	**B**arden, **C**ooper and **S**chrieffer
BTK	**B**londer, **T**inkham and **K**lapwijk
TB	**T**ight-**B**inding
BdG	**B**ogoliubov and **d**e **G**ennes
DBdG	**D**irac, **B**ogoliubov and **d**e **G**ennes
HDSC	**H**eavily **D**oped **S**uperconductor
LDOS	**L**ocal **D**ensity **O**f **S**tates
CAR	**C**rossed **A**ndreev **R**eflection
EC	**E**lectron **C**o-tunneling
IBS	**I**nterface **B**ound **S**tates
SWCN	**S**ingle **W**alled **C**arbon **N**anotube
QD	**Q**uantum **D**ot
DQD	**D**ouble **Q**uantum **D**ot
EOM	**E**quation **O**f **M**otion

To my parents.

Chapter 1

Preface and outline.

The two main topics of these thesis are the proximity induced superconductivity in graphene and superconductivity mediated nonlocal transport. Superconductivity is therefore the main link throughout this work. The achievement of a microscopic theory for superconductivity was one of the landmarks for the quantum theory in the last century. It took more than forty years, from its discovery in 1911 to the publication of the BCS theory in 1957. And still today, more than one century after the discovery, a wide range of issues remain unexplained. From high critical temperature superconducting compounds to the more recently discovered iron-based superconductors, the formal theories for superconductivity have been tested to many different limits. Some questions have been answered, but many more have raised. This work is not centered around exotic superconducting phenomena in novel compounds. Quite the contrary, in the systems described here, the superconducting electrodes are usually bulk metals for which the BCS theory works perfectly fine. The interest of this work is another kind of limit to the theory: In the particular case of a normal metal contacted with a superconductor, *how dimensionality affects the formation of superconductivity?* and *how the superconducting pairing amplitude penetrates into the normal metal?*. Phonon-mediated superconductivity is a purely 3D property and the BCS theory was developed for the bulk of metals. As a consequence, reducing one or more of the dimensions of a superconducting material affects its behavior. Specifically, the spatial extension of superconductivity, or more precisely, of a Cooper pair, is given by the superconducting coherence length. If one or more of the dimensions of the metal-superconductor link, or only of the metal part, is reduced below the superconducting coherence length, the formation of Cooper pairs and therefore the appearance of superconductivity is affected. This is what has been called *mesoscopic* superconductivity.

The recent discovery of graphene, a one-atom thick material and thus the closest to a 2D crystal, opened new and very interesting possibilities for the study of mesoscopic superconductivity. During the years 2004 and 2005, the group of Geim in Manchester published the discovery of free-standing graphene and the demonstration of the equivalence of its charge carriers with massless relativistic fermions. The physics community has resonated with this discovery, with more than ten thousand articles published in over six years. In addition to its low-dimensionality, the possibility of describing electrons in graphene as massless relativistic particles opens a new playground for studying relativistic effects on the framework of superconductivity. Furthermore, being a very thin layer, when graphene is deposited on top of another material, it has the ability to inherit some structural properties of the host. In particular, superconductivity and ferromagnetism can be induced in graphene by proximity from a host material, even though these two phenomena are not intrinsic properties of graphene. Subsequently, graphene in contact with a superconducting electrode is described as a graphene-based link where part of the graphene layer is in the superconducting state and the rest in the normal one.

On the other hand, the second main topic of this thesis is devoted to the study of nonlocal processes mediated by the presence of a superconductor. Transport through the interface between a normal metal and a superconductor is microscopically understood using the concept of Andreev reflection. An Andreev reflection involves an electron incoming from the normal region into the superconducting one that is reflected as a hole, injecting a Cooper pair into the superconductor. In other words, if the electron, a filled state on the conduction band, has an excitation energy below the superconducting gap, can not be transferred into the superconductor due to the absence of available states. Subsequently, there are only two possible outcomes, it can be normally reflected or it can be paired with another electron with opposite momentum and spin to be transferred as a Cooper pair into the superconductor. In the latter case, the total charge injected into the superconductor is $2e$, and an empty state is left in the normal region. As a consequence, this empty state, with opposite momentum and spin to the incoming electron, is the reflected hole, thus completing the Andreev process.

An interesting consequence of the Andreev reflection appears when one considers the time-reversal of this process. Indeed, a Cooper pair injected from the superconductor into the normal metal creates an electron and a hole states which have opposite momentum and spin. This process is therefore a natural source of spin entanglement. A Cooper pair splitter is thus the name given to the solid-state device which is able to inject split Cooper pairs, i.e., beams of electrons and holes with opposite spin, into independent normal electrodes.

Andreev reflection is a nonlocal process where the incoming electron and the reflected hole can be separated a distance of the order of the superconducting coherence length. However, as the reflected hole follows back the path of the incoming electron, if electrons are injected from an electrode, the reflected holes will be headed to the same source, making impossible to independently detect both signals. An early proposal for a Cooper pair splitting device considered the possibility of having two electrodes, the source of electrons and the detector of the spin entangled holes, separated a distance smaller than the superconducting coherence length. Such a device takes advantage of the intrinsic non-locality of the Andreev reflection. In addition, graphene offers a new interesting possibility. The two-dimensional character of graphene, together with the particular dispersion relation where the conduction and the valence bands touch at one point, open the possibility of having a new type of Andreev reflection where the hole experiences an specular reflection. This new Andreev reflection, enhanced in the low-doping regime, can be exploited to detect the reflected holes in the same graphene layer where the electrons are being injected. Additionally, while in a normal metal electrons and holes belong to the conduction band, owing to the high tunability of the dispersion relation of graphene, electrons and holes can belong to different bands, enhancing the efficiency of a graphene-based Cooper pair splitter.

Furthermore, recent experiments have made an incredible progress in the implementation of Cooper pair splitters based in carbon nanotubes and InAs nanowires. Both systems have the peculiarity of being almost one-dimensional. Due to this fact, an enhancement of the coherence length was measured in this systems. As a consequence, the splitting efficiency was highly increased compared with previous experiments. Carbon nanotubes are rolled sheets of graphene and the low-energy behavior of their charge carriers is also explained using the Dirac equation. Furthermore, electron-electron interactions in carbon nanotubes can be enhanced to work in a regime where only one isolated energy level is relevant for transport. This quantum dot regime, which is often referred to as a zero-dimensional system, is capital in the implementation of this new type of Cooper pair splitters.

1.1 Outline.

This thesis is divided into four main chapters. Each chapter begins with an introduction to the subject treated, which also serves to outline the results presented and their relation with other works. A great part of the bibliography is therefore presented in these introductions. Additionally, at the end of each chapter, together with a summary of the main conclusions, a relation with the rest of the thesis is included.

In Chapter 2, this thesis begins introducing and reviewing the basic transport properties of graphene. From a tight-binding description of the hexagonal lattice of graphene, the relativistic Dirac equation is reached for the low-energy regime. The intrinsic relativistic character of charge carriers in graphene is highlighted reviewing some striking properties like the Klein paradox, the minimum of conductivity and the appearance of electron-hole charge puddles at the Dirac point. Also in this chapter there is a brief introduction to superconductivity and the superconducting proximity effect, which is responsible for a rich interplay between conventional transport of charge in metals with the unique transport without resistance characteristic of superconductors. Specifically, the Andreev reflection is presented as the microscopic mechanism to explain how an electrical current behaves when flowing from a normal metal into a superconductor. As a consequence, the same phenomena is explored in graphene and a new kind of Andreev reflection is presented which is intrinsically rooted in the relativistic and two-dimensional nature of transport in graphene. Finally, a brief presentation of the Green function techniques, which are widely used throughout the rest of the thesis, is introduced.

Chapter 3 is used to present the application of the Green function techniques to graphene layers. To do so, two theoretical frameworks are used: a tight-binding model for graphene, which provides a microscopic description, and a continuous model based on the Dirac equation, which, in many cases, enables to have an analytic description. The Green functions for graphene layers with different edge orientations are presented, together with the ones corresponding to superconducting graphene regions[1]. Subsequently, the results for the different models are compared.

With Chapter 4, the main part of the thesis is presented. In this chapter, the graphene-superconductor interface is explored in great detail. First, two different models to microscopically describe superconducting electrodes are presented and their effect on the Andreev reflection at the interface is studied. Next, the proximity effect in a graphene-superconductor hybrid system is analyzed. For finite graphene layers with edges, the appearance of a minigap in the density of states of graphene is studied both analytically and numerically. The proximity effect is further analyzed using the local density of states. This allows to present results for finite and semi-infinite graphene layers and to explore the role of the edges in the transmission at the interface with the superconductor. Finally, the previous results are justified within a simple model for the formation of interface bound states at the graphene-superconductor interface. These states are robust against moderate disorder and the flowing of a supercurrent at the interface.

[1] Superconducting graphene regions are the ones in contact with a host material in the superconducting state.

Finally, Chapter 5 and Chapter 6 are devoted to the study of non local phenomena in graphene and in carbon nanotubes, respectively. In the case of graphene, two different situations are considered: nonlocal effects in the normal region of a graphene-superconductor system and the possibility of having transport between two independent graphene layers connected by a superconducting region. The former is a very instructive illustration of the new Andreev reflection presented in Chapter 2 and detailed in Chapter 4, although is still far from experimental realization. The latter is a novel realization of a Cooper pair splitter that exploits the analogy between the propagation of electron beams in graphene-based *pnp* junctions and that of photons in metamaterials with negative refraction index. On the other hand, nonlocal transport for the case of carbon nanotubes has a closer relation with experimental results. Indeed, a description is presented of two previous independent experiments presenting similar proposals for the realization of Cooper pair splitters based on carbon nanotubes and InAs nanowires. Subsequently, a microscopic theory for Cooper pair beam splitters based on carbon nanotubes is introduced in detail. The possibility of enhancing the splitting efficiency of the experimental proposals by taking them into the non-linear regime is discussed. Finally, the theoretical model is used to fit and reproduce the experimental results of the Paris group in the same proposed regime.

In addition, some appendices have been included to account for the details of some calculations. Although they can be interesting and useful for the specialized reader, they are not part of the main discourse and including them in the chapters can be omitted in a first reading.

Chapter 2

Background and theoretical framework.

2.1 Graphene basics.

A flat one atom thick layer of carbon atoms arranged in a honeycomb lattice is known as graphene. The study of graphene dates back to 1947 when Wallace [1] applied band theory to the study of one-atom thick layer of graphite as a building block for the three dimensional material [1, 2]. In 1984, graphene was predicted to be an excellent condensed matter analogue of $(2+1)$-dimensional quantum electrodynamics [3], however this remained just as an 'academic' prediction. The great interest on carbon-based materials reached a peak in the 90's with the discovery of carbon nanotubes [4]. The properties of these virtually one-dimensional materials are easily understood through the ones of two-dimensional graphite [5]. The International Union of Pure and Applied Chemistry (IUPAC) gave the following definition of graphene in 1994 "the term graphene should be used to designate the individual carbon layers in graphite intercalation compounds" [6]. In spite of the theoretical importance of graphene, it was regarded as a virtual material since it was believed to be unstable with respect to the formation of curved structures such as fullerenes and carbon nanotubes. Few-layer graphite on a substrate was an experimental reality way before 2004, but it is not until that year when the Manchester group lead by Novoselov and Geim discovered free-standing graphene [7]. The two-dimensional nature of graphene was quickly confirmed [8] and, more importantly, the behavior of its carriers as massless Dirac fermions [9]. A new definition is given by Geim in a recent review: "graphene is a single atomic plane of graphite which–and this is essential–is sufficiently isolated from its environment to be considered free-standing" [10]. In the following years, close to ten thousand articles have been published with the

word 'graphene' on their title[1] and graphene is known for some record-breaking properties. In addition to be the thinnest and strongest known material in the universe, "its charge carriers exhibit giant intrinsic mobility, have zero effective mass, and can travel for micrometers without scattering at room temperature. Graphene can sustain current densities six orders of magnitude higher than that of copper, shows record thermal conductivity and stiffness, is impermeable to gases, and reconciles such conflicting qualities as brittleness and ductility" [10]. In recognition for their pioneering work, Geim and Novoselov won the Nobel Prize in Physics in 2010 "for groundbreaking experiments regarding the two-dimensional material graphene".

Apart from its outstanding mechanical and optical properties, the most relevant feature of graphene related to transport is its low-energy dispersion relation. The Fermi surface of graphene at half-filling is reduced to six points where two equivalent bands touch. Due to the honeycomb lattice symmetry of graphene only two of these points are relevant. In the low-energy regime, the two equivalent bands of graphene reduce to two conical bands, referred to as "valleys", that touch at the two inequivalent charge neutrality points, known as "Dirac points". The behavior of charge carriers in this regime is analogous to that of massless Dirac fermions. As a consequence, graphene offers the possibility to test in the laboratory interesting phenomena which is usually out of experimental range. This striking property triggered an outstanding research activity in the condensed matter community. A wide range of high-energy phenomena, such as half-integer quantum Hall effect and Klein tunneling, were predicted and measured in graphene.

Graphene displays another fascinating property. In spite of having relatively weak electronic correlations, different phenomena such as ferromagnetism and superconductivity can be induced in graphene by proximity to a host material. Indeed, depositing a graphene layer on top of a superconducting electrode, the region of the layer that covers the superconductor inherits the pairing correlation between electrons and holes by means of the proximity effect [11–14]. This peculiarity opens a wide range of possibilities. In particular the study of the rich interplay between superconductivity and relativistic phenomena in graphene-superconductor hybrid structures.

Due to the still very short live of graphene and the immense interest on its research, any attempt to produce an up-to-date review of its properties quickly becomes obsolete. On the other hand, the basic properties of graphene have been known for sixty years. As a consequence, although it is easy to find many detailed reports of the basic transport properties of graphene, new review articles appear frequently to account for the most recent experimental and theoretical updates. A list of the most recent and complete reviews is provided here. A good review of the new interesting transport properties of

[1] Data taken from ISIWEB up to 2011.

graphene can be found in Ref. [15], although the basics about the low-energy dispersion relation of graphene were clearly exposed in the articles by Wallace [1], Slonczewski and Weiss [2] and Semenoff [3]. Similarly, Ref. [5] reviews the case of carbon nanotubes, which very frequently is analogous to that of graphene. A more thorough and updated review for the transport properties of graphene is found in Ref. [16]. The similarities between the tight-binding approach and the continuous quantum electrodynamics model in two-dimensions, with special emphasis on the symmetries, are described in Ref. [17]. Ref. [18] gives a short introduction to the interplay between relativistic Dirac particles and superconductivity. Klein tunneling and negative refraction are reviewed in a very pedagogical way in Ref. [19]. An updated overview of the fabrication and electronic properties of graphene nanostructures, with a detailed description of recent reports on graphene-based quantum dots can be found in Ref. [20]. In the same line, Ref. [21] provides both experimental and theoretical updates and Ref. [22] accounts for the possible application of graphene-based quantum dots for spin *qubits* from a theoretical point of view. Finally, the effect of disorder on the transport properties of graphene has been recently reviewed in Ref. [23] and briefly in Ref. [24].

This Chapter is organized as follows: We begin with a microscopic tight-binding model for graphene which includes many of its basic characteristics. Specifically, we explain how the low energy excitations of graphene within the tight-binding approximation can be effectively described with the Dirac equation. As a consequence, we explore the relativistic behavior of charge carriers in graphene, emphasizing striking properties like Klein tunneling, pseudo-diffusive transport, the minimum of conductivity and the appearance of charge puddles. Next, we introduce the superconducting proximity effect in metal-superconductor hybrid structures. Moreover, we explain the Andreev reflection mechanism as the microscopic process that allows to describe transport in such systems. Subsequently, we introduce the special Andreev reflection in graphene, highlighting its differences with the case of normal metals. Finally, we briefly introduce the basics of the Green functions techniques.

2.1.1 From tight-binding model to Dirac's equation.

In this section we derive the band structure of graphene within the tight-binding approximation. From the energy dispersion relation of graphene we obtain the Dirac equation in the low-energy regime. This derivation was first introduced by Wallace in 1947 [1] when studying the band theory of graphite. The results presented here are analogous to that work.

The honeycomb structure of graphene is formed by combining two triangular lattices, denoted A and B, or equivalently, as a triangular lattice with a basis of two atoms per unit cell. In any case, a unit cell contains one atom from each lattice and thus the vectors $\mathbf{a}_{1,2} = (1, \pm\sqrt{3})a/2$ are defined as the primitive translations and $a = |\mathbf{a}_1| = |\mathbf{a}_2| = \sqrt{3}a_0 \approx 0.246\text{nm}$ is the lattice constant. The corresponding reciprocal lattice vectors are $\mathbf{b}_{1,2} = (1, \pm 1/\sqrt{3})2\pi/a$.

Any atom from a determined sublattice, say A, is connected to its three nearest neighbors from the other sublattice, B, via the vectors $\delta_1 = (\mathbf{a}_1 - \mathbf{a}_2)/3 = (0, 1/\sqrt{3})a$, $\delta_2 = \mathbf{a}_1/3 + 2\mathbf{a}_2/3 = (1, -1/\sqrt{3})a/2$ and $\delta_3 = -2\mathbf{a}_1/3 - \mathbf{a}_2/3 = (1, -1/\sqrt{3})a/2$. Subsequently, any pair of atoms from a unit cell can be labeled through the integers n_1 and n_2 by the vectors $\mathbf{R}_A = n_1\mathbf{a}_1 + n_2\mathbf{a}_2$ and $\mathbf{R}_B = n_1\mathbf{a}_1 + n_2\mathbf{a}_2 + \delta_1$.

The carbon atoms in the graphene plane are connected by strong covalent bonds due to the sp^2 hybridization of the atomic orbitals $2s$, $2p_x$ and $2p_y$. The $2p_z$ orbitals are perpendicular to the graphene plane, have zero overlap with the rest and can be treated independently. They form the π bonds of graphene, while the in-plane overlap is called a σ bond. We can thus provide a basis of wavefunctions for the lowest energy states in graphene with the two Bloch functions constructed from the atomic orbitals for the two inequivalent carbon atoms at A and B,

$$\Phi_i(\mathbf{r}) = \frac{1}{\sqrt{N}} \sum_{\mathbf{R}_i} e^{i\mathbf{k}\mathbf{R}_i} \varphi(\mathbf{r} - \mathbf{R}_i), \text{ with } i = A, B.$$

N is the number of unit cells, $\varphi(\mathbf{r})$ is the normalized $2p_z$ orbital of the isolated carbon atom and the summation is taken over all possible lattice vectors. From the Schrödinger equation $\mathbf{H}\Psi = E\Psi$, with $\Psi = C_A\Phi_A + C_B\Phi_B$, one can obtain the transfer integral matrix $H_{ij} = \langle\Phi_i|H|\Phi_j\rangle$ and the overlap integral matrix $S_{ij} = \langle\Phi_i|\Phi_j\rangle$. The energy dispersion relation for the system is therefore obtained from the secular equation $\det[\mathbf{H} - E\mathbf{S}] = 0$. Since the two atoms of the unit cell are identical, the Hamiltonian matrix element H_{AA}, which represents the interaction of an atom at site A with itself and the rest of the A atoms in the lattice, is exactly the same as H_{BB}. As a consequence, $H_{AB} = H^*_{BA}$. One can further neglect the overlap between wave functions centered at different atoms thus having $S_{AB} = S_{BA} = 0$. Furthermore, assuming a proper normalization of the wave functions we have $S_{AA} = S_{BB} = N = 1$. Under these approximations the resulting secular equation becomes trivially $E^{\pm} = H_{AA} \pm |H_{AB}|$, where E^+ represents the eigenvalue for the symmetric combination of wave functions, which form the valence band or the bonding π energy band, and E^- is the antisymmetric conduction band or the anti-bonding π^* band.

Within the nearest neighbors tight-binding approximation, every atom, say A, interacts only with itself and the surrounding three B atoms. The diagonal elements become constant terms representing the energy of an electron on the $2p_z$ orbital of carbon, including the effect of the periodic potential of the lattice: $H_{AA} = E_{2p}$. If the atoms of the unit cell were different, as it is the case for boron nitride (BN), the on-site energy E_{2p} would be different for B and N and the dispersion relation would show a gap between the π and π^* bands. That is not the case of graphene, formed only by carbon atoms, and we can thus take $E_{2p} = E_F = 0$.

On the other hand, the off-diagonal terms are

$$\begin{aligned} H_{AB} &= H^*_{BA} = \langle \Phi_A | H | \Phi_B \rangle \\ &= \sum_{\mathbf{R}_A} \sum_{\mathbf{R}_B} e^{i\mathbf{k}(\mathbf{R}_A - \mathbf{R}_B)} \langle \varphi(\mathbf{r} - \mathbf{R}_A) | H | \varphi(\mathbf{r} - \mathbf{R}_B) \rangle \\ &= t_g \sum_{\delta_i} e^{i\mathbf{k}\delta_i} = t_g e^{i\mathbf{k}(\mathbf{a}_1 - \mathbf{a}_2)/3} \left[1 + e^{i\mathbf{k}\mathbf{a}_2} + e^{-i\mathbf{k}\mathbf{a}_1} \right] \\ &= t_g \left[\exp\left(i \frac{k_y a}{\sqrt{3}} \right) + 2 \cos \frac{k_x a}{2} \exp\left(-i \frac{k_y a}{2\sqrt{3}} \right) \right], \end{aligned} \tag{2.1}$$

where we have used that the wave functions φ_i are radially symmetric in the graphene plane and that the distance between the A atom and its three neighbors is the same to define the tight-binding integral $t_g > 0$. The substitution into the secular equation is straightforward and the resulting energy dispersion relation for a graphene plane in the tight-binding approximation is

$$E^{\pm}(k_x, k_y) = E_F \pm t_g \sqrt{1 + 4\cos^2 \frac{k_x a}{2} + 4 \cos \frac{k_x a}{2} \cos \frac{\sqrt{3} k_y a}{2}}. \tag{2.2}$$

Since graphene's honeycomb lattice contains two atoms per unit cell (two sublattices) the excitation spectrum contains two branches (bands) which are symmetrical around $E = 0$. These bands touch at six points in momentum space given by the roots of $E(\mathbf{k}) = 0$

$$\begin{aligned} k_x &= \pm \frac{4\pi}{3a} \quad , \quad k_y = 0 \\ k_x &= \pm \frac{2\pi}{3a} \quad , \quad k_y = \pm \frac{2\pi}{\sqrt{3}a}. \end{aligned} \tag{2.3}$$

At half-filling, which is the pertinent situation for the study of graphene and other carbon-based materials, the band structure given by Equation 2.2 has six isolated Fermi points instead of a Fermi line. These are the six corners of the first Brillouin zone which, due to the symmetry of the hexagonal lattice, correspond to only two independent states.

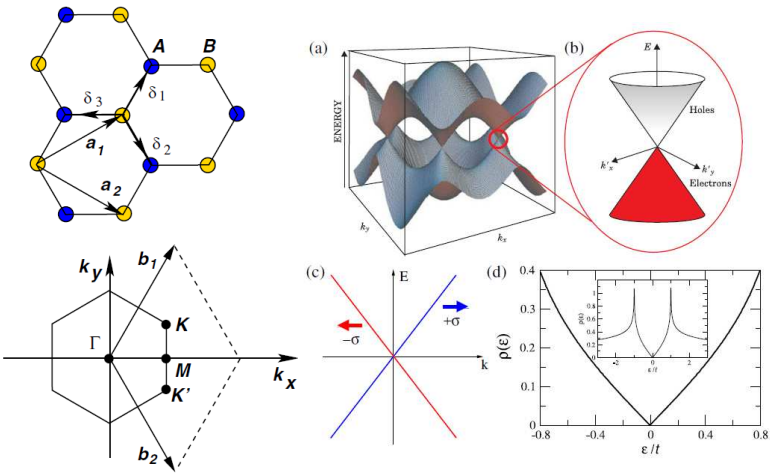

FIGURE 2.1: (a) graphene lattice showing the unit cell and the primitive translations. (b) Brillouin Zone of graphene showing the reciprocal lattice vectors and the high-symmetry points Γ, K, K' and M. (c) Graphene dispersion relation evaluated from Equation 2.2. The inset shows a Dirac valley at the low-energy regime. (d) Model energy dispersion from Equation 2.4, showing the chirality of each branch. (e) Density of states of graphene.

This result is of capital importance since it allows to study the low-energy excitations of graphene by taking the continuum limit at any two independent Fermi points. As a consequence, if we choose the two independent Fermi points

$$\mathbf{K}_{\pm} = (\pm\frac{4\pi}{3a}, 0), \tag{2.4}$$

any wave vector in the proximity of $\mathbf{K}_{\pm}$ is written as $\mathbf{k} = (\pm\frac{4\pi}{3a} + \delta k_x, \delta k_y)$. By substituting in Equation 2.1 we obtain

$$\begin{aligned} t_g \left[\exp\left(i\frac{\delta k_y a}{\sqrt{3}}\right) + 2\cos\left(\pm\frac{2\pi}{3} + \frac{\delta k_x a}{2}\right)\exp\left(-i\frac{\delta k_y a}{2\sqrt{3}}\right)\right] \\ \approx \pm\frac{\sqrt{3}}{2} t_g a \left(\delta k_x \mp i\delta k_y\right) + \mathcal{O}\left((a\delta\mathbf{k})^2\right). \end{aligned}$$

As a result,

$$E^{\pm}(\mathbf{k}) \approx \pm\frac{\sqrt{3}}{2} t_g a|\mathbf{k}| = \pm\hbar v_F|\mathbf{k}|. \tag{2.5}$$

This implies that the energy dispersion relation is conical in the proximity of a Fermi point. A striking consequence is that the Fermi velocity, defined as $\hbar v_F = \sqrt{3}t_g a/2$, is independent of both the energy and the momentum. The best experimental estimates of $t_g \approx 2.5$eV and $a \approx 0.14$nm give $v_F \approx 10^6$m/s in the absence of any carriers. In the presence of charge carriers this value is slightly modified without affecting the results presented here [16]. The linearity of the dispersion relation holds accurately up to an energy $E_C < 0.4t_g \sim 1$eV, which allows to introduce a cutoff wave vector $k_c = E_c/\hbar v_F \approx 0.25\text{nm}^{-1}$.

In the usual continuum approximation for lattice theories in condensed matter physics, i.e. the effective mass theory, one has a quadratic dispersion relation. Furthermore, an effective Schrödinger equation can be implemented in which all many-body effects are included in the effective mass parameter. On the contrary, graphene is a zero band-gap semiconductor with a linear low-energy dispersion for electrons and holes in the conduction and valence bands, respectively.

The linearity of the dispersion relation, with an energy independent Fermi velocity, is not the only striking result for the low-energy spectra of graphene. Indeed, the fact of having two atoms per unit cell or two equivalent and independent sublattices A and B implies that the two linear branches of the dispersion relation become independent of each other. This degree of freedom due to the sublattices defines a *pseudospin* quantum number equivalent to the electron spin. As a result, the low-energy, long-wavelength, effective 2D continuum Schrödinger equation for spinless carriers in the proximity of graphene Fermi point $\mathbf{K}_{\pm}$ becomes

$$\{\hbar v_F \left[\pm k_x \hat{\sigma}_x + k_y \hat{\sigma}_y\right] - E_F \hat{\sigma}_0\} \, \Phi_{\pm}(x, y) = E \Phi_{\pm}(x, y). \tag{2.6}$$

Pauli matrices $\hat{\sigma}_{x,y}$ (with $\hat{\sigma}_0$ the 2×2 identity matrix) are acting on graphene lattice subspace and $\Phi_{\pm}(x, y)$ is a 2D spinor wave function although we are not taking into account the real spin. Equation 2.6 is exactly the equation for massless chiral Dirac fermions in 2D, known as Weyl's equation for neutrinos, with the only difference that the spinor acts in the pseudospin rather than in the real spin. As a result, we shall refer to the Fermi points of Eqs. 2.3 and 2.4 as *Dirac* points or *valleys*. Intervalley scattering requires a large momentum transfer or strong lattice scale scattering. It is therefore weak and usually ignored in the description of the low energy states in graphene.

A series of experiments conducted by the Manchester group leaded by Geim triggered an intense research activity in graphene. Not only they isolated graphene but also demonstrated the relativistic behavior of electrons. In Ref. [7], the method to obtain one-atom thick graphite was presented. It was further developed in Ref. [8]. It was demonstrated that few and even mono layer graphite behaved like a two dimensional semimetal. There was a small overlap between the conduction and the valence bands and a strong ambipolar electric field effect was measured. Additionally, in Ref. [9] the relativistic behavior of carriers in graphene was demonstrated. A linear dependence of the conductivity on the gate voltage was measured. Mobilities up to 15,000 $\mathrm{cm^2 V^{-1} s^{-1}}$ were measured for electrons and holes. Furthermore, the measurement of half-integer quantum Hall effect corroborated once more the two-dimensional relativistic nature of carriers in graphene.

2.1.2 Relativistic behavior of low-energy carriers in graphene.

Wave functions around each Dirac point satisfy Equation 2.6 with E being the excitation energy of an electron-like quasiparticle. If we consider that momentum along the y-axis ($\hbar q$) is conserved, the wave function can be written as $\Phi_{\pm}(x,y) = e^{iqy}\phi_{\pm}(x)$. With the replacement $\mathbf{k}\,(q) = (-i\partial_x, q)$ in Dirac's equation, we obtain the following linear independent solutions for each valley

$$\begin{aligned}\phi_{+}(x) &= c_1^{+}e^{ikx}\varphi_1 + c_2^{+}e^{-ikx}\varphi_2\\ \phi_{-}(x) &= c_2^{-}e^{ikx}\varphi_2 + c_1^{-}e^{-ikx}\varphi_1,\end{aligned}$$

with

$$\varphi_{1,2} = \begin{pmatrix} 1 \\ \pm s e^{\pm i\alpha} \end{pmatrix}, \tag{2.7}$$

$s = \mathbf{sgn}(E + E_F)$ and $e^{\pm i\alpha} = \hbar v_F(k \pm iq)/(E_F + E)$. The constants $c_{1,2}^{\pm}$ are determined by boundary conditions for the wave functions $\phi_{\pm}\,(x)$. In a one-valley description of graphene equation 2.7 describes an oscillating wave where s is the band index ($s = 1$ for the conduction band and $s = -1$ for the valence band) and $\alpha(\mathbf{k})$ is the angle between the wave vector $\mathbf{k}$ and the x-direction. Let us define the chirality operator as the projection of the pseudo-spin operator on the momentum direction [2]

$$\hat{C} \equiv \frac{\mathbf{k}\cdot\hat{\sigma}}{|\mathbf{k}|}.$$

In the absence of an external potential this operator commutes with the Hamiltonian and becomes a conserved quantity. The eigenvalues of the chirality are given by the band index $s = \pm 1$. On the other hand, the velocity operator can be defined as $\hat{\mathbf{v}} \equiv -i\left[\mathbf{r}, \hat{H}\right] = \hat{\sigma}$. Therefore, the average velocity of a plane wave is given by $\mathbf{v} = s\mathbf{k}/|\mathbf{k}|$. As a result, an electron and a hole propagating in the valence band have the same average velocity and move in the same direction. However, their electric current is opposite since they have opposite charge.

An important consequence of the conservation of chirality is the absence of backscattering. Any two electron states propagating in opposite directions have opposite chirality, resulting in vanishing probability for reflection. This fact was first exposed by Ando for the one-dimensional case of carbon nanotubes [25, 26].

Another striking property of graphene is the relativistic transmission through a potential barrier, also known as Klein tunneling [27]. A classical barrier confines all particles with

[2] This is in fact the helicity operator, which is a function of physical quantities and thus has physical sense. However, in the relativistic limit with zero effective mass both quantities are the same. We adopt the standard in the literature and hereon we call this quantity chirality instead of helicity.

energy lower than the barrier height. In quantum mechanics, the wave function of non-relativistic particles with energy lower than the barrier height can still leak out into the classically forbidden region, giving rise to quantum tunneling. It is well known that the transmission through such quantum barrier decreases exponentially with the height and width of the barrier. On the other hand, for Dirac particles, the transmission probability depends only weakly on the barrier height, approaching unity with increasing barrier height [28]. As it was demonstrated in the previous sections, the Dirac Hamiltonian allows for both positive and negative energy states, i.e. electrons and holes. While a potential barrier is repulsive for electrons, it is attractive for holes. The opposite happens for a potential well. At any potential barrier one needs to match the electronic states outside the barrier with the hole states inside. Since the larger the barrier is, the greater the matching between electron and hole states is, the transmission is also greater. As a consequence, the transmission becomes perfect for an infinite barrier.

In other words, Klein tunneling is a relativistic effect in which electrons and holes are coupled by means of an electrostatic potential. The conservation of chirality, previously explained, implied that backscattering is forbidden in graphene. It is another consequence of the analogy of charge carriers in graphene with relativistic massless Dirac fermions that tunneling through a potential barrier happens with unit efficiency at normal incidence [28]. An striking conclusion is that graphene *pn* junctions are essentially transparent. This fact has been demonstrated experimentally in several works [29–33]. It is also the reason why graphene-based quantum dots are so experimentally challenging [20–22]. Furthermore, graphene *pn* junctions away from normal incidence behave as negative refraction index interfaces [34].

A direct consequence of Klein tunneling in graphene is that both the *pnp* junction and the *n-n'-n* junctions have finite transmission coefficients. And, more importantly, graphene's conductivity at zero doping, i.e. at the Dirac point, is finite [35, 36]. A graphene sheet contacted by two heavily electron doped contacts allows for testing the ballistic conductivity at the Dirac point. In other words, the crossover from the *pnp* junction regime into the *n-n'-n* junction of the source-graphene-drain configuration gives exactly the conductivity of graphene in the absence of charge carriers. By *ballistic* conductivity we are referring to the case of noninteracting electrons at zero temperature in the limit of no disorder. The absence of scattering in a non-Dirac metal yields that the semiclassical electrical conductivity is infinite, since there is nothing to impede the electron motion. The same argument implies that the conductivity would vanish as the carrier density is tuned to zero, giving rise to a metal-insulator transition.

The conductivity of a system governed only by the Dirac equation (Equation 2.6) can be obtained by calculating the transmission probability of modes confined in a strip of

width W and length L connected to heavily doped contacts [35, 36]. For transport along the $\hat{x}$-direction, the transmission probability for a transverse mode has the form

$$T_n = \frac{1}{\cosh^2(q_n L)}\,, \tag{2.8}$$

where the transverse momentum q_n depends on the details of the precise boundary condition of the strip [36, 37]. This transmission probability is given strictly by evanescent modes since both the energy and the doping are zero at the Dirac point. It is important to stress that this result is obtained in the absence of disorder, interactions and at zero temperature, i.e. this is a ballistic transmission with a dependence on the length of the sample L. This dependence, along with the distribution of eigenvalues of the transmission matrix resembles that of a diffusive system. This is known as *pseudo-diffusivity* of graphene at the charge neutrality point [38, 39].

For wide enough strips the conductivity of the system is independent of the boundary conditions and is found by summing over the modes,

$$\begin{aligned} \sigma &= g_s g_v \frac{L}{W}\frac{e^2}{h}\sum_n T_n(\hat{x}) = \frac{e^2}{h}\frac{2L}{\pi}\int_{-\infty}^{\infty}\frac{dq}{\cosh^2(qL)} \\ &= \frac{4}{\pi}\frac{e^2}{h} \quad \text{for } W >> L\,. \end{aligned} \tag{2.9}$$

The condition for the existence of a well defined -size independent- conductivity is the dependence of the transmission probability on the product qL [Eq. (2.8)] and the linear dispersion of the carriers. The condition $W \gg L$ allows the sum of the transmissions over the modes to be written as an integral over q in Eq. (2.9). The crucial features for this minimum of the conductivity are the gapless character of the spectrum and specially the chirality of the carriers.

In the previous results, the chemical potential is assumed to be constant over the graphene layer, with a discontinuity at the electrodes. This simplification was proven to be insufficient. It is well known that the spatial distribution of charge close to the Dirac point is not uniform. In low doped graphene, as in other 2D semiconductors, strong charge inhomogeneities appear. These inhomogeneities are known as electron-hole puddles[3] and are due to a random distribution of charge in the environment and, in a small contribution, to the ripples associated with the substrate roughness or the intrinsic wrinkles of suspended graphene. Contrary to the case of 2D semiconductors, transport at the charge neutrality point in the presence of puddles is still possible [40, 41]. Indeed, the boundaries between these charge puddles are *pn* junctions which, for the case of

[3] In the case of 2D semiconductors, the puddles are formed by either electrons or holes depending on the doping. In graphene at the Dirac point, the puddles are a mixture of electron and hole-doped inhomogeneities.

graphene, have finite transparency. Transport close to the Dirac point has been successfully compared to percolating currents in networks of *pn* junctions [42], although the theoretical picture of transport at undoped graphene remains incomplete. However, the experiments of Refs. [40, 41], in agreement with previous numerical calculations [43], were able to give some values for the size and strength of the charge puddles. Subsequently, the density fluctuations can be considered to have a characteristic length of up to 30nm, with a measured strength of around $25 - 30$meV.

2.2 Superconductivity basics I. Proximity effect.

Superconductivity is the phenomenon by which many materials develop zero electrical resistance and perfect diamagnetism below a critical temperature and magnetic field. The vanishing of electrical resistance was discovered by Kamerlingh Onnes [44] in 1911 while studying the properties of metals at extremely low temperatures. In 1933, Meissner and Ochsenfeld [45] measured the *expulsion* of magnetic fields by a material in the superconducting state. A phenomenological theory for this phenomenon, known as the Meissner effect was developed by the London brothers in 1935 [46]. In 1954 Landau and Ginzburg published a phenomenological theory of superconductivity [47] in which they introduced the superconducting order parameter. A microscopic theory of superconductivity was formulated 46 years after its discovery by Bardeen, Cooper and Schrieffer (BCS theory [48]). In this theory, a phonon-mediated attractive interaction between electrons is the responsible for the transition into the superconducting state.

The main feature of superconductivity is the absence of resistance below a finite temperature T_C. Furthermore, the drop in the resistance is very sharp, implying a phase transition. A common picture of conductivity relates the electrical resistance with the scattering of electrons with the vibrational excitations of the lattice (phonons). By lowering the temperature, the phonons are continuously suppressed reaching a minimum at $T = 0$, where only the lattice defects and impurities contribute to the scattering of electrons. This result is independent of the temperature and insufficient to explain the appearance of superconductivity. The BCS microscopic theory of superconductivity demonstrates the formation of a new many-body ground state. In s-wave superconductors, Cooper pairs are formed by coupling two electron of opposite spin. The resulting pair has total spin 0 and therefore can be considered a boson. Cooper pairs occupy the same many-body ground state. This is the BCS ground state Ψ_{BCS} which contains the sum of all Cooper pairs in the material. Since the Coulomb interaction causes a repulsing force between any electrons, there has to be an attractive force between electron pairs in the conduction band. A weak, phonon-mediated, attractive interaction between

electrons close to the Fermi surface is the responsible to overcome the Coulomb repulsion. Electrons in a metal create local distortions in the lattice which act as an indirect attractive force upon other electrons. When this attraction overcomes the Coulomb repulsion a Cooper pair is formed.

Thus, Ψ_{BCS} describes a collective excitation with momentum k_{BCS} where all the individual Cooper pairs have zero momenta relative to k_{BCS}. The individual Cooper pairs are spatially overlapped. The typical length scale of the collective mode ξ_{BCS} is much greater than the mean distance between individual electrons in the metal. This is known as the 'BCS coherence length' and is a fundamental parameter that characterizes the superconductor. This collective mode provides a direct interpretation of the vanishing resistance of a superconductor. Since all individual Cooper pairs overlap at Ψ_{BCS}, the scattering of one of them requires an equivalent change of momentum in the rest. This would require a large amount of energy and therefore the scattering of Cooper pairs is highly suppressed. However, the supercurrent given by the collective mode can not be infinite since it is limited by the density of Cooper pairs.

In the superconducting state the attraction between electrons overcomes the Coulomb repulsion. This makes the formation of Cooper pairs energetically favorable. This coupling between electrons opens a gap in the spectrum since it is impossible to have an individual excitation with energy below the one required to form a Cooper pair. We must introduce the 'BCS gap parameter' Δ_{BCS} as another of the fundamental parameters in the characterization of a superconductor.

The resulting 'BCS density of states' is

$$\frac{N_{BCS}(E)}{N(0)} = \begin{cases} \frac{|E-\mu|}{\sqrt{(E-\mu)^2-\Delta_{BCS}^2}} & , |E-\mu| > \Delta_{BCS} \\ 0 & , |E-\mu| < \Delta_{BCS} \end{cases} \tag{2.10}$$

where $N(0)$ represents the density of states on the normal state. In the inset of Figure 2.2, we show the experimental results of Ref. [49] for the DOS of a bulk superconductor. It is shown how no quasi-particle is allowed below the superconducting gap of width $2\Delta_{BCS}$. All the states are *pushed* to the edges of the gap, forming two characteristic peaks at $E - \mu = \pm\Delta_{BCS}$.

A metal in electrical contact with a superconductor can develop superconducting features such as infinite conductance and perfect diamagnetism. We consider the superconductor as a reservoir where the electrons are condensed into Cooper pairs and the normal metal as a gas of free electrons. The proximity effect is the phenomenon in which the electrons in the normal metal acquire superconducting correlations through the diffusion at the

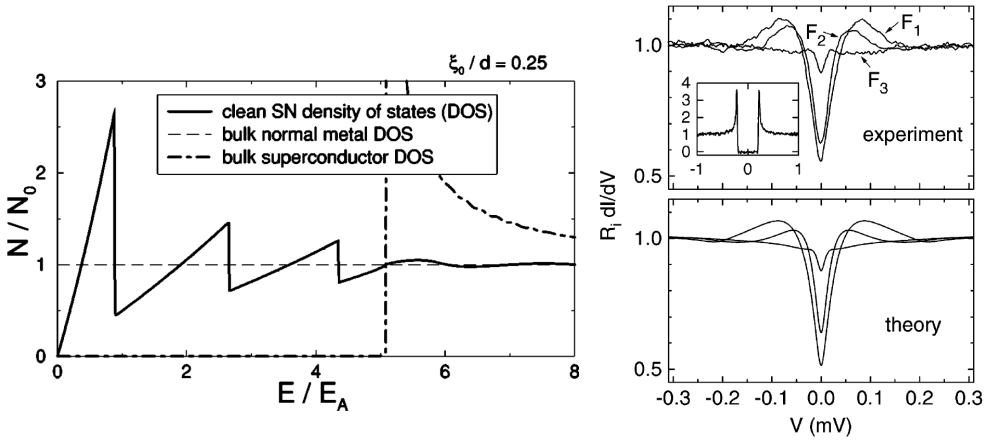

FIGURE 2.2: Proximity effect in a normal-superconductor junction. (a) Left: Normalized DOS for the ballistic case. The bulk normal and superconductor cases are included. Results extracted from Ref. [50]. (b) Right: Differential conductance in the tunnel regime for the diffusive case. Both experimental and theoretical results are extracted from Ref. [49]. The inset shows the bulk experimental results for the superconductor.

contact between the normal metal and the superconductor. The behavior of the superconducting order parameter in the distances close to this interface is therefore crucial to study how the correlations leak into the normal region. Following the Ginzburg-Landau theory [47] a superconducting order parameter $\Delta(x)$, which only depends on the distance from the interface, contains all the information about the propagation of superconductivity into the normal region. This theory accounts for the macroscopic equilibrium properties close to the critical temperature. However, it is not valid when $T \to 0$. In this case, for ballistic junctions, the BTK model [51], developed in the early 1980s and introduced in the next section, gives a microscopic explanation. The theory of non-equilibrium superconductivity developed in the 1990s reconciled these two limit cases into a complete description of the proximity effect. In this theory the order parameter $\Delta(x, E)$ contains both the spatial and the energy dependence of the density of states $N_{BCS}(x, E)$. Hence, in the absence of magnetic fields, the natural unit of length for the variation of $\Delta(x, E)$ is the superconducting coherence length ξ_{BCS} and the energy dependence is given by the density of states of the bulk superconductor $N_{BCS}(E)$.

In the ballistic case, the electron mean free path l is much greater than the superconducting coherence length ξ_{BCS}. Consequently, the variation of the order parameter at the normal metal-superconductor interface can be considered abrupt. Therefore, we have $\Delta(x) = 0$ for the normal region and $\Delta(x) = \Delta_0$, with Δ_0 constant, at the superconductor[4]. The combination of constant density of states at the normal metal with a BCS-like density of states in the superconductor results in the DOS shown in the left panel of Figure 2.2. For an excitation energy greater than the gap, the DOS tends to

[4]This step-like form of the superconducting pairing potential is known as "rigid boundary condition".

the case of the isolated normal metal. Inside the gap, there is a finite DOS for energies up to zero.

On the other hand, the diffusive regime is defined when l is small compared with the superconducting coherence length. For this case we show in the right panel of Figure 2.2 the experimental results of Ref. [49], compared with the theoretical predictions using Usadel equation. In the inset it is shown the experimental DOS for the bulk superconductor. In spite of having a well-defined BCS density of states, where the sharp edges at the gap can be observed, the DOS inside the normal region is smooth with a characteristic V-shaped dip at low voltages. For a diffusive NS junction, the number of states within the gap presents two maxima for energies close to the gap and is highly reduced for lower energies. The proximity effect is decreased for larger distances to the interface.

2.3 Superconductivity basics II. Andreev reflection.

2.3.1 The concept of Andreev reflection.

At the interface between a normal metal and a superconductor, the superconducting pairing potential can convert an electron from the normal region into a hole, creating a Cooper pair in the superconductor. This process is known as Andreev reflection [52] and is responsible for transport in NS junctions. The electron is a filled state with energy E above the Fermi energy E_F in the normal metal. If E is lower than the superconducting energy gap Δ, single-particle tunneling into the superconductor is forbidden since there are no available states. This quasi-particle may only enter the superconducting region if it forms a Cooper pair. In order to do that it must couple with another electron from the normal region with opposite wave vector and spin. Therefore, the empty state below the Fermi energy left behind by this electron is the *reflected* hole. As a consequence, a total charge of $2e$ is transmitted from the normal region to the superconductor. Time-reversal symmetry yields that an incident hole from the normal region is Andreev reflected as an electron at the interface.

This effect was first introduced by A. F. Andreev when studying the heat transport at NS interfaces [52]. Andreev reflection is the microscopic mechanism which explains how a dissipative current from the normal metal transforms into a supercurrent at the NS interface.

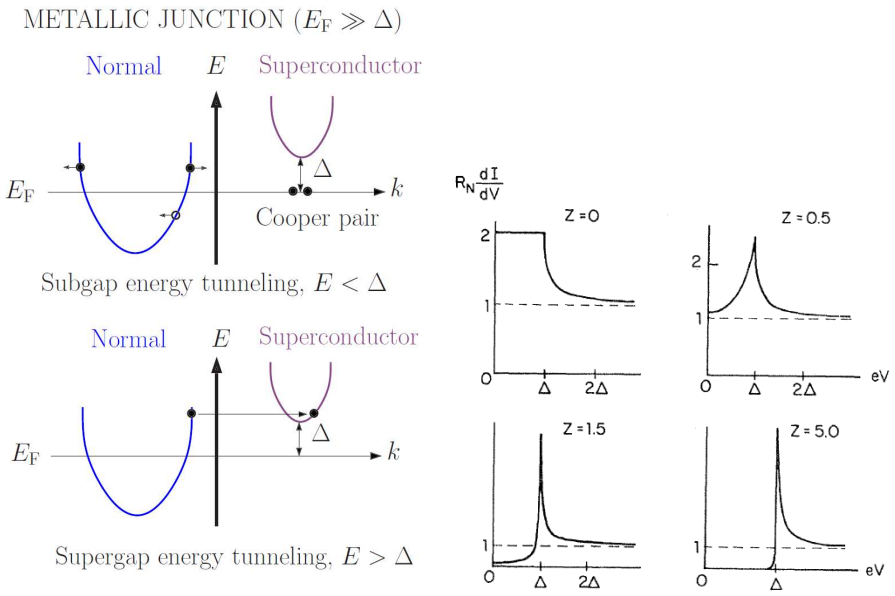

FIGURE 2.3: Sketch of the Andreev reflection at a metallic junction. Conductance at the metallic NIS junction.

The most common metals have Fermi energies E_F that are much greater than the superconducting energy gap Δ[5]. By neglecting the terms of the order Δ/E_F[6], the incident electron and the reflected hole have the same wave vector which lies at the edge of the Fermi surface. While the velocity of a conduction band electron is parallel to its wave vector, the velocity of a conduction band hole is opposite to its wave vector and the hole is *retroreflected*. It is common to say that, in the Andreev reflection, the hole traces back the path of the incident electron.

2.3.2 Transport at a normal metal-superconductor interface.

The Bogoliubov-de Gennes (BDG) equations describe the quasi-particle excitations in non-uniform superconductors. They are among the most useful techniques for describing phase-coherent normal-superconductor (NS) hybrid structures. In a superconductor the quasi-particle excitations consist of a mixture of electron-like and hole-like states. The BDG equations are two coupled linear differential equations describing the amplitudes $u(x, E)$ and $v(x, E)$ of an excitation of energy E on the electron and hole states. They are expressed as,

$$\begin{pmatrix} H - E_F & \Delta(x) \\ \Delta^*(x) & E_F - \mathcal{T}H\mathcal{T}^{-1} \end{pmatrix} \begin{pmatrix} u(x) \\ v(x) \end{pmatrix} = E \begin{pmatrix} u(x) \\ v(x) \end{pmatrix}, \tag{2.11}$$

[5]For example, Copper and Aluminum have Fermi energies of 7 eV and 11.7 eV, respectively [53]. On the other hand, the bulk superconducting gap of Aluminum is 0.15 meV [54].

[6]This approximation is known as Andreev approximation

where H is the single-particle Hamiltonian of the system (i.e. Schrödinger or Dirac-Weyl, depending on if we are describing traditional semiconductors or graphene), $\mathcal{T}$ is the time-reversal operator and $\Delta(x)$ is the pairing potential between electrons and holes.

A simple example is a one-dimensional normal-superconductor junction with an insulating barrier at the interface (NIS system). By substituting H in Equation 2.11 by the Schrödinger Hamiltonian in one dimension and taking $\Delta(x) = \Delta_0\theta(x)$, with $\theta(x)$ being the Heaviside step function, we are describing an impurity-free one-dimensional junction with one normal region and one superconducting region. We consider an incoming electron from the normal region into the superconductor and we allow it to be either transmitted as a Cooper pair or reflected as a hole. Matching wave functions at the interface we obtain that the Andreev reflection probability is [7] $R_{eh} = |r_{eh}|^2 = |u_0/v_0|^2$. The probability of Andreev reflection is thus unity inside the superconducting gap and decays exponentially outside. This one-dimensional result is easily expanded for the 3D case, where electron normal reflection is included. The result is similar, nonetheless. In a famous article from 1982, Blonder, Tinkham and Klapwijk (BTK model [51]) used for the first time this formalism based on the BDG equations to describe superconducting microconstrictions. They solved the problem introduced here, using both plane waves to consider impurity-free systems and a Dirac delta-like potential at the point between the normal and the superconductor electrodes to include all the possible scattering processes at the interface. The intensity of the barrier is controlled by a parameter Z, which allows to go from the absence of barrier ($Z = 0$) to the case of strong barrier ($Z \gg 1$). By studying the probability of each microscopic process and its contribution to the current they obtained the conductance results shown in Figure 2.3. The two limiting cases of zero barrier and strong barrier are very pedagogical. In the former, the probabilities of normal reflection and transmission of electrons into hole-like excitations are both zero. Thus, Andreev reflection for energies below the gap is perfect (i.e. occurs with unit probability as in the one-dimensional case) and transmission of electrons into the superconductor as electron-like excitations is $T_{ee} = 1 - R_{eh}$, thus contributing to the conductance only for energies over the gap. This behavior is particular of metallic junctions. On the other hand, for strong barrier the Andreev reflection probability is strongly suppressed while normal reflection R_{ee} dominates inside the gap. This behavior

[7] In the one-dimensional case, we consider plane wave solutions of Equation 2.11 of the form $(u_0, v_0) \times e^{ik_S^e x}$, where $u_0^2(v_0^2) = \mathbf{min}[1, E/\Delta_0](1 \pm \sqrt{E^2 - \Delta^2}/E)/2$ are the BCS coherence factors and the wave vector has the form $k_S^{e,h}(E > 0) = \sqrt{2m(E_F^S \pm \sqrt{E^2 - \Delta_0^2})/\hbar^2}$. The wave vector for the normal region is obtained for $\Delta_0 \to 0$, limit in which $(1, 0)$ and $(0, 1)$ represent electron and hole quasi-particles, respectively. The matching of the wave functions reads

$$\begin{pmatrix} 1 \\ 0 \end{pmatrix} e^{ik_N^e x} + r_{eh} \begin{pmatrix} 0 \\ 1 \end{pmatrix} e^{ik_N^h x} = \begin{pmatrix} u_0 \\ v_0 \end{pmatrix} e^{ik_S^e x}. \tag{2.12}$$

The normalization is done over the incident flow and thus r_{eh} is the Andreev reflection amplitude.

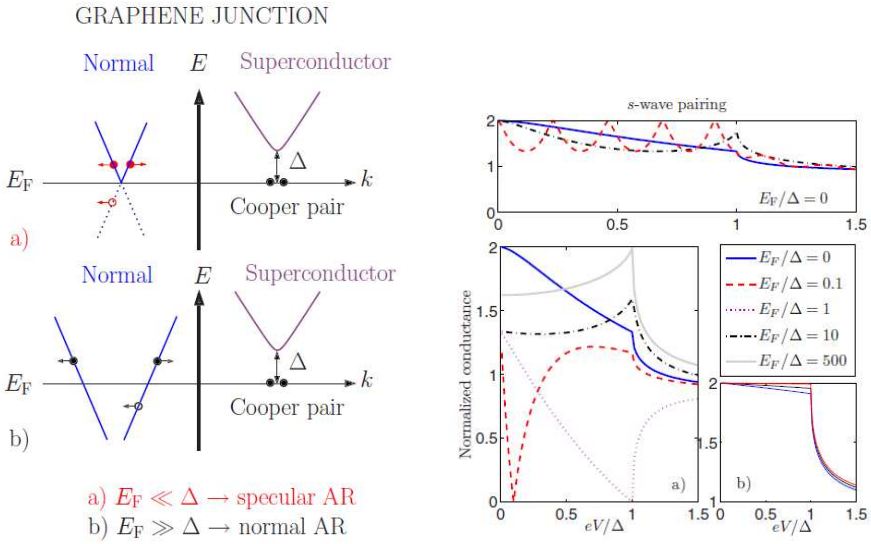

FIGURE 2.4: Sketch of the Andreev reflection at a graphene junction. Conductance at the graphene-based NS and NIS systems.

is characteristic of classical tunnel junctions. Thus, the BTK model continuously connects this two limit cases. The importance of this simple model was demonstrated by the experiments conducted by Blonder and Tinkham [55]. There is an excellent agreement between the theoretical predictions and the experimental $I-V$ curves for Cu-Nb point contacts. Thus, the importance of the Andreev reflection for describing the transport on superconducting junctions was demonstrated.

2.3.3 The BTK model applied to graphene.

In a seminal article by Beenakker in 2006 [56], the BTK model was applied to a graphene-based NS system. Substituting the Dirac-Weyl Hamiltonian of Equation 2.6 into Equation 2.11, we reach what are commonly known as the Dirac-Bogoliubov-de Gennes (DBDG) equations. Two important features rapidly arise. First, while in a metallic junction electron and hole-like states are only coupled through the superconducting pairing potential, in graphene these states are related with each other also through time-reversal symmetry. Second, the Fermi energy of a metal is much greater than the rest of the energy scales like the excitation energy and the superconducting gap. This means that both electron and hole states belong to the conduction band. However, the Fermi energy in graphene can be comparable or even smaller than the excitation energy and the gap. The conduction and the valence bands in graphene touch at the Dirac point and Andreev conversion of electrons into holes can occur in different bands. In Figure 2.4 we show the plots of the conductance for a graphene-based NS junction, showing the two distinctive regimes of low-doping, which enhances inter-band Andreev reflection

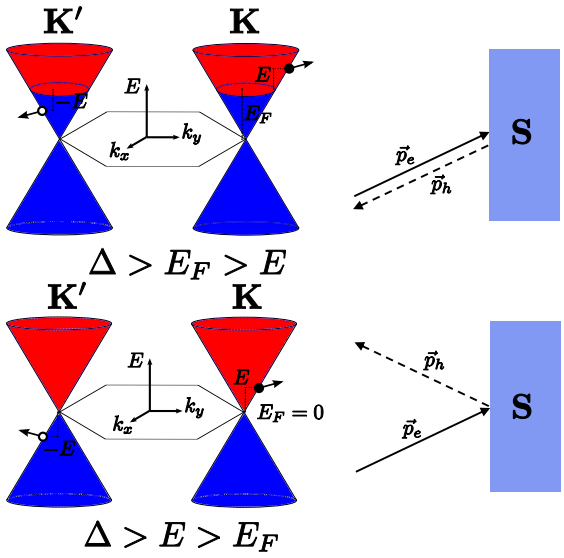

FIGURE 2.5: Andreev reflection in graphene. (a) Andreev retro-reflection. (b) Specular Andreev reflection.

and high-doping, which is mainly due to intra-band Andreev reflection and is equivalent to the metallic junction behavior, with a small barrier. Furthermore, the study of the graphene NIS junction done in Ref. [57] showed another important difference with the metallic junctions: the conductance is an oscillatory function of the effective barrier strength. The amplitude of these oscillations is maximum when the Fermi levels of the normal and the superconducting region are aligned and it can be zero for large Fermi vector mismatch[8]. In addition to that, a maximum value of the conductance can be reached at zero bias for a finite barrier, in stark contrast with the case of metallic junctions (see Figure 2.4).

2.3.4 Andreev reflection in graphene: specular versus retro.

An schematic description of Andreev reflection in the conical band structure of graphene is shown in Figure 2.5. The Cooper pair must carry zero total momentum, so the electrons are taken from opposite corners of the Brillouin zone ($\pm\mathbf{K}$). Therefore, Andreev reflection mixes graphene's valleys [56]. The electron excitations of Figure 2.5 are from the conduction band (filled states with $E > 0$, from one valley). When $E < E_F$, which is the usual case of traditional NS junctions, the reflected hole remains in the conduction band (in graphene it still belongs to the other valley). This *intraband* Andreev reflection applies if $E < E_F$. When $E > E_F$, the hole is reflected into the valence band. When $E_F = 0$, the reflected hole is always an empty state below the Fermi energy so, in undoped graphene, Andreev reflection is an *interband* process at all excitation energies.

[8]For a detailed study of both the NS and the NIS cases see Ref. [58].

Interband Andreev reflection does not exist in usual metals which have an excitation gap between the conduction and valence bands much larger than Δ.

It is considered a basic feature of Andreev reflection that the hole produced upon electron-hole conversion retraces the trajectory of the incident electron. Then, one says that Andreev reflection has a *retro*-reflection character when all components of the velocity change sign and then the hole follows back the path of the incident electron.

The mean-field approximation for superconductivity demands that the superconducting coherence length $\xi = \hbar v_F/\Delta$ is much greater than the Fermi wave length on the superconductor $\lambda_F^S = \hbar v_F/(E_F^S + U_0)$. There is no restriction over the relative magnitude of ξ and the Fermi wave length in the normal region. An impurity-free graphene-based NS system has the following dispersion relation

$$E = \sqrt{|\Delta|^2 + \left(E_F \pm \hbar v_F \sqrt{k_x^2 + k_y^2}\right)}, \tag{2.13}$$

where k_x is the projection of the momentum in the direction transversal to the interface, while k_y is the projection parallel to the interface. The energy includes the two branches of the spectrum of graphene, corresponding to the conduction and valence bands. Let the superconducting region be in the infinite half-plane $x < 0$. The quantities k_y and E are conserved upon reflection, so an incident electron from the normal region, belonging to valley $\mathbf{K}$, will have transverse momentum $k_e^- + K$. Here, k_e^- is one of the two solutions of Equation 2.13 with negative slope. The other solution with negative slope, i.e. k_h^-, represents a hole going to the interface, while the two solutions with positive slope ($k_{e,h}^+$) represent outgoing electron and hole excitations. In the interface, it will form a Cooper pair reflecting a hole with transverse momentum $k_e^+ - K$. The slope of the momentum is proportional to the expectation value of the velocity ($v_i = \hbar^{-1}\partial E/\partial k_i$). Fixed E_F and E, for an incoming electron with k_e^- there are only two possible reflected momenta: k_e^+ for electrons and k_h^+ for holes. For $E < E_F$, the reflected hole is in the conduction band while it is in the valence band if $E > E_F$. Since a conduction band hole moves opposite to its wave vector, both projections of the velocity change sign. Therefore, we associate intraband Andreev reflection with retro-reflection. On the other hand, a valence band hole moves in the same direction as its wave vector. The reflection only changed the sign of the component of the velocity perpendicular to the interface, while the component parallel to the interface remains unchanged. This is a *specular* Andreev reflection which we associate with intraband reflections.

As E increases from zero to E_F and beyond, there is a transition from retro-reflection to specular reflection. The reflection angle α_{out} (measured relative to the direction of normal incidence) first becomes greater than the angle of incidence α_{in}, then jumps from

$+90°$ to $-90°$ at $E = E_F$ (where it can not be defined), and finally approaches $-\alpha_{in}$ when $E \geq E_F$ [56]. Specifically, there is no Andreev reflection beyond a critical angle of incidence $\alpha_c = \arcsin |E - E_F| / (E + E_F)$.

2.3.5 Nonlocal transport and crossed Andreev reflection.

Andreev reflection is intrinsically a nonlocal process. Indeed, it takes place in a coherence volume of size ξ_{BCS}, the characteristic length associated to the superconducting gap Δ_{BCS}. As a consequence, the incident electron and the reflected hole can be separated by hundreds of nanometers. Could it be possible to independently measure these two coherent currents?

In an article in 2000, G. Deutscher and D. Feinberg [59] considered a multi-terminal system formed by two point contacts coupled to a superconductor and separated by a distance L smaller than the superconducting coherence length. When studying transport at subgap voltages and temperatures they realized that Cooper pairs made of electrons coming one from each tip can be injected into the superconductor. This process is known as *crossed* Andreev reflection (CAR). Subsequently, it was shown that another process involving the coherent tunneling of two electrons into each normal electrode is possible [60]. This process is called electron co-tunneling (EC) and its contribution to the nonlocal conductance is the opposite to the one due to the CAR processes. It can exactly cancel the CAR contribution in the tunnel regime. At the same time, *local* Andreev reflection can occur at each normal electrode, giving an extra contribution to the nonlocal conductance which usually is hard to distinguish from that coming from CAR processes.

Nonetheless, study of the nonlocal conductance can give evidence of the presence of CAR processes. The time-reversal of a CAR process is that in which each electron from a Cooper pair coming from the superconductor coherently tunnels into a different normal electrode. An independent measure of these processes is thus equivalent to measure the splitting of a Cooper pair. This splitting is therefore a source of entanglement and has many possible applications in quantum information theory.

The cancellation between the EC and the CAR contributions to the nonlocal conductance for thick tunnel barriers was shown to be removed by introducing ferromagnetic leads [60, 61], increasing the barrier transparency [62–64] or taking into account Coulomb interactions [65]. The importance of non-equilibrium effects at large bias voltages has been also analyzed [66].

A series of recent experiments have demonstrated these facts. In 2004, Beckmann *et al.* [67] measured the nonlocal resistance of an Aluminum bar with two ferromagnetic wires forming point contacts to the Aluminum. When the Aluminum was in the superconducting state, they observed a nonlocal spin-dependent resistance. The spatial decay of this signal was controlled by the superconducting coherence length rather than by the normal state spin-diffusion length. Furthermore, the energy dependence on the probability of EC and CAR was measured by S. Russo *et al.* [68]. They found that CAR dominated over EC at high energies, with the Thouless energy of the superconductor being the energy scale for the crossover. This indicates that the phase coherence of the processes is playing a fundamental role. Further experiments corroborated this fact, along with the key role played by the contact resistances and the excitation energy of the particles [69–71].

Another multi-terminal device was proposed by P. Recher *et al.* [72] in 2001. In this case, the superconductor is weakly coupled by tunnel barriers to two quantum dots (QDs). Each QD is treated as a one-level system and is also weakly coupled to a normal lead. If the QDs are in the Coulomb blockade regime, the probability for the state with two electrons on the same dot is suppressed. Electrons coming from the superconductor tunnel into separate dots and therefore into separate leads with higher probability. When the energy levels of the dots coincide, the splitting of the Cooper pairs from the superconductor is enhanced. The study of entanglement in similar systems was performed in Refs. [73] and [74]. Similar predictions were reached for other mesoscopic systems like Luttinger liquids [75].

2.4 Methodology: Green functions techniques.

Green functions techniques are applied in a wide range of mathematical and physical problems. From the solution of differential equations in Classical Mechanics or Electromagnetism to the diagrammatic theory of Quantum fields. In Quantum Mechanics the Green function is often interpreted as the inverse of a differential operator. Since both Schrödinger and Dirac equations are differential equations, we can obtain different Green functions for each Hamiltonian. In this section, a brief introduction of single-particle Green functions with some basic definitions is presented.

2.4.1 Equilibrium Green functions.

2.4.1.1 General definition of the Green functions. Properties, physical quantities and Dyson equation.

The definition of the Green functions can be generalized to any single-particle problem. Let $\mathbf{H}$ be the Hamiltonian of a one-particle system, the retarded and advanced Green functions are thus defined as

$$\mathbf{G}^{r,a}(E) = \lim_{\eta \to 0} \left[(E \pm i\eta)\, \mathbf{I} - \mathbf{H} \right]^{-1}, \tag{2.14}$$

with $\mathbf{I}$ the identity operator. Equation 2.14 is an identity between operators and thus independent of the chosen representation. Thus, we can obtain an expression equivalent to Equation 2.14 as a function of the eigenvalues ϵ_n and the eigenfunctions $|\varphi_n>$ of the Hamiltonian that reads

$$\mathbf{G}^{r,a}(E) = \lim_{\eta \to 0} \sum_n \frac{|\varphi_n><\varphi_n|}{E - \epsilon_n \pm i\eta}.$$

The local density of states can be expressed as a function of the eigenstates of the Hamiltonian as

$$\rho(\mathbf{r}, E) = \sum_n |<\mathbf{r}|\varphi_n>|^2 \delta(E - \epsilon_n),$$

where the spatial vector $\mathbf{r}$ is generalized to any number of spatial dimensions. As a consequence, the imaginary part of the Green function is associated with the local density of states (LDOS) as

$$\rho(\mathbf{r}, E) = \mp \frac{1}{\pi} \mathrm{Im}\left[\mathbf{G}^{r,a}(\mathbf{r}, E) \right]. \tag{2.15}$$

Subsequently, the *local* terms of the Green function with $\mathbf{r} = \mathbf{r}'$ always verify that $\mathrm{Im}\left[\mathbf{G}^r(E)\right] \leq 0$ and $\mathrm{Im}\left[\mathbf{G}^a(E)\right] \geq 0$. It is also a consequence of the general definition of the Green functions in Equation 2.14 that $\mathbf{G}^r = [\mathbf{G}^a]^\dagger$.

The Green function techniques are very useful in order to describe arbitrary perturbations of the system. Let the Hamiltonian be expressed as $\mathbf{H} = \mathbf{H}_0 + \mathbf{V}$, where $\mathbf{H}_0$ is the Hamiltonian of a system with known Green functions $\mathbf{G}^{(0)r,a}$, and $\mathbf{V}$ a single-particle perturbation. We can write the Green functions of the total system $\mathbf{H}$ using the Green functions of the already solved system $\mathbf{H}_0$. From Equation 2.14 we write

$$\mathbf{G}^{r,a}(E) = \lim_{\eta \to 0} \left[(E \pm i\eta)\, \mathbf{I} - \mathbf{H}_0 - \mathbf{V} \right]^{-1}.$$

We already know the solution to the non-perturbed system

$$\mathbf{G}^{(0)r,a}(E) = \lim_{\eta \to 0} \left[(E \pm i\eta)\, \mathbf{I} - \mathbf{H}_0 \right]^{-1}.$$

It is straightforward to combine these two results to obtain an expression for the Green functions of the coupled system, which reads

$$\mathbf{G}(E) = \mathbf{G}^{(0)}(E) + \mathbf{G}^{(0)}(E)\mathbf{V}\mathbf{G}(E), \tag{2.16}$$

where we have omitted the labels for retarded and advanced Green functions because this equation is satisfied by any Green function. Equation 2.16 is known as Dyson equation and is very useful to include interactions to a single-particle Hamiltonian. Furthermore, an interesting application of Dyson equation is when the non-perturbed Hamiltonian $\mathbf{H}_0$ is a subspace of the Hilbert space of the total Hamiltonian $\mathbf{H}$. In this case, the extra degrees of freedom from $\mathbf{H}$ not included in $\mathbf{H}_0$ can be treated as the perturbation $\mathbf{V}$. Specifically, say we have a system divided into two regions, $\mathbf{H} = \mathbf{H}_1 + \mathbf{H}_2$. We are able to calculate the Green functions of the system, $\mathbf{G}$, projected into one of the regions, say 1, as

$$\mathbf{P}_1\mathbf{G}\mathbf{P}_1 = \left[(E \pm i\eta)\,\mathbf{I} - \mathbf{H}_1 - \mathbf{\Sigma}\,(E)\right]^{-1},$$

where $\mathbf{P}_1$ are projectors into the subspace 1 and the extra degrees of freedom from the region 2 are included as an operator with an energy dependence, $\mathbf{\Sigma}(E)$, which is known as the electronic self-energy. The self-energy is thus defined as

$$\mathbf{\Sigma}\,(E) = \mathbf{V}_{12}\left[(E \pm i\eta)\,\mathbf{I} - \mathbf{H}_2\right]^{-1}\mathbf{V}_{21}.$$

The main effect of the self-energy is to project the degrees of freedom of the subspace 2 as a renormalization of the energy levels of the subspace 1. The Green function techniques are therefore a powerful tool to obtain the response of a system to any perturbation at any point of the space and to include hard to calculate degrees of freedom as a renormalization of the solutions of well-known problems.

In Chapter 3, we show how to obtain the Green functions of a semi-infinite graphene layer, i.e., with one edge, in the normal and the superconducting state. Dyson equation makes it straightforward to use this result to obtain the Green functions of a finite graphene layer (with two edges) and also of the normal-superconductor coupled system.

In this Thesis we mainly use retarded Green functions so hereon we will refer to them simply as 'Green functions', unless otherwise specified. It is also assumed that the imaginary part of the energy is present although it is omitted in many expressions.

As an straightforward example, we can calculate the Green function associated to a free Dirac particle. From the two-dimensional Dirac equation

$$\hat{H}(x,y)\psi(x,y) = E\psi(x,y),$$

we can apply the definition given in Equation 2.14 to obtain

$$\lim_{\eta\to 0}\left[E \pm i\eta - \hat{H}(x,y)\right]\hat{G}^{r,a}(x,x';y,y') = \delta(x-x')\delta(y-y'). \tag{2.17}$$

It is easy to give a physical interpretation to the Green function by solving the case of free single particle using $\hat{H} = -i\hbar v_F\left(\hat{\sigma}_x\partial_x + \hat{\sigma}_y\partial_y\right)$. Because there is no external potential, the Hamiltonian is invariant under translations. This implies that the Green function depends only on the difference $\mathrm{r}-\mathrm{r}'$. An ambiguity in the sign of the definition of the spatial differences $x-x'$ and $y-y'$ is taken into account with the introduction of an infinitesimal imaginary part in the energy, i.e. $E \to E \pm i\eta$. Assuming the Green functions are zero at the boundaries $|x-x'| \to \infty$ and $|y-y'| \to \infty$, we can Fourier transform Equation 2.17 and make the substitution $-i\partial_{x,y} \to k_{x,y}$ to obtain

$$\begin{aligned}
\hat{G}^{r,a}(x,x';y,y') &= \iint \frac{\mathrm{d}k_x}{2\pi}\frac{\mathrm{d}k_y}{2\pi} e^{ik_x|x-x'|+ik_y|y-y'|}\hat{G}^{r,a}_{\mathbf{k}}(k_x,k_y) \\
\hat{G}^{r,a}_{\mathbf{k}}(k_x,k_y) &= \frac{\hbar v_F}{(E\pm i\eta)^2 - \hbar^2 v_F^2(k_x^2+k_y^2)}\begin{pmatrix} \frac{E\pm i\eta}{\hbar v_F} & k_x - ik_y \\ k_x + ik_y & \frac{E\pm i\eta}{\hbar v_F}\end{pmatrix}
\end{aligned}$$

The Green function is physically interpreted as a quantity that gives the amplitude of propagation for a particle, hence the common name of *propagator*. In that sense, the retarded Green function corresponds to the propagation of a free-particle at (x',y') toward a different point (x,y). In this case, they are plane-waves propagating through the two-dimensional space with their source at (x',y'). On the other hand, the advanced Green functions represent plain-waves converging into (x',y') from every point of the space.

2.4.1.2 Single-particle Green function for a many-body system.

The Green functions techniques are very successfully applied to many-body problems. The Green functions represent solutions of the equation of motion of the system, which has a structure similar to a differential equation. They contain the relevant information for a given problem and are thus the building blocks for the solution of the system. The retarded Green function for a system of many fermions is defined as

$$G^R(\mathbf{k},s,t;s',t') = -i\theta(t-t')\langle\left\{c_{\mathbf{k}s}(t), c^\dagger_{\mathbf{k}s'}(t')\right\}\rangle, \tag{2.18}$$

where the indexes s, s' label the spin degree of freedom and the anti-commutator $\{\cdots\}$ is defined as $\{A,B\} = AB + BA$. In a system with translational invariance there is only a spatial dependence on the differences $\mathbf{r}'-\mathbf{r}$. Thus, the notation has been simplified in

terms of creation and destruction operators in the basis of the wave vectors $\mathbf{k}$. For a non-interacting particle this result reduces to the definition given in Equation 2.14. Since the operator $c_{\mathbf{k}s}(t)$ is an eigenfunction of the many-body Hamiltonian governing the system, these Green functions represent the amplitude of propagation of a particle between two points of space taking into account the interaction due to the rest of the particles of the system. An straightforward example is given by a non-interacting Hamiltonian in a general basis $|i\rangle$ of the form $H_0 = \sum_{ij} t_{ij} c_j^\dagger c_i$. Equation 2.14 transforms into

$$\sum_k \left(\delta_{ik}\left(\omega + i\eta\right) - t_{ik}\right)\left(\mathbf{G}_0^R\right)_{kj}(\omega) = \delta_{ij}.$$

$\mathbf{G}_0^R$ is the retarded Green function corresponding to the Hamiltonian H_0 in matrix form. If the basis is diagonal, one has $t_{ij} = \delta_{ij}\epsilon_i$ and thus[9]

$$\left(\mathbf{G}_0^R\right)_{ij}(\omega) = \frac{1}{\omega + i\eta - \epsilon_i \delta_{ij}}.$$

With this non-interacting result one can use Equation 2.16 to introduce a perturbation of the type $\mathbf{H} = \mathbf{H}_0 + \mathbf{H}_{int}$ just doing

$$\mathbf{G}^R(\omega) = \left[(\omega + i\eta)\mathbf{I} - \mathbf{H}_0 - \mathbf{\Sigma}(\omega)\right]^{-1},$$

where $\mathbf{I}$ is the identity matrix and the self-energy $\mathbf{\Sigma}(\omega)$ is interpreted as the matrix that dynamically renormalizes the matrix elements of the unperturbed Hamiltonian $\mathbf{H}_0$. In the case of a diagonal problem, the self-energy renormalizes the energy levels of the system as

$$\left(\mathbf{G}^R\right)_{ij}(\omega) = \frac{1}{\omega + i\eta - \epsilon_i - \Sigma_i(\omega)}\delta_{ij}.$$

This result is formally equivalent to the single-particle problem. In that case, the degrees of freedom of a subspace of the total system are included into the description of the rest of the system. In the many-body case, the different interactions between the components of the system can be impossible to treat separately, but they can be integrated out into self-energy. Subsequently, the self-energy is included in the Green function describing a part of the system that is easier to handle. As a consequence, different approximations can be done to the self-energy and included into the Green function of the total system. Finding the appropriate self-energy for a many-body system is usually a highly non-trivial problem that goes beyond the scope of this Thesis. In the following chapters, a single-particle picture is used to describe the physics of the systems described.

[9] By taking $\hbar = 1$ there is an equivalence between energies and frequencies that simplifies the notation.

2.4.1.3 The Bogoliubov-de Gennes equations and the Nambu formalism.

The transport properties of normal-superconductor hybrid systems are mainly studied through the LDOS and the current-voltage ($I-V$) characteristics. These two properties are determined by the equilibrium and non-equilibrium Green functions of the system. Therefore, the Green functions of the system, obtained from the Bogoliubov-de Gennes (BDG) equations introduced in Equation 2.11, are of capital importance in the description of these systems. Equation 2.11 is expressed in Nambu space, which contains the $SU(2)$ symmetry given by the pairing potential between electrons and holes. Thus, we can define the fermion field operators

$$\begin{aligned} \psi(\mathbf{r},t) &= \begin{pmatrix} \mathbf{c}_\uparrow(\mathbf{r},t) \\ \mathbf{c}_\downarrow^\dagger(\mathbf{r},t) \end{pmatrix} \\ \psi^\dagger(\mathbf{r},t) &= \begin{pmatrix} \mathbf{c}_\uparrow^\dagger(\mathbf{r},t) & \mathbf{c}_\downarrow(\mathbf{r},t) \end{pmatrix}, \end{aligned} \tag{2.19}$$

where $\mathbf{c}_s^\dagger(\mathbf{r},t)$ and $\mathbf{c}_s(\mathbf{r},t)$ are the fermion operators of creation and destruction of a particle with spin s and space-time coordinates $(\mathbf{r},t)$. This notation was first introduced by Anderson [76] in the study of the RPA of the Coulomb correlation energy in the BCS theory and developed by Nambu [77] in the study of the Gauge invariance of the BCS theory. It exploits the fact that the superconducting pairing amplitude Δ introduces non-zero correlations of the type $\langle \mathbf{c}_\uparrow^\dagger(\mathbf{r},t)\mathbf{c}_\downarrow^\dagger(\mathbf{r}',t')\rangle$ and $\langle \mathbf{c}_\downarrow(\mathbf{r},t)\mathbf{c}_\uparrow(\mathbf{r}',t')\rangle$. These correlations, which do not conserve the number of particles and should be zero in the normal state, measure the probability amplitude of creating and destroying a Cooper pair, respectively. We can thus define the retarded Green function as

$$\check{G}^r(\mathbf{r},t;\mathbf{r}',t') = -i\theta(t-t') \begin{pmatrix} \langle \mathbf{c}_\uparrow(\mathbf{r},t)\mathbf{c}_\uparrow^\dagger(\mathbf{r}',t')\rangle & \langle \mathbf{c}_\uparrow(\mathbf{r},t)\mathbf{c}_\downarrow(\mathbf{r}',t')\rangle \\ \langle \mathbf{c}_\downarrow^\dagger(\mathbf{r},t)\mathbf{c}_\uparrow^\dagger(\mathbf{r}',t')\rangle & \langle \mathbf{c}_\downarrow^\dagger(\mathbf{r},t)\mathbf{c}_\downarrow(\mathbf{r}',t')\rangle \end{pmatrix}. \tag{2.20}$$

In the absence of external fields, one needs to impose that the Green functions fulfill the inhomogeneous BDG equations

$$i\hbar\frac{\partial}{\partial t}\check{G}^r(\mathbf{r},t;\mathbf{r}',t') - \int \mathrm{d}\mathbf{r}''\check{H}(\mathbf{r},\mathbf{r}'',t)\check{G}^r(\mathbf{r}'',t;\mathbf{r}',t') = \hbar\delta(t-t')\delta(\mathbf{r}-\mathbf{r}'),$$

where

$$\check{H}(\mathbf{r},\mathbf{r}',t) = \begin{pmatrix} \delta(\mathbf{r}-\mathbf{r}')\mathbf{H}_e(\mathbf{r},t) & \Delta(\mathbf{r},\mathbf{r}',t) \\ \Delta^*(\mathbf{r},\mathbf{r}',t) & -\delta(\mathbf{r}-\mathbf{r}')\mathbf{H}_e^*(\mathbf{r},t) \end{pmatrix},$$

and $\mathbf{H}_e(\mathbf{r},t)$ is any single-electron Hamiltonian. Thus, we can write the BDG equations in the integral form

$$\theta(t-t')\begin{pmatrix} u(\mathbf{r},t) \\ v(\mathbf{r},t) \end{pmatrix} = i\int \mathrm{d}t'\mathrm{d}\mathbf{r}' \begin{pmatrix} \mathrm{G}^r_{11}(\mathbf{r},t;\mathbf{r}',t') & \mathrm{G}^r_{12}(\mathbf{r},t;\mathbf{r}',t') \\ \mathrm{G}^r_{21}(\mathbf{r},t;\mathbf{r}',t') & \mathrm{G}^r_{22}(\mathbf{r},t;\mathbf{r}',t') \end{pmatrix} \begin{pmatrix} u(\mathbf{r}',t') \\ v(\mathbf{r}',t') \end{pmatrix}.$$

As a consequence, we identify the retarded Green function $\check{G}^r(\mathbf{r},t;\mathbf{r}',t')$ as the propagator of the quasi-particles from the space-time coordinates $(\mathbf{r}',t')$ to any other point $(\mathbf{r},t)$, with $t>t'$. The diagonal components $\mathrm{G}^r_{11}(\mathbf{r},t;\mathbf{r}',t')$ and $\mathrm{G}^r_{22}(\mathbf{r},t;\mathbf{r}',t')$ describe the electron and hole-like propagators while the non-diagonal components include the processes featuring conversion of electrons into holes.

When the Hamiltonian does not have an explicit dependence on time, the Green function from Equation 2.20 is written as $\check{G}^r(\mathbf{r},t;\mathbf{r}',t') = \check{G}^r(\mathbf{r},\mathbf{r}';t-t') = \check{G}^r(\mathbf{r},\mathbf{r}';\tau)$. One can thus define the Fourier transform

$$\check{G}^r(\mathbf{r},\mathbf{r}';E) = \int_{-\infty}^{\infty} \mathrm{d}\tau e^{iE\tau/\hbar}\check{G}^r(\mathbf{r},\mathbf{r}';\tau),$$

that now fulfills the time-independent inhomogeneous BDG equations

$$E\check{G}^r(\mathbf{r},\mathbf{r}';E) - \int \mathrm{d}\mathbf{r}''\check{H}(\mathbf{r},\mathbf{r}'')\check{G}^r(\mathbf{r}'',\mathbf{r}';E) = \hbar\delta\left(\mathbf{r}-\mathbf{r}'\right).$$

2.4.2 Non-equilibrium Green functions. The Keldysh formalism.

In this section the Keldysh non-equilibrium Green functions are briefly presented. An extended review, full of historical information, is given in Ref. [78]. A detailed formalism is introduced in Ref. [79].

The Keldysh technique is a formalism for the treatment of out-of-equilibrium interacting many-body systems. It was developed by L.V. Keldysh in 1964 [80] to study the Green functions of systems beyond the linear response or the adiabatic approach. The Keldysh technique is a generalization of the diagrammatic perturbation theory for the equilibrium that includes new propagators in such a way that the diagrammatic structure of the theory remains invariant.

We start with the definition of the Hamiltonian of the system $\mathbf{H} = \mathbf{H}_0 + \mathbf{V}(t)$. This system is analogous to the perturbed system in the equilibrium case, but now $\mathbf{H}_0$ is a Hamiltonian without interactions and $\mathbf{V}(t)$ is a time-dependent perturbation which may include external potentials or interaction terms. We suppose that the interaction can be adiabatically "switched on and off" at $t\to\pm\infty$. This means that we can continuously evolve the state at $t\to-\infty$ into the one at $t\to\infty$. At equilibrium both states are

only distinguished by a phase factor due to a symmetry in time. Out of equilibrium this states can be different because the perturbation has a dependence on time. Keldysh [80] suggested to increase the temporal evolution $-\infty \to t \to \infty$ by returning the state to $-\infty$. In the Keldysh path, the initial and the final states are both at $t \to -\infty$ and thus are distinguished only by a phase factor. The first branch of Keldysh path, $-\infty \to t \to \infty$, is usually labeled by $+$, while the second branch, $\infty \to t \to -\infty$, is labeled by $-$. The operator $\mathbf{T}_C$ is then responsible of the alignment of the different temporal parameters along the Keldysh path. As a consequence, the propagators in the Keldysh formalism are defined in an analogous way to the equilibrium,

$$\mathbf{G}(\mathbf{r}, t_\alpha; \mathbf{r}', t_\beta) = -i \frac{\langle \Psi_H | \mathbf{T}_C \left[\mathbf{\Psi}_\sigma(\mathbf{r}, t_\alpha) \mathbf{\Psi}^\dagger_\sigma(\mathbf{r}', t_\beta) \right] | \Psi_H \rangle}{\langle \Psi_H | \Psi_H \rangle}.$$

The wave vectors $|\Psi_H\rangle$ are in the Heisenberg representation while the operators $\mathbf{\Psi}_\sigma(\mathbf{r}, t_\alpha)$ have a time-dependence and are in the interaction picture. The labels $\alpha, \beta = \pm$ represent the branch of the Keldysh time-contour. Analogously, for a discrete basis of states $|i\rangle$, like the ones used in tight-binding models, we have

$$\mathbf{G}_{ij}(t_\alpha, t_\beta) = -i \frac{\langle \Psi_H | \mathbf{T}_C \left[\mathbf{c}_{i\sigma}(t_\alpha) \mathbf{c}^\dagger_{j\sigma}(t_\beta) \right] | \Psi_H \rangle}{\langle \Psi_H | \Psi_H \rangle}.$$

To reduce the notation involved in the definitions of the Green functions for the Keldysh formalism we hereon show only the results for a discrete basis.

We have thus increased the number of propagators by four, with the possibilities

$$\begin{aligned}
\mathbf{G}_{ij}(t_+, t_+) &\equiv \mathbf{G}^{++}_{ij}(t_+, t_+) = -i\langle \mathbf{T} \left[\mathbf{c}_{i\sigma}(t) \mathbf{c}^\dagger_{j\sigma}(t') \right] \rangle \\
\mathbf{G}_{ij}(t_+, t_-) &\equiv \mathbf{G}^{+-}_{ij}(t_+, t_-) = i\langle \mathbf{c}^\dagger_{j\sigma}(t') \mathbf{c}_{i\sigma}(t) \rangle \\
\mathbf{G}_{ij}(t_-, t_+) &\equiv \mathbf{G}^{-+}_{ij}(t_-, t_+) = -i\langle \mathbf{c}_{i\sigma}(t) \mathbf{c}^\dagger_{j\sigma}(t') \rangle \\
\mathbf{G}_{ij}(t_-, t_-) &\equiv \mathbf{G}^{--}_{ij}(t_-, t_-) = -i\langle \bar{\mathbf{T}} \left[\mathbf{c}_{i\sigma}(t) \mathbf{c}^\dagger_{j\sigma}(t') \right] \rangle
\end{aligned}$$

The first and last Green functions have both time arguments in the $+$ and $-$ branches, respectively. Thus, $\mathbf{T}$ is the causal time-ordering operator and $\bar{\mathbf{T}}$ is the anti-causal time-ordering operator. The latter is used because the Keldysh-contour branch $-$ goes from positive time at $+\infty$ to negative time at $-\infty$. $\mathbf{G}^{+-}_{ij}$ is of fundamental interest due to the fact that at equal times it corresponds to the distribution of electrons out of equilibrium. It is thus related with the electrical current[10]. The Green functions are not independent

[10] The temperature is a parameter that is not explicitly included on Keldysh formalism. This fact is used to include it in an indirect form. $\mathbf{G}^{+-}_{ij}$, for $t = t' = 0$ and $i = j$, is therefore reduced to

$$\mathbf{G}^{+-}_{ii}(0) = i\langle \mathbf{n}_{i\sigma} \rangle = \int_{-\infty}^{\infty} \frac{\mathrm{d}\omega}{2\pi} \mathbf{G}^{+-}_{ii}(\omega).$$

and obey the causality condition $\mathbf{G}_{ij}^{++} + \mathbf{G}_{ij}^{--} = \mathbf{G}_{ij}^{+-} + \mathbf{G}_{ij}^{-+}$.

It is useful to define a matrix Green function

$$\hat{\mathbf{G}} = \begin{pmatrix} \mathbf{G}^{++} & \mathbf{G}^{+-} \\ \mathbf{G}^{-+} & \mathbf{G}^{--} \end{pmatrix},$$

where the coordinates dependence has been omitted for simplicity. The causality condition is included demanding that $\det\left[\hat{\mathbf{G}}\right] = 0$. The breaking of the time symmetry results in the $SU(2)$ representation of the propagator space, represented by the notation $\cdot\hat{\cdot}\cdot$ on the matrix Green function. Formally, the non-equilibrium formalism is equivalent to the perturbation theory but doubling the matrix dimension. It is then possible to complete the diagrammatic procedure, but the details are beyond the scope of this introduction. However, it is important to include the result for the Dyson equation, which is still valid out of equilibrium, and reads

$$\hat{\mathbf{G}}(t,t') = \hat{\mathbf{g}}(t,t') + \int \mathrm{d}t_1 \int \mathrm{d}t_2 \hat{\mathbf{g}}(t,t_1)\hat{\mathbf{\Sigma}}(t_1,t_2)\hat{\mathbf{G}}(t_2,t'). \tag{2.21}$$

The spatial dependence is omitted and the non-perturbed propagators are represented by $\hat{\mathbf{g}}$ instead of $\hat{\mathbf{G}}^{(0)}$ for simplicity. The self-energy $\hat{\mathbf{\Sigma}}$ is a matrix in the Keldysh $SU(2)$ space. In the stationary case, the Green functions depend only on the difference in times and it is possible to Fourier transform Equation 2.21 into an energy dependent algebraic equation that reads

$$\hat{\mathbf{G}}(E) = \hat{\mathbf{g}}(E) + \hat{\mathbf{g}}(E)\hat{\mathbf{\Sigma}}(E)\hat{\mathbf{G}}(E).$$

In the superconducting state, the breaking of gauge symmetry due to the order parameter yields that the propagators have to be written in Nambu $SU(2)$ space as it is done in Equation 2.20 for the retarded Green function $\check{G}^r$. The notation $\cdot\check{\cdot}\cdot$ corresponds to Nambu space. The non-equilibrium propagator is expressed both in Nambu and Keldysh spaces in the generalized form

$$\check{\hat{\mathbf{G}}}_{ij}(t_\alpha, t_\beta) = -i\langle \mathbf{T}_C \left[\psi_i(t_\alpha)\psi_j^\dagger(t_\beta)\right]\rangle,$$

where the fermion field operators are defined in Equation 2.19 and $\alpha, \beta = \pm$. The electrical current depends only on the element $\check{\mathbf{G}}^{+-}$, which is given by

$$\check{\mathbf{G}}_{ij}^{+-}(t,t') = i \begin{pmatrix} \langle \mathbf{c}_{j\uparrow}^\dagger(t')\mathbf{c}_{i\downarrow}(t)\rangle & \langle \mathbf{c}_{j\downarrow}(t')\mathbf{c}_{i\uparrow}(t)\rangle \\ \langle \mathbf{c}_{j\uparrow}^\dagger(t')\mathbf{c}_{i\downarrow}^\dagger(t)\rangle & \langle \mathbf{c}_{j\downarrow}(t')\mathbf{c}_{i\uparrow}^\dagger(t)\rangle \end{pmatrix}.$$

As a consequence, we have $\mathbf{G}_{ii}^{+-}(\omega) = 2i\pi\rho_{ii}(\omega)f(\omega)$, with $f(\omega)$ being the equilibrium Fermi distribution for electrons. Analogously, we have $\mathbf{G}_{ii}^{-+}(\omega) = -2i\pi\rho_{ii}(\omega)\left[1 - f(\omega)\right]$. This indicates that, for any chosen basis, we always have $\mathbf{G}_{ii}^{+-}(\omega) \propto f(\omega)$ and $\mathbf{G}_{ii}^{-+}(\omega) \propto 1 - f(\omega)$.

2.4.3 Normal transport.

Describing transport properties of metallic junctions requires the use of non-equilibrium Green functions. They are essential to give a microscopic description of the junctions and treat many-body effects properly. A calculation of the tunneling current of metallic junctions separated by an insulator within the Keldysh formalism was first introduced in Ref. [81]. An analogous description is introduced here, highlighting the important aspects of the theory but without going into detail.

A typical junction consists of three separated systems representing two macroscopic electrodes, denoted L and R, and a central region C representing the junction. The Hamiltonian of the system H_0 is therefore divided into the Hamiltonians of each region as $H = H_L + H_C + H_R + V \equiv H_0 + V$, where V represents a perturbation. The different regions in H_0 are assumed to be in local thermal equilibrium (i.e. in the Keldysh contour they belong to the initial state at $t \to -\infty$). In a compact notation we can define a Hamiltonian matrix

$$\mathbf{H} = \begin{pmatrix} H_L & V_{LC} & 0 \\ V_{CL} & H_C & V_{CR} \\ 0 & V_{RC} & H_R \end{pmatrix},$$

where the effect of the perturbation is divided as well into the interaction between different regions. By introducing the Keldysh Green function operator

$$\mathbf{G}^{+-} = (1 + \mathbf{G}^r V)\, \mathbf{G}^{+-(0)}\, (1 + \mathbf{G}^a V)\,,$$

where the Green retarded and advanced Green functions $\mathbf{G}^{r,a}$ are the ones previously introduced. The unperturbed Green function operator is defined as

$$\mathbf{G}^{+-(0)} = \left(\mathbf{G}^{a(0)} - \mathbf{G}^{r(0)}\right) f_{L,R},$$

with $f_{L,R} = \left(e^{\beta\left(\omega - \mu_{L,R}\right)} + 1\right)^{-1}$ the Fermi electronic distributions at the electrodes L and R. These factors include the effect of the temperature with the usual notation $\beta = (k_B T)^{-1}$.

The final state after the introduction of the perturbation is independent of the value of $G_C^{+-(0)}$, so it is common to take $G_C^{+-(0)} = 0$ to simplify.

The Keldysh Green function operator allows to calculate the current at each electrode as

$$I_L = \frac{2e}{h} \int \mathrm{d}\omega \mathrm{Tr}\left[V_{LC}\mathbf{G}_{CL}^{+-} - V_{CL}\mathbf{G}_{LC}^{+-}\right].$$

An analogous expression is obtained for I_R. Further manipulation leads to

$$I_L = I_R = \frac{8e}{h}\int \mathrm{d}\omega \left(f_L(\omega) - f_R(\omega)\right) \mathrm{Tr}\left[\Gamma_L \mathbf{G}^r \Gamma_R \mathbf{G}^a\right],$$

with $\Gamma_{L,R} = \mathrm{Im}\Sigma_{L,R}$ and $\Sigma_{L,R} = V_{C(L,R)} G^{(0)}_{L,R} V_{(L,R)C}$.

2.4.4 Extension to the superconductor state.

Following the previous results, one can consider now that the central part C is in the superconductor state. The system thus represent a NSN junction. This implies the need to expand the formalism to the Nambu space. All the Green functions previously introduced are expanded as follows

$$\check{\mathbf{G}}^{r,a(0)}_{L,R} = \begin{pmatrix} \check{\mathbf{G}}^{r,a(0)}_{L,R,e} & 0 \\ 0 & \check{\mathbf{G}}^{r,a(0)}_{L,R,h} \end{pmatrix} = \begin{pmatrix} \left[\omega \pm i\eta - \mathrm{H}_{L,R}\right]^{-1} & 0 \\ 0 & \left[\omega \pm i\eta + \mathrm{H}_{L,R}\right]^{-1} \end{pmatrix}.$$

The unperturbed Green function is also expanded as $\check{\mathrm{G}}^{+-(0)}_{L,R} = \left(\check{\mathrm{G}}^{a(0)}_{L,R} - \check{\mathrm{G}}^{r(0)}_{L,R}\right)\check{f}_{L,R}$, where the Fermi electronic distribution has also been expanded to

$$\check{f}_{L,R} = \begin{pmatrix} f^e_{L,R} & 0 \\ 0 & f^h_{L,R} \end{pmatrix},$$

with $f^{e,h}_{L,R} = \left(e^{\beta\left(\omega \pm \mu_{L,R}\right)} + 1\right)^{-1}$.

The currents are computed form the expression

$$I_\mu = \frac{e}{h}\int \mathrm{d}\omega \mathrm{Tr}\left[\check{\tau}_z \left(V_{\mu C}\check{\mathrm{G}}^{+-}_{C\mu} - V_{C\mu}\check{\mathrm{G}}^{+-}_{\mu C}\right)\right],$$

with $\mu = L, R$ and $t\check{a}u_z$ the Pauli matrix in Nambu space. At subgap voltages (i.e. when $\mu_{L,R} < \Delta$), the current is reduced to

$$I_\mu = \frac{2e}{h}\int \mathrm{d}\omega \left[\left(f^e_\mu - f^h_\mu\right) R_{A\mu} + \left(f^e_\mu - f^h_{\bar{\mu}}\right) T_{CAR} + \left(f^e_\mu - f^e_{\bar{\mu}}\right) T_{EC}\right], \tag{2.22}$$

where if $\mu = L, R$ then $\bar{\mu} = R, L$. In this important result are summarized all the microscopic processes that give a contribution to the subgap current. Indeed, the current measured at electrode μ depends on the local Andreev reflection that take place at that electrode

$$R_{A\mu} = 4\mathrm{Tr}\left[\Gamma^e_\mu \mathbf{G}^r \Gamma^h_\mu \mathbf{G}^a\right], \tag{2.23}$$

with $\Gamma_\mu^{e,h} = \mathrm{Im}\Sigma_\mu^{e,h}$. Also included in the current are the nonlocal processes like the crossed Andreev reflection (CAR)

$$T_{CAR} = 4\mathrm{Tr}\left[\Gamma_\mu^e \mathbf{G}^r \Gamma_{\bar{\mu}}^h \mathbf{G}^a\right], \tag{2.24}$$

and the electron co-tunneling (EC)

$$T_{EC} = 4\mathrm{Tr}\left[\Gamma_\mu^e \mathbf{G}^r \Gamma_{\bar{\mu}}^e \mathbf{G}^a\right]. \tag{2.25}$$

Chapter 3

Green functions techniques for graphene.

3.1 Introduction.

This chapter is organized as follows: we start describing the edge Green function of a semi-infinite graphene layer for the tight-binding model. We use this result as a building block for the description of the finite isolated layer. Next, we introduce the method for obtaining the Green functions through the asymptotic solutions of the Dirac-Bogoliubov-de Gennes equations. Then we obtain the Green functions of a graphene layer with armchair and zigzag edges. For both cases we start with the normal solutions and, subsequently, expand the results to Nambu space to obtain the superconducting results. Finally, we expose a method to combine different continuous solutions using a microscopic Dyson equation. The results presented in this Chapter have been published in [82] and [83].

3.2 Green functions in the tight-binding model.

3.2.1 Tight-binding description of isolated graphene layers.

We concentrate here in the derivation of the edge Green function for a semi-infinite graphene layer with armchair orientation. We assume that there is translational symmetry in the direction parallel to the edge (y). The semi-infinite system can be decomposed into lines of sites in the y direction which are coupled by hopping elements with the neighboring lines on the x direction. The unit cell on each line includes two sites

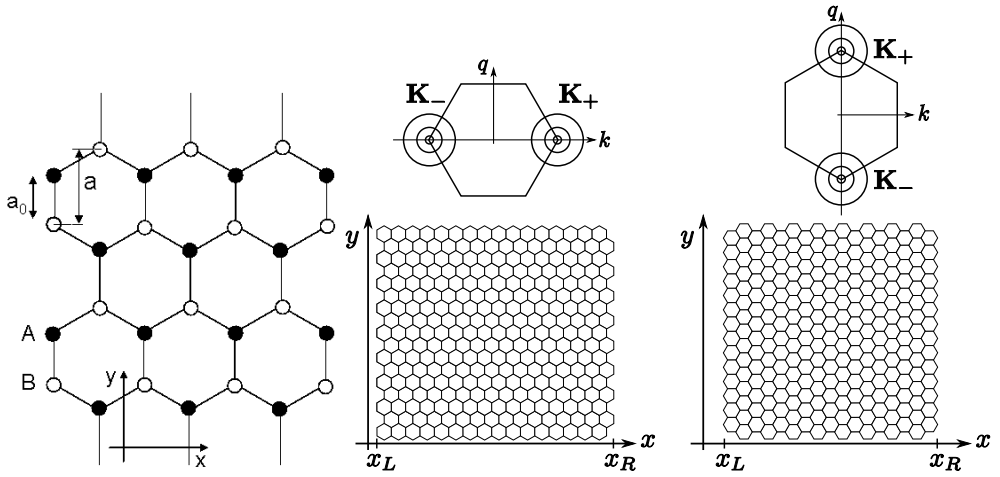

FIGURE 3.1: Geometry of the systems treated in this work: a horizontally finite sheet of graphene with armchair edges (left) or zigzag edges (right). The sheets are assumed to be infinite in the vertical direction. The edges are located at positions x_L and x_R. These positions can be taken to be infinite, representing a bulk of graphene (infinite plane) or a semi-infinite layer (infinite half-plane). For each geometry we represent the chosen Dirac points in the Brillouin zone.

corresponding to each hexagonal sublattice that are denoted by A and B. These sites are coupled by a hopping element t_g within the unit cell. Thus, the cell Hamiltonian is given by

$$\hat{h} = \begin{pmatrix} \epsilon & t_g \\ t_g & \epsilon \end{pmatrix}.$$

The hopping elements between neighboring lines couple also sites of type A with sites of type B but should include a phase factor $e^{\pm iqa}$ due to the displacement of the cells in the y direction. The hopping matrix in the A-B space (both in the forward and in the backward direction) can be written as $\hat{t}(q) = t_g \hat{U}(q)$, where

$$\hat{U}(q) = \begin{pmatrix} 0 & e^{iqa} \\ e^{-iqa} & 0 \end{pmatrix}.$$

The self-similarity of the semi-infinite system with one additional line of sites leads to the following implicit equation for the edge Green function

$$\hat{g}(q,\omega) = \left[\omega \hat{I} - \hat{h} - t_g^2 \hat{U}(q)\hat{g}(q,\omega)\hat{U}(q)\right]^{-1}.$$

Hereafter we implicitly assume that ω stands for $\omega \pm i\eta$ and that the limit $\eta \to 0$ is taken to obtain the retarded or the advanced component respectively. We can now define $\hat{\tilde{g}} = \hat{U}\hat{g}$ which satisfies the simpler equation

$$\hat{\tilde{g}} = \left[\hat{X}(q,\omega) - t_g^2 \hat{\tilde{g}}\right]^{-1},$$

where $\hat{X}(q,\omega) = (\omega\hat{I} - \hat{h})\hat{U}(q)$.

To obtain an explicit expression for $\hat{\tilde{g}}$ it is useful to perform a basis rotation in order to diagonalize the matrix $\hat{X}$. The general form of this rotation is $\hat{R} = \hat{R}_1\hat{R}_2$ where $\hat{R}_1 = e^{iqa/2\hat{\sigma}_z}$, $\hat{\sigma}_z$ being the z-Pauli matrix acting on the sublattice space and

$$\hat{R}_2 = \frac{1}{\sqrt{-2\sin\alpha}} \begin{pmatrix} e^{i\alpha/2} & e^{-i\alpha/2} \\ ie^{-i\alpha/2} & ie^{i\alpha/2} \end{pmatrix},$$

where $\cos\alpha = t_g \sin qa/(\omega - \epsilon)$. The eigenvalues of $\hat{X}$ are $x_{1,2} = -t_g \cos qa \pm \sqrt{(\omega-\epsilon)^2 - t_g^2 \sin^2 qa}$. We thus get

$$\begin{aligned} \hat{g}(q,\omega) = \begin{pmatrix} g & f \\ f' & g \end{pmatrix} &= \frac{1}{t_g}\hat{U}\hat{R}_1\hat{R}_2 \begin{pmatrix} e^{i\phi_1} & 0 \\ 0 & e^{-i\phi_2} \end{pmatrix} \hat{R}_2^{-1}\hat{R}_1^\dagger \\ &= \frac{1}{2t_g \sin\alpha} \begin{pmatrix} e^{i\phi_1} - e^{-i\phi_2} & ie^{iqa}\left[e^{-i(\alpha-\phi_1)} - e^{i(\alpha-\phi_2)}\right] \\ -ie^{-iqa}\left[e^{i(\alpha+\phi_1)} - e^{-i(\alpha+\phi_2)}\right] & e^{i\phi_1} - e^{-i\phi_2} \end{pmatrix} \end{aligned} \quad (3.1)$$

where $\cos\phi_{1,2} = x_{1,2}/(2t_g)$. The eigenvalues $e^{i\phi_1}$ and $e^{-i\phi_2}$ have been chosen so that the resulting Green functions have the proper behavior when the frequency goes to infinity.

3.2.2 Finite graphene layer

Starting from the results of the previous section one can obtain the Green functions of a finite graphene layer by introducing a perturbation consisting in breaking the bond between the N-th line and its neighbors on the $N+1$ line. From Dyson's equation we obtain the following set of coupled equations

$$\begin{aligned} \hat{g}^F_{n,n} &= \hat{g}_{n,n} - \hat{g}_{n,N+1}\hat{t}\hat{g}^F_{N,n} \\ \hat{g}^F_{N,n} &= \hat{g}_{N,n} - \hat{g}_{N,N+1}\hat{t}\hat{g}^F_{N,n}, \end{aligned} \quad (3.2)$$

where the superindex F stands for the finite system and the subindexes i, j indicate the lines within the layer. On the other hand the elements $\hat{g}_{N,N+1}$ can be expressed as $\hat{g}_{N,N+1} = \hat{g}^F_{N,N}\hat{t}\hat{g}_{N+1,N+1}$. We now use that $\hat{g}_{1,1} = \hat{g}$ and $\hat{g}_{n,N} = \hat{g}_{N,n} = \left(\hat{g}\hat{t}\right)^{N-n}\hat{g}_{n,n}$, where $\hat{g}$ corresponds to the surface Green function for the semi-infinite system derived in the previous section. Also we have $\hat{g}_{N+1,N+1} = \left[\hat{g} - \hat{t}\hat{g}^F_{N,N}\hat{t}\right]^{-1}$ and $\hat{g}_{n,n} = \left[\hat{I} - \left(\hat{g}\hat{t}\right)^{2n}\right]\left[\hat{I} - \left(\hat{g}\hat{t}\right)^{2}\right]^{-1}\hat{g}$, which allows to obtain

$$\begin{aligned}
\hat{g}^F_{n,n} &= \left[\hat{I} - \left(\hat{g}\hat{t}\right)^2\right]^{-1}\left[\hat{I} - \left(\hat{g}\hat{t}\right)^{2(N+1)}\right]^{-1}\left[\hat{I} - \left(\hat{g}\hat{t}\right)^{2n}\right]\left[\hat{I} - \left(\hat{g}\hat{t}\right)^{2(N-n+1)}\right]\hat{g} \\
\hat{g}^F_{n,N} &= \left[\hat{I} - \left(\hat{g}\hat{t}\right)^{2(N+1)}\right]^{-1}\left[\hat{I} - \left(\hat{g}\hat{t}\right)^{2n}\right]\left(\hat{g}\hat{t}\right)^{N-n}\hat{g}.
\end{aligned} \tag{3.3}$$

Making use of the rotation matrix defined in the previous section these quantities can be written in the following rather simple form

$$\begin{aligned}
\hat{g}^F_{n,n} &= \frac{1}{t_g}\hat{R}\begin{pmatrix} \frac{\sin n\phi_1}{\sin\phi_1}\frac{\sin(N-n+1)\phi_1}{\sin(N+1)\phi_1} & 0 \\ 0 & \frac{\sin n\phi_2}{\sin\phi_2}\frac{\sin(N-n+1)\phi_2}{\sin(N+1)\phi_2} \end{pmatrix}\hat{R}^{-1}\hat{U} \\
\hat{g}^F_{n,N} &= \frac{1}{t_g}\hat{R}\begin{pmatrix} \frac{\sin n\phi_1}{\sin(N+1)\phi_1} & 0 \\ 0 & \frac{\sin n\phi_2}{\sin(N+1)\phi_2} \end{pmatrix}\hat{R}^{-1}\hat{U}.
\end{aligned} \tag{3.4}$$

One can have the expression for the borders of the layer setting $n = 1$ or $n = N$. Then, the eigenvalues of the Green functions become $\sin N\phi_i / \sin(N+1)\phi_i$ and $\sin\phi_i / \sin(N+1)\phi_i$, with $i = 1, 2$, for the $\hat{g}^F_{1,1} = \hat{g}^F_{N,N}$ and $\hat{g}^F_{1,N} = \hat{g}^F_{N,1}$ cases, respectively. This expressions are equivalent to those for a finite tight-binding chain [84].

The poles of these Green functions determine the spectral properties of the layer. These poles are fixed by the condition $\sin(N+1)\phi_{1,2} = 0$, which is satisfied by $\phi_{1,2} = m\pi/(N+1)$, where m is an integer. One can associate this condition with the quantization of the transverse momentum which is used in the continuous model for describing armchair nanoribbons [37]. At the charge neutrality condition the existence of zero energy states requires $\phi_{1,2} = \pm 2\pi/3$, which can only be satisfied for $N = 3p + 2$ (in a more compact notation for $N \bmod 3 = 2$). Therefore the layers can be classified into metallic, for the $N \bmod 3 = 2$ case, and insulating for the other cases ($N \bmod 3 = 0, 1$). In the insulating cases the gap in the spectrum is $2E_g$, where $E_g \simeq \pi\hbar v_F/3L$, $L = Na/\sqrt{3}$ being the length of the layer. It should be noted that electron states in the metallic case are doubly degenerate, while the degeneracy is removed in the insulating cases [37].

3.3 Continuous approach to graphene layers with edges.

A complete description of the low energy electron excitations on a graphene layer is reached by superposing solutions on both valleys. Each solution $\Phi_{\pm}$ is modulated by a rapidly varying plane wave from each valley $e^{i\mathbf{K}_{\pm}\cdot\mathbf{r}}$ [5] thus giving

$$\Phi(x,y)=e^{iqy}\phi(x)=e^{iqy}\left[e^{iKx}\phi_{+}(x)+e^{-iKx}\phi_{-}(x)\right]. \tag{3.5}$$

This wave function is solution of Schrödinger's equation for a Hamiltonian that combines both valleys. However, it is helpful to use a four-component spinor notation for the wave function made from the two-dimensional spinors for each valley in which the phase factors are omitted (i.e. $\psi^T=\left(\phi_+^T,\phi_-^T\right)=\left(\phi_+^A,\phi_+^B,\phi_-^A,\phi_-^B\right)$) [17]. This new notation is useful in order to calculate the full Green function of the system, including both valley and pseudospin degrees of freedom. The four-dimensional spinor obeys the equation $\check{H}\psi(x)=E\psi(x)$, where

$$\check{H}=\begin{pmatrix}\hat{H}_{+} & 0\\ 0 & \hat{H}_{-}\end{pmatrix} \tag{3.6}$$

is the Dirac Hamiltonian in sublattice and valley spaces. We are using the notation $\cdot\check{\cdot}\cdot$ for 4×4 matrices and $\cdot\hat{\cdot}\cdot$ for 2×2 matrices.

The Green function associated to $\Psi(x,y)=e^{iqy}\psi(x)$ is $\check{G}_{\psi}(x,x',y)=\int\check{G}_{\psi}(x,x';q)\,e^{iqy}dq$, where $\check{G}_{\psi}(x,x';q)$ satisfies the 4×4 matrix equation

$$\begin{gathered}\left[\check{H}(q)-E\check{I}\right]\check{G}_{\psi}(x,x';q)=\delta(x-x')\check{I}\\ \begin{pmatrix}\hat{H}_{+}-E & 0\\ 0 & \hat{H}_{-}-E\end{pmatrix}\begin{pmatrix}\hat{G}_{\psi}^{++} & \hat{G}_{\psi}^{+-}\\ \hat{G}_{\psi}^{-+} & \hat{G}_{\psi}^{--}\end{pmatrix}=\delta(x-x')\check{I},\end{gathered} \tag{3.7}$$

with $\check{I}$ the 4-dimensional identity matrix. Hereafter we implicitly assume that E stands for $E+i\eta$ and that the limit $\eta\to0$ has been taken to obtain the retarded component of the Green function. From the elements of the full Green function $\check{G}_{\psi}$ we can define a valley superposed Green function $\hat{G}_{\phi}$, associated with the wave function of Eq. (3.5), as

$$\hat{G}_{\phi}(x,x',y,y')=\int\mathrm{d}q e^{iq(y-y')}\sum_{\mu,\nu=+,-}e^{i(\mathbf{K}_{\mu}\cdot\mathbf{r}-\mathbf{K}_{\nu}\cdot\mathbf{r}')}\hat{G}_{\psi}^{\mu\nu}(x,x';q). \tag{3.8}$$

Besides allowing valley mixing, this Green function include the phase factors $\exp\left[i\left(\mathbf{K}_{\mu}\mathbf{r}-\mathbf{K}_{\nu}\mathbf{r}'\right)\right]$ which are crucial to describe the presence of well defined edges or interfaces at the atomic scale. This valley superposed Green function is derived in the next sections for armchair and zigzag edges.

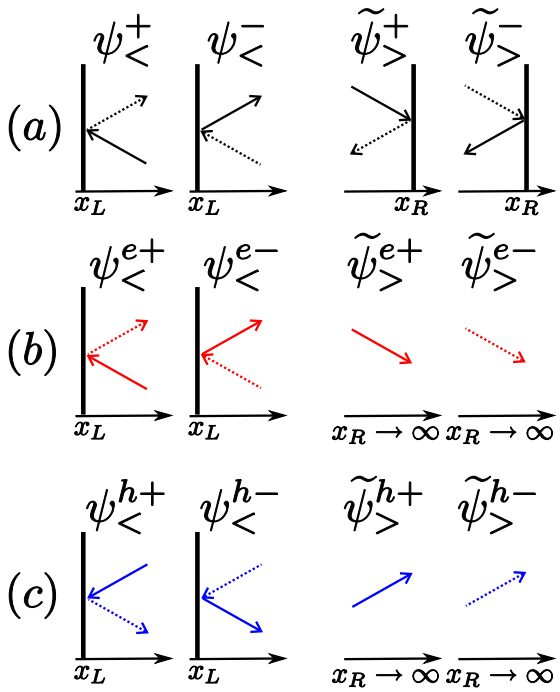

FIGURE 3.2: Schematic representation of the asymptotic solutions of Eq. (3.7) for a system with armchair edges. Scattering at an armchair edge always changes the valley projection. The processes with non zero probability combine solutions on the left edge with one valley projection (e.g. $\psi^{+}_{<}$) with solutions on the right with the opposite valley index ($\widetilde{\psi}^{-}_{>}$). (a) Example of valley mixing at armchair edges (x_L and x_R) for incident particles with a fixed valley index, where solid (dashed) lines represent particles with valley index $+$ ($-$). Reflection processes for electron (b) and hole-like (c) quasiparticles. For a semi-infinite region, x_R goes to infinity and the asymptotic solutions are outgoing plane waves. For zigzag edges we have the same behavior without the change in the valley index.

The method that we implement to calculate the Green function is based in using the asymptotic solutions of the differential equation (3.7). Basically, we extend the method used in Refs. [85, 86] to the relativistic Bogoliubov-de Gennes equations. Thus, the full Green function in pseudospin and valley spaces can be written as

$$\check{G}_{\psi}\left(x,x';q\right)=\begin{cases}\sum\limits_{\mu,\nu=+,-}A_{\mu\nu}\psi^{\mu}_{<}\left(x\right)\cdot\widetilde{\psi}^{\nu T}_{>}\left(x'\right)\cdot\check{\gamma} & ;x<x'\\ \sum\limits_{\mu,\nu=+,-}A'_{\mu\nu}\psi^{\mu}_{>}\left(x\right)\cdot\widetilde{\psi}^{\nu T}_{<}\left(x'\right)\cdot\check{\gamma} & ;x>x'\end{cases}, \tag{3.9}$$

where the indexes μ and ν represent different valley projections of the asymptotic solutions. We build the Green's function using tensor products as $\hat{G}(x \lessgtr x') \propto \psi^{\mu}_{<(>)}(x)\cdot\widetilde{\psi}^{\nu T}_{>(<)}(x')$. Where $\psi^{\mu}_{<}(x)$ and $\psi^{\nu}_{>}(x)$ are the asymptotic solutions that fulfill the boundary conditions to the left and right edges of the system, respectively. In Figure 3.2 (a) the possible processes for an armchair edge are shown. The labels μ and ν are always determined by the valley index of the incident particle. On the other hand, $\widetilde{\psi}^{\nu}_{<(>)}(x')$ represent asymptotic solutions for the transposed Dirac's equation with the

same boundary conditions and opposite wave number $\widetilde{\psi}^{\nu}_{<(>)}(\mathbf{r}) = \exp(-iqy)\widetilde{\psi}^{\nu}_{<(>)}(x)$. Since $\check{H}^T(-q) = \check{H}(q)$, the wave functions $\widetilde{\psi}^{\nu T}_{<(>)}(x)$ fulfill the same differential equation than $\psi^{\nu}_{<(>)}(x)$. The constants $A^{(\prime)}_{\mu\nu}$ are determined from the condition

$$\sum_{\mu,\nu=+,-} A'_{\mu\nu}\psi^{\mu}_{>}(x)\cdot\psi^{\nu T}_{<}(x)\cdot\check{\gamma} - \sum_{\mu,\nu=+,-} A_{\mu\nu}\psi^{\mu}_{<}(x)\cdot\psi^{\nu T}_{>}(x)\cdot\check{\gamma} = -\frac{i}{\hbar v}\hat{\tau}_z\otimes\hat{\sigma}_x, \quad (3.10)$$

which is obtained integrating Eq. (3.7) around $x = x'$.

In our definition of the Green functions in Eq. (3.9) we have introduced the parity matrix $\check{\gamma}$ in order to make the scalar product $\bar{\psi}\hat{G}\psi$ invariant under Lorentz transformations and spatial inversion (parity transformation). Here $\bar{\psi}$ is the *adjoint* Dirac spinor defined as $\bar{\psi} = \psi^{\dagger}\check{\gamma}$. The transformation rule for Dirac spinors is $\psi \to \psi' = \check{S}\psi$, where $\check{S}$ is a 4×4 matrix that fulfills $\check{S}^{\dagger}\check{\gamma}\check{S} = \check{\gamma}$. With this rule, the product $\left(\bar{\psi}\psi\right)' = \bar{\psi}\check{S}^{\dagger}\check{\gamma}\check{S}\psi' = \bar{\psi}\psi$ is Lorentz invariant (for a complete description of the symmetries of Dirac fermions see Ref. [17]). Now, since $\check{G} \propto \psi\psi^T\check{\gamma}$, we have that $\check{G} \to \check{G}' = \check{S}\check{G}\check{\gamma}\check{S}\check{\gamma}$ and the product $\left(\bar{\psi}\check{G}\psi\right)' = \psi^{\dagger}\check{S}\check{\gamma}\left(\check{S}\check{G}\check{\gamma}\check{S}\check{\gamma}\right)\check{\gamma}\psi = \psi^{\dagger}\check{\gamma}\check{G}\psi = \bar{\psi}\check{G}\psi$ is also Lorentz invariant. The matrix $\check{\gamma}$ in reciprocal space changes both valley and pseudospin indexes. Then, since the spinor is in the basis (A_+, B_+, A_-, B_-) the matrix $\check{\gamma}$ can be written as $\check{\gamma} = \hat{\tau}_x\otimes\hat{\sigma}_x$ and we can check that the Hamiltonian $\check{H}$ is transformed with $\check{\gamma}$ as $\check{\gamma}\check{H}(\mathbf{p})\check{\gamma} = \check{H}(-\mathbf{p})$. In the next section, where the armchair edge is studied, we use this form of the matrix $\check{\gamma}$. A simplified form of matrix $\check{\gamma}$ for one valley is also derived and used for zigzag edges.

3.3.1 Armchair edges

We can now apply this method to derive the Green functions for a layer of graphene with armchair edges. Within the geometry depicted in the left panel of Figure 3.1, the direction perpendicular to the edge may be infinite or have a finite size W. In this later case, we have two edges at positions x_L and x_R. The main characteristic of an armchair edge is that scattering at the edges changes the valley index. This is a direct result of vanishing either the wave function [Eq. (3.5)] or its derivative on both lattices at the armchair edge. Asymptotic solutions for this system correspond to incoming waves from one valley that are reflected on the other valley. All possible processes are illustrated in Figure 3.2(a). The index $\pm$ symbolizes an incoming wave around the Dirac point $\mathbf{K}_{\pm}$ that is reflected at the interface. For incident waves reflected at the left ($<$) or at the

right (>) edge we have the four-dimensional spinors in valley and lattice spaces

$$\psi^{+}_{<(>)}(x) = e^{\mp ikx}\begin{pmatrix}\varphi_{2(1)}\\0\end{pmatrix} + r^{+}_{L(R)}e^{\pm ikx}\begin{pmatrix}0\\\varphi_{2(1)}\end{pmatrix} \tag{3.11}$$

$$\psi^{-}_{<(>)}(x) = e^{\mp ikx}\begin{pmatrix}0\\\varphi_{1(2)}\end{pmatrix} + r^{-}_{L(R)}e^{\pm ikx}\begin{pmatrix}\varphi_{1(2)}\\0\end{pmatrix} \tag{3.12}$$

The reflection amplitudes $r^{\pm}_{L(R)}$ are calculated imposing boundary conditions to the two-dimensional wave function of Eq. (3.5) at the edge $x_{L(R)}$, this is $\phi(x_L) = \phi(x_R) = 0$ or $\partial_x\phi(x_L) = \partial_x\phi(x_R) = 0$, which yields

$$\begin{aligned} r^{\pm}_{R} &= s e^{\pm 2i(K\mp k)x_R} \\ r^{\pm}_{L} &= s e^{\pm 2i(K\pm k)x_L}, \end{aligned} \tag{3.13}$$

where $s = \pm$ corresponds to the case in which the wave function $(-)$ or its derivative $(+)$ is vanished at the interface. The main differences between both cases are studied in the next section. For simplicity we have chosen that $x_L \in (-\infty, 0]$ and $x_R \in [0, \infty)$. Combining the asymptotic solutions, as has been explained in the previous section, we obtain a general expression for the full Green function with armchair edges ($\check{G}^{\text{arm}}_{\psi}$) equivalent to Eq. (3.9). The constants $A^{(\prime)}_{\mu=\nu}$ in this equation correspond to processes in which the excitation changes its valley projection when it propagates from one edge to the other. Therefore, these processes have zero probability and, from Eq. (3.10), one explicitly obtains $A^{(\prime)}_{++} = A^{(\prime)}_{--} = 0$, $A_{+-} = A'_{+-} = -i/\left(2\hbar v\cos\alpha\left(1 - r^{+}_{L}r^{-}_{R}\right)\right)$ and $A_{-+} = A'_{-+} = -i/\left(2\hbar v\cos\alpha\left(1 - r^{-}_{L}r^{+}_{R}\right)\right)$. Substituting these results in $\check{G}^{\text{arm}}_{\psi}$ we can derive the valley superposed Green function for a layer of graphene with armchair edges

$$\begin{aligned} \hat{G}^{\text{arm}}_{\phi}\left(x,x'\right) = {} & \frac{-i}{2\hbar v\cos\alpha\left(1 - r^{-}_{L}r^{+}_{R}\right)}\Big[e^{i(K+k)|x-x'|} + r^{-}_{L}r^{+}_{R}e^{-i(K+k)|x-x'|} \\ & + r^{-}_{L}e^{i(K+k)(x+x')} + r^{+}_{R}e^{-i(K+k)(x+x')}\Big]\varphi_1\varphi^{\dagger}_1 + \frac{-i}{2\hbar v\cos\alpha\left(1 - r^{+}_{L}r^{-}_{R}\right)} \\ & \times\Big[e^{-i(K-k)|x-x'|} + r^{+}_{L}r^{-}_{R}e^{i(K-k)|x-x'|} + r^{+}_{L}e^{-i(K-k)(x+x')} + r^{-}_{R}e^{i(K-k)(x+x')}\Big]\varphi_2\varphi^{\dagger}_2. \end{aligned} \tag{3.14}$$

The poles of the Green function are determined by $\cos\alpha = 0$, $\left(1 - r^{-}_{L}r^{+}_{R}\right) = 0$ and $\left(1 - r^{+}_{L}r^{-}_{R}\right) = 0$. The first one results in the bulk dispersion relation $\hbar v\,|q| = |E_F + E|$. In the second and third cases we reach the condition $2(K_{\pm} + k_n)W = 2n\pi$, with $W = x_R - x_L$ and n an integer. Thus, the allowed values of the transverse momentum for a finite armchair sheet are $k_n = \frac{n\pi}{W} \mp \frac{4\pi}{3a}$, independently of the boundary condition chosen for the armchair edges. This result is in agreement with previous works on graphene nanoribbons with armchair edges [37].

We now consider the case of a superconducting graphene region, where the description of electron and hole excitations is done within Nambu space. We assume a s-wave pairing which leads to a constant gap Δ which is diagonal in sublattice space. The system is then represented by the BdGD equation written in lattice, Nambu and valley spaces (8×8 matrix). It reads

$$\begin{pmatrix} \hat{H}_+ - E_F^S & \Delta & 0 & 0 \\ \Delta^* & E_F^S - \hat{H}_+ & 0 & 0 \\ 0 & 0 & \hat{H}_- - E_F^S & \Delta \\ 0 & 0 & \Delta^* & E_F^S - \hat{H}_- \end{pmatrix} \begin{pmatrix} \phi_+^e \\ \phi_-^h \\ \phi_-^e \\ \phi_+^h \end{pmatrix} = E \begin{pmatrix} \phi_+^e \\ \phi_-^h \\ \phi_-^e \\ \phi_+^h \end{pmatrix}, \quad (3.15)$$

with E positive unless otherwise specified. Each valley Hamiltonian is written as $\hat{H}_\pm = -i\hbar v \left[\pm\partial_x\hat{\sigma}_x + \partial_y\hat{\sigma}_y\right]$. Two-dimensional spinors $\phi_\pm^{e,h}$ represent electron or hole like excitations for each valley in lattice space. Whenever the pairing potential is assumed constant, the low energy spectrum is given by $E = \sqrt{\Delta^2 + \left(E_F^S - \hbar v\sqrt{k^2+q^2}\right)^2}$. We define the transversal momentum as $\hbar v k_{e,h}^S = \sqrt{\left(E_F^S \pm \Omega\right)^2 - \left(\hbar v q\right)^2}$, with $\Omega = \sqrt{E^2 - \Delta^2}$. The solutions of the BdGD equation are a direct product of graphene's bulk solutions and the usual BCS solutions. The pair potential couples electron and hole-like excitations with opposite momentum, which means different valley index, thus ϕ^e and ϕ^h correspond to different valleys. This allows us to reduce the degrees of freedom of the problem to Nambu and pseudospin spaces.

In order to study a semi-infinite superconducting graphene region with an armchair edge extending from $x_L = 0$ to $x_R \to \infty$, we define a finite and constant pair potential $\Delta(x) = \Theta(x)\Delta$. Reflection amplitudes are then fixed to $r_L^+ = r_L^- = \mp 1 \equiv r$ and $r_R^+ = r_R^- = 0$. The asymptotic solutions are

$$\psi_<^{e(h)+}(x) = \left\{ e^{\mp ik_{e(h)}x} \begin{pmatrix} \varphi_{2e(1h)} \\ 0 \end{pmatrix} + re^{\pm ik_{e(h)}x} \begin{pmatrix} 0 \\ \varphi_{2e(1h)} \end{pmatrix} \right\} \otimes \begin{pmatrix} u(v) \\ v(u) \end{pmatrix} \quad (3.16)$$

$$\psi_>^{e(h)+}(x) = e^{\pm ik_{e(h)}x} \begin{pmatrix} \varphi_{1e(2h)} \\ 0 \end{pmatrix} \otimes \begin{pmatrix} u(v) \\ v(u) \end{pmatrix} \quad (3.17)$$

$$\psi_<^{e(h)-}(x) = \left\{ e^{\mp ik_{e(h)}x} \begin{pmatrix} 0 \\ \varphi_{1e(2h)} \end{pmatrix} + re^{\pm ik_{e(h)}x} \begin{pmatrix} \varphi_{1e(2h)} \\ 0 \end{pmatrix} \right\} \otimes \begin{pmatrix} u(v) \\ v(u) \end{pmatrix} \quad (3.18)$$

$$\psi_>^{e(h)-}(x) = e^{\pm ik_{e(h)}x} \begin{pmatrix} 0 \\ \varphi_{2e(1h)} \end{pmatrix} \otimes \begin{pmatrix} u(v) \\ v(u) \end{pmatrix}, \quad (3.19)$$

where $\varphi_{ie(h)}$, with $i = 1, 2$, is obtained from Equation 2.7 making $\alpha \to \alpha_{e(h)}^S$ and defining $e^{i\alpha_{e(h)}^S} = \hbar v \left(k_{e(h)}^S + iq\right)/|E_F^S \pm \Omega|$ and $u^2\left(v^2\right) = \left(1 \pm \Omega/E\right)/2$. The function $\psi_<^{e(h)}$ describes an incoming electron-like (hole-like) quasiparticle with energy $E > E_F^S$ ($E < E_F^S$)

and valley index $\pm$ that is reflected at x_L into an electron-like (hole-like) quasiparticle with valley index $\mp$.

The 8×8 matrix Green's function can be written as the superposition of all possible quasi-electron and quasi-hole injection processes depicted in Figs. 3.2(b) and 3.2(c). The resulting Green function, written in Nambu, valley and pseudospin spaces, has the form

$$\check{\tilde{G}}^S_\psi\left(x<x'\right)=\begin{cases}\displaystyle\sum_{\substack{j=e,h\\ \mu,\nu=+,-}} A^j_{\mu\nu}\psi^{j\mu}_<\left(x\right)\cdot\psi^{j\nu T}_>\left(x'\right)\left(\check{\gamma}\otimes\hat{\tau}_0\right) & ;x<x'\\ \displaystyle\sum_{\substack{j=e,h\\ \mu,\nu=+,-}} A'^j_{\mu\nu}\psi^{j\mu}_>\left(x\right)\cdot\psi^{j\nu T}_<\left(x'\right)\left(\check{\gamma}\otimes\hat{\tau}_0\right) & ;x>x'\end{cases}, \tag{3.20}$$

where $\tau_{x,y,z}$ and τ_0 are Pauli matrices in Nambu space. The parity matrix $\check{\gamma}$ is diagonal in this space and only acts on graphene's valley and pseudospin degrees of freedom.

As in the normal case, the coefficients $A^{(\prime)j}_{\mu,\nu}$ with $\mu=\nu$ vanish as they correspond to processes which change the valley polarization without reflection at the edges. Additionally, the processes that couple quasi-electron with quasi-hole and vice versa have zero probability. This can be explicitly found from the condition given by Eq. (3.10) where $A^{(\prime)j}_{\mu=\nu}=0$, $A^e_{+-(-+)}=A'^e_{-+(+-)}=iEe^{+(-)i\alpha_e}/\left(2\hbar v\Omega\cos\alpha_e\right)$ and $A^h_{-+(+-)}=A'^h_{+-(-+)}=iEe^{+(-)i\alpha_h}/\left(2\hbar v\Omega\cos\alpha_h\right)$. Thus, after applying boundary conditions and solving Eq. (3.10), the valley superposed Green function in Nambu space for a superconducting region with an armchair edge is

$$\check{G}^{S,\mathrm{arm}}_\phi\left(x,x'\right)=\frac{-i}{2\hbar v}\left\{\left[\hat{A}^S_e+\hat{A}^S_h\right]\otimes\left(\frac{E}{\Omega}\hat{\tau}_0+\frac{\Delta}{\Omega}\hat{\tau}_x\right)+\left[\hat{A}^S_e-\hat{A}^S_h\right]\otimes\hat{\tau}_z\right\}, \tag{3.21}$$

with the following definitions

$$\begin{aligned}\hat{A}^S_{e(h)} &= f_{e(h)}\left(\cos^{-1}\alpha^S_{e(h)}\hat{\sigma}_0+\tan\alpha^S_{e(h)}\hat{\sigma}_y\right)\pm ig_{e(h)}\hat{\sigma}_x\\ f_{e(h)} &= \cos\left[K\left(x'-x\right)\right]e^{\pm ik^S_{e(h)}|x'-x|}+r\cos\left[K\left(x'+x\right)\right]e^{\pm ik^S_{e(h)}(x'+x)}\\ g_{e(h)} &= \mathrm{sgn}\left(x'-x\right)\sin\left[K\left(x'-x\right)\right]e^{\pm ik^S_{e(h)}|x'-x|}+r\sin\left[K\left(x'+x\right)\right]e^{\pm ik^S_{e(h)}(x'+x)}.\end{aligned}$$

It is interesting to take this expression to the heavily doped limit in which $E^S_F\gg E,\Delta,\hbar vq$ and thus $\cos\alpha^S_{e,h}\to 1$ and $\sin\alpha^S_{e,h}\to 0$. Within this approximation, for a microscopic distance $x_0\sim a$ from the interface we have

$$\check{G}^{S,\mathrm{arm}}_\phi\left(x_0,x_0\right)\approx\frac{-i}{\hbar v}\left\{\left[1+r\cos 2Kx_0\right]\hat{\sigma}_0\otimes\left(\frac{E}{\Omega}\hat{\tau}_0+\frac{\Delta}{\Omega}\hat{\tau}_x\right)+ir\sin 2Kx_0\hat{\sigma}_x\otimes\hat{\tau}_z\right\}. \tag{3.22}$$

For the boundary condition of vanishing the derivative of the wave function ($r = 1$), we can evaluate the Green function at the edge ($x_0 = 0$). Thus,

$$\check{G}_{\phi}^{S,\mathrm{arm}}(0,0) \approx -\frac{2i}{\hbar v \Omega}\left(E\hat{\sigma}_0 \otimes \hat{\tau}_0 + \Delta\hat{\sigma}_0 \otimes \hat{\tau}_x\right), \tag{3.23}$$

which corresponds to the momentum independent BCS Green function without sublattice structure [82]. Then, $2/\hbar v$ corresponds to an averaged Fermi energy DOS per unit length for the superconductor.

On the other hand, for the boundary condition over the wave function ($r = -1$) the Green function vanishes at $x_0 = 0$. For finite x_0, the Green function can exhibit a structure in pseudospin space given by the last term in Eq. (3.22). This expression is used in the following sections when we microscopically couple normal and superconducting regions.

3.3.2 Zig-zag edges

The geometry of the graphene sheet is now set to have a zigzag edge along the y-axis. With this new orientation of the layer the Brillouin zone rotates as illustrated in the upper part of the right panel of Figure 3.1, which allows to select the Dirac points at $\mathbf{K}_{\pm} = (0, \pm K)$. We still call $\hbar q$ the conserved momentum along the y direction. We consider either a finite layer with edges at positions x_L and x_R or a semi-infinite one in which x_L or x_R goes to infinity. Zigzag edges are formed by a line of atoms all pertaining to one sublattice. These edges do not mix valleys so we can treat them separately and use a Dirac Hamiltonian of just one valley, $\hat{H}_+ = \hbar v\left(k\hat{\sigma}_x + q\hat{\sigma}_y\right) - E_F\hat{\sigma}_0$. Thus, the asymptotic wave functions including a reflection at the edge are

$$\phi_<(x) = e^{-ikx}\varphi_2 + r_L e^{ikx}\varphi_1 \tag{3.24}$$

$$\phi_>(x) = e^{ikx}\varphi_1 + r_R e^{-ikx}\varphi_2. \tag{3.25}$$

The reflection amplitudes depend on the atoms chosen to form the zigzag edge. Thus, if we choose the border at x_L to be formed by atoms of A (B) lattice, the one at x_R is formed by atoms pertaining to B (A) lattice (see right panel of Figure 3.1). Imposing the boundary conditions $\phi_<(x_L)|_{A(B)} = \phi_>(x_R)|_{B(A)} = 0$ we obtain the reflection amplitudes:

$$r_{L(R)}^{A} = -e^{\pm i\alpha}e^{\mp 2ikx_{L(R)}} \quad r_{L(R)}^{B} = e^{\mp i\alpha}e^{\mp 2ikx_{L(R)}}. \tag{3.26}$$

When combining the asymptotic solutions to build the Green functions, as it was done in the previous section, the elements of the full Green function that mix valleys $(+-, -+)$

are zero. In what follows the full Green function is understood to represent only a projection over one valley (i.e. $\check{G}_{\psi}^{\mathrm{zz},++}$). Following the steps given in the previous sections we can write

$$\hat{G}_{\psi}^{\mathrm{zz}}(x,x') = \begin{cases} A\phi_{<}(x)\cdot\phi_{>}^{T}(x')\cdot\hat{\gamma} & ;x<x' \\ A'\phi_{>}(x)\cdot\phi_{<}^{T}(x')\cdot\hat{\gamma} & ;x>x' \end{cases} . \tag{3.27}$$

For the case of a graphene sheet with zigzag edges, we have set the Dirac points to be at $\mathbf{K}_{\pm} = (0, \pm K)$. Thus, the Hamiltonian on each valley is given by $\hat{H}_{\pm}^{\mathrm{zz}} = \hbar v\left[k\hat{\sigma}_x \pm q\hat{\sigma}_y\right] - E_F\hat{\sigma}_0$. The Hamiltonian of the full system is related with the one given in Eq. (3.6) by $\check{H}_{\mathrm{zz}} = \check{T}\check{H}\check{T}$, with

$$\check{T} = \check{T}^{-1} = \begin{pmatrix} 1 & 0 \\ 0 & \hat{\sigma}_z \end{pmatrix}. \tag{3.28}$$

The matrix $\check{\gamma} = \hat{\tau}_x \otimes \hat{\sigma}_x$ is then transformed as $\check{\gamma}_{\mathrm{zz}} = \check{T}\check{\gamma}\check{T} = \hat{\tau}_y \otimes \hat{\sigma}_y$. When we apply this matrix to $\check{H}_{\mathrm{zz}}$ we have $\check{\gamma}_{\mathrm{zz}}\left(\check{H}_{\mathrm{zz}}(\mathbf{k})\right)\check{\gamma}_{\mathrm{zz}}^{-1} = \check{H}_{\mathrm{zz}}(-\mathbf{k})$, which corresponds to a parity transformation.

Since the zigzag boundary conditions do not mix valleys we can work only with one valley ($\mathbf{K}_{+}$) using Hamiltonian $\hat{H}_{+}^{\mathrm{zz}} = \hat{H}_{+}$. For this Hamiltonian the effect of the parity transformation, restricted to the sublattice subspace, is equivalent to set $\hat{\gamma} = \hat{\sigma}_z$.

For a ribbon of graphene with the left zigzag edge of type B (and thus the right one of type A) we have

$$\hat{G}_{\psi}^{\mathrm{zz}}(x,x') = \frac{-i}{2\hbar v\cos\alpha\left(1 - r_L^B r_R^A\right)} \times \begin{cases} e^{ik(x'-x)}\varphi_2\varphi_2^{\dagger} + r_L^B r_R^A e^{-ik(x'-x)}\varphi_1\varphi_1^{\dagger} + \\ +r_L^B e^{ik(x'+x)}\varphi_1\varphi_2^{\dagger} + r_R^A e^{-ik(x'+x)}\varphi_2\varphi_1^{\dagger} & ;x<x' \\ \\ e^{ik(x-x')}\varphi_1\varphi_1^{\dagger} + r_L^B r_R^A e^{-ik(x-x')}\varphi_2\varphi_2^{\dagger} + \\ +r_L^B e^{ik(x+x')}\varphi_1\varphi_2^{\dagger} + r_R^A e^{-ik(x+x')}\varphi_2\varphi_1^{\dagger} & ;x>x' \end{cases} \tag{3.29}$$

For the other valley we obtain the same result with the change $\varphi_{1,2} \leftrightarrow \varphi_{2,1}$. As it was explained in the previous section, $\cos\alpha = 0$ gives the bulk dispersion relation. Furthermore, if the layer has a finite width which is set to $W = x_R - x_L$, the condition $1 - r_L^B r_R^A = 0$ transforms into

$$e^{2ikW} = \frac{q+ik}{q-ik}. \tag{3.30}$$

For k real, this expression leads to the quantization of transverse momentum in the ribbon (i.e. $q = k_n/\tan k_n W$). On the other hand, if the transverse momentum is a pure imaginary number ($k = -iz$) Eq. (3.30) transforms into

$$e^{-2zW} = \frac{q-z}{q+z}, \tag{3.31}$$

whose solutions correspond to surface states, at $E = E_F$, localized along the edges of the ribbon [37].

Analogously to the armchair case, we now consider a superconducting region spread over the $x > 0$ infinite half-plane with a zigzag edge at $x = 0$. If we couple electronic excitations with $\mathbf{K}_+$ index to hole-like quasiparticles with the other valley index, Eq. (3.15) is reduced to a 4×4 matrix equation in Nambu and pseudospin spaces

$$\begin{pmatrix} \hat{H}_+ - E_F^S & \Delta \\ \Delta^* & E_F^S - \hat{H}_+ \end{pmatrix} \begin{pmatrix} \phi_+^e \\ \phi_-^h \end{pmatrix} = E \begin{pmatrix} \phi_+^e \\ \phi_-^h \end{pmatrix}. \tag{3.32}$$

The asymptotic wave functions for quasi-electron and quasi-hole injection are written in Nambu and pseudospin space as

$$\phi_<^{e(h)}(x) = \left\{ e^{\mp ikx} \varphi_{2e(1h)} + r_L^{B,e(h)} e^{\pm ikx} \varphi_{1e(2h)} \right\} \otimes \begin{pmatrix} u\,(v) \\ v\,(u) \end{pmatrix} \tag{3.33}$$

$$\phi_>^{e(h)}(x) = e^{\pm ikx} \varphi_{1e(2h)} \otimes \begin{pmatrix} u\,(v) \\ v\,(u) \end{pmatrix}, \tag{3.34}$$

where the edge has been chosen to be formed by atoms from sublattice B. Boundary conditions for the wave function at the zigzag edge determine the reflection amplitudes. Thus, for electronic excitations we substitute $\alpha \to \alpha_e^S$ in Eq. (3.26), while we change $\alpha \to -\alpha_h^S$ for hole excitations. The resulting Green's function for a semi-infinite superconducting region reads

$$\check{G}_\psi^{S,zz}(x,x') = \frac{-i}{2\hbar v} \left\{ \left[\hat{Z}_e^S + \hat{Z}_h^S \right] \otimes \frac{1}{\Omega} \left(E\hat{\tau}_0 + \Delta \hat{\tau}_x \right) + \left[\hat{Z}_e^S - \hat{Z}_h^S \right] \otimes \hat{\tau}_z \right\}, \tag{3.35}$$

where

$$\hat{Z}_{e(h)}^S = \frac{e^{\pm ik_{e(h)}^S (x+x')}}{2\cos\alpha_{e(h)}^S} e^{\mp i\alpha_{e(h)}^S} \varphi_{1e(2h)} \varphi_{2e(1h)}^\dagger + \frac{e^{\pm ik_{e(h)}^S |x'-x|}}{2\cos\alpha_{e(h)}^S} \begin{cases} \varphi_{2e(1h)} \varphi_{2e(1h)}^\dagger & ; x < x' \\ \varphi_{1e(2h)} \varphi_{1e(2h)}^\dagger & ; x > x' \end{cases}. \tag{3.36}$$

When Eq. (3.35) is evaluated at the edge of the graphene layer it reduces to

$$\begin{aligned} \check{G}_\psi^{S,zz}(0,0) = {} & \frac{-i}{2\hbar v} \left\{ \begin{pmatrix} e^{-i\alpha_e^S} + e^{i\alpha_h^S} & 0 \\ 0 & 0 \end{pmatrix} \otimes \frac{1}{\Omega} \left(E\hat{\tau}_0 + \Delta\hat{\tau}_x \right) + \begin{pmatrix} e^{-i\alpha_e^S} - e^{i\alpha_h^S} & 0 \\ 0 & 0 \end{pmatrix} \otimes \hat{\tau}_z \right\} \\ & + \frac{-i}{2\hbar v} \begin{cases} \begin{pmatrix} 0 & -1 \\ 0 & 0 \end{pmatrix} \otimes \hat{\tau}_z & ; 0 < x < x' \\ \begin{pmatrix} 0 & 0 \\ 1 & 0 \end{pmatrix} \otimes \hat{\tau}_z & ; 0 < x < x' \end{cases} \end{aligned} \tag{3.37}$$

Furthermore, in the heavily doped limit ($E_F^S \gg E, \Delta, \hbar v q$), the previous expression reduces to

$$\check{G}_{\psi}^{S,\mathrm{zz}}(0,0) \approx \frac{-i}{2\hbar v}\left\{(\hat{\sigma}_0+\hat{\sigma}_z)\otimes\frac{1}{\Omega}\left(E\hat{\tau}_0+\Delta\hat{\tau}_x\right)\mp\frac{1}{2}\left(\hat{\sigma}_x\pm i\hat{\sigma}_y\right)\otimes\hat{\tau}_z\right\}, \tag{3.38}$$

where the sign identifies the cases with $x < x'$ or $x > x'$. Thus, in this limit we roughly have a BCS Green function projected to the site A.

3.3.3 Bulk Green's functions.

If we set all the reflection amplitudes to zero in Eq. (3.15) we obtain the bulk solution for an infinite graphene layer

$$\hat{G}_{\phi}^{\mathrm{bulk}}(x,x') = \frac{-i}{2\hbar v\cos\alpha}\times\begin{cases} e^{i(K+k)|x-x'|}\varphi_1\varphi_1^{\dagger}+e^{-i(K-k)|x-x'|}\varphi_2\varphi_2^{\dagger} & ;x<x' \\ e^{i(K+k)|x-x'|}\varphi_2\varphi_2^{\dagger}+e^{-i(K-k)|x-x'|}\varphi_1\varphi_1^{\dagger} & ;x>x' \end{cases} \tag{3.39}$$

Thus, the local propagator for a bulk of graphene is

$$\hat{G}_{\phi}^{\mathrm{bulk}}(x=x') = \frac{-i}{2\hbar v\cos\alpha}\left[\varphi_1\varphi_1^{\dagger}+\varphi_2\varphi_2^{\dagger}\right] = \frac{-i}{\hbar v}\left[\cos^{-1}\alpha\hat{\sigma}_0+\tan\alpha\hat{\sigma}_y\right]. \tag{3.40}$$

Furthermore, the bulk LDOS is obtained integrating this simple result, thus giving $\rho_{\mathrm{bulk}}(E) = 2\left(E+E_F\right)/\hbar^2v^2$.

On the other hand, vanishing the reflection coefficient (r) in Eq. (3.21) we reach the bulk solution for an infinite superconducting region. The local valley superposed Green function is then written as

$$\begin{aligned}\check{G}_{\phi}^{S,\mathrm{bulk}}(x=x') = \frac{-i}{2\hbar v}\Bigg\{&\left(\cos^{-1}\alpha_e^S\hat{\sigma}_0+\tan\alpha_e^S\hat{\sigma}_y\right)\otimes\frac{1}{\Omega}\left(E\hat{\tau}_0+\Delta\hat{\tau}_y+\hat{\tau}_z\right)\\ &+\left(\cos^{-1}\alpha_h^S\hat{\sigma}_0+\tan\alpha_h^S\hat{\sigma}_y\right)\otimes\frac{1}{\Omega}\left(E\hat{\tau}_0+\Delta\hat{\tau}_y-\hat{\tau}_z\right)\Bigg\}.\end{aligned} \tag{3.41}$$

In the heavily doped limit, the Green's function loses all structure in sublattice space,

$$\check{G}_{\phi}^{S,\mathrm{bulk}}(x=x') \approx \frac{-i}{\hbar v\Omega}\left(E\hat{\tau}_0+\Delta\hat{\tau}_y\right), \tag{3.42}$$

and is equivalent to the bulk BCS Green function.

3.4 Continuous model versus tight-binding model.

3.4.1 Dyson equation for coupling separate regions.

Once the expressions for bulk, armchair and zigzag graphene sheets, as well as for the semi-infinite superconducting regions have been obtained, we concentrate in the determination of the Green functions for the coupled system. This amounts in principle to solve the integral Dyson equation

$$\hat{G}_\phi(x,x') = \hat{g}_\phi(x,x') + \int dx_1 dx_2 \hat{g}_\phi(x,x_1)\hat{V}(x_1,x_2)\hat{G}_\phi(x_2,x'), \tag{3.43}$$

where now $\hat{G}_\phi$ denotes the valley superposed Green function of the coupled system, $\hat{g}_\phi$ corresponds to the uncoupled ones and $\hat{V}$ is an appropriate perturbation describing the coupling between the two regions. In general, we must use valley superposed Green functions in Dyson's equation to have a microscopic description of the coupling between graphene layers. In order to simplify the model while still keeping the possibility to describe interfaces of arbitrary transparency we shall assume that the perturbation only connect points on an atomic scale close to the interface. We thus define a general perturbation

$$\hat{V}(x_1,x_2) = \beta t_g a_{eff} \delta(x_1 - x_0)\,\delta(x_2 + x_0)\,\hat{\sigma}_x, \tag{3.44}$$

where $\beta \in [0,1]$ is a dimensionless parameter that controls the transparency of the interface and x_0 is a microscopic distance from the interface. The effective hopping matrix $t_g a_{eff}\hat{\sigma}_x$ has a structure dictated by the change of sublattice associated with the hopping between the two graphene sheets at the interface. In this expression a_{eff} represents an "effective distance" which we determine from the condition that the bulk graphene result is recovered when coupling two semi-infinite regions with $\beta = 1$.

We first discuss the case of two semi-infinite graphene sheets with armchair edges. The simplest possible choice would be $x_0 \to 0^+$, which can be applied when the condition of vanishing the derivative of the wave function at the edge has been taken. In this way one may convert Eq. (3.43) into an algebraic equation, which for the local Green functions at the interface can be written as

$$\hat{G}_{R(L)} = \left[\hat{g}^{-1}_{R(L)} - (\beta t_g a_{eff})^2\,\hat{\sigma}_x \hat{g}_{L(R)} \hat{\sigma}_x\right]^{-1}, \tag{3.45}$$

where R, L denotes $(x,x') \to (0^\pm, 0^\pm)$ and $\hat{g}_{L(R)}$ are given by

$$\hat{g}_{L(R)} = \frac{-2i}{\hbar v}\left(\cos^{-1}\alpha\hat{\sigma}_0 + \tan\alpha\hat{\sigma}_y\right). \tag{3.46}$$

One can check that the bulk Green function is recovered for $a_{eff} = \sqrt{3}a/4$, which therefore sets the condition of perfect transparency for this case.

A slightly more cumbersome matching condition has to be introduced if one would like to reproduce the limiting results of the TB model for such an interface [82]. This requires using the Green functions obtained by vanishing the wave function at the edges of the graphene sheet and take $x_0 = a/4$. One obtains then a Dyson equation like (3.45) with R, L denoting $(x, x') = (\pm\frac{a}{4}, \pm\frac{a}{4})$ and $\hat{g}_{L,R}$ given by

$$\hat{g}_{L(R)} = \frac{-\sqrt{3}i}{2\hbar v}\left[\sqrt{3}\left(\cos^{-1}\alpha\hat{\sigma}_0 + \tan\alpha\hat{\sigma}_y\right) - i\hat{\sigma}_x\right]. \tag{3.47}$$

These expressions exactly reproduce the TB results in the continuum limit, this is $a \to 0$ but with $Ka \to 4\pi/3$ [87]. One can further check that for this case the bulk graphene result is recovered for $a_{eff} = a/2$ which is the distance between lines of atoms along the x direction in an armchair edge.

We now focus on zigzag edges. In this case one can disregard the valley mixing but care should be taken due to the discontinuity of the Green functions at $x = x'$. As discussed in the previous section we select the condition of vanishing one of the wave function components at the interface and take $x_0 \to 0^+$. The precise value of $x_0 \sim a$ is here irrelevant because the Dirac points lie along the y direction.

When we evaluate Eq. (3.29) at the edge of each region we get

$$\hat{g}_L = \frac{-i}{\hbar v}\begin{cases} \begin{pmatrix} 0 & -1 \\ 0 & e^{-i\alpha} \end{pmatrix} \equiv \hat{g}_L^+ & ; x < x' \to 0^- \\ \begin{pmatrix} 0 & 0 \\ 1 & e^{-i\alpha} \end{pmatrix} \equiv \hat{g}_L^- & ; x' < x \to 0^- \end{cases} \tag{3.48}$$

$$\hat{g}_R = \frac{-i}{\hbar v}\begin{cases} \begin{pmatrix} e^{-i\alpha} & -1 \\ 0 & 0 \end{pmatrix} \equiv \hat{g}_R^+ & ; x < x' \to 0^+ \\ \begin{pmatrix} e^{-i\alpha} & 0 \\ 1 & 0 \end{pmatrix} \equiv \hat{g}_R^- & ; x' < x \to 0^+ \end{cases} \tag{3.49}$$

where we have implicitly assumed a $A(B)$ termination for the $L(R)$ graphene sheet. The Green function of the coupled system must be constructed including the discontinuity of the uncoupled Green's functions at the edges, i.e for $x, x' < 0$

$$\hat{G}_L\left(x, x'\right) = \hat{g}\left(x, x'\right) + \left(t_g a_{eff}\right)^2 \hat{g}\left(x, 0^-\right)\hat{\sigma}_x\left[1 - \left(t_g a_{eff}\right)^2 \hat{g}_R^-\hat{\sigma}_x\hat{g}_L^+\hat{\sigma}_x\right]^{-1}\hat{g}_R^-\hat{\sigma}_x\hat{g}\left(0^-, x'\right), \tag{3.50}$$

where $\hat{g}\left(x,0^{-}\right)=\exp\left(-ikx\right)\hat{g}_{L}^{+}$, $\hat{g}_{L}\left(0^{-},x'\right)=\exp\left(-ikx'\right)\hat{g}_{L}^{-}$ and $\hat{g}\left(x,x'\right)$ corresponds to Eq. (3.29) with $r_{L}^{B}=0$. When $x<x'$, and using that for this case $r_{L}^{B}=-r_{R}^{A}$, this results in

$$\hat{G}_{L}\left(x,x'\right)=\frac{-i}{2\hbar v\cos\alpha}\left[e^{ik(x-x')}\varphi_{2}\varphi_{2}^{\dagger}+e^{-ik(x+x')}r_{R}^{A}\varphi_{2}\varphi_{1}^{\dagger}\left(1-\frac{\beta^{2}\left(1+e^{-2i\alpha}\right)}{\frac{3a^{2}}{4a_{eff}^{2}}+\beta^{2}e^{-2i\alpha}}\right)\right], \tag{3.51}$$

where we have replaced $t_{g}=2\hbar v/(\sqrt{3}a)$. The bulk result is recovered at perfect transparency ($\beta=1$) for $a_{eff}=\sqrt{3}a/2$, which corresponds to the horizontal separation between atoms of the same sublattice. This result corresponds to the projection over the point $\mathbf{K}_{+}$. For the other valley, the same result with $\varphi_{1}\leftrightarrow\varphi_{2}$ is reached and the bulk result is recovered for perfect transparency superposing both valleys.

3.5 Conclusion and discussion.

In this Chapter we have presented the Green function methods for both the continuous and the tight-binding model. We have demonstrated the equivalence of both approaches for describing the properties of graphene. In particular, expressions for the Green function of the graphene normal-superconductor system are given in Chapter 4. We have also presented a novel method for combining them using a microscopic Dyson equation for the continuous model.

Chapter 4

The graphene-superconductor interface.

4.1 Introduction.

Graphene is not intrinsically a superconductor. However, due to its two-dimensional nature, graphene is a material which can easily inherit the bulk properties of other materials when in contact with them. For this reason, Heersche *et al.* in 2007 [11, 88] opened a way for exploring superconductivity in graphene and also graphene-superconductor hybrid structures. In these works, a graphene sample was contacted with two closely spaced superconducting electrodes and supercurrents carried by electrons and holes, depending on the doping of the graphene layer, were measured. Their results demonstrated that transport at the Dirac point between a graphene layer and a superconductor was phase coherent. Furthermore, the contact between graphene and the bulk superconductor was very transparent at the atomic scale. Further experiments corroborated these results and measured Multiple Andreev Reflections in similar graphene-based Josephson junctions [12–14].

The physical consequence of the good contact achieved between the superconductor and the graphene layer deposited on top of it is that superconducting pairing correlations are induced in graphene by means of the proximity with the superconductor. Indeed, in a series of theoretical works prior to these experiments, a graphene-based ballistic Josephson junction was studied where the superconducting electrodes were approximated by heavily doped graphene electrodes with an induced pairing correlation [89–91]. A ballistic Josephson junction is that junction where the distance between the superconducting electrodes L is much smaller than the width W of the contacts. A superconducting graphene electrode consists of a graphene layer with a high doping,

compared to the superconducting gap and the excitation energy, where the superconducting order parameter is finite. Consequently, these electrodes describe a graphene layer where superconductivity has been induced by proximity with a superconducting material. In particular, Titov and Beenakker predicted in Ref. [89] a non-vanishing Josephson current at the Dirac point, feature that was measured in Ref. [11]. This supercurrent is due to the peculiar band structure of graphene.

In addition to the Josephson junction, a graphene-based NS system has been predicted to behave differently to the metallic NS junction. The seminal work by Beenakker in 2006 [56], already explained in Chapter 2, predicted a new type of Andreev reflection at a low-doped graphene-based NS junctions. Additionally, the tunneling conductance of a graphene NIS junction was studied in Ref. [57], presenting also distinctive behavior from the normal metal counterpart. Next, the effect of Andreev reflection on the peculiar conductivity minimum of graphene was studied for a NS system in Ref. [38]. While Andreev reflection increases the ballistic conductance away from the Dirac point, the minimum of conductivity remained unaltered. This pseudo-diffusive transport at the Dirac point was also found in short ballistic metal-graphene-metal junctions for arbitrary dopings and magnetic fields [39]. The possibility of having a different symmetry on the superconducting order parameter like d-wave was studied in Refs. [92] and [58].

In all these works the microscopic structure of the graphene-superconductor interface was not studied. Neither it was the influence of the new type of Andreev reflection on the density of states. The first work in which the effect of having a determined orientation of the graphene edge at the NS interface is taken into account was Ref. [93], where the local density of states of a zigzag nanoribbon coupled to a superconductor was studied. In line with this work, in Ref. [94] the density of states of a Josephson junction was studied in the regime where the superconducting coherence length is much smaller than the separation between superconductors.

In this chapter we present a microscopic study of the graphene-superconductor junction with especial attention to the interface. Two models are considered for the study of the NS interface: one in which a bulk-BCS superconductor is coupled to a graphene layer and another in which the superconducting region is represented by a heavily doped graphene with a superconducting pairing amplitude. The latter case maintains graphene sublattice structure inside the superconducting region, which is essential to have perfect transmission between the normal and the superconducting regions. In addition, a microscopic description of the interface allows to define a particular orientation of the graphene edges, i.e. armchair or zigzag. The influence on the LDOS and the Andreev conductance of the type of superconducting electrode, together with the graphene edge orientation, is analyzed. Finally, it is shown that all the microscopic properties of the

graphene-based NS junctions can be qualitatively explained by the presence of interface bound states which appear due to the interplay of Andreev and normal reflection. These states are obtained using a simple model which can be solved analytically.

4.2 Modeling the graphene-superconductor interface.

The aim of this section is to analyze different ways to describe the interface between a graphene layer and a superconductor. In the recent literature it has been assumed that a superconducting electrode deposited on top of graphene induces a finite pairing amplitude and introduces a finite level of doping which shifts the Fermi level of the graphene layer far away from the Dirac point [56, 89]. This heavily doped superconducting graphene (HDSC) model provides a simple boundary condition for the effective Dirac-Bogoliubov-De Gennes equations describing the interface.

One can alternatively imagine that the graphene layer is coupled directly to a bulk superconducting electrode by means of a sharp interface which breaks the coherence between the two graphene sublattices. We shall refer to this case as the *bulk-BCS* model. We analyze the differences between these two models, schematically represented in Figure 4.1.

The influence of the leads on the conductivity of graphene in the normal state has been studied in several works (see for example Refs. [95–97]). In Ref. [95] it was demonstrated that transport in a weakly doped graphene sample contacted to normal electrodes depended only quantitatively but not qualitatively on the form of the leads when a large number of transversal modes is considered (i.e. when the width of the graphene layer is much greater than the length). In particular, at the Dirac point, the conductivity is mainly due to evanescent modes [35, 36] and obeys Ohm's law, decaying proportionally to the length of the sample. However, in Ref. [96] the effect of the width on a graphene nanoribbon with zigzag edges contacted to metallic electrodes was studied for arbitrary doping. They realized that the conductance at the Dirac point is independent of the hopping integral at the interface when the normal leads are modeled as a square lattice with two sites. The main property of the square lattice is that it maintains graphene's internal structure.

4.2.1 HDSC graphene electrodes versus bulk-BCS electrodes.

The two different superconducting electrodes are modeled using the Green functions techniques presented in Chapter 3. A microscopic description of the electrodes can be

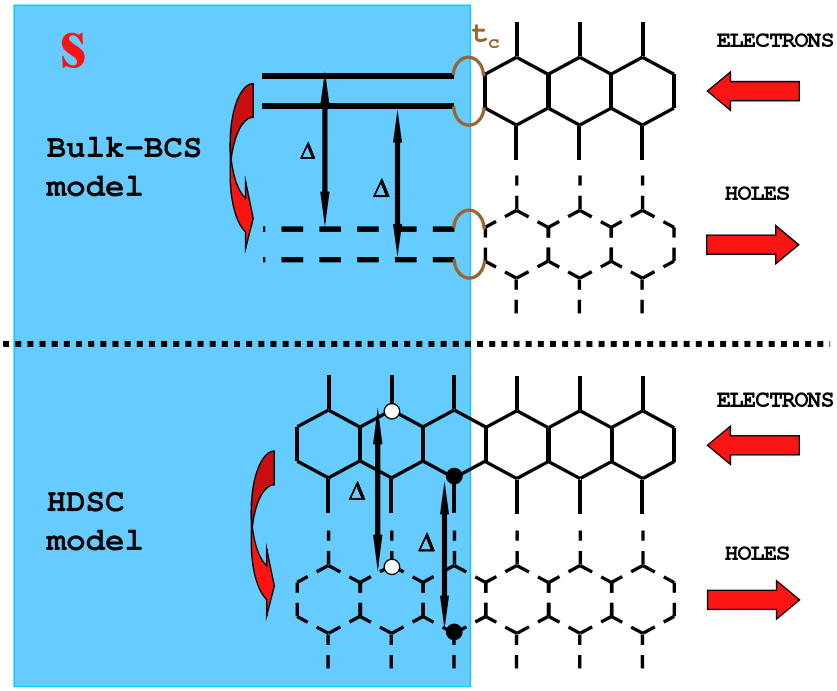

FIGURE 4.1: Schematic picture of an Andreev reflection in the bulk-BCS and in the HDSC models. In the first case, the sites on each sublattice of the graphene edge are coupled to the superconductor through independent channels thus breaking the coherence of the honeycomb structure. In the other case, the coupling with the superconducting region maintains this structure. See text for more details.

reached using the tight-binding (TB) model. The presence of superconducting correlations requires to introduce the Nambu space describing electron and hole propagation within the graphene layer. All Green functions acquire a 2×2 structure in Nambu space. For the uncoupled graphene we have

$$\check{\hat{g}} = \begin{pmatrix} \hat{g}_e & 0 \\ 0 & \hat{g}_h \end{pmatrix}, \tag{4.1}$$

where $\hat{g}_e$ corresponds to the propagators obtained in Section 3.2 and $\hat{g}_h$ is obtained from $\hat{g}_e$ by changing $\epsilon \to -\epsilon$ and $t_g \to -t_g$ (notice that we use the hat symbol to denote the sublattice space while the check symbol indicates the Nambu space).

The effect of the coupling with the superconducting electrode can be introduced by means of a self-energy $\check{\hat{\Sigma}}$ which renormalizes the uncoupled Green functions. Thus, the local Green function on the graphene edge at the interface is determined by $[\check{\hat{g}}^{-1} - \check{\hat{\Sigma}}]^{-1}$.

In the case of the bulk-BCS model the self-energy is momentum independent and does not have a structure in the sublattice space; i.e.

$$\check{\hat{\Sigma}} = \pi\rho_s t_c^2 \check{\tau}_z \check{g}_{BCS} \check{\tau}_z \otimes \hat{I}, \tag{4.2}$$

where $\check{\tau}_z$ is the z Pauli matrix in Nambu space and t_c^2 is the mean square hopping element between the graphene layer and the superconducting electrode. This quantity controls the value of the parameter $\beta = t_c^2 \pi \rho_s / t_g$ which characterizes the quality of the interface. ρ_s is the density of states of the superconducting electrode at the Fermi level in the normal state. On the other hand, $\check{g}_{BCS} = g_s \check{I} + f_s \check{\tau}_x$ stands for the dimensionless BCS Green function, i.e. $g_s = -\omega/\sqrt{\Delta^2 - \omega^2}$ and $f_s = \Delta/\sqrt{\Delta^2 - \omega^2}$, where the superconducting electrode is supposed to have electron-hole symmetry. This model thus consists of coupling a one-dimensional metallic chain in the superconducting state to each atom of the graphene edge. The Green functions describing the superconducting electrode are the bulk ones. The form of the electrodes is therefore not important since we are interested only in a small window of energies around the Fermi level. As a consequence, the effects of finite bandwidth have been neglected for the uncoupled superconductor. This approximation is justified when the excitation energy and the doping level of the normal region are both comparable to the superconducting gap, which is much smaller than the superconducting bandwidth.

We would like now to derive the expression of the self-energy within the HDSC model. The building blocks for this problem are the TB uncoupled Green functions of a semi-infinite graphene layer described in Chapter 3. We first notice that in the heavily doped limit one has $|\epsilon| >> |\omega|, t_g \sin qa$ for the relevant range of frequencies and q values. Thus in $\hat{R}_2$ one has $\alpha \to \pi/2$. In the new basis the system is equivalent to a tight-binding chain with site energies $\epsilon \pm t_g$ and local pairing fixed by Δ. Although the exact Green function for this system is rather complicated, for low excitation energies it can be approximated by

$$\hat{R}_2^{-1} \check{\hat{g}} \hat{R}_2 \simeq \begin{pmatrix} \pi\rho_+ & 0 \\ 0 & \pi\rho_- \end{pmatrix} \otimes \check{g}_{BCS} + \frac{1}{2t_g^2} \begin{pmatrix} \epsilon + t_g & 0 \\ 0 & \epsilon - t_g \end{pmatrix} \otimes \check{\tau}_z, \tag{4.3}$$

where $\pi\rho_\pm = \sqrt{1 - \left(\frac{\epsilon \pm t_g}{2t_g}\right)^2}/t_g$. By further taking the approximation $|\epsilon| << t_g$ and transforming back into the site representation we obtain the following self-energy

$$\check{\hat{\Sigma}}/t_g \simeq \frac{\sqrt{3}}{2} \check{\tau}_z \check{g}_{BCS} \check{\tau}_z \otimes \hat{I} - \frac{1}{2} \check{\tau}_z \otimes \hat{\sigma}_x. \tag{4.4}$$

Notice that, in contrast to the first model, the self-energy in the HDSC model does exhibit a structure in the sublattice space. However, it satisfies the condition $\det \check{\hat{\Sigma}}/t_g =$

1. This structure turns out to be of importance in connection to Andreev reflection as discussed in the next section.

In the following we use a general form of the model self-energies, which can be expressed as

$$\check{\hat{\Sigma}} = \beta \check{\tau}_z \check{g}_{BCS} \check{\tau}_z \otimes \hat{I} - \gamma \check{\tau}_z \otimes \hat{\sigma}_x. \tag{4.5}$$

Thus, appropriate values for β and γ will correspond to the different models (i.e. $\gamma = 0$ with arbitrary β for the bulk-BCS model, while $\beta = \sqrt{3}/2$ and $\gamma = 1/2$ in units of t_g, for the HDSC model).

4.2.2 Influence of the electrodes on the Andreev reflection.

As it was introduced in Chapter 2, the Andreev reflection is the basic mechanism for the conversion of a quasiparticle current into a supercurrent at the interface between a normal metal and a superconductor. In the case of a graphene-superconductor interface, where the normal region is described within the TB model introduced in Section 4.2 and the superconductor is either the bulk-BCS or HDSC type, there are two channels for the incident electrons with a given wave vector q corresponding to the states which diagonalize the $\hat{X}$ matrix. The reflected hole can be in either of these two channels. Our microscopic theory can thus describe a more general situation than the idealized model for the interface used in [56] which assumes only one channel for the reflected hole for a given wave vector.

The Andreev reflection amplitudes can be expressed in terms of Green functions. Generalizing previous works [98, 99] we can derive the expression

$$\hat{r}_A(q,\omega) = 2i\hat{A}_e^{1/2} \left\{ \check{\hat{\Sigma}} \left[\check{\hat{I}} - \check{\hat{g}} \check{\hat{\Sigma}} \right]^{-1} \right\}_{eh} \hat{A}_h^{1/2}, \tag{4.6}$$

where $\hat{A}_{e,h}(q,\omega) = \left(\hat{g}_{e,h}(q,\omega) - \hat{g}^{\dagger}_{e,h}(q,\omega) \right)/2i$. Using the general form of the model self-energies discussed in the previous section allows us to reduce the expression of $\hat{r}_A$ to

$$\hat{r}_A = 2i\hat{A}_e^{1/2} \beta f_s \left[\hat{I} - \beta g_s \left(\hat{g}_e + \hat{g}_h \right) - \gamma \left(\hat{g}_h \hat{\sigma}_x - \hat{\sigma}_x \hat{g}_e \right) - (\beta^2 + \gamma^2) \hat{g}_h \hat{g}_e \right]^{-1} \hat{A}_h^{1/2}. \tag{4.7}$$

This expression becomes particularly simple when $\epsilon = 0$ because $g^e = g^h$, $f^e = -f^h$ and $f'^e = -f'^h$ due to electron-hole symmetry. So $\hat{r}_A$ is an scalar quantity given by

$$\hat{r}_A = \frac{4\beta f_s \left(\mathrm{Im} g^2 - |f - f'^*|^2 \right)}{1 - \mathrm{Tr} \left[\left(\beta g_s \hat{I} \mp \gamma \hat{\sigma}_x \right) \hat{g}_{e,h} \right] - (\beta^2 + \gamma^2) \det \hat{g}_{e,h}} \hat{I}, \tag{4.8}$$

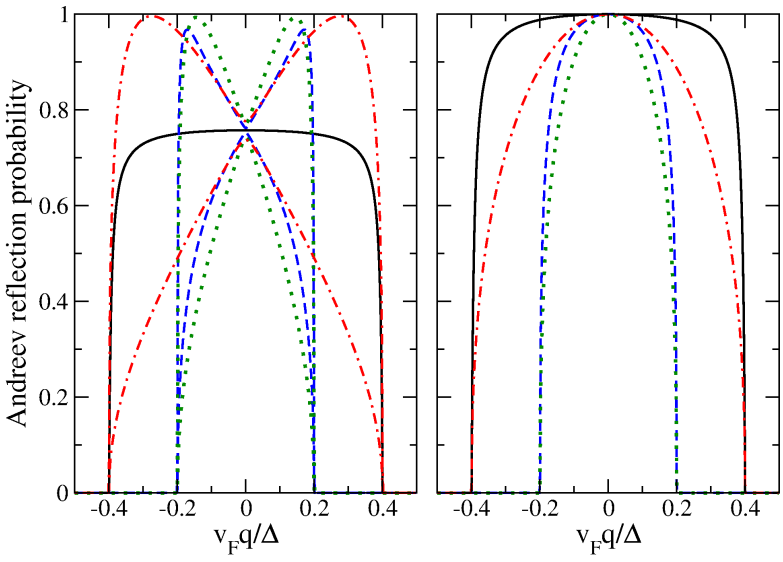

FIGURE 4.2: Andreev reflection probability on the two eigenchannels as a function of the parallel momentum q for fixed energy $\omega = 0.2\Delta$. The left panel corresponds to the bulk-BCS model (with $\beta = 1$) and the right one to the HDSC model. The different curves correspond to different values of the doping level ϵ: 0 (full lines), 0.1 (dashed lines), 0.3 (dotted lines) and 0.4Δ (dashed-dotted lines).

where $\mathrm{Tr}\left[\left(\beta g_s \hat{I} \mp \gamma \hat{\sigma}_x\right) \hat{g}_{e,h}\right] = [2\beta g_s g - \gamma(f + f')]$ and $\det \hat{g}_{e,h} = (g^2 - ff')$.

In general doping conditions (i.e. when $\epsilon \neq 0$), $\hat{r}_A$ is not a scalar within the bulk-BCS model. The eigenvalues of $\hat{r}_A \hat{r}_A^\dagger$ give the Andreev reflection probability decomposed into two eigenchannels for each wave vector q. The evolution of these eigenvalues for fixed ω and increasing ϵ as a function of q is shown in the left panel of Figure 4.2. Their maximum value is reached for $\beta = 1$ and it never exceeds ~ 0.76 at normal incidence. Within the HDSC model, however, $\hat{r}_A$ remains scalar for arbitrary doping and it always reaches the unitary limit at $q = 0$ (see right panel of Figure 4.2).

It is also interesting to analyze the physical character of the Andreev reflection in the two models. The information on how the eigenchannels of the uncoupled structure are connected by an Andreev process is contained in the matrix $\hat{R}_e \hat{r}_A \hat{R}_h^{-1}$. As $\hat{r}_A$ is a scalar within the HDSC model, the channel mixing is determined by $\hat{R}_e \hat{R}_h^{-1}$. This is also the case for the bulk-BCS model at zero doping. In this case we have $\alpha_h = \pi - \alpha_e$ and thus electrons injected in one channel emerge as holes in the opposite one. The momentum in the y direction is conserved in this process and therefore this type of reflection corresponds to what has been described in [56] as *specular Andreev reflection*. On the other hand for $\epsilon \neq 0$ and $\omega \to 0$ we have $\alpha_h = \alpha_e$ which corresponds to the usual (retro) reflection where holes are reflected on the same channel as the incident electron. For intermediate doping situations both types of reflection would be present although with a dominance of specular (retro) reflection for $\omega > \epsilon$ ($\omega < \epsilon$).

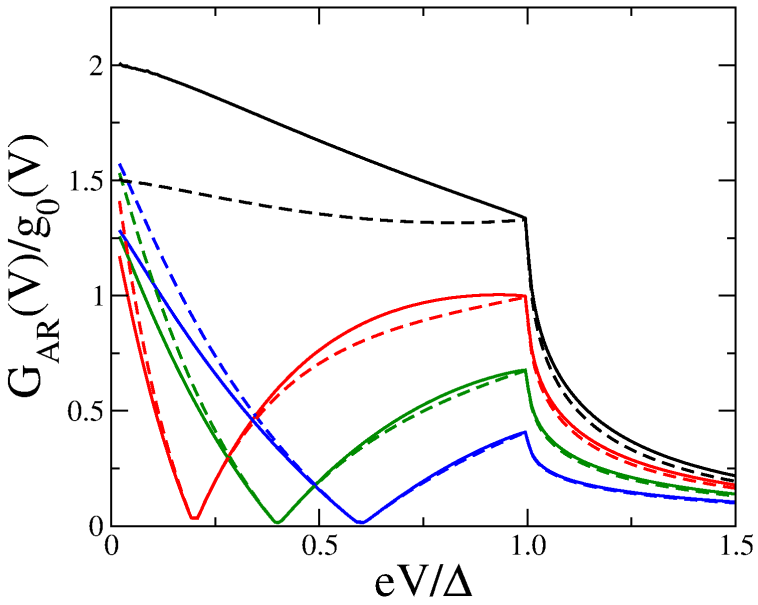

FIGURE 4.3: Total differential conductance per unit length due to Andreev reflection G_{AR} normalized to the conductance per unit length of a ballistic graphene layer $g_0(V) = \frac{4e^2}{h}(eV+\epsilon)/(\pi\hbar v_F)$. The results for the HDCS model (full lines) and for the bulk-BCS model (dashed lines) are compared with increasing doping level $\epsilon = 0, 0.2, 0.4$ and 0.6Δ.

To complete the analysis of the present section we have computed the differential conductance per unit length due to Andreev processes, given by [51]

$$G_{AR} = \frac{2e^2}{h}\frac{1}{2\pi}\int_{-\frac{\pi}{a}}^{\frac{\pi}{a}} dq \mathrm{Tr}\left[\hat{r}(q,eV)\hat{r}^{\dagger}(q,eV)\right]. \tag{4.9}$$

The results for G_{AR} within the two models are shown in Fig. 4.3. As suggested in Ref. [56] we normalize the result by the conductance per unit length of a ballistic graphene sheet, which in the low energy limit is given by $g_0(V) = \frac{4e^2}{h}(eV+\epsilon)/(\pi\hbar v_F)$. As can be observed, at the charge neutrality point the HDSC model yields a maximum of ratio $G_{AR}/g_0 = 2$ at zero voltage, which drops to ~ 1.33 for $\epsilon > 0$, in agreement with the results of Ref. [56]. This ratio is of the order of ~ 1.63 in the bulk-BCS model with $\beta = 1$ regardless of the doping level. The qualitative behavior of the differential conductance with ϵ is similar in both models and agree with the results of Ref. [56].

4.2.3 Conclusions.

Two models have been introduced to describe the superconducting electrode within the TB approach. On the one hand, a bulk macroscopic superconductor is contacted to the graphene layer. The internal structure of graphene, based on the combination of two sublattices, is therefore interrupted at the NS interface. The scattering introduced by

this interface is responsible of not reaching perfect transmission between the graphene layer and the superconductor.

On the other hand, the superconductor is modeled as a graphene layer with high doping and a pairing correlation amplitude. The interface maintains the internal structure and the coupling between the normal and the superconducting regions is perfect. The results for this model are equivalent to the ones obtained in Ref. [56] where the mode matching at the interface was perfect.

In the following section the proximity effect on the normal graphene region is studied. These two situations are considered within the TB approach. However, the results for the continuous model, which give a clear analytical insight on the effect of the superconductor on the local density of states, are considered to be equivalent to the HDSC model. The reason for doing so is that the continuous model considers perfect matching of the wave functions at the NS interface.

4.3 Proximity effect on a graphene layer.

When contacted by a superconducting host, the behavior of electrons in a normal metal is altered. As it was explained in Section 2.2, the superconducting pairing amplitude does not vanish abruptly at the interface with the normal metal. Quite the contrary, it penetrates the normal metal inducing some of the characteristics of the superconductor on it. In particular, the density of states of the normal region develops a gap Δ limited by sharp peaks for energies $E = \pm\Delta$. The states within the gap are no longer accessible since the pairing amplitude favors the coupling between electrons and holes and are *pushed* outside the gap. The superconducting pairing amplitude decays inside the normal region until the usual properties of the metal are recovered far away from the interface. This decaying is controlled by the superconducting coherence length ξ. Insight on the proximity effect can be obtained by analyzing the local density of states (LDOS). The LDOS is the density of states at a particular point inside the normal region. As a consequence, it depicts both the effect of the pairing amplitude on the normal density of states and its decay away from the interface.

The study of the proximity effect on a graphene-based NS junction is of capital importance to understand the rich interplay between the superconducting correlations and the Dirac spectrum and in order to have a clear picture of the mesoscopic superconductivity on a truly two-dimensional material. The LDOS on graphene-based hybrid superconductor systems was studied prior to this work in Ref. [93] (zigzag edged NS) and Ref. [94] (SNS junction). Explain. More recent studies include ...

A particular feature of the proximity effect on diffusive SNS and NS junctions is the appearance of a sharp cut-off in the energy spectrum below which the density vanishes completely, i.e. the minigap E_g. The minigap is smaller than the superconducting gap and depends on the concentration of impurities and on the length of the normal region L. In the limit $L \gg \xi$, e.g. for a semi-infinite normal region, there is no minigap. For the case of SNS junctions, the minigap also depends on the phase difference between the superconductors φ. In particular, for a short diffusive Josephson junction the minigap has the simple form $E_g = \Delta \cos\varphi/2$ [100]. In general, the existence of a minigap is a highly non-trivial phenomenon. For more details see for example Ref. [101].

4.3.1 Equation for the minigap.

Using the previous results one can analyze the effect of the coupling with the superconductor on the spectral properties of a graphene layer of finite size. Again, we will focus on the differences between the bulk-BCS and the HDSC models for the interface. A finite graphene layer coupled to a superconductor is studied within the TB approach. As it is demonstrated in Section 3.2, the Green function of a finite layer with armchair edges and N sites is constructed from the semi-infinite case. From the Dyson's equation it is straightforward to obtain the Green functions at the edge of the layer (labeled as 1) when the coupling to the superconductor is introduced on the opposite edge (labeled as N). Then, for an arbitrary line n inside the layer we have

$$\check{\hat{G}}_{n,n} = \check{\hat{g}}^F_{n,n} + \check{\hat{g}}^F_{n,N}\check{\hat{\Sigma}}\left[\check{\hat{I}} - \check{\hat{g}}^F_{N,N}\check{\hat{\Sigma}}\right]^{-1}\check{\hat{g}}^F_{N,n}, \tag{4.10}$$

where $\check{\hat{\Sigma}}$ stands for the general form of the self-energy introduced in Sec. 4.2. We can further reduce this expression to

$$\begin{aligned}\check{\hat{G}}_{n,n} &= \check{\hat{g}}^F_{n,n} + \check{\hat{g}}^F_{n,N} \\ &\times \begin{pmatrix} \left[\beta g_s - \gamma\hat{\sigma}_x + \left(\beta^2+\gamma^2\right)\hat{g}^{Fh}_{N,N}\right]\hat{D}_e^{-1} & -\beta f_s \hat{D}_h^{-1} \\ -\beta f_s \hat{D}_e^{-1} & \left[\beta g_s + \gamma\hat{\sigma}_x + \left(\beta^2+\gamma^2\right)\hat{g}^{Fe}_{N,N}\right]\hat{D}_h^{-1} \end{pmatrix} \check{\hat{g}}^F_{N,n}.\end{aligned} \tag{4.11}$$

The quantities $\hat{D}_e$ and $\hat{D}_h$ have the following general form, expressed in the graphene sublattice space

$$\begin{aligned}\hat{D}_e &= \hat{I} - \beta g_s(\hat{g}^F_e + \hat{g}^F_h) - \gamma(\hat{g}^F_e\hat{\sigma}_x - \hat{\sigma}_x\hat{g}^F_h) - (\beta^2+\gamma^2)\hat{g}^F_e\hat{g}^F_h \\ \hat{D}_h &= \hat{I} - \beta g_s(\hat{g}^F_e + \hat{g}^F_h) - \gamma(\hat{g}^F_h\hat{\sigma}_x - \hat{\sigma}_x\hat{g}^F_e) - (\beta^2+\gamma^2)\hat{g}^F_h\hat{g}^F_e\end{aligned}$$

As it was exposed in the previous section, in the limit where $\epsilon = 0$ these two denominators become equal and simplify to an scalar, D, because $\beta g_s(\hat{g}_e^F + \hat{g}_h^F) + \gamma(\hat{g}_e^F\hat{\sigma}_x - \hat{\sigma}_x\hat{g}_h^F) = \mathrm{Tr}\left[\left(\beta g_s\hat{I} \mp \gamma\hat{\sigma}_x\right)\hat{g}_{e,h}^F\right]$, and $\hat{g}_e^F\hat{g}_h^F = \det\hat{g}^F$. Then

$$D = 1 - \mathrm{Tr}\left[\left(\beta g_s\hat{I} \mp \gamma\hat{\sigma}_x\right)\hat{g}_{e,h}^F\right] - \left(\beta^2+\gamma^2\right)\det\hat{g}_{e,h}^F \ . \tag{4.12}$$

Using the expression of the finite layer Green functions and the rotation given in Section 3.2 one can easily show that

$$\det\left[\hat{g}_{e,h}^F\right] = -\frac{1}{t_g^2}\frac{\sin\left(N\phi_1\right)\sin\left(N\phi_2\right)}{\sin\left[(N+1)\phi_1\right]\sin\left[(N+1)\phi_2\right]} \ ,$$

$$\begin{aligned}\mathrm{Tr}\left[\left(\beta g_s\hat{I} \mp \gamma\hat{\sigma}_x\right)\hat{g}_{e,h}^F\right] &= \frac{1}{t_g\sin\alpha}\left\{\frac{\sin\left(N\phi_1\right)\sin\left[(N+1)\phi_2\right]\left[\beta g_s - \gamma\sin\left(\alpha+q\right)\right]}{\sin\left[(N+1)\phi_1\right]\sin\left[(N+1)\phi_2\right]}\right. \\ &- \left.\frac{\sin\left(N\phi_2\right)\sin\left[(N+1)\phi_1\right]\left[\beta g_s + \gamma\sin\left(\alpha-q\right)\right]}{\sin\left[(N+1)\phi_1\right]\sin\left[(N+1)\phi_2\right]}\right\} \ .\end{aligned}$$

The zeroes of D determine the poles of the coupled system Green functions. From them one can thus analyze the distortion of the spectrum due to the superconducting proximity effect. For the charge neutrality case, this zeroes can be obtained from the expression

$$\begin{aligned}\frac{-\beta\omega^2}{\sqrt{\omega^2 - t_g^2\sin^2 qa}\sqrt{\Delta^2-\omega^2}} &= \frac{\sin\left[(N+1)\phi_1\right]\sin\left[(N+1)\phi_2\right] + (\beta^2+\gamma^2)\sin\left(N\phi_1\right)\sin\left(N\phi_2\right)}{\sin\left(N\phi_1\right)\sin\left[(N+1)\phi_2\right] - \sin\left(N\phi_2\right)\sin\left[(N+1)\phi_1\right]} \\ &+ \frac{\gamma}{\sin\alpha}\frac{\sin\left(\alpha+q\right)\sin\left(N\phi_1\right)\sin\left[(N+1)\phi_2\right] + \sin\left(\alpha-q\right)\sin\left(N\phi_2\right)\sin\left[(N+1)\phi_1\right]}{\sin\left(N\phi_1\right)\sin\left[(N+1)\phi_2\right] - \sin\left(N\phi_2\right)\sin\left[(N+1)\phi_1\right]} \ .\end{aligned} \tag{4.13}$$

The spectrum corresponds to a series of subbands which disperse quadratically as a function of q in the small q limit. As in the uncoupled case, detailed in Section 3.2, the precise form of the dispersion relation depends on the value of N mod 3. In the case where the uncoupled layer is metallic (N mod 3 = 2) the coupling to the superconductor induces a *minigap* in the lowest band. The existence of this minigap in the spectrum is similar to what is found for diffusive conductors and can be associated to the pseudo-diffusive behavior of graphene at the charge neutrality point [38, 102]. For the cases N mod $3 = 0, 1$ the uncoupled layer is insulating and the coupling of the superconductor just leads to a renormalization of the gap in the spectrum. We denote by E_g^* the lowest energy level for all three cases.

The dependence E_g^* as a function of N and the interface parameters β and γ can be obtained from Equation 4.13 with $q = 0$. For large N this level decreases as $1/N$

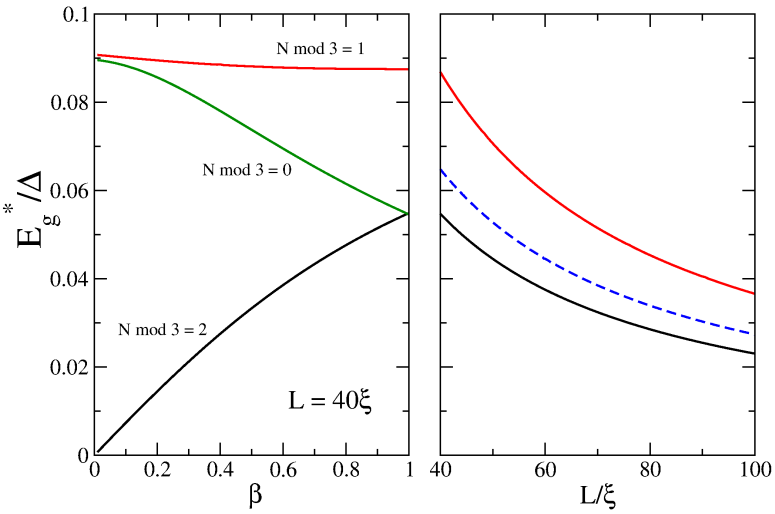

FIGURE 4.4: Evolution of the lowest energy level E_g^* of a finite graphene layer coupled to a superconductor as a function of β within the bulk-BCS model for $L = 40\xi$ (left panel) and with the length of the layer L within both the bulk-BCS (at $\beta = 1$) and the HDSC models (right panel). In the case of the bulk-BCS model for arbitrary β three different behaviors are found depending on the N mod 3 value. On the contrary, a universal behavior of E_g^* is found within the HDSC model regardless of the N value (see text).

with a prefactor which depends on N mod 3 and the interface parameters. Figure 4.4 describes the behavior of E_g^* both in the bulk-BCS and in the HDSC models. The left panel shows the lowest energy state within the bulk-BCS model as a function of the interface transparency parameter (β) for fixed N. The three cases $N \bmod 3 = 0, 1, 2$ are shown. As can be observed, in the metallic case the minigap evolves from zero at $\beta = 0$ to a maximum value at $\beta = 1$. On the other hand, the two insulating cases exhibit different behavior. While the starting value at $\beta = 0$ is fixed by E_g in both cases, in the case $N \bmod 3 = 0$ it decreases until it reaches the same value as the one of the $N \bmod 3 = 2$ case for $\beta = 1$. On the other hand E_g^* remains approximately constant for $N \bmod 3 = 1$. This behavior indicates that the proximity effect is almost negligible in this case. The right panel shows the behavior of the lowest energy state as a function of N both in the bulk-BCS model with $\beta = 1$ and in the HDSC. The results are universal (i.e. independent of the ratio Δ/t_g) when plotted as a function of L/ξ, where $\xi = \hbar v_F/\pi\Delta$ is the superconducting coherence length. It is interesting to note that while in the bulk-BCS model two limiting $1/L$ curves, corresponding to $N \bmod 3 = 0, 2$ and $N \bmod 3 = 1$, appear, in the HDSC model E_g^* lay on the same $1/L$ curve regardless of N (dashed line in Figure 4.4).

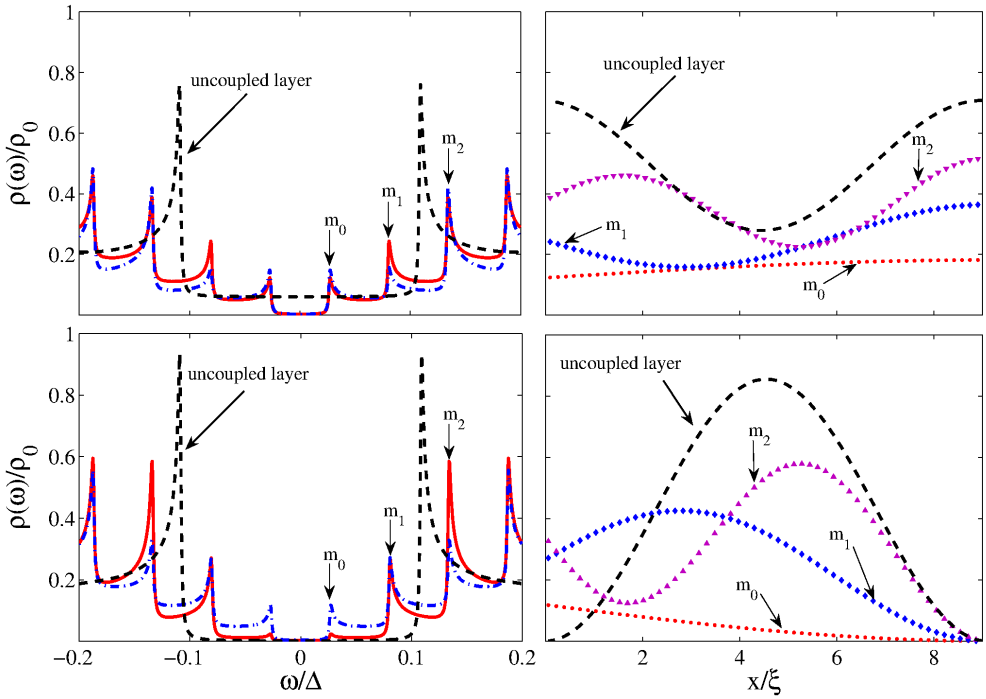

FIGURE 4.5: Spatial variation of the LDOS on a finite layer ($L = 9\xi$) in the HDSC model. The plots on the top panels correspond to the lines inside the layer with $n \bmod 3 = 1, 2$ and those on lower ones correspond to $n \bmod 3 = 0$. The uncoupled layer has a metallic behavior ($N \bmod 3 = 2$). The LDOS for this case at the edges of the layer (top left panel) and at the center of the layer (lower left panel) is plotted with dashed lines. When coupled to the superconductor, the LDOS is modified by the appearance of a minigap (denoted as m_0 in the pictures) and with the breaking of the uncoupled bands into a pair of subbands (m_1 and m_2 in the pictures). The evolution of the LDOS along the layer is shown in the right panels. The results are normalized to the LDOS of a bulk graphene layer with zero doping at $\omega = \Delta$, denoted by ρ_0.

4.3.2 Local density of states.

We define the electronic local density of states (LDOS) on a line n within the graphene layer as

$$\rho_n(\omega) = \frac{a}{(2\pi)^2} \int_{-\frac{\pi}{a}}^{\frac{\pi}{a}} dq \mathrm{TrIm}\left[\hat{G}_{n,n}(q,\omega)\right], \tag{4.14}$$

which has been normalized to one electron per site and spin. The LDOS thus defined is measured in units of $a/\hbar v_F$. However, to study the proximity effect it is more convenient to normalize the LDOS with the density of a bulk graphene layer with zero doping at $\omega = \Delta$, ρ_0, which for $\Delta \ll \hbar v_F/a$ is given by $\Delta/2\pi(a/\hbar v_F)^2$. The results thus obtained do not depend on the choice of the ratio Δ/t_g used in our tight-binding calculations.

The LDOS on a metallic layer ($N \bmod 3 = 2$) is shown in Figure 4.5. The results for the coupled case within the HDCS model are compared with the results for the uncoupled case. It is typically found that the number of singularities in the LDOS (associated with the number of subbands) in a given energy interval is doubled as compared to the uncoupled case. This effect is due to the breaking of the double degeneracy of the bands due to the coupling with the superconductor. The LDOS also exhibits an oscillatory behavior with the position on the layer. This behavior reflects the properties of the electronic wave functions and, as in the case of isolated nanoribbons [37], is distinct for lines with $n \bmod 3 = 1, 2$ and lines with $n \bmod 3 = 0$. We thus illustrate these cases separately on the top and on the lower panels of Figure 4.5.

The right panels of Figure 4.5 show the evolution along the layer of the LDOS close to the singularities. We illustrate this evolution at three different energies corresponding to the lowest first singularities, indicated by $m = 0, 1$ and 2 in Figure 4.5. For reference we also show the spatial variation of the LDOS close to the first singularity for the uncoupled case. In this case the LDOS reaches a maximum value at the edges of the layer and a minimum in the middle for lines $n \bmod 3 = 1, 2$, while the opposite behavior is found for $n \bmod 3 = 0$. In the coupled case one can still identify the singularities with the oscillation pattern in the LDOS but it does no longer reach an extreme value at the edge of the layer in contact with the superconductor.

As final remark we note that in the case of insulating nanoribbons the coupling to the superconductor just induces a shift singularities in the spectrum but do not change their number. This is due to the non-degenerate character of the bands of the uncoupled layer.

4.3.3 Semi-infinite graphene layer within the TB approach.

The results of the previous section can be extended to analyze the spectral properties of a semi-infinite graphene layer coupled to a superconductor. The local Green function on a line n is given by

$$\check{\hat{g}}_{n,n} = \left[\check{\hat{G}}^{-1}_{n,n} - t_g^2 \check{\hat{g}}\right]^{-1},$$

where $\check{\hat{G}}_{n,n}$ is the Green function for a finite graphene layer coupled to a semi-infinite superconducting layer obtained in the previous section and $\check{\hat{g}}$ is the Green function for the edge of the semi-infinite layer.

Figure 4.6 illustrates the spatial variation of the LDOS on a semi-infinite graphene layer and the effect of varying the doping level within the bulk-BCS model. For reference we show the LDOS for the uncoupled case on the upper panels. As can be observed,

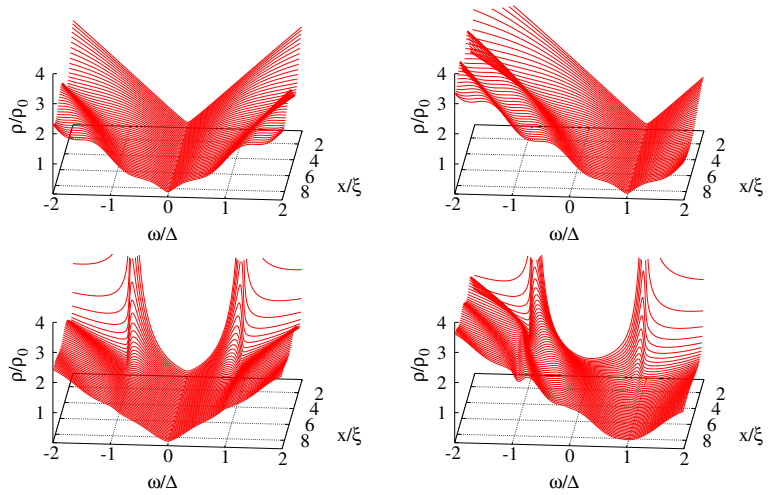

FIGURE 4.6: LDOS on lines of type $n \bmod 3 = 1$ for a semi-infinite graphene layer coupled to a superconductor within the bulk-BCS model (lower panels). The upper panels show the corresponding results for the uncoupled case. The plots on the left correspond to the undoped case while those on the right correspond to $\epsilon = \Delta$.

the uncoupled LDOS exhibits long wavelength oscillations on the $\sim \hbar v_F/|\omega|$ scale on top of the characteristic V shape behavior. These oscillations are a surface effect which decreases in amplitude inside the layer as shown in Fig. 4.7, where the LDOS profile at $\omega = 2\Delta$ is plotted on a larger scale. A similar effect has been shown to occur in the case of nanoribbons with zigzag edges [93].

The superconducting proximity effect is manifested by the appearance of sharp peaks in the LDOS for energies $|\omega| \sim \Delta$ (lower panels on Figure 4.6). These peaks distort the V shape density of states, an effect which decays within a few times the coherence length inside the layer. The small oscillations on the $\hbar v_F/|\omega|$ scale are reduced as compared to the uncoupled case but are still observable within the bulk-BCS model (indicated by the full line in Figure 4.7).

The overall behavior of the LDOS within the HDSC model is very similar, although in this last case the $\hbar v_F/|\omega|$ oscillations are further suppressed (dashed line in Figure 4.7).

The right panels in Figure 4.6 illustrate the effect on the LDOS of a displacement from the charge neutrality condition by applying a gate potential (finite ϵ). It is observed that the V shape is essentially rigidly displaced while the peaks induced by the proximity effect remain fixed at $\omega \sim \pm\Delta$. On the other hand, the wavelength of the oscillation pattern is in this case set by $\hbar v_F/|\omega - \epsilon|$.

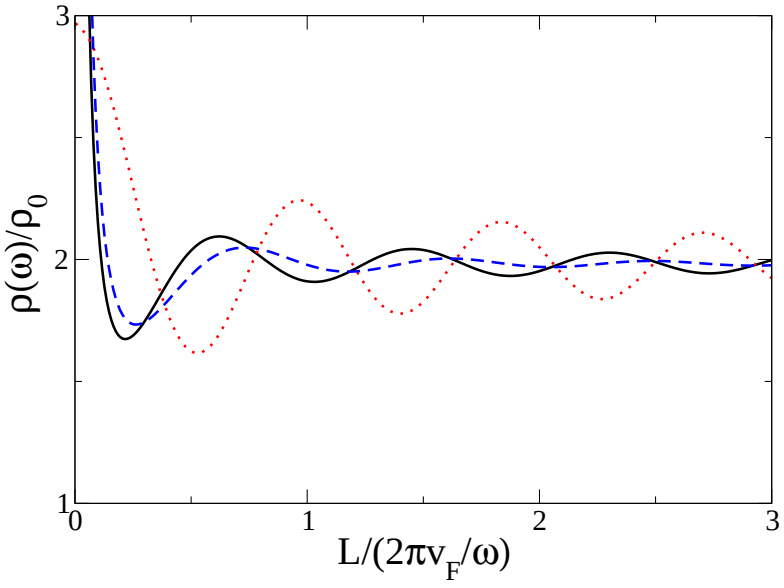

FIGURE 4.7: Oscillation pattern on the LDOS of a semi-infinite armchair graphene layer at zero doping within the bulk-BCS model (full line), the HDCS model (dashed line) and in the uncoupled case (dotted line). The energy is fixed at $\omega = 2\Delta$.

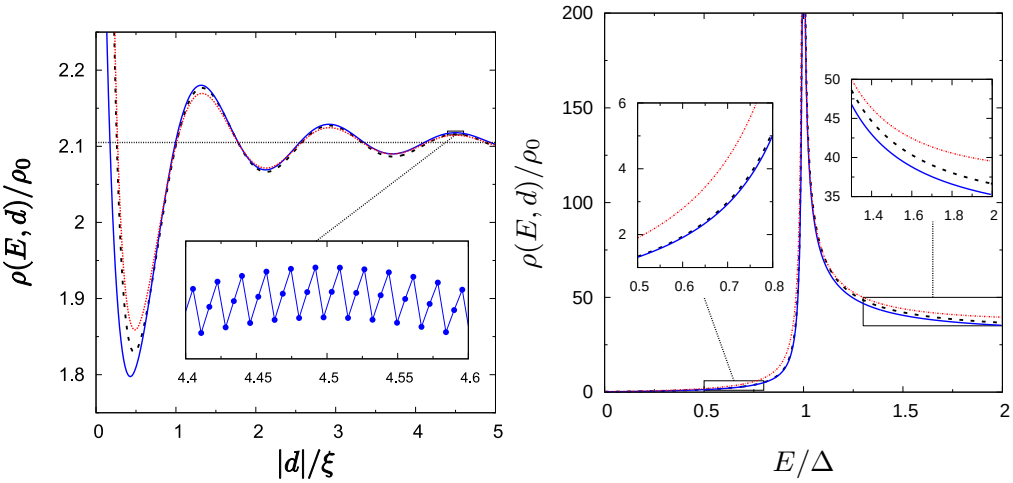

FIGURE 4.8: LDOS in the normal region with $E_F = 0$ for a semi-infinite layer of graphene with armchair edges coupled to a superconducting region (left panel). Profiles for both boundary conditions (full blue line when vanishing the wave function and full red line for the derivative) are equivalent to the TB results (dashed line). The right panel shows the oscillating behavior of the LDOS for $E = 2\Delta$ along the direction transversal to the interface. The transversal distance d is normalized to the BCS superconducting coherence length ξ. All the results show the same oscillating behavior around the bulk value. The oscillatory behavior at the atomic scale is shown in the inset for the boundary condition of vanishing the wave function.

4.3.4 LDOS within the continuous approach. Influence of the edges.

We complete the analysis of the graphene-based NS junction using the results by the continuous model introduced in Section 3.3. All the ingredients necessary to analyze the graphene-superconductor coupling within the continuous approach have been already introduced in that section and in Section 3.4. In the present section, we analytically derive the Green function of the coupled system both for armchair and zigzag edges. We locate the interface at $x = 0$, parallel to the y axis, with the normal region covering the $x < 0$ infinite half-plane. Since the superconducting region is represented in Nambu space, in order to use Dyson's equation as has been explained in Section 3.4, the Green's functions of the normal region are written as

$$\check{g}_L = \begin{pmatrix} \hat{g}_e & 0 \\ 0 & \hat{g}_h \end{pmatrix}. \tag{4.15}$$

Electron excitations are states above the Fermi energy. Therefore, $\hat{g}_e$ corresponds to the Green function of a semi-infinite graphene layer with armchair or zigzag edges at the interface. We set $\alpha_e = \alpha$, with $\hbar v_F k_e = \sqrt{(E_F + E)^2 - (\hbar v_F q)^2}$. On the other hand, hole excitations have energies below E_F. Thus, $\hat{g}_h$ corresponds to the same equations but with the change $\alpha_h = \arcsin \hbar v_F q / (E_F - E)$, with $\hbar v_F k_h = \sqrt{(E_F - E)^2 - (\hbar v_F q)^2}$. For the superconducting region (R), $\check{g}_R$ stands in Dyson's equation for the Green function of the semi-infinite superconducting region, with either an armchair or a zigzag edge at the interface.

The coupling with the superconductor appears in the Green function as a perturbation of the semi-infinite result $\check{g}_L$. Thus we can write

$$\check{G}_L(x, x') = \check{g}_L(x, x') + \delta\check{G}(x, x'), \tag{4.16}$$

where $\delta\check{G}$ is the correction with respect to the uncoupled case. Our formalism allows in principle to obtain analytical results for $\delta\check{G}$ in the case of arbitrary effective hopping and coordinates x and x'.

For the case of an armchair interface, using the boundary conditions of vanishing the derivative of the wave function and setting $\beta = 1$, for $x = x'$ we can write the perturbation $\delta\check{G}$ of Equation 4.16 as

$$\begin{aligned} \delta\hat{G}^{\mathrm{arm}}_{ee}(x = x') \;=\; & \frac{i}{\hbar v_F}\frac{e^{-2ik_e x}}{\cos\alpha_e}\left\{\begin{pmatrix} \cos 2Kx & -i\sin(2Kx + \alpha_e) \\ -i\sin(2Kx - \alpha_e) & \cos 2Kx \end{pmatrix}\right. \\ & \left. + \frac{N_{\mathrm{arm}}}{D_{\mathrm{arm}}}\begin{pmatrix} \sin\alpha_e & -i \\ i & \sin\alpha_e \end{pmatrix}\right\}, \end{aligned} \tag{4.17}$$

where we have defined the auxiliary quantities

$$N_{\text{arm}} = 2\sin\alpha_e\left(1+\frac{E}{\Omega}\cos\alpha_h\right)+\frac{\Delta^2}{\Omega^2}\left(\sin\alpha_e-\sin\alpha_h\right) \tag{4.18}$$

$$D_{\text{arm}} = 2+2\cos\alpha_e\cos\alpha_h+2\frac{E}{\Omega}\left(\cos\alpha_e+\cos\alpha_h\right)+\frac{\Delta^2}{\Omega^2}\left[1+\cos\left(\alpha_e+\alpha_h\right)\right] \tag{4.19}$$

The denominator D_{arm} contains information on the spectral properties of the coupled system. It will be described in detail in the following section. For the calculation of the LDOS it is necessary to obtain the diagonal components of the local Green's function ($[ee,AA]$ and $[ee,BB]$). Whenever $Kx=n\pi$, they simplify to

$$G^{\text{arm}}_{L|ee,AA}(x,x)=G^{\text{arm}}_{L|ee,BB}(x,x)=\frac{-i}{\hbar v_F}\left\{\frac{1}{\cos\alpha_e}-e^{-2ik_e x}\frac{N_{\text{arm}}}{D_{\text{arm}}}\tan\alpha_e\right\}. \tag{4.20}$$

We now analyze a normal-superconductor graphene junction with a zigzag edge at $x=0$. We impose that the normal region at $x<0$ ends with a zigzag edge formed by A atoms. The superconducting region (at $x>0$) has therefore an edge formed by atoms from the B sublattice. For these conditions we obtain the following correction for Equation 4.16

$$\delta\check{G}^{\text{zz}}_{ee}(x,x') = -\frac{i\beta^2 e^{-ik_e(x+x')}}{\hbar v_F D_{\text{zz}}}\left[\frac{E}{\Omega}+\beta^2\frac{e^{i\alpha_h}}{\cos\alpha_h}\right]\begin{pmatrix}1 & e^{-i\alpha_e}\\ -e^{-i\alpha_e} & -e^{-2i\alpha_e}\end{pmatrix}, \tag{4.21}$$

with

$$D_{\text{zz}}=1+\beta^2\frac{E}{\Omega}\left(\frac{e^{-i\alpha_e}}{\cos\alpha_e}+\frac{e^{i\alpha_h}}{\cos\alpha_h}\right)+\beta^4\frac{e^{-i\alpha_e}e^{i\alpha_h}}{\cos\alpha_e\cos\alpha_h}. \tag{4.22}$$

The electronic LDOS per unit length for a distance $x=x'\equiv d$ is defined as

$$\rho(E,d)=\frac{-1}{\pi}\int_{-\infty}^{\infty}dq\,\text{Tr}\left[\text{Im}\left\{\check{G}_{L|ee}\left(q,E;d,d\right)\right\}\right] \tag{4.23}$$

The left panel of Figure 4.8 shows the LDOS for an armchair edge close to the interface ($d=-0.1\xi$) obtained using the boundary conditions of vanishing the wave function or its derivative. For comparison we also show in this figure the results obtained for the TB model calculations. The results of Figure 4.8 are normalized to the density of a bulk graphene layer with zero doping at $E=\Delta$, $\rho_0=2\Delta/\hbar^2v_F^2$ (see the bulk results calculated in Section 3.3). The discrepancies between the different matching conditions tend to disappear when we move away from the interface, as it is shown in the right panel of Figure 4.8. This panel also illustrates the oscillatory behavior of the LDOS inside the normal region of graphene around the bulk value (indicated by the dashed line). The period of the oscillation is given roughly by $\hbar v_F/E$ and the amplitude decreases with the distance to the interface. When studying the spatial evolution of the LDOS

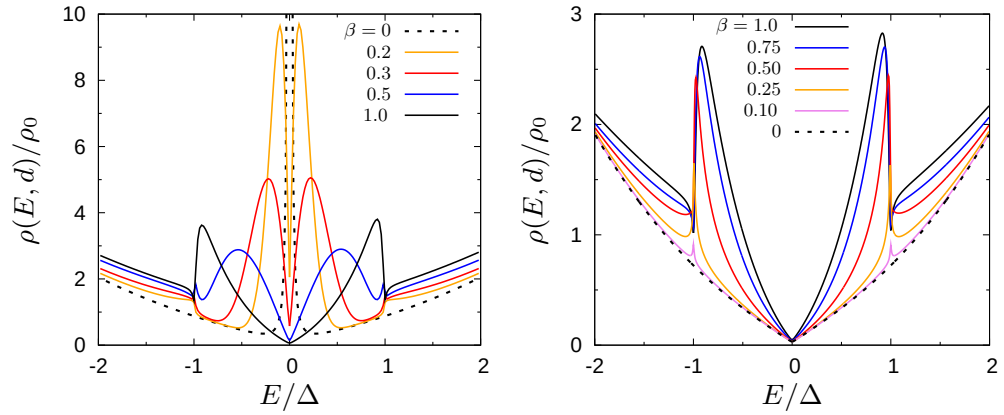

FIGURE 4.9: LDOS profiles, at a distance $d = -0.41\xi$ inside the normal region with $E_F = 0$, for different transparencies of the zigzag (left panel) and armchair (right panel) interface. In the zigzag case, the edge state splits and evolves into a band inside the superconducting gap when the transparency β goes from 0 (uncoupled case represented by a dashed black line) to 1 (perfect transparency, solid black line). For the armchair case the superconducting proximity effect is manifested by the appearance of sharp peaks in the LDOS for energies $E \sim \Delta$.

of an armchair layer of graphene, it is well known that there is an oscillatory behavior at the atomic scale [37, 82]. As it is explained in the previous section for the case of the semi-infinite layer, this is a direct result of the valley mixing that happens at an armchair edge. For the sake of clarity, the evolution of the LDOS with the direction transverse to the interface shown in the right panel of Figure 4.8 has been calculated for values $|x|/a = 3n$, with n a positive integer. Similar profiles are reached for different multiplicities of the coordinate x. The oscillatory behavior at the atomic scale is shown in the inset of this panel for the boundary conditions of vanishing the wave function.

On the other hand, the left panel of Figure 4.9 shows the LDOS for a zigzag edge at a distance inside the normal region $d = -0.4\xi$. The results correspond to different values of the parameter β controlling the interface transparency. For the uncoupled case with $\beta = 0$, a localized edge state appears at $E = E_F$ (dashed line in Figure 4.9). However, for a non-zero transparency the edge state splits and evolves into a band inside the superconducting gap. By further increasing the parameter β, this band gives rise to the peaks in the DOS for energies around $E = \pm\Delta$, when $\beta = 1$. This effect is analyzed in detail in the next section.

It is important to emphasize that although the surface state at $E = E_F$ for zigzag edges has been thoroughly studied, our results demonstrate that the superconducting proximity effect splits this state and produces a shift that depends on the transparency between the normal and superconducting regions.

The LDOS for the armchair case with the same set of parameters is illustrated in the right panel of Figure 4.9. As can be observed there is no localized state for the uncoupled case ($\beta = 0$) and when β increases, two peaks arise around $E = \pm\Delta$.

The coupling with the superconductor depends on the edge type when the transparency is not perfect. This is a direct consequence of the differences between armchair and zigzag edges in graphene. On the contrary, for a perfect transparency, the profile of the LDOS is independent of the edge type. The main characteristic of this profile, with respect to the corresponding result for a metal in contact with a superconductor, is the enhancement of the density of states within the gap.

4.3.5 Conclusions.

Equation for the minigap and minigap evolution with the length of the normal region. LDOS of the finite and semi-infinite normal regions. Introduction of states inside the gap. Influence of the model for the superconductor. Influence of the edge orientation when the coupling is not perfect.

We have presented a theoretical analysis of the proximity effect at a graphene-superconductor interface. We have studied the effect of the coupling with the superconductor on the spectral properties of finite and semi-infinite graphene layers. For finite layers, we have obtained a simple expression for the energy spectrum of the coupled system, which can be numerically evaluated asily. We have shown that a metallic ribbon develops a minigap whose size inversely decreases with the length of the layer. This effect can be associated with the pseudodiffusive behavior of graphene. The induced minigap is slightly smaller in the bulk-BCS model with $\beta = 1$ than in the HDSC model.

For the semi-infinite case, the proximity effect manifests in the appearance of peaks in the DOS for frequencies $|\omega| \sim \Delta$. These peaks rapidly decay inside the graphene sheet for distances a few times the superconducting coherence length ξ. On the other hand, the LDOS keeps its characteristic V shape for zero doping for frequencies $|\omega| < \Delta$.

4.4 Proximity induced interface bound states.

The properties of bound states arising from multiple Andreev reflections in S-graphene-S junctions have been analyzed in Refs. [94] and [103]. However, as we show in this section, the special electronic properties of graphene are such that bound states can be formed even at isolated single junctions. The aim of this section is to demonstrate the existence of these interface bound states (IBS) and to analyze their properties for different types

of graphene-superconductor junctions. This section is organized as follows: First, we justify the existence of the IBS using a simple model based on the matching of the wave functions that are solution of the Dirac-Bogoliubov-de Gennes equations for different regions. After completing the analysis for the case of the simple model, which implicitly assumes a decoupling of the two valleys in the graphene band structure, we consider more microscopic models for junctions formed along armchair or zig-zag edges. We study the effect of an additional potential barrier at the interface and the possibility to modify the states by a supercurrent flowing through the superconductor. We finally discuss how robust are these bound states to the effect of disorder on the graphene sample.

4.4.1 IBS from solution matching at a graphene NIS system

The mechanism for the emergence of these states can be understood from the scheme depicted in the left panel of Figure 4.10. As is usually assumed, the junction can be modeled as an abrupt discontinuity between two regions described by the Bogoliubov-de Gennes-Dirac equation, taking a finite superconducting order parameter Δ and large doping $E_F^S \gg \Delta$ on the superconducting side and zero order parameter and small doping $E_F \sim \Delta$ on the normal side. For the analysis it is instructive to include an artificial intermediate normal region with $\Delta = 0$ and $E_F^I = E_F^S$, whose width, d, can be taken to zero at the end of the calculation. This intermediate region allows to spatially separate normal reflection due to the Fermi energy mismatch from the Andreev reflection associated to the jump in Δ. As shown in Figure 4.10 (case i), an incident electron from the normal side with energy E and parallel momentum $\hbar q$ such that $\hbar v_F q < |E - E_F|$ is partially transmitted into the intermediate region and after a sequence of normal and Andreev reflections would be reflected as a hole. This process can either correspond to retro or specular Andreev reflection depending on whether $E < E_F$ or $E > E_F$ [56]. For $\hbar v_F q \geq |E \pm E_F|$ neither electron or holes can propagate within the graphene normal region. However, virtual processes like the one depicted in Figure 4.10 (case ii) would be present. These correspond to sequences of Andreev and normal reflections within the intermediate region. A bound state emerges when the total phase ϕ accumulated in such processes reach the resonance condition $\phi = 2n\pi$.

It is quite straightforward to determine the dispersion relation for the IBS from the model represented in the left panel of Figure 4.10. The phase accumulated by a sequence of normal and Andreev reflections in the intermediate region can be obtained from the corresponding coefficients r_e, r_h and r_A. Following Ref. [56], one obtains

$$r_{e,h} = e^{i\alpha_{e,h}^I} \frac{e^{-i\alpha_{e,h}^I} - e^{-i\alpha_{e,h}}}{e^{i\alpha_{e,h}^I} + e^{-i\alpha_{e,h}}}, \tag{4.24}$$

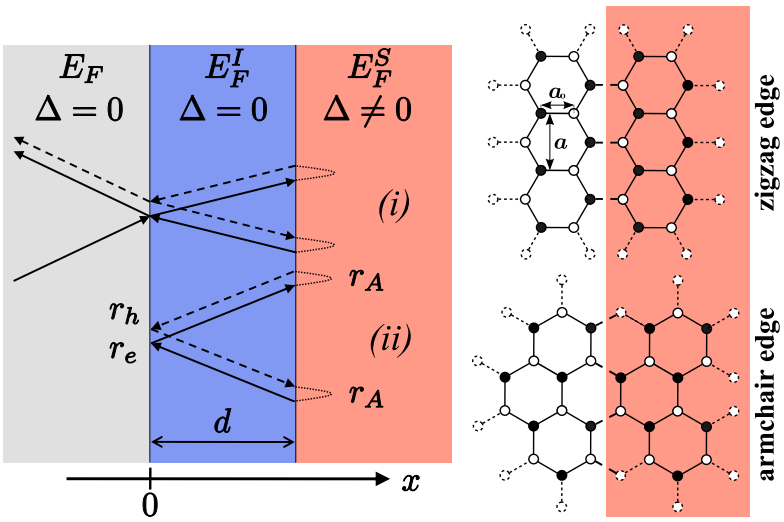

FIGURE 4.10: Simple model for the emergence of the IBS (left panel). It illustrates the scattering processes taking place at a graphene-superconductor interface with an intermediate heavily doped normal graphene region of width d. Cases (i) and (ii) correspond to the case $\hbar v_F q < |E \pm E_F|$ and $\hbar v_F q > |E \pm E_F|$ respectively with $\Delta > E > E_F$. (Right panel) Graphene-superconductor junctions along different edges. On the superconducting side (shaded areas) the on-site order parameter Δ is finite and the doping level is high ($E_F^S \gg \Delta$).

where $\alpha_{e,h}^{(I)} = \arcsin \hbar v_F q/(E \pm E_F^{(I)})$. The condition $E_F^I \gg \Delta, E, \hbar v_F q$ allows to take $\alpha_{e,h}^I \simeq 0$. On the other hand, in the region of evanescent electron and hole states for graphene ($|\hbar v_F q| > |E \pm E_F|$), $r_{e,h}$ becomes a pure phase factor $e^{i\varphi_{e,h}}$, with $\varphi_{e,h} = -2\text{sign}(q/(E \pm E_F)) \arctan e^{\lambda_{e,h}}$ and $\lambda_{e,h} = \text{sign}(q)\text{arcosh}(\hbar v_F q/|E \pm E_F|)$. For the Andreev reflection coefficient between regions I and S one has $r_A = e^{i\varphi_A}$, where $\varphi_A = \arccos E/\Delta$, as it corresponds to the Andreev reflection at an ideal N-S interface with $E_F^S \gg \Delta$ [51]. In the limit $d \to 0$ the total phase accumulated is thus $\phi = 2\varphi_A + \varphi_e + \varphi_h$, from which one obtains the following dispersion relation

$$\frac{E}{\Delta} = \pm \frac{e^{(\lambda_e+\lambda_h)/2} - \text{sign}(E^2 - E_F^2) e^{-(\lambda_e+\lambda_h)/2}}{2\sqrt{\cosh \lambda_e \cosh \lambda_h}}. \tag{4.25}$$

This dispersion simplifies to $E/\Delta = \pm \hbar v_F q/\sqrt{(\hbar v_F q)^2 + \Delta^2}$ at the charge neutrality point (i.e. for $E_F = 0$). In this case the IBS approaches zero energy for $q \to 0$ and tend asymptotically to the superconducting gap for large q. Notice also that the decay of the states into the graphene bulk region ($x < 0$ in the left panel of Figure 4.10) is set by $e^{x/\xi_{e,h}}$, where $\xi_{e,h} = \hbar v_F/[|E \pm E_F|\sinh(\lambda_{e,h})]$ for the electron and hole components respectively, which can be clearly much larger than the superconducting coherence length $\xi_0 = \hbar v_F/\Delta$ when $E_F \ll \Delta$. It is also interesting to notice that the IBS survive when $E_F > \Delta$, i.e. in the regime corresponding to the usual Andreev retro-reflection, but with a much smaller spatial extension.

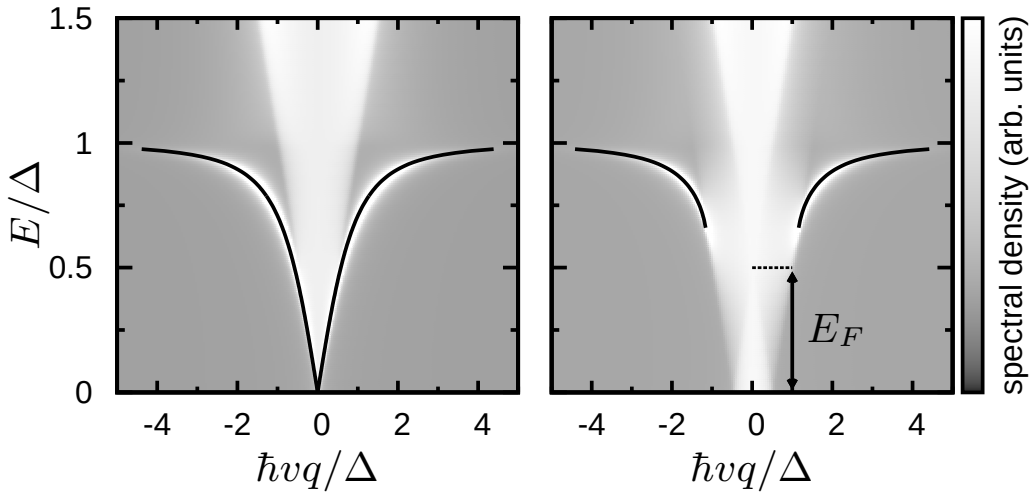

FIGURE 4.11: Gray-scale plot of the spectral density at a distance $\sim \xi_0$ from the interface defined along an armchair edge. The results were obtained using the HDSC model for $E_F = 0$ (left panel) and $E_F = \Delta/2$ (right panel). The full lines indicate the position of the IBS determined from Equation 4.25.

In order to analyze the existence and the characteristics of the IBS for different types of graphene-superconductor junctions we make use of the Green function formalism based on tight-binding and continuous models for these junctions that was introduced in Chapter 3. Within the TB approach, the retarded green functions at the interface $\check{\hat{G}}(E,q)$ are given by $\left[\check{\hat{g}}^{-1} - \check{\hat{\Sigma}}\right]^{-1}$, where $\check{\hat{g}}$ corresponds to the surface of the uncoupled semi-infinite graphene layer and $\check{\hat{\Sigma}}$ is the self-energy associated to the coupling with the superconductor. In general all these quantities have a 2×2 structure both in the sublattice (indicated by the hat symbol $\cdot\hat{\cdot}\cdot$) and the Nambu (indicated by the check symbol $\cdot\check{\cdot}\cdot$) spaces. Once these quantities for each type of interface have been determined, the existence of an IBS can be established by analyzing the equation $\det\left[\check{\hat{g}}^{-1} - \check{\hat{\Sigma}}\right] = 0$.

On the other hand, within the continuous model the coupling with the superconductor is included in the perturbation $\delta\check{G}$ from Equation 4.16. The condition for a bounded state at the interface is thus included in the denominator of this perturbation. Depending of the type of edge, a different conditions is obtained from Equation 4.19 and Equation 4.22.

4.4.2 Interface along an armchair edge.

We begin with the TB model to study the effect of the superconducting electrode on the IBS. We consider an interface constructed along an armchair edge, as schematically depicted in the right panel of Figure 4.10. In a rather generic way one can write $\check{\hat{g}} = \hat{g}_e(\check{\tau}_0 + \check{\tau}_z)/2 + \hat{g}_h(\check{\tau}_0 - \check{\tau}_z)/2$ and $\check{\hat{\Sigma}}/t_g = \beta\check{\tau}_z\check{g}_{BCS}\check{\tau}_z + \gamma\check{\tau}_z\hat{\sigma}_x$, where $\hat{g}_{e,h}$ describe the propagation of e and h components in the uncoupled graphene layer, $\check{g}_{BCS} = g\check{\tau}_0 + f\check{\tau}_x$ with $g = -Ef/\Delta = -E/\sqrt{\Delta^2 - E^2}$ being the BCS dimensionless Green functions,

and β and γ are parameters which allow to control the transparency and the type of interface. As it was discussed in Section 4.2, $\gamma = 0$ corresponds to a model in which the coherence between the sublattices of graphene is broken on the superconducting side (bulk-BCS model), whereas for $\beta = \sqrt{3}/2$ and $\gamma = 1/2$ corresponds to the ideal case where superconductivity is induced on the graphene layer by a superconducting electrode deposited on top, thus leading to a heavily doped graphene superconductor (HDSC).

To make further analytic progress we take the limit $E, \Delta, \hbar v_F q \ll t_g$ in the Green functions $\hat{g}_{e,h}$ introduced in Section 3.2, where t_g denotes the hopping element between neighboring sites in the graphene layer. In this case and for $\hbar v_F q > |E \pm E_F|$, $\hat{g}_{e,h}$ adopt the form $t_g \hat{g}_{e,h} = -\frac{1}{2}\left[\sqrt{3}\left(\mu_{e,h}\hat{\sigma}_0 + \nu_{e,h}\hat{\sigma}_y\right) \pm \hat{\sigma}_x\right]$, where $\mu_{e,h} = \text{sign}(q)/\sinh\lambda_{e,h}$ and $\nu_{e,h} = \text{sign}(E \pm E_F)/\tanh\lambda_{e,h}$. The Green functions matrix has the property $\hat{g}_{e,h}^{-1} = -t_g^2 \hat{g}_{e,h}^T \mp t_g \sigma_x$. Using this property and the definition for the self-energy the equation for the IBS in this case becomes

$$\det\left[t_g^2 \hat{g}_h \hat{g}_e + \beta g t_g \left(\hat{g}_e + \hat{g}_h\right) + \gamma t_g \left(\hat{\sigma}_x \hat{g}_e - \hat{g}_h \hat{\sigma}_x\right) - (\beta^2 + \gamma^2)\right] = 0 \tag{4.26}$$

For the HDSC model (i.e. $\beta = \sqrt{3}/2$ and $\gamma = 1/2$) the equation for the IBS reduce to the one already found within the simple analytical model (Equation 4.25). This leads to a single root for arbitrary doping which is four-fold degenerate due to valley and spin symmetry. Figure 4.11 shows a color-scale plot of the spectral density at a distance $\sim \xi_0$ from the interface on the graphene layer with two different doping conditions. The full lines correspond to the IBS dispersion obtained by solving Equation 4.25. As can be observed, the minimal energy for the IBS, E_{min}, depends on E_F. Further analysis of Equation 4.25 reveals that it satisfies the cubic equation $E_{min}^3 + E_{min}^2 E_F - \Delta^2 E_F = 0$, thus evolving between 0 and Δ as E_F increases. The transition between $E_{min} > E_F$ and $E_{min} < E_F$ occurs at $E_F = \Delta/\sqrt{2}$. The presence of the IBS manifests also in the appearance of singularities in the LDOS around $E = \pm\Delta$, as it is clearly exposed in the previous section (see Figure 4.6, for example).

On the other hand, for the bulk-BCS model (i.e. $\gamma = 0$ and $\beta \in (0, 1)$) one obtains

$$\begin{aligned} &\frac{3}{2}\beta^2 g^2(\mu_e\mu_h + \nu_e\nu_h - 1) + \sqrt{3}\beta g(\mu_e + \mu_h)(1 + \beta^2) \\ &+\frac{\beta^2(1 + 2\beta^2)}{2} + \frac{3}{4}(1 + 2\beta^2)(\nu_e\nu_h - \mu_e\mu_h) + \frac{1}{4} = 0. \end{aligned} \tag{4.27}$$

In this case the degeneracy associated to the two valleys in the band-structure of graphene is generally broken (except for $E_F = 0$). The roots gradually evolve toward

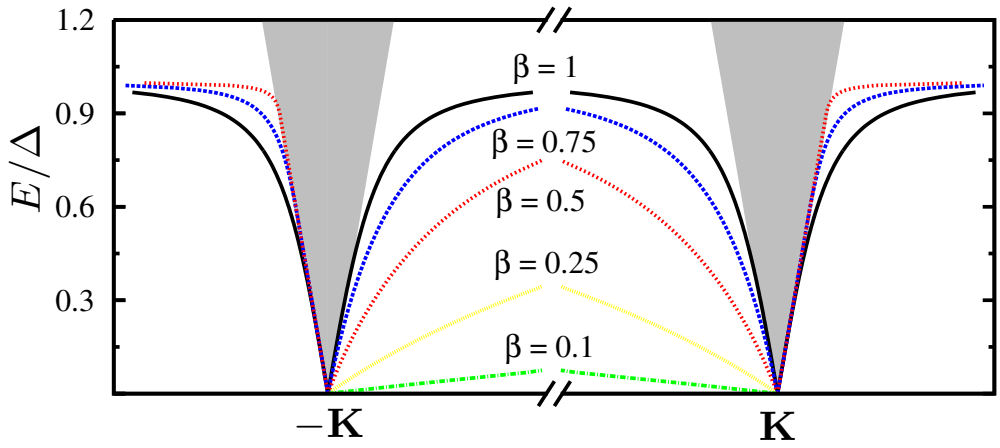

FIGURE 4.12: Dispersion relation for the IBS on a zig-zag interface for decreasing parameter β controlling the coupling with the superconductor. The parallel momentum q in Equation 4.30 is measured from the Dirac points at $K = \pm 2\pi/3a$.

the linear dispersion $|E + E_F| = \hbar v_F q$ as $\beta \to 0$, which corresponds to the armchair edge state of the isolated graphene layer [57].

The continuous approach gives further analytic insight. In particular, from Equation 4.19, the condition $D_{\text{arm}} = 0$ is satisfied by states with energy given by

$$\frac{E}{\Delta} = \pm \frac{e^{(\lambda_e+\lambda_h)/2} - \text{sign}(E^2 - E_F^2)e^{-(\lambda_e+\lambda_h)/2}}{2\sqrt{\cosh\lambda_e \cosh\lambda_h}}, \tag{4.28}$$

where we define $\lambda_{e,h} = \text{sign}(q)\text{arcosh}(\hbar v_F q/|E \pm E_F|)$ for evanescent electron or hole states with $|\hbar v_F q| > |E_F \pm E|$. This is the same result that is obtained within the simple model in Equation 4.25 and for the HDSC model in the TB approach. The equivalence between the HDSC model within the TB approach with the continuous model has been already exposed in the previous section (see Figure 4.8) and, in more detail, in Section 3.4.

4.4.3 Interface along a zig-zag edge.

We now consider an interface along a zig-zag edge as illustrated in the right panel of Figure 4.10. The Green functions for the semi-infinite zig-zag edge can be obtained following the same formalism as in Chapter 3. In the continuous limit $\hat{g}_{e,h}$ becomes

$$t_g \hat{g}_{e,h} = \begin{pmatrix} ie^{-i\alpha_{e,h}} & \mp e^{i\pi/3} \\ \mp e^{-i\pi/3} & 0 \end{pmatrix}, \tag{4.29}$$

where, as in Equation 4.24, $\sin\alpha_{e,h} = (\hbar v_F q)/(E \pm E_F)$ but with q measured with respect to the point $\mathbf{K} = 2\pi/3a$; where a is the lattice constant indicated in the right panel of Figure 4.10. There exists an additional branch where q is measured from the opposite Dirac point at $-\mathbf{K}$. The self-energy due to the coupling with the superconductor is in this case $\check{\tilde{\Sigma}} = \beta t_g(\hat{\sigma}_0 + \hat{\sigma}_z)\,(\check{\tau}_z \check{g}_{BCS} \check{\tau}_z)\,/2$. The equation for the IBS then becomes

$$\frac{E}{\Delta} = \pm \frac{e^{(\lambda_e+\lambda_h)/2} - \mathrm{sign}(E^2 - E_F^2)\beta^2 e^{-(\lambda_e+\lambda_h)/2}}{\sqrt{(e^{\lambda_e} + \beta^2 e^{-\lambda_e})(e^{\lambda_h} + \beta^2 e^{-\lambda_h})}}, \tag{4.30}$$

which looks very similar to Equation 4.25 except for the presence of the parameter β controlling the coupling and the already mentioned redefinition of the parallel momentum q. An interesting property of zig-zag edges is the presence of zero energy states for total parallel momentum between $(-\mathbf{K}, \mathbf{K})$ and $E_F = 0$ (for more details see Ref. [15]). When the coupling to the superconductor is turned on by increasing the parameter β, one observes that the zero energy states evolve acquiring a finite slope. These states can thus be identified with the IBS for this type of interface. This is illustrated in Figure 4.12. When the coupling parameter β reaches 1 the usual dispersion of the simplest analytical model is recovered. Analogously, when this denominator of Equation 4.21 is set to zero one obtains the dispersion relation for the IBS along this edge,

$$\frac{E}{\Delta} = \pm \frac{e^{(\lambda_e+\lambda_h)/2} - \beta^2\mathrm{sign}(E^2 - E_F^2) e^{-(\lambda_e+\lambda_h)/2}}{\sqrt{(e^{\lambda_e} + \beta^2 e^{-\lambda_e})(e^{\lambda_h} + \beta^2 e^{-\lambda_h})}}, \tag{4.31}$$

which is in perfect agreement with the previous result.

4.4.4 Effect of a supercurrent.

A supercurrent flowing on the superconducting side of the junction modifies the spatial variation of the phase of the order parameter which produces a Doppler shift in the energy of the quasiparticles. This shift, obtained from the Bogoliubov-de Gennes-Dirac equations within the Andreev approximation, is given by $\eta = (\hbar v_F)^2 q_s q / E_F^S$, where $\hbar q_s$ is the momentum of the Cooper pairs assumed to be parallel to the interface. This result is equivalent to the one found in Refs. [104] and [105] for conventional and two-band superconductors. Notice that for this analysis we go beyond the limit $E_F^S \to \infty$ taken in the initial simple model. The expression for the reflection coefficients of Equation 4.24 still holds but $\alpha_e^I \simeq -\alpha_h^I \equiv \alpha^I = \arcsin \hbar v_F q / E_F^S$ is kept finite. On the other hand, the phase of the Andreev reflection coefficient between the intermediate region and the current-carrying superconductor becomes $\varphi_A = \arccos E'/\Delta(q_s)$, where $E' = E + \eta$. At zero temperature, due to Landau criterion, the order parameter is unaffected by the supercurrent while $\hbar v_F q_s \lesssim \Delta\,(0)$ [104, 105]. Therefore, in this condition, $\Delta(q_s) \simeq$

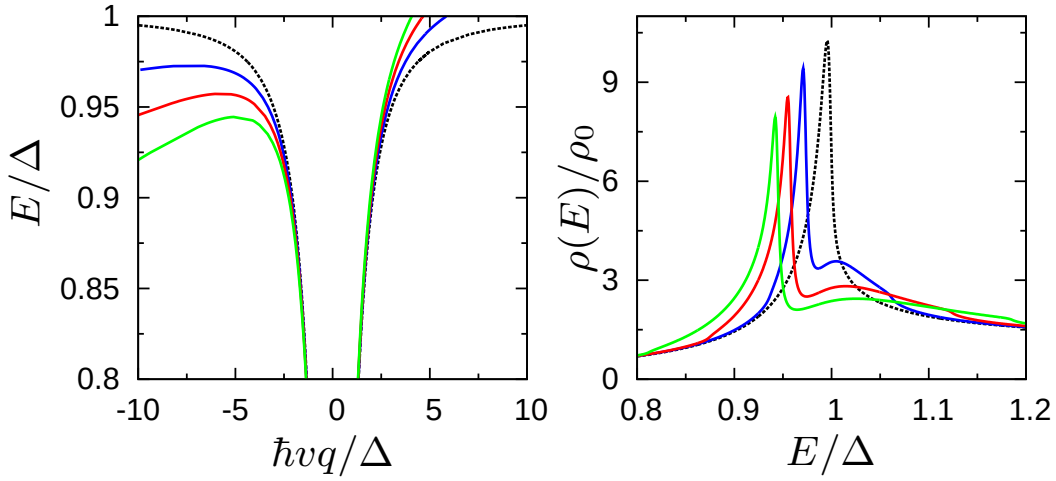

FIGURE 4.13: Effect of a supercurrent flowing on the superconducting electrode on the dispersion relation (left panel) and on the local density of states at a distance $\sim \xi_0/10$ from the interface normalized to $\rho_0 = \Delta(a/\hbar v_F)^2/2\pi$ (right panel). The results correspond to $\hbar v_F q_s/\Delta = 0.0, 0.25, 0.5$ and 0.75 with $E_F^S = 100\Delta$.

$\Delta(0) \equiv \Delta$. For the case $E > E_F$ we thus get the following modified equation for the IBS within the simple model sketched in Figure 4.10

$$\frac{E'}{\Delta} = \pm \frac{\sinh(\lambda_e + \lambda_h)/2 + \sin\alpha^I \sinh(\lambda_e - \lambda_h)/2}{\sqrt{(\cosh\lambda_e - \sin\alpha^I)(\cosh\lambda_h + \sin\alpha^I)}}. \tag{4.32}$$

Figure 4.13 illustrates the effect of a supercurrent both in the dispersion relation of the IBS (left panel) and in the local density of states close to the interface (right panel). For $q_s = 0$, the IBS manifest in a finite LDOS for $E < \Delta$ and a sharp peak at $E = \Delta$. Qualitatively, the presence of a supercurrent breaks the symmetry with respect to inversion of the parallel momentum $\hbar q$ and leads to a splitting of the singularity at $E \simeq \Delta$ in the LDOS. Note that this implies the appearance of an induced net current on the graphene side (for $|x| \lesssim \xi$). For $E_F = 0$ the distortion of the dispersion relation for finite and small q_s is given by $E(q_s, q) = E(0, q) + (\hbar v_F q)^2\eta/((\hbar v_F q)^2 + \Delta^2)$.

A more quantitative analysis of the effect of a supercurrent requires the estimation of the parameter E_F^S. This parameter is very much dependent on the fabrication methods and material properties of the metallic electrodes deposited on top of the graphene layer. According to the *ab-initio* calculations of Ref. [106] for Pd on graphene a typical estimate would be $E_F^S \sim 0.1eV$, which for a superconductor like Nb gives a ratio $E_F^S/\Delta \sim 100$. The results on Figure 4.13 have been obtained for this ratio.

4.4.5 Effects of disorder on the IBS.

We notice that the inclusion of weak disorder along the interface, introducing a small uncertainty in the parallel momentum δq, would not prevent the emergence of IBS provided that $\delta q \ll \Delta\hbar v_F$. However, the electron-hole inhomogeneity in graphene (i.e., charge puddles [40, 41]) is a type of charge disorder that has to be taken into account.

The results previously presented correspond to an infinite layer of pristine graphene connected to a superconductor modeled as it is introduced in Section 4.2. A more realistic model should include size effects such as a graphene layer with a finite length, along with the possibility of electron-density inhomogeneities. Although the effect of having a finite length in the normal region can be treated within both the continuous and the TB models, the latter is more suitable to explore the effect of disorder.

Within the TB model, we define an impurity-free graphene layer of horizontal length $L = dN$ and periodic boundary conditions along the vertical direction to effectively have an infinite width. The horizontal finite length of the layer depends on the number of cells N and the typical size of a cell, which is $d = \sqrt{3}a_0$ for the armchair orientation and $d = 3a_0$ for the zigzag one, with a_0 the distance between nearest carbon atoms. The details of the TB model have been already introduced in Section 3.2. Disorder is introduced as a two-dimensional superlattice potential. This potential is built combining piecewise potentials along the vertical and the horizontal directions, with spatial periodicity d_y and d_x, respectively. The strength of the potential, δV, takes random values in the range $[-V_0, V_0]$ over an area of typical size $d_x d_y$. This two-dimensional superlattice potential is equivalent to the *chessboard* potential introduced in Appendix A, with the peculiarity that the shape of each piecewise potential is not a series of consecutive barriers and wells but a random step-like profile.

The results for a graphene layer of horizontal length $L = \sqrt{3}800a_0$, with armchair edges, coupled to a superconductor are presented in Figure 4.14. The left panel has been calculated in the absence of the disordered potential. The results are similar to the undoped case presented in Figure 4.6: A clear peak at $E = \Delta$, which rapidly decays inside the normal region after a few times the superconducting coherence length. The finite length of the graphene layer manifests as the appearance of some energy states close to the gap edge. When the disorder is taken into account (right panel), the peak at the edge of the gap remains unaltered and the decay is comparable to the non-disordered case. However, the weight of the states below the gap becomes more important, which makes the LDOS profile more noisy. The envelope of the LDOS is still comparable to the non-disordered case, but small fluctuations appear. The main effect of disorder can be seen as an effective doping, which does not alter deeply the LDOS.

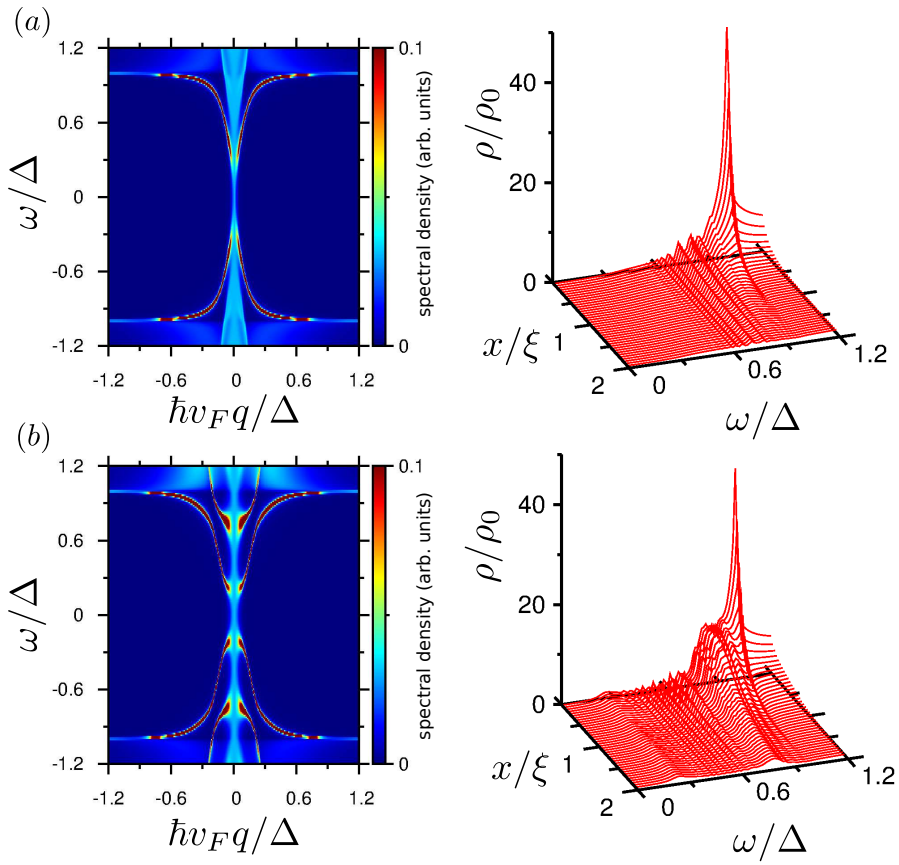

FIGURE 4.14: LDOS for a graphene layer of length $L = 197$ nm (800 armchair cells) coupled to a superconductor on an armchair edge calculated within the TB model. For the simulation, the superconducting gap has been chosen to be $\Delta = 0.005t_g$. The left panel shows the results for the case without disorder. For the right panel, a superlattice potential of strength $V_0 = 0.01t_g$, with spatial periods $d_x = 22$ nm and $d_y = 10$ nm, has been applied.

The strength of the superlattice potential used in these simulations is $V_0 = 0.01t_g \approx 27$ meV, which is comparable to the greatest estimation for the measured strength of the charge inhomogeneities in graphene [41]. The periodicity of the superlattice potential has been chosen to be $d_x \approx 22$ nm and $d_y \approx 10$ nm. This is, however, slightly smaller than the typical length of a charge puddle in graphene, which has a average size of 30 nm. In spite of this, the results presented are close enough to suppose that a bigger period for the superlattice potential would not affect considerably the LDOS profiles.

4.4.6 Conclusions.

We have shown that interface bound states appear at graphene-superconductor junctions. The properties of these states are sensitive to the type of edge forming the interface, its transparency, and the doping conditions of the graphene layer. We have demonstrated that the interface states evolve toward the edge states of the isolated

graphene layer when the transparency of the interface is reduced. We have also shown that they can be modulated by a supercurrent flowing through the superconductor in the direction parallel to the interface. Even when our analysis has been restricted to interfaces along armchair or zig-zag edges we expect the appearance of IBS to be a general property of any edge orientation. Additionally, the inclusion of weak disorder along the interface introducing a small uncertainty in the parallel momentum δq would not prevent the emergence of IBS provided that $\delta q \ll \Delta/\hbar v_F$. On the other hand, the presence of charge inhomogeneities in the normal region introduces small fluctuations in the LDOS profile. However, the IBS and, consequently, the envelope of the LDOS are robust against a disorder strength comparable to the measured strength of the charge puddles. As a final remark we would like to comment that the existence of IBS induces long-range superconducting correlations between distant points on the graphene layer that are close to the interface. This property could be exploited to detect crossed Andreev processes and therefore entangled electron pairs using weakly coupled STM probes on a graphene-superconductor junction in a configuration such as the one proposed in Ref. [107]. The analysis of nonlocal transport in this system is the aim of the next chapter.

4.5 Conclusion and discussion.

A microscopic description of a graphene-based NS junction has been presented. Special emphasis in the different superconducting electrodes is given. The proximity effect is studied, with results for the minigap induced in the normal region. The LDOS on the normal region is studied, distinguishing the case of a semi-infinite normal region and a finite one and also the different graphene edges. The effect of the edge orientation (zigzag and armchair) on the coupling with the superconductor is treated. A simple model for the formation of bound states at the graphene-superconductor interface is given. These states give more microscopic insight on the LDOS profiles. The results presented here are very useful for studying nonlocal transport in graphene, which is the subject of the next Chapter.

We expect that these findings can be useful to analyze future scanning tunneling microscopy experiments on graphene sheets with superconducting electrodes.

Chapter 5

Nonlocal transport in graphene.

5.1 Induced pairing correlations.

5.1.1 Electron-hole correlations on the NS system.

How does the proximity with the superconducting interface affect the nonlocal transport? We know that the effect of coupling a superconductor (heavily doped graphene) to a semi-infinite graphene layer is the appearance of peaks in the DOS for energies near the value of the superconducting gap Δ (see Chapter 4). These peaks decay inside the graphene layer for distances of the order of the superconducting coherence length ξ. The formation of these peaks is due to interface bound states in the graphene-superconductor junction. We have to understand how this affects the nonlocal transport near the interface.

The coupling with the superconductor induces correlations between electron and hole-like excitations in the normal region by the proximity effect. We can map the spatial variation of these correlations using the Green function of the coupled system. The element $\check{G}_{L|eh,AA}(x,x',y)$, from Equation 4.16, corresponds to the injection of electron excitations at the point x' on the $y=0$ axis and its propagation as a hole excitation to the rest of the plane (x,y) after an electron-hole conversion at the interface. The probability $P_{e\to h}$ that an electron injected at $(x',0)$ would be converted into a hole at (x,y) is proportional to

$$P_{e\to h} \propto \left| \int_{-\infty}^{\infty} dq e^{iqy} \check{G}_{L|eh,SS'}\left(q,E;x,x'\right) \right|^2, \tag{5.1}$$

with $S,S'=A,B$.

For analyzing the induced pairing correlations, in the normal graphene layer with armchair edges coupled to a superconductor, the electron-hole elements of $\delta\check{G}$ in Equation 4.16 are needed. We set $\beta = 1$, thus having perfect transparency, and for any values of x and x' these elements reduce to

$$\begin{aligned}\hat{G}^{\rm arm}_{L|eh,AA(BB)}(x,x') = \\ \frac{-ie^{-ik_e x}e^{ik_h x'}}{\hbar v D_{\rm arm}}\frac{\Delta}{\Omega}\left\{\cos\left[K\left(x-x'\right)\right]\left[1+\cos\left[\alpha_e-\alpha_h\right]+\frac{E}{\Omega}\left(\cos\alpha_e+\cos\alpha_h\right)\right]\right. \\ \left.+\frac{1}{2}\sin\left[K\left(x-x'\right)\right]\frac{\cos\alpha_e-\cos\alpha_h}{\cos\alpha_e\cos\alpha_h}\left[\sin\alpha_e+\sin\alpha_h+\frac{E}{\Omega}\sin\left[\alpha_e-\alpha_h\right]\right]\right\}.\end{aligned} \tag{5.2}$$

On the other hand, for a zigzag interface, the electron-hole component of the Green function is given by

$$\check{G}^{\rm zz}_{L|eh}(x,x') = \frac{i\beta^2 e^{-ik_e x}e^{ik_h x'}}{\hbar v D_{\rm zz}}\frac{\Delta}{\Omega}\begin{pmatrix} 1 & e^{i\alpha_h} \\ -e^{-i\alpha_e} & -e^{-i\alpha_e}e^{i\alpha_h}\end{pmatrix}. \tag{5.3}$$

In our study of the spatial variation of the superconducting correlations we set $x' = -\xi$. We find it interesting to explore the change in the induced pair correlations for electrons injected within the gap ($E < \Delta$) when the doping level varies from $E_F \gg \Delta$ (left panel of Figure 5.1) to $E_F \ll \Delta$ (right panel). As it was demonstrated in Ref. [56], these two limiting cases correspond to the regimes in which Andreev reflection exhibits respectively a retro or a specular character. In these limits and in the case of perfect transparency, the main difference between an armchair edge and a zigzag one is that the atomic oscillations happen along the x or y axis, respectively. Thus, we only analyze the results for an armchair edge with a fixed multiplicity. In Figure 5.1 these two cases are shown for an incident energy $E = 0.75\Delta$. In the case $E_F > \Delta$, shown in the left panel, electron-hole conversion occurs mainly for $y \simeq 0$ decaying fast for $y \gtrsim \xi$. This confinement of the pairing correlations on the y direction is a consequence of the underlying diffraction pattern for the injected electrons at one point which has a spatial extension of the order of $\hbar v/E_F$. The behavior is drastically different in the limit $E_F < E < \Delta$ for which specular reflection is enhanced (right panel). In addition to the electron-hole conversion for normal incidence, the results exhibit the presence of long-range superconducting correlations along the y axis, provided that $x \sim \xi$. These long-range correlations can be directly associated with the presence of IBSs which in this regime have a spatial extension inside the normal region which is much larger than ξ. At the same time, the extended correlations can be interpreted as a signature of divergent Andreev reflection trajectories characteristic of the regime $E_F \ll \Delta$.

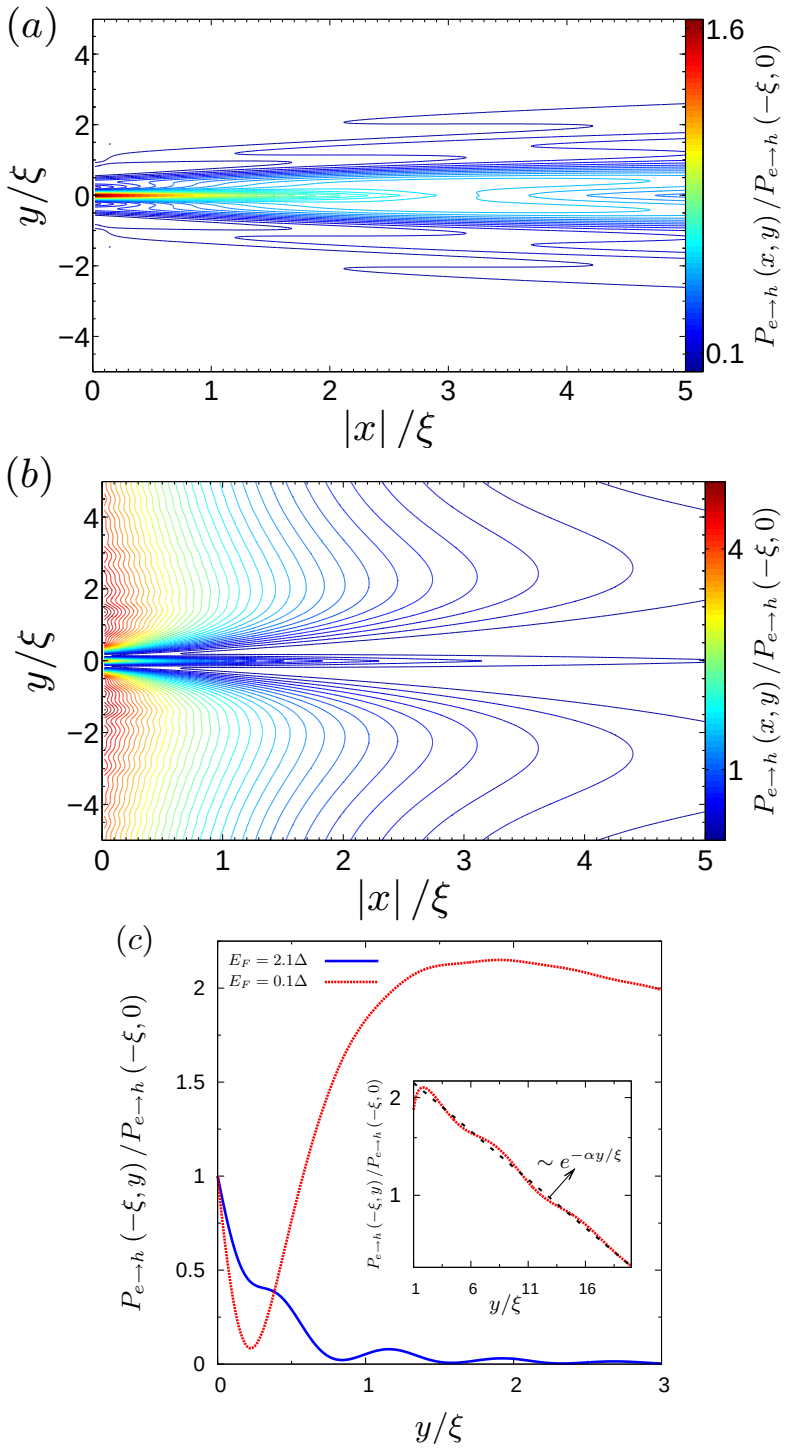

FIGURE 5.1: Spatial mapping of induced pairing correlations in the normal region of graphene. The results show the squared absolute value of the Fourier transform of $\check{G}_{L|eh,AA}$ for an incident energy $E = 0.75\Delta$ and $x' = -\xi$. The panel on the left shows the case $E_F > \Delta$ with $E_F = 2.1\Delta$, in which retro-reflection is enhanced. The right panel shows the opposite case $E_F < \Delta$, with $E_F = 0.1\Delta$, in which specular reflection dominates.

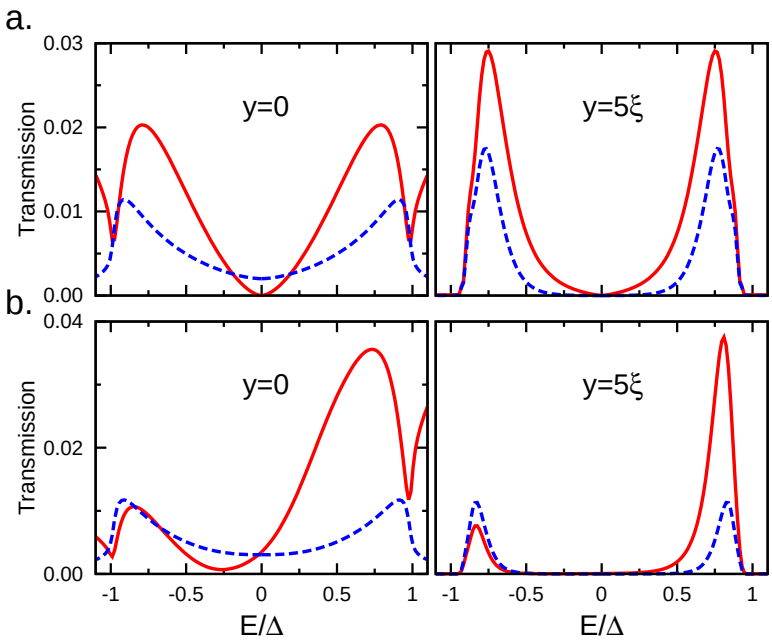

FIGURE 5.2: Comparison between TB and BdGD model. For the region of positive energies (top panel), $\left|\check{G}_{ee,AA}\right|^2$ and $\left|\check{G}_{eh,AA}\right|^2$ are represented using both models. In the other region (bottom panel), we represent $\left|\check{G}_{hh,AA}\right|^2$ and $\left|\check{G}_{he,AA}\right|^2$. For the TB model two lines with different multiplicity are shown. The Fermi energy is 0.5Δ and the spatial separation is 500 in units of each model. I think that the main differences are due to the different units of length used in each model.

5.1.2 Long-range proximity effect.

The proximity of the superconductor induces long range superconducting correlations between distant points on the graphene layer that are close to the interface [83]. This property could be exploited to detect crossed Andreev processes and therefore entangled electron pairs using weakly coupled STM probes on a graphene-superconductor junction, in a configuration like the one proposed in Ref. [107, 108].

When we study the electronic properties for two positions of a graphene sheet coupled to a superconducting region, we will focus in the propagation of electrons from one point to another [*electron co-tunneling* (EC)] and the possibility that an incoming electron from one point is reflected in the interface as a hole which propagates to the second position [*crossed Andreev reflection* (CAR)]. We will see how each phenomenon can be enhanced for different energy regions when the Fermi energy is of the same order of the superconducting gap.

We begin by setting an injection point for electrons at a fixed transversal distance to the interface $d \equiv x = x' = -0.6\xi$. Figure 5.2 shows the dependence on the energy of both the EC and the CAR transmissions when the system is doped but the Fermi energy is

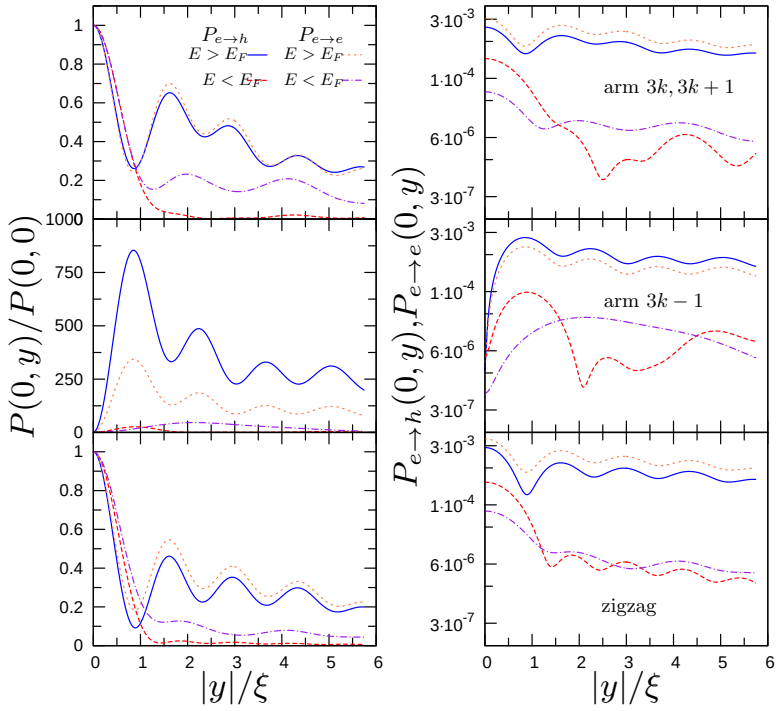

FIGURE 5.3: Graphene layer with $W = 500a_0$ coupled to a superconductor (S^R). Injection at $y = 0$ and $x' = -\xi/4$ ($x' = -\xi$ for semi-infinite zigzag). $E = 0.85\Delta$ for the specular case and $E = 0.25\Delta$ for the retro-reflected one. $E_F = 0.5\Delta$.

within the superconducting gap. T_{CAR} is always symmetric with the energy while T_{EC} is only symmetric when $E_F = 0$. As a result, there is an energy window in which T_{EC} is reduced and can be comparable or even lower than T_{CAR}. By varying the doping of the normal region we get an energy range in which electron-hole conversion is more probable than electron transmission. However, when $E_F \gg \Delta$, T_{EC} is symmetric and greater than T_{CAR} so the structure around Dirac's point is essential if we want to study when T_{CAR} is enhanced.

Whenever the injection point is close enough to the interface the proximity effect allows to have superconducting correlations even at long distances from the injection point. We show this long range behavior parallel to the superconductor-graphene interface in Figure 5.3. We set the injection point at $d = -\xi/4$. We then plot electron-electron propagation and electron-hole conversion of the injected electrons along the interface at $d = 0$ as a function of the vertical distance y. We set the doping of the normal region to be $E_F = 0.5\Delta$ and inject electrons within the gap ($E < \Delta$). We plot the results for electrons in the conduction band $E > E_F$ and from the valence band $E < E_F$. These two cases correspond to the regimes in which Andreev reflection is, respectively, specular or *retro* [56]. Results for both armchair and zigzag edges clearly show how electron-hole conversion has a short vertical range when retro-reflection dominates. However, when Andreev reflection has a specular character, the probability of electron-hole conversion

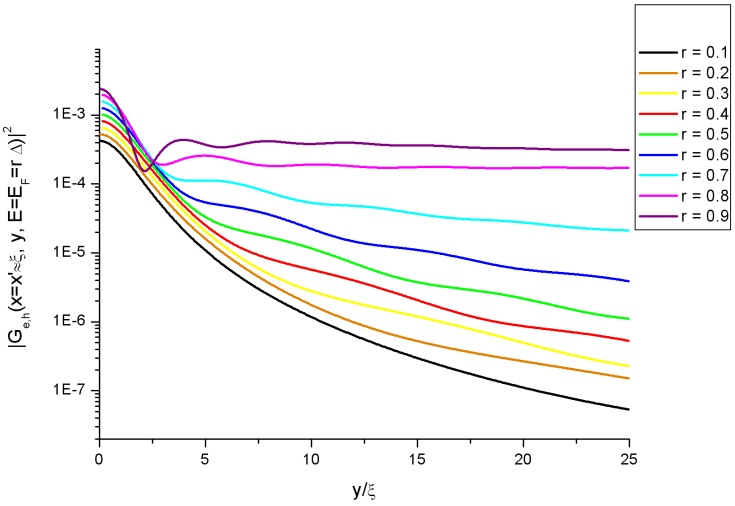

FIGURE 5.4: Plot of G_{CAR} as function of the vertical separation y for different values of $E = E_F = r\Delta$. The linear conductance becomes flat for values of r over $1/\sqrt{2}$. This effect is controlled by the parameter η.

is almost constant even for vertical distances of tens of the superconducting coherence length ξ.

The long-range behavior of the linear conductance is due to a singularity in $\hat{G}_L[ee, eh]$. In the simplest case in which $E = E_F = r\Delta$, with $0 < r < 1$, the Fourier transform can be written as $\mathcal{G}(x, y) = \int e^{f(x,y;q)} g(q) dq$, with

$$\begin{aligned} g(q) &= \frac{\sqrt{1-\frac{q^2}{4r^2}} + \frac{iq}{2r} - \frac{ir}{\sqrt{1-r^2}}}{\sqrt{1-\frac{q^2}{4r^2}}\left(2+\frac{1}{1-r^2}\right) - \frac{ir}{2r(1-r^2)} + \frac{2r}{\sqrt{1-r^2}}} \\ &= \frac{1}{2}\frac{1}{q-\frac{1}{\sqrt{1-r^2}}}\left[q - 2\sqrt{1-r^2} - 2ir\sqrt{1-\frac{q^2}{4r^2}}\right] \end{aligned} \tag{5.4}$$

When we check the condition $g(q_0) = 0$, we conclude that the pole $q_0 = \left(1-r^2\right)^{-1/2}$ only exists for $r \geq 1/\sqrt{2}$. The residue for this pole is

$$R = \frac{2r^2-1}{\sqrt{1-r^2}} \exp\left\{\frac{2r^2 x \pm iy}{\sqrt{1-r^2}}\right\}, \tag{5.5}$$

where $x < 0$. In the limit $|x| \to \infty$ the contribution of the residue to the integral is negligible. The contribution of the exponential to the integral is also important. We can use the saddle point approximation to determine the contribution to the integral. The saddle point is obtained from the first derivative of $f(q) = (x \pm iy)q - ix\sqrt{4r^2 - q^2}$

$$f'(q_s) = 0 \to q_s = -\frac{2r\,(x \pm iy)}{\sqrt{(x \pm iy)^2 - x^2}}. \tag{5.6}$$

Under this approximation, the integral is given by

$$\begin{aligned} I(x,y;r) &\approx \sqrt{2\pi}\frac{e^{f(q_s)}}{|f''(q_s)|^{1/2}}g(q_s) = \\ &= -\frac{4\pi r}{\hbar v\sqrt{1-r^2}}|x||(x+iy)^2-x^2|^{-3/4} \\ &\quad \times \exp\left\{\frac{2r}{\sqrt{(x+iy)^2-x^2}}(x|x|-(x+iy)^2)\right\}g(q_s) \qquad (5.7) \\ g(q_s) &= \frac{(1-r^2)((x+iy)-|x|)-ir\sqrt{1-r^2}\sqrt{y^2-i2xy}}{|x|(2r^2-1)+x+iy-2ir\sqrt{1-r^2}\sqrt{y^2-i2xy}} \qquad (5.8) \end{aligned}$$

If we set $x=\xi$, the evolution with y is an exponential decay which must be dominant when $r<1/\sqrt{2}$. When $r\geq 1/\sqrt{2}$, the residue begins to gain importance giving the oscillatory behavior around a determined value shown in Figure 5.4. The long-range decay of the integral is controlled by the parameter η which was omitted in this calculation.

5.2 Selective focusing of electrons and holes in a graphene-based Veselago lens.

5.2.1 Electron optics in graphene.

In the previous section, the possibility to exploit specular Andreev reflection in graphene to observe paired electrons within a single graphene layer connected to a superconductor was studied. As it is explained, the entangled electrons would be distinguishable along diverging trajectories on the normal region of the NS junction. However, independent detection of electron beams depending on their angle with the NS interface is a rather complicated issue due to quantum interference effects. That is not the case in optics, where different rays can be filtered depending on their angle, or focused in different spatial regions.

The possibility of fine-tuning the density of carriers in graphene together with their resemblance to massless particles like photons have made graphene a promising candidate for testing photonic analogies in electron transport. As an example, an electron beam flowing through a single *pn* junction experiences negative refraction [109] and thus this system has been proposed as the electronic equivalent of a Veselago lens [110]. Thanks to this analogy, striking properties of the meta-materials such as perfect-lensing [111] could be explored in graphene. In particular, supercollimation of electron beams [112] has been proposed for graphene under periodic potentials and the focusing of electron beams has been studied in circular graphene *pn* junctions [113], graphene nanoribbons [114] and the surface of topological insulators [115]. The analogy between beam optics

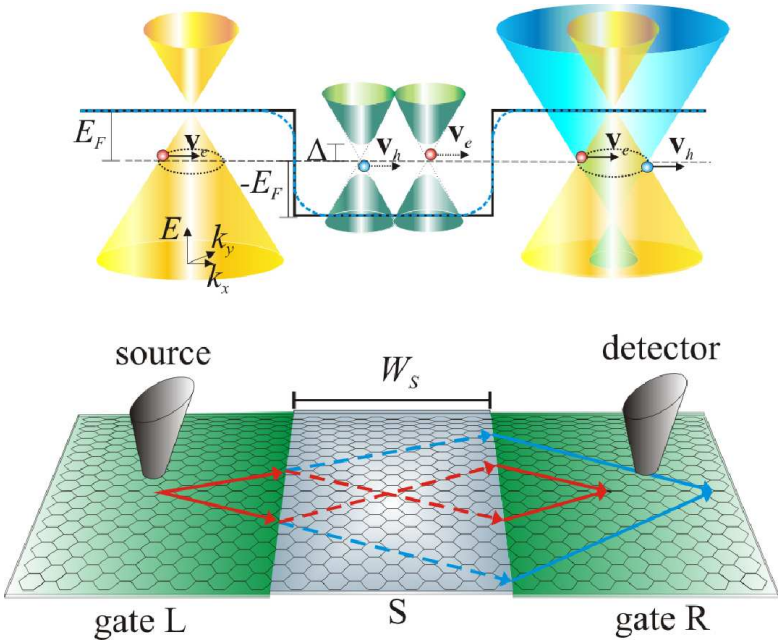

FIGURE 5.5: Graphene superconducting *pnp* junction. The band structure of each region is shown on top for the case when the normal electrodes L and R are adjusted to have the opposite doping level than the superconducting central region S. Incoming electrons from the left electrode (solid red lines) transform into evanescent electron and hole-like excitations inside the superconductor (dashed red and blue lines, respectively). In the right region, electrons and holes (solid blue lines) focus into distinct regions.

and Dirac electrons in graphene has been studied in detail for flat, convex and concave graphene *pn* junctions [116]. Graphene-based Veselago lenses have also been proposed as *filtering* systems for spin-polarized electron beams [117]. All these proposals are sustained in the advances in the construction of ballistic *pnp* junctions in graphene [31, 118–120]. Additionally, good contact can be achieved between lithographically defined superconducting electrodes and graphene layers [11, 12, 14], with the possibility of reaching almost ballistic transport in the presence of superconducting electrodes [13].

In a graphene-based normal-superconductor-normal (GSG) junction, local and crossed (CAR) Andreev reflections can occur if the width of the central superconducting electrode is comparable to the superconducting coherence length. The relativistic dispersion relation of graphene, with the valence and the conduction band touching at the Dirac point, enables to observe a theoretically pure CAR process in a GSG junction [121]. The time-reversal of these processes corresponds to the splitting of a Cooper pair from the superconductor into an entangled electron pair in the normal electrodes [59]. Although progress has been achieved in the experimental realization of Cooper pair splitters using carbon nanotube and semiconducting nanowire quantum dots [122, 123], it is expected that graphene can provide even better conditions for the entanglement detection.

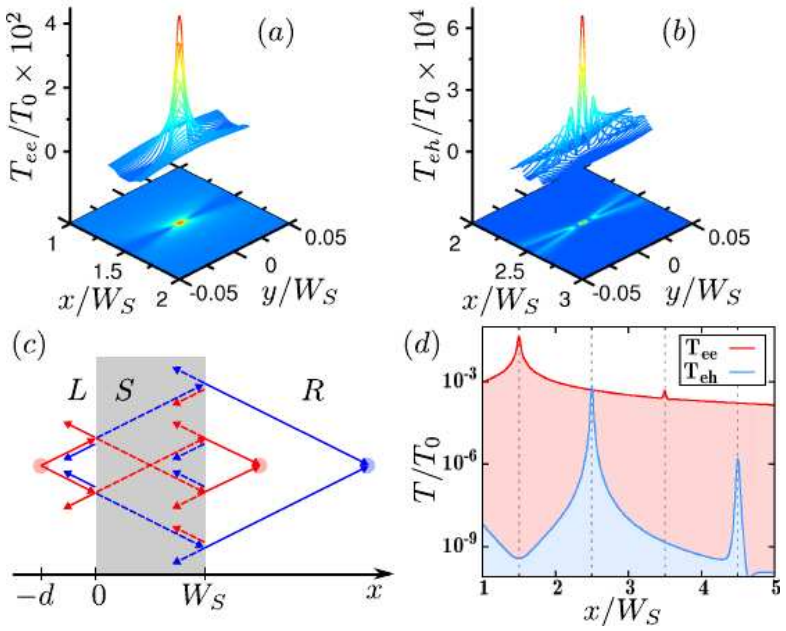

FIGURE 5.6: Spatially separated focusing of electrons and holes in region R after injecting electrons in region L. (a) Map of the electron transmission $T_{ee}(x, y)$ near the focusing point $x = 3W_S/2$. The width of the superconducting region is $W_S = \xi \sim 1\mu$m and the doping levels are $|E_F^{L,S,R}| = 0.5$ eV. (b) For the same parameters, map of the hole transmission $T_{eh}(x, y)$ near the focusing point $x = 5W_S/2$. (c) Sketch of the trajectories of electrons and holes through the superconductor into the region R. See the text for details. (d) Logarithmic scale plot of the transmission of electrons (red) and holes (blue) into region R for $y = 0$, showing the profiles of (a) and (b) where the peaks due to internal reflections can be distinguished.

In this section we propose to create a Veselago lens in a GSG junction to focus electrons and holes in different spatial regions. The idea is schematically depicted in Figure 5.5. A graphene sheet is deposited on top of two independent gate electrodes and a central superconducting electrode (denoted L, R and S respectively). The superconducting electrode shifts the electronic bands of the underlying graphene region by transference of electrons to produce an n-doping effect. Subsequently, the doping level of each normal region is adjusted by the gate electrodes so the system behaves as a *pnp* junction but with the peculiarity that superconductivity is induced in the central region. Injection of electrons can be realized in the L region by means of a local probe, and when the central electrode is in the normal state the system acts as a Veselago lens focusing electrons at the region R. When superconductivity is "switched on", evanescent electron and hole-like states are created in the graphene region located under the central electrode. In the right electrode, electrons and holes become propagating waves again and are focused into regions separated by hundreds of nanometers. This spatial separation would allow the detection of the transmitted holes by means of a second local probe (detector in Figure 5.5).

5.2.2 Independent focusing of electrons and holes

For modeling the Veselago lens depicted in Figure 5.5, we consider an infinite plane of graphene with a superconducting electrode covering the region $0 < x < W_S$, while the regions $x < 0$ (L) and $x > W_S$ (R) remain in the normal state. Although graphene is not intrinsically superconducting, the superconducting electrode can induce a pairing amplitude Δ by proximity effect [82, 93, 124]. We choose the width of the central region to be comparable to the superconducting coherence length $W_S = \xi = \hbar v_F/\Delta$. For a typical superconductor like Pb or Al $\Delta \sim 1$ meV and thus $\xi \sim 0.5 - 1\mu$m. An Al or Pd/Al electrode in the superconducting state induces an n doping in the underlying graphene region estimated as $E_S^F \sim -0.5$ eV [125]. Since the gate potentials of the normal regions can be adjusted independently, we choose them to be $E_F^{L,R} = -E_F^S$. This set of parameters define a *pnp* junction with a central superconducting electrode.

The low energy excitations of the system are described by the Dirac-Bogoliubov-de Gennes (DBdG) equations

$$\begin{pmatrix} H - V(x) & \Delta(x) \\ \Delta(x) & V(x) - H \end{pmatrix} \begin{pmatrix} u \\ v \end{pmatrix} = E \begin{pmatrix} u \\ v \end{pmatrix}, \tag{5.9}$$

where $H = \hbar v_F \left(\hat{\sigma}_x k + \hat{\sigma}_y q\right)$ is the one-particle Dirac Hamiltonian with Fermi velocity v_F, $\Delta(x)$ is the pairing amplitude, $V(x)$ is the potential profile and $E > 0$ is the excitation energy. We impose rigid boundary conditions at the normal-superconducting interfaces to the pairing and the electrostatic potentials such that $\Delta(|x| > W_S) = 0$, $\Delta(|x| < W_S) = \Delta$ and $V(x < 0) = E_F^L$, $V(0 < x < W_S) = E_F^S$, $V(x > W_S) = E_F^R$. Whenever the pairing potential is assumed constant and nonzero, the low-energy spectrum is given by $E = \sqrt{\Delta^2 + \left(E_F^S - \hbar v_F \sqrt{k^2 + q^2}\right)^2}$. We define the momentum perpendicular to the interfaces as $\hbar v_F k_\pm = \sqrt{\left(E_F^S \pm \Omega\right)^2 - q^2}$, with $\Omega = \sqrt{E^2 - \Delta^2}$ and $\hbar q$ the conserved momentum parallel to the interfaces. The pairing potential couples electrons and holes from different valleys. Equation 5.9 is therefore written in Nambu and pseudospin space, omitting the valley and spin degeneracies.

The transport properties can be expressed in terms of one-particle Green functions which satisfy $\left[(E \pm i0^+) - \mathcal{H}(x)\right] G^{r,a}(x, x') = \delta(x - x')$, where $\mathcal{H}$ denotes the full Hamiltonian of the left hand side of Equation 5.9. We calculate the Green functions by solving separately each region and combining the results following the method explained in Section 3.4. To fully resolve spatially the Green functions we use the Fourier transform $\mathcal{G}(x, x'; y - y') = \int \mathrm{d}q e^{iq(y-y')} G(x, x')$. Therefore, by setting the electron injection in the left region ($x' < 0$) we analyze the electron transmission into the right region defining

$T_{ee} \propto \mathrm{Tr}\,|\mathcal{G}_{ee}(x,x';y-y')|^2$ and the CAR probability as $T_{eh} \propto \mathrm{Tr}\,|\mathcal{G}_{eh}(x,x';y-y')|^2$, where the trace is done in the pseudospin space.

The transmission probabilities $T_{ee}(x,y)$ from region L to region R [i.e., electron cotunneling (EC)], and $T_{eh}(x,y)$ (CAR probability) are defined so (x,y) denotes the detector coordinates when the source coordinates are $(-d,0)$. In Figure 5.6 we show the result of the microscopic calculation for the transmission probabilities. T_{ee} exhibits a well-defined peak at $3d$ while we obtain a maximum of T_{eh} at $5d$, as it is shown in Figure 5.6(a) and Figure 5.6(b), respectively. Both results are normalized to $T_0 = T_{ee}(-d,0)$. The intensity of the electron focusing is much higher than that of the holes, i.e., $T_{ee}(3d,0) \sim 100 T_{eh}(5d,0)$, thus indicating that the EC signal is much greater than the CAR signal. However, the spatial separation between peaks is exactly the width of the superconducting region, which is of the order of 1 μm. This would allow to detect each signal independently as we discuss in more detail below.

These results can be qualitatively explained with a simple analysis of the group velocities of the particles at each region [see Figure 5.6(c)]. For a perfectly symmetric *pnp* junction, the normal regions L and R are p doped with $E_F > 0$, while the superconducting region S is n doped with $-E_F$. In the heavily doped regime $|E_F| \gg \Delta, E$, an analysis of the propagation of waves based on classical trajectories is sensible since $\lambda_F \ll W_S$. Even for the evanescent waves within the superconducting region and with $|E| < \Delta$, this type of analysis is valid considering waves with $k_F^S \sim k_F^{L,R} \sim E_F/\hbar v_F$. Subsequently, the angle of incidence and transmission of particles is defined as $\phi(k_y, E_F) = \pm \arcsin[\hbar v_F k_y / E_F]$, where the sign depends on the doping level of each region. As a result, the group velocities of electrons and holes can be written as $\mathbf{V}_{e,h} = \pm \varepsilon v_F \mathbf{k}_{e,h}/|\mathbf{k}_{e,h}| = \pm \varepsilon v_F\,(\cos\phi, \sin\phi)$, where $\varepsilon = 1(-1)$ for quasiparticles in the conduction (valence) band. From the conservation of the component of the wave vector parallel to the interface, we reach the electronic equivalent of Snell's law at each interface [109, 115] which allows us to define a relative refraction index at each interface $n_{LS,SR} = \sin\phi^{L,S}/\sin\phi^{S,R} = -\varepsilon$. Taking into account the sign due to the band index (conduction or valence) and the one due to particle index (electron or hole), when the particle type is the same at both sides of the interface ($\varepsilon = 1$), the change of band causes a negative refraction with $n = -1$. On the other hand, when the particle type is not conserved ($\varepsilon = -1$), there is no negative refraction and $n = 1$. This explains the classical trajectories sketched in Figure 5.5 and Figure 5.6(c): Incoming electrons from the region L (solid red lines) transform into electron and hole-like excitations inside the superconductor (dashed red and blue lines, respectively). While the former experiences a negative refraction because the particle type is conserved, the latter follows the same path as the incoming electron. At the

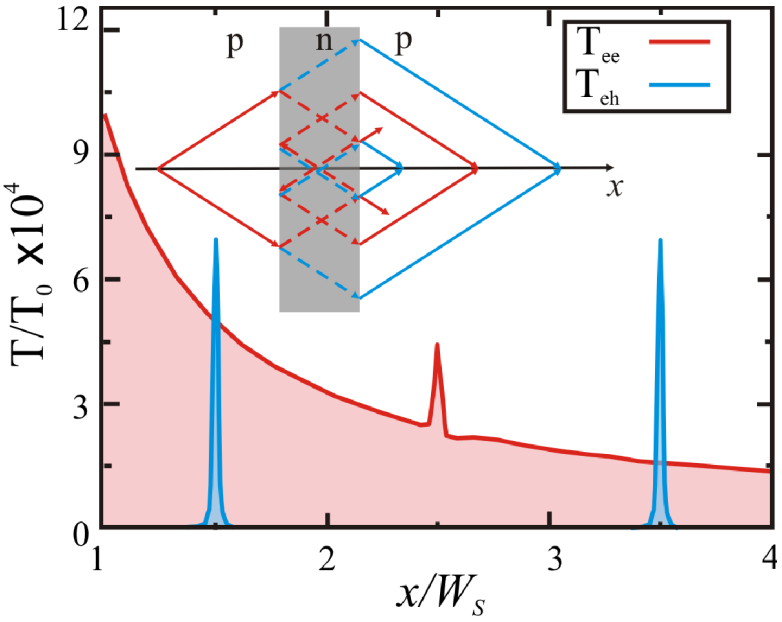

FIGURE 5.7: Injection at a distance greater than the width of the superconductor. Microscopic calculation for $T_{ee}(x,0)$ and $T_{eh}(x,0)$ when the injection of electrons is done at $d=-3W_S/2$. The inset shows a sketch of the classical trajectories. Notice that the peak of T_{eh} at $x=3.5W_S$ is ~ 5 times larger than the EC background.

second interface, the processes that preserve the particle type experience a negative refraction and are focused to form an image in the optical axis x (for an analysis of the transmission amplitudes, see Appendix B).

Furthermore, at each interface *specular* reflection occurs when the particle type is conserved, while *retro*-reflection happens otherwise [Figure 5.6(c)]. Electron and hole-like excitations can endure two consecutive specular reflections inside the superconductor to create a new electron or hole beam in the normal region R. This leads to a sequence of alternated electron and hole focusing points at the optical axis. In Figure 5.6(d) we show the microscopic calculation in which we obtain peaks of T_{ee} at $x=(2m-\frac{1}{2})W_S$ and peaks of T_{eh} at $x=(2m+\frac{1}{2})W_S$, with $m=1,2,....$ The intensity of these peaks decays exponentially with the distance to the superconductor, consistent with the behavior of the proximity effect in a graphene-superconductor interface [82, 93, 124].

While the previous analysis explains the separate focusing of electrons and holes, it would be desirable that the background EC conductance at the CAR peak could be further reduced. This can be achieved by increasing the injection distance d. Indeed, the injection point $(-d,0)$ determines the origin of the sequence of focusing points in which the separation between maxima of T_{ee} and that of T_{eh} is W_S. For $d<W_S$ the sequence of points starts always with a maximum of T_{ee}. On the other hand, for $d>W_S$, electrons are only transmitted into the region R after two or more internal

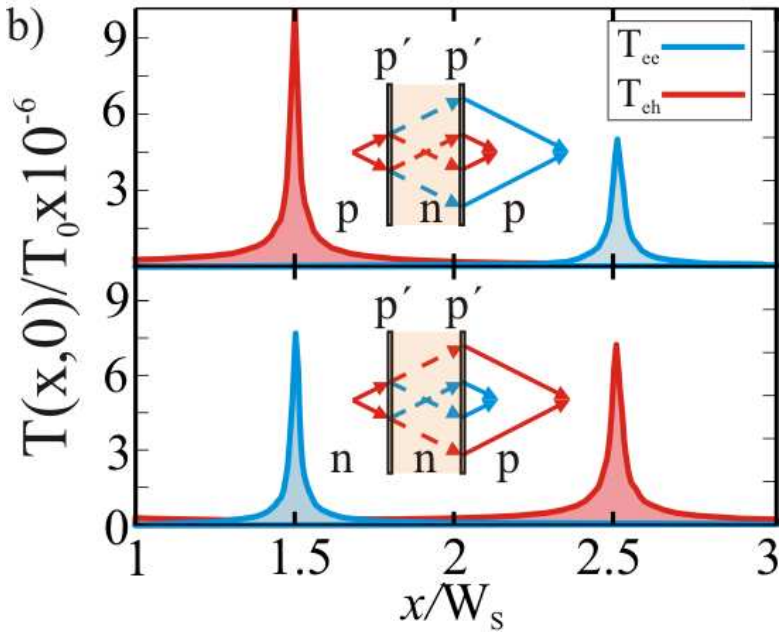

FIGURE 5.8: Tunnel junction. Microscopic calculation for the *p-p'-n-p'-p* junction in the limit of thin barrier with the same parameters of Figure 5.6 (top) and when the sign of the doping of region L is changed, thus having a *n-p'-n-p'-p* junction (bottom).

specular reflections. However, a combination of one specular reflection and one retro-reflection, which changes the particle type, allows for a hole focusing point at $x = 1.5W_S$, i.e., to the left of the electron focusing point at $x = 2.5W_S$ (see Figure 5.7 for a sketch of the trajectories and the microscopic calculation). The intensity of this peak is the same as the CAR peak appearing at $x = 3.5W_S$, to the right of the electron focusing point, which comes from a transmitted hole without internal reflections. Both peaks of T_{eh} in Figure 5.7 are greater than the peak of T_{ee}; in particular the peak at $x = 3.5W_S$ is ~ 5 times larger than the background EC contribution.

5.2.3 Focusing in the tunnel limit

We now describe a *p-p'-n-p'-p* junction, where the *p'* regions are narrow normal intermediate regions with a large energy potential for the quasiparticles (see the sketch in the top panel of Figure 5.8). These regions act as an insulating barrier between the normal and the superconducting regions. As it was studied in Refs. [57, 58], in the limit of thin barrier, these regions introduce a Fermi vector mismatch such that the reflection and transmission amplitudes exhibit an oscillatory behavior as a function of the barrier strength χ (see more details in Appendix B). Recreating the conditions of Figure 5.6 in this system, i.e. injection at $-d = -W_S/2$ and dopings $E_F^{L,R} = -E_F^S = 0.5$ eV, the barrier strength can be tuned so that the CAR and EC signals are of the same order of

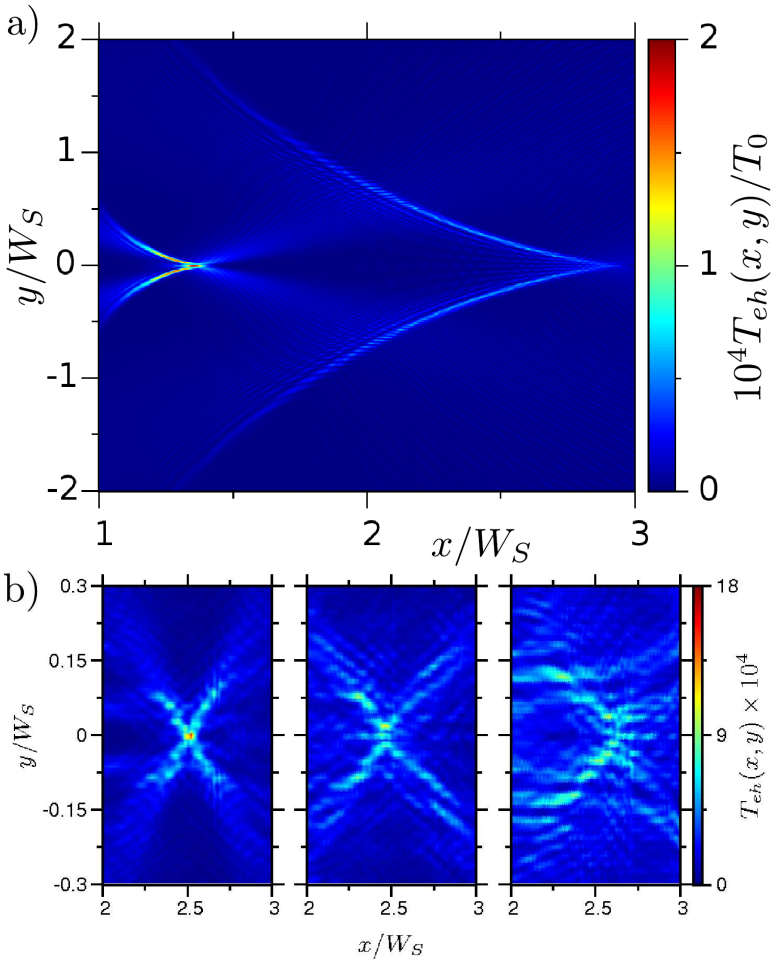

FIGURE 5.9: Deviations from the ideal case: caustic curves and disorder. (a): Map of $T_{eh}(x, y)$ for an asymmetric *pnp* junction. We set $E_F^R = 0.4$ eV and keep the rest of the parameters the same as in Figure 5.7, where $d > W_S$. The refracted waves in the right region form a characteristic interference pattern showing two caustic curves near the cusp for each of the transmitted holes. (b): Map of $T_{eh}(x, y)$ for a *pnp* junction calculated using the TB model. The length of the central superconducting region is $W_S = 85.2$ nm. The gate potentials used are $E_F^{L,R} = -E_F^S = 0.6$ eV, with $\Delta = 2.7$ meV. The left panel includes no disorder. The central panel has $V_0 = 54$ meV. The right panel has $V_0 = 81$ meV. The smearing of the potential for the three panels has a range of ~ 35 nm.

magnitude but focus at different points. We show in the top panel of Figure 5.8 how the intensity of the T_{ee} peak is slightly the double of the T_{eh} one. The Fermi vector mismatch introduced by the barriers allows to change the sign of the doping for the region L, thus having a *n-p'-n-p'-p* junction where the focusing of CAR and EC are spatially exchanged with respect to the previous case (see bottom panel of Figure 5.8). We should notice here that this exchange of electron and hole trajectories can not be done in a perfectly transmitting *nnp* junction since the change of sign in the first interface is necessary to create hole-like excitations inside the superconductor.

5.2.4 Deviations from the ideal case

We have considered thus far that each interface is a perfectly symmetric *pn* junction, i.e. $E_F^p = -E_F^n$. If the doping level of one of the regions is not perfectly aligned with the next we have that $n \neq -1$ for that interface. In Figure 5.9(a) we show a map of $T_{eh}(x, y)$ with $E_F^L = -E_F^S = 0.5$ eV and $E_F^R = 0.4$ eV where the refraction index of the SR interface becomes $n = -E_F^R/E_F^L = -0.8$. For this case the classical trajectories are deformed at the region R. The focal points are displaced from the ones shown in Figure 5.7 and the envelope of the refracted rays becomes a caustic curve [126]. The focusing pattern is reproduced but the intensity of the cusps is not the same, as was the case for the symmetric junction. Caustic curves for electrons in asymmetric *pn* junctions have been predicted to appear [109, 113, 115] but we show here that these curves appear in spite of being originated from hole-like excitations inside the superconductor. We thus conclude that a doping imbalance between regions has the same effect on the CAR signal as that on the EC one.

The results presented thus far correspond to an infinite layer of pristine graphene under a perfectly sharp potential profile. As it is done in Section 4.4, one can go beyond the ideal case including size effects such as a graphene layer with a finite length, a potential profile varying smoothly along the sample and the inclusion of charge puddles [40, 41]. Using a tight-binding model with a two-dimensional superlattice potential we explore the stability of the focusing pattern under these premises. We define a defect-free graphene strip of total length $W \sim 900$ nm, with a central superconducting region of length $W_S \sim 90$ nm and coupled to normal metallic electrodes at the edges. A smearing of the potential profile within a range of $30 - 40$ nm is introduced at each normal-superconductor interface. In addition, we introduce random inhomogeneities of the potential profile of strength V_0 over an area of typical length $d \sim 20 - 30$ nm (the details of the superlattice potential are presented in Appendix A).

We show in the left panel of Figure 5.9(b) the TB results for $T_{eh}(x, y)$ in the absence of disorder ($V_0 = 0$). The focusing spot at $x = 2.5W_S$ is clearly distinguishable although some diffraction effects are present due to the finite length of the system and the smearing of the potential. When we introduce disorder of strength $V_0 = 54$ meV (central panel) the intensity of the focusing spot is reduced but its size remains almost unchanged. In the right panel, when the disorder strength is increased to $V_0 \sim 81$ meV, diffraction effects overcome the focusing pattern. The smearing of the potential has a range of ~ 35 nm for the three panels. As it was demonstrated in Ref. [114] for a smooth *pn* junction, the smearing of the potential introduces a small diffraction effect in the transmission, reducing the intensity of the focusing point, but leaving the extension of the spot almost unchanged. We also find that the focusing pattern is robust against disorder caused by

charge puddles of width $\sim 20-30$ nm and strength $V_0 \lesssim 80$ meV. These parameters are well above the measured inhomogeneities in graphene, which are bounded to 30 meV over $20-30$ nm [40, 41].

5.2.5 Conclusions.

In conclusion we have shown that selective focusing of electrons and holes can be produced in a GSG junction. In addition, the geometry can be tuned in order that the CAR peak dominates over the EC background. We have also shown that the focusing is robust against deviations from the ideal conditions. Under these premises, a possible experimental realization of this proposal is sketched in Figure 5.5, where electrons are injected at the source electrode and collected at the detector electrode. If the source is a fixed electrode, a mobile detector would be able to distinguish between the EC signal and the CAR signal by moving from one focusing point to the other. On the other hand, if the detector is fixed, by moving the source electrode the focusing pattern can be adjusted to reach the fixed electrode. Although the nonlocal electron-hole transmission is reduced by a factor of 10^{-4} with respect to the transmission at the injection point, the total nonlocal conductance can reach a measurable value when adding the contribution of many channels. These properties open an interesting route for the detection of entangled electron pairs over distances of ~ 1 μm.

Chapter 6

Cooper pair splitters based on carbon nanotubes.

6.1 Cooper pair beam splitters in double quantum dots.

Producing entangled electron pairs in a solid state device from the splitting of Cooper pairs [72–75] is a challenging possibility which is starting to generate an intense experimental effort [67–71, 122, 123]. A basic splitting device is a three terminal system with a central superconducting lead (S) in between two normal (N) ones, as depicted in the upper panel of Figure 6.1. When a Cooper pair is injected from the S lead it can either be transmitted as a whole to one of the N leads by means of a *local* Andreev process [Figure 6.1(a)] or split so that each of the electrons in the pair is transmitted to a different lead, which corresponds to a *crossed* Andreev process (CAR) [Figure 6.1(b)] [59]. Initial experimental devices were based on nanolitographically defined diffusive samples [67–71]. In this case a key issue which was extensively addressed theoretically was the competition between CAR processes and direct tunneling of electrons between the normal leads. The cancellation between both contributions to the nonlocal conductance for thick tunnel barriers was shown to be removed by introducing ferromagnetic leads [60, 61], increasing the barrier transparency [62–64] or taking into account Coulomb interactions [65]. The importance of non-equilibrium effects at large bias voltages has been also analyzed [66]. More recent experiments are oriented towards tunable double quantum dots systems based either on carbon nanotubes [122] or InAs nanowires [123]. In spite of the difference in materials the systems realized in both experiments were conceptually equivalent. They did correspond, however, to different physical regimes: while in Ref. [122] the hybridization by direct tunneling between the dots was dominant, in Ref. [123] the direct tunneling appeared to be negligible. In both works the Cooper pair

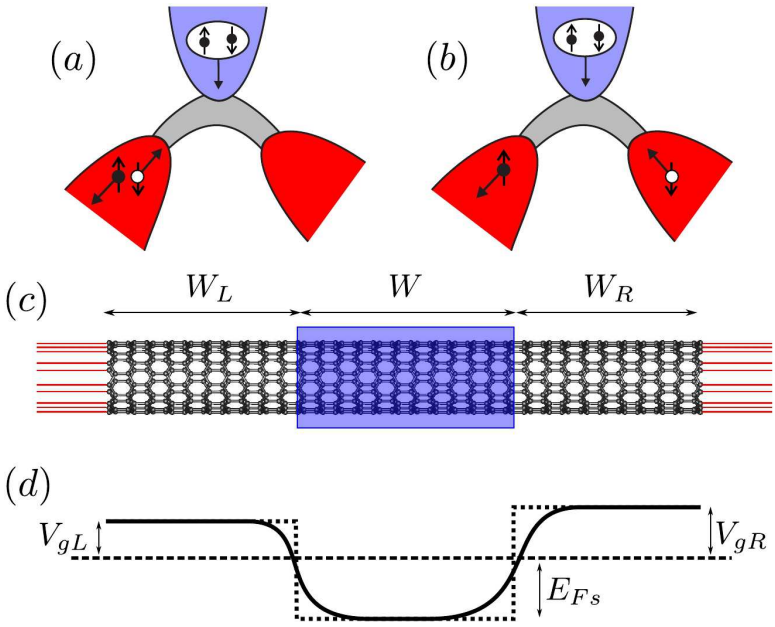

FIGURE 6.1: Schematic representation of local (a) and nonlocal (b) Andreev processes in a generic Cooper pair splitter. (c) Specific geometry considered in this work: a finite SWCNT coupled to normal leads at its ends and a central superconducting lead. The lower image (d) illustrates the potential profile along the tube.

splitting action was demonstrated indirectly by analyzing the changes in the behavior of the conductance when going from the normal to the superconducting state. Both works pointed out an unexpectedly high efficiency for CAR, much higher than what would be predicted by theories which do not take into account the direct inter-dot tunneling [72–75]. Still further experimental and theoretical efforts are needed in order to demonstrate the splitting unambiguously and to reach the nearly 100% efficiency which could be necessary for entanglement detection [127].

This section is organized as follows: We begin with a SWCNT in the normal state without e-e interactions in order to analyze the inter-dot coupling. Subsequently, we switch on superconductivity in the central electrode and study the probability of the CAR processes and the splitting efficiency. Finally, we map the problem into a minimal model where analytical insight into the non-linear regime and the effect of interactions is obtained.

6.2 Experiments on Carbon nanotubes and InAs nanowires.

Two recent experiments have shown that Cooper pairs can be split in a controlled fashion in double quantum dot structures. In one case, the electron entangler was based on single walled carbon nanotubes [122], while the other was based on InAs nanowires [123]. Both

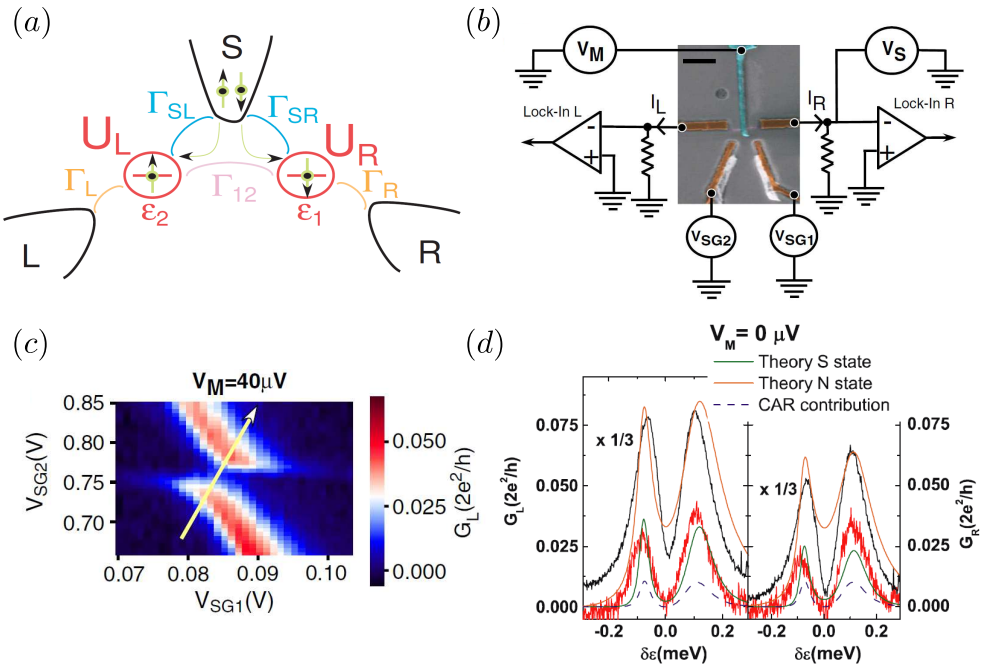

FIGURE 6.2: (a) Sketch of the model used for the Cooper pair splitters. (b) SEM image, in false colors, of the Cooper pair splitter device based on carbon nanotubes, with the two biasing schemes sketched. (c) Conductance map as a function of the gates for an anticrossing in the superconducting state. (d) Measurements of the conductance in the normal state (black solid lines) and in the superconducting state (red [medium gray] solid lines) for G_R and G_L along the direction of the yellow arrow of (c). For the sake of clarity, the normal state conductances have been multiplied by 1/3. The model calculations are in green [dark gray] solid lines for the superconductor state and in orange [light gray] solid lines for the normal state. In blue dashed lines, the CAR probability. Images taken from Ref. [122].

experiments exploit the possibility of individually tuning the levels of each dot by means of independent gates. At the same time, in the quantum dot regime, a sufficiently large Coulomb interaction on each dot prohibits the possibility of having two electrons on the same dot. Subsequently, both experiments are a good realization of the model proposed by Recher *et al.* for a Cooper pair splitter [72] [see Figure 6.2(a)].

Using the parameters defined in Figure 6.2(a), we analyze the different regimes in which each experiment has been realized. On the one hand, for the experiment from Ref. [123], the superconducting gap is $\Delta \approx 150$ μeV, corresponding to a central electrode made from aluminum. The width of the superconducting lead was ~ 150 nm, while the distance between the central electrode and the metallic contacts is ~ 350 nm. The setup is therefore symmetric, with the broadening of the QD levels of the order $\Gamma_L = \Gamma_R = \Gamma \approx 0.5$ meV. The DQD is taken into the Coulomb blockade regime with a charging energy of $U = U_L = U_R \approx 2 - 4$ meV. The conductance at each electrode, G_L and G_R, is determined applying a small voltage $V_M \approx 5 - 10$ μV to the superconducting lead

and measuring the currents through the normal electrodes. For this setup, the maximal change in the non-local conductance, relative to the mean conductance, was $\sim 9\%$ at 20 mK.

On the other hand, for the experiment from Ref. [122], the central superconducting electrode, $80-100$ nm wide, is an aluminum-palladium bilayer and the spacing between the two normal contacts is between 600 nm and 1.2 μm. A SEM image of the experimental setup is shown in Figure 6.2(b) including a sketch of the two biasing schemes used: characterization and beam splitter. For characterization, the device is operated as a series double dot by setting $V_M = 0$ and $V_S \neq 0$, thus allowing for sequential tunneling through the double dot. This setup was used to find the energy regime in which the system showed the charge stability diagram characteristic of a coupled double quantum dot. Specifically, a honeycomb stability diagram with spatially separated avoided crossings was found [128]. The details of one of these avoided crossings, in the superconducting state, are shown in Figure 6.2(c), were the conductance $G_L = \mathrm{d}I_L/\mathrm{d}V_S$ is mapped as a function of the gate voltages V_{SG1} and V_{SG2} close to a resonance. Subsequently, the device was operated as a beam splitter by setting $V_M \neq 0$ and $V_S = 0$. The measure of the conductance out of resonance, now defined as $G_{L,R} = \mathrm{d}I_{L,R}/\mathrm{d}V_M$, allowed them for an estimation of the superconducting gap and the electronic temperature as 85 μeV and 100 mK, respectively. When the voltage applied is smaller than the superconducting gap, i.e. $V_M < 85$ μV, there is only injection of Cooper pairs into the DQD. The striking result of Figure 6.2(c) clearly shows a contribution to the conductance at $V_M = 40$ μeV, which can only be understood if Andreev reflections are taking place at resonance. The conductance measurements are shown in Figure 6.2(d) for both the normal (black solid line) and the superconducting (red solid line) states. The former are reduced by a factor 1/3 for the sake of clarity. A fit to a minimal model like the one sketched in Figure 6.2(a) yields the following hierarchy of energy scales: $U_{L,R} \approx 1$ meV, $\Gamma_{12}, \Gamma_{L,R} \approx 100$ μeV and $\Gamma_{SL,SR} \approx 10$ μeV. As a consequence, a contribution of split Cooper pairs up to 35% for G_L and 55% for G_R was found.

Although both SWCN and InAs nanowires are almost one-dimensional systems and, in these works, both are taken into the DQD regime, one would expect slightly different behaviors. Specifically, SWCN are clean almost ballistic systems while transport at InAs nanowires is diffusive. However, the results that we obtain in this section from microscopic models based in carbon nanotubes can be generalized to the case of the nanowires.

6.3 Microscopic theory of Cooper pair beam splitters in carbon nanotubes.

We proceed to analyze microscopically the case of double quantum dots (DQD) defined on single-walled carbon nanotubes (SWCNTs) and show that the two regimes of Refs. [122, 123] can be reached in metallic or semiconducting tubes. We consider the situation illustrated in Figure 6.1(c) and 6.1(d) where the central electrode modifies the electrostatic potential and induces a pairing amplitude on the portion of the tube underneath without breaking its continuity. In agreement with the experimental observations we show that in this case the splitting efficiency decays rather weakly with the width of the central electrode [123]. Our results also suggest how to increase the splitting efficiency up to a level close to 100% by operating the devices in the non-linear regime.

We focus on zigzag SWCNTs which allow to consider both metallic and semiconducting cases. If the coupling to the central lead is sufficiently smooth on the atomic scale we may assume that intervalley scattering is weak and the K-K' degeneracy is preserved. For this case and when the radius is of the order of 1 nm or smaller it is important to consider curvature effects which produce a finite band gap in metallic tubes and enhances the effect of spin-orbit (SO) interactions. We use two complementary approaches for describing the electronic states in the zigzag SWCNT: a tight-binding (TB) model and a continuous description based on the Bogoliubov-de Gennes-Dirac equations. While the latter allows analytic insight, the numerical TB calculations allow to identify effects due disorder or arbitrary spatial variation of the electrostatic potential along the tube.

Within the continuous description the system is characterized by the equations

$$\begin{pmatrix} H^e_{\tau,s} - E_F & \Delta(x) \\ \Delta(x) & E_F - H^e_{\tau,s} \end{pmatrix} \begin{pmatrix} u_{\tau,s} \\ v_{\tau,s} \end{pmatrix} = E_{\tau,s} \begin{pmatrix} u_{\tau,s} \\ v_{\tau,s} \end{pmatrix} \tag{6.1}$$

where $H^e_{\tau,s} = -i\hbar v_F \partial_x \cdot \sigma_x + \tau \hbar v_F q_n \sigma_y + \tau \delta_0 s - \tau \delta_1 s \sigma_y + V(x)$ is the normal state effective Hamiltonian for the n mode (corresponding to a quantized momenta q_n around the tube), $\Delta(x)$ is the induced pairing amplitude and $V(x)$ the electrostatic potential profile along the tube. In these equations σ_μ are Pauli matrices in sublattice space, and $\tau, s = \pm$ correspond to the valley and spin indexes respectively. Finally, the terms in δ_0 and δ_1 take into account the SO interaction as in Refs. [129, 130]. The momenta q_n take the values $\frac{2\pi}{3Na_0}\left(n \pm \frac{p}{3}\right) - q_{curv}$, with $p = N \mathrm{mod} 3 = 0, \pm 1$ and N being the number of atoms in the cross section. Depending on whether $p = 0$ or $p = \pm 1$ the tube is metallic or semiconductor, respectively. The curvature effect is included in $q_{curv} = E_{curv}/\hbar v_F$, where $E_{curv} \simeq \pi^2 |V_{pp\pi}|/4N^2$ with $|V_{pp\pi}| \simeq 2.7$ eV. In the normal homogeneous case the corresponding energy levels for longitudinal wave vector k are

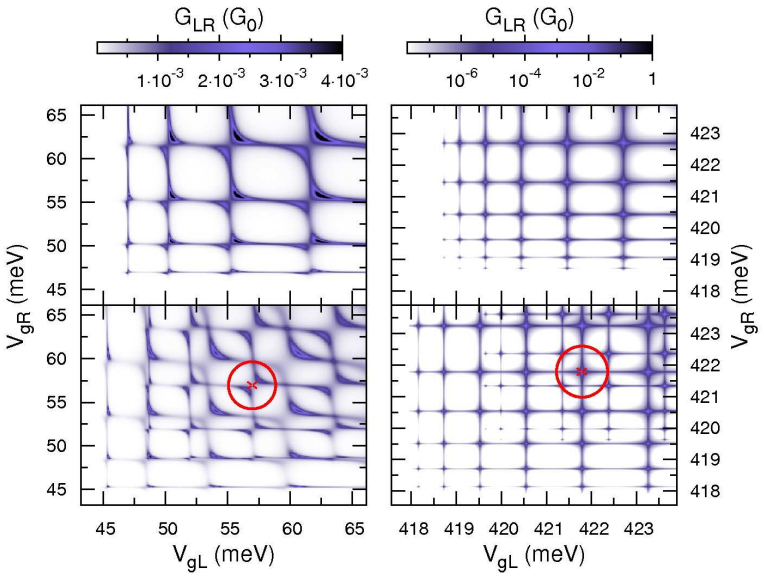

FIGURE 6.3: Left panel: Conductance map for a metallic tube ($N = 12$) in the normal state for the p-n-p region with (lower) and without (upper) SO interactions. Right panel: Same for the semiconducting tube ($N = 11$) but in a logarithmic scale. The geometrical parameters are $W = W_{L,R} = 170nm$.

thus given by $E^n_{\tau,s}(k) = \hbar v_F \sqrt{(q_n + \tau s \delta_1)^2 + k^2} + \delta_0 \tau s$. The transport properties can be expressed in terms of Green functions which satisfy $(E - \mathcal{H}_{\tau,s}(x))G_{\tau,s}(x, x') = \delta(x - x')$, where $\mathcal{H}_{\tau,s}(x)$ denotes the full Hamiltonian on the left hand side of Equation 6.1. We obtain these quantities by solving first for the uniform finite regions and then matching the result using the method explained in detail in Section 3.4.

6.3.1 Normal state.

We start by analyzing the linear conductance along the tube, G_{LR}, when the central lead is in the normal state. In Figure 6.3 we show a map of G_{LR} in the $V_{gL} - V_{gR}$ plane, obtained using the TB model in the usual nearest neighbors approximation with a hopping parameter $t \equiv V_{pp\pi}$. As a first approximation the potential profile along the tube is assumed to change discontinuously as represented by the dashed lines in Figure 6.1(d). The lateral leads are modeled by ideal 1D channels weakly coupled to the ends of the tube, as represented schematically in Figure 6.1(c). We fix the tunneling rates to these leads to a value $\Gamma_{L,R} \sim 0.01t$ which is consistent with the conductance values observed in Ref. [131] for the lowest energy states of a SWCNT quantum dot. To model the effect of the central lead we rely on the results of ab-initio calculations for the case of Al electrodes [125, 132]. According to Ref. [125] these produce a n-doping effect, leading to a shift of the tube bands $E_{Fs} \sim -0.5$ eV for an ideal interface. On the other hand in the normal state it would induce a broadening of the tube levels of the order of a few meV [132] which suggests a typical value $\Gamma_S \sim 1meV$ for the corresponding

tunneling rate. We choose the length of the central region to be set initially to ~ 200 nm, slightly bigger than the experiments from Ref. [122] and closer to the one from Ref. [123]. We consider tubes with $N = 11, 12$ which corresponds to radii $R \sim 0.43, 0.47$ nm respectively. In the metallic case curvature effects lead to the opening of a narrow gap, which can be estimated as $E_g \simeq E_{curv} \simeq 45$ meV. The curvature gap is apparent in the upper left panel of Figure 6.3. On the other hand, in the semiconducting case the gap is $E_g \simeq 412$ meV (top right panel of Figure 6.3). It should be noticed that for these diameters and for gate potentials of the order of 0.5 eV only the lowest energy mode, corresponding to $n = 0$, gives a significant contribution to the transport properties.

For positive V_{gL}, V_{gR}, i.e. in the *pnp* regime, the conductance displays a DQD behavior as shown in Figure 6.3. The metallic case (left panels) exhibits an anticrossing pattern similar to the one found in the experiments of Ref. [122]. As the gate potentials V_{gL}, V_{gR} become increasingly positive the conductance map exhibits resonances along lines $V_{gL} + V_{gR} \sim const$ indicating the delocalization of the electronic states due to Klein tunneling. The confinement of the dot states is much more pronounced in the semiconducting case where the Klein tunneling is less significant. We have used a logarithmic scale in this case in order to enhance the visibility of the conductance peaks. When SO scattering is introduced (lower panels in Figure 6.3), there is a general splitting of the conductance peaks of the order of ~ 2 meV due to the breaking of the spin-valley degeneracy. Close to the gap edges this splitting is of the same order as the mean level separation.

6.3.2 Superconducting state.

When superconductivity in the central lead is switched-on pairing correlations within the tube are induced by proximity effect. The size of the induced gap Δ_i is set by Γ_S. We shall assume that temperature is zero and that the energy E of the injected electrons from the normal leads is smaller than Δ_i. Then $R_{AL}(E)$ and $R_{AR}(E)$ denote the local Andreev reflection probabilities at the L, R leads while $T_{CAR}(E)$ corresponds to the CAR processes. When operated as a beam splitter a finite voltage difference V is applied between the S and the normal leads and the non-linear conductance is given by

$$G_{L(R)}(V) = G_0(T_{CAR}(V) + T_{CAR}(-V) + 2R_{AL(R)}(V)),$$

with $G_0 = 2e^2/h$ (notice that at finite energy, in general, $T_{CAR}(E) \neq T_{CAR}(-E)$ due to the breaking of the electron-hole symmetry). Thus we can define the splitting efficiency as

$$\eta = G_0 \frac{T_{CAR}(V) + T_{CAR}(-V)}{G_L(V) + G_R(V)}.$$

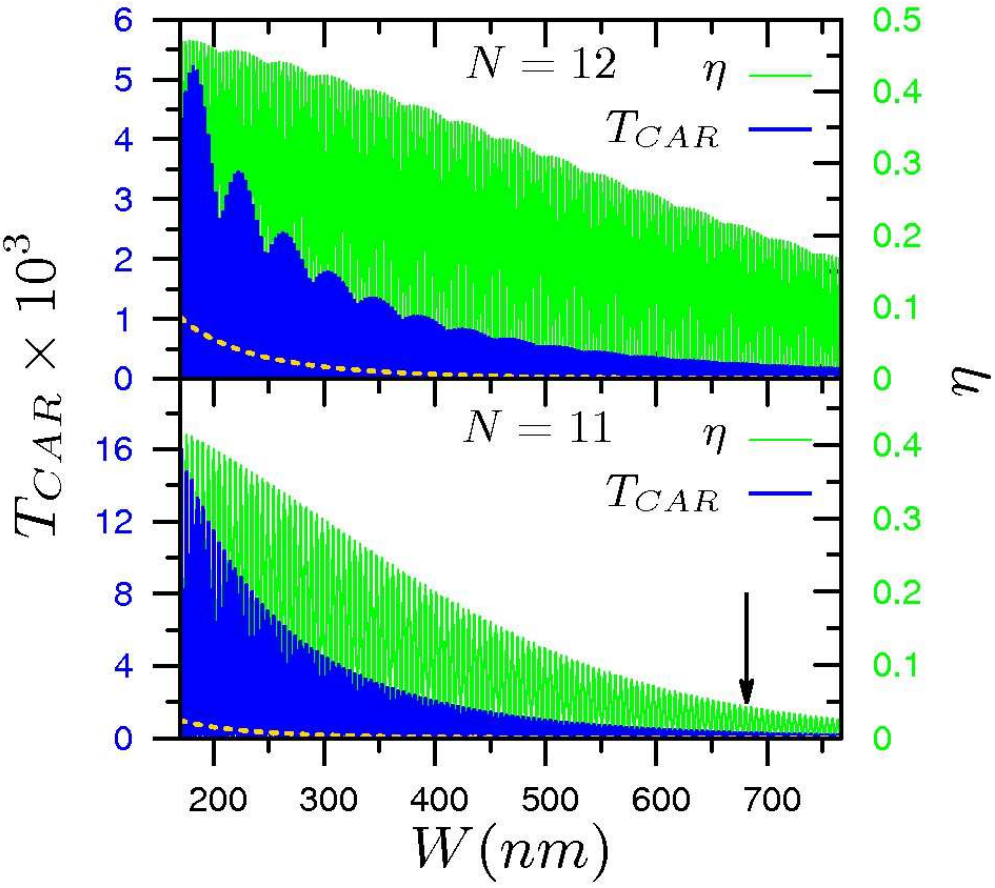

FIGURE 6.4: Evolution of the CAR probability (blue or dark grey) and the splitting efficiency η (green or light grey) in the linear regime as a function of the length W of the central electrode for a metallic SWCNT with $N = 12$ (upper panel) and a semiconducting one with $N = 11$ (lower panel). The gate potentials $V_{gL,gR}$ are fixed at the points indicated by the circles in Figure 6.3. The dashed lines represent the decay of the CAR probability for a 3D bulk superconductor times a factor 10^3.

Within our model the CAR coefficients decay exponentially on the scale $\xi_0 = \hbar v_F/\Delta_i \sqrt{1-(\hbar v_f q/E_{Fs})^2}$, where $q = q_0 \pm \delta_1/\hbar v_F$ exhibiting oscillations on the scale $\lambda_F = \hbar v_F/|E_{Fs}|$, as illustrated for the linear regime in Figure 6.4. In these plots we have fixed the gate voltages at the values indicated by the circles in Figure 6.3. The CAR probability decays more slowly in the metallic case ($N = 12$) due to the longer effective coherence length of this case. In both cases, however, the decay is remarkably slower than in a 3D bulk BCS superconductor where the prediction is $\sim \exp(-2W/\xi_0)/(k_F W)^2$ [60, 61], indicated by the dashed lines in Figure 6.4. This is a consequence of the single channel character of the connection between the dots in the present system and explains the rather large efficiency values estimated in recent experiments [123]. As can be observed the efficiency η decreases from 0.4 at $W \sim 200nm$ to < 0.05 at $W \sim 700nm$ in the semiconducting case, while it varies between 0.5 and 0.2 for the metallic tube within the same W range. For large W the overall evolution of η is well described by

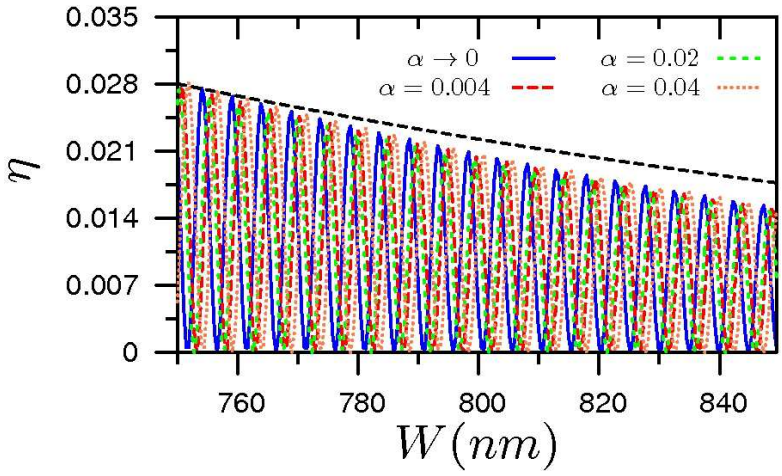

FIGURE 6.5: Evolution of the splitting efficiency η as a function of the length W of the central electrode for $N = 11$, calculated with the smooth potential given by Equation 6.3. Different values of the parameter α are shown representing different electrostatic potential profiles. The asymptotic behavior $\eta \sim 1/(1 + \exp 2W/\xi(q))$ is indicated by the black dashed line. The gate potentials $V_{gL,gR}$ are fixed at the values indicated by the center of the circles of Figure 6.3 in the main text.

the expression $\eta \sim 1/(1 + \exp 2W/\xi_0)$.

This qualitative behavior is also found for a smoother potential profile. For the results of Figure 6.3 and Figure 6.4 the electrostatic potential profile along the tube has been assumed to change discontinuously at the interfaces with the central region. It is thus defined as

$$V(x) = \begin{cases} V_{gL} & , \quad 0 \leq x \leq W_L \\ E_{Fs} & , \quad W_L < x \leq W_L + W \\ V_{gR} & , \quad W_L + W < x \leq W_T \end{cases} , \tag{6.2}$$

where $W_T = W_L + W + W_R$. However, a more realistic description would correspond to a smooth potential as the one defined by

$$\begin{aligned} V(x) \quad = \quad & E_{Fs} + \frac{V_{gL} - E_{Fs}}{\pi} \left[\frac{\pi}{2} - \arctan \frac{x - W_L}{\alpha} \right] \\ & + \frac{V_{gR} - E_{Fs}}{\pi} \left[\frac{\pi}{2} + \arctan \frac{x - W_L - W}{\alpha} \right] , \end{aligned} \tag{6.3}$$

where the parameter α controls the smearing of the potential at the interfaces. This smooth electrostatic potential displaces the position of the energy levels of the dots, thus changing the position of the resonance in the V_{gL}-V_{gR} map. Nevertheless, the overall features of the conduction maps are not modified. In Figure 6.5 we show the evolution of the splitting efficiency η as a function of the length W of the central electrode for a semiconducting case with $N = 11$ and gate potentials corresponding to the resonance indicated by the center of the red circles of Figure 6.3. Different values of the parameter

α are shown along with the case $\alpha \to 0$ which is exactly equivalent to the square barrier potential given by Equation 6.2. The main effect of the smeared potential is a change of phase in the oscillatory pattern at the atomic scale. However, in all cases, the efficiency fits very well to the functional form $\eta \sim 1/(1+\exp 2W/\xi(q))$ indicated by the black dashed line in Figure 6.5.

6.3.3 Map into a minimal model and non-linear regime.

Further analytic insight is provided by mapping the system into a minimal model, valid around the crossing points between dot resonances, in which we keep just one two-fold degenerate electron level $E_{L,R}$ in each dot. The effect of SO interactions is to break the fourfold degeneracy and it is thus implicitly taken into account in the minimal model. In the combined dot-Nambu space the model properties can be expressed in terms of bispinor fields $\Psi_\mu = (d_{\mu\uparrow}, d^\dagger_{\mu\downarrow})^T$ where $\mu = L, R$ and $d^\dagger_{\mu\sigma}$ creates dot electrons. In the absence of interactions this reduced model is characterized by a retarded Green function matrix of the form $\hat{G}^{(0)} = \left[E - \hat{h}_0 + i\hat{\Gamma} - \hat{\Sigma}(E)\right]^{-1}$, where $(\hat{h}_0)_{\mu\nu,\alpha\beta} = E_\mu \delta_{\mu\nu}\delta_{\alpha\beta}(-1)^{\alpha+1}$, with $\mu, \nu \equiv L, R$, $\alpha, \beta \equiv 1, 2$ are the Nambu indexes, $(\hat{\Gamma})_{\mu\nu,\alpha\beta} = \tilde{\Gamma}_\mu \delta_{\mu\nu}\delta_{\alpha\beta}$, with $\tilde{\Gamma}_\mu = \Gamma_\mu a_0/W_\mu$, correspond to the effective tunneling rates to the normal leads and $\hat{\Sigma}$ is a matrix self-energy describing the coupling with the central superconducting region (see Appendix C). Of particular importance for determining the splitting performance of the device is the quantity $\Sigma_{LR,12}$ associated with the interdot CAR processes. In the long W limit this reduces to

$$\Sigma_{LR,12} \sim \frac{t a_0 e^{-W/\xi(E)}}{2\sqrt{W_L W_R}} \frac{\Delta_i}{\sqrt{E^2 - \Delta_i^2}} \sin(k_0 W + \alpha_s), \tag{6.4}$$

where $k_0 = \sqrt{(E_{Fs}/\hbar v_F)^2 - q^2}$, $e^{i\alpha_s} = \hbar v_F(k_0 + iq)/E_{Fs}$ and $\xi(E) = \xi_0 \Delta_i / \sqrt{\Delta_i^2 - E^2}$. To the lowest order in $\hat{\Sigma}$, we find that

$$T_{CAR}(E) \sim \left| \frac{\Sigma_{LR,12}}{[E - E_L + i\tilde{\Gamma}_L)(E + E_R + i\tilde{\Gamma}_R)} \right|^2,$$

which suggests that it would be maximized for $E \sim E_L \sim -E_R$. Further analysis shows that $\eta \to 1$ could be obtained provided that $\Delta_i > |E_L| \gg \tilde{\Gamma}_{L,R} e^{W/\xi(E_L)}$. As we show below these predictions are confirmed by the full calculations where we additionally include the effect of interactions.

For this purpose we assume a constant charging energy $U_{L,R} \gg \Delta_i$ acting on each dot and apply the equation of motion (EOM) technique with a Hartree-Fock decoupling at the level of the two-body Green functions as described in Appendix D. This

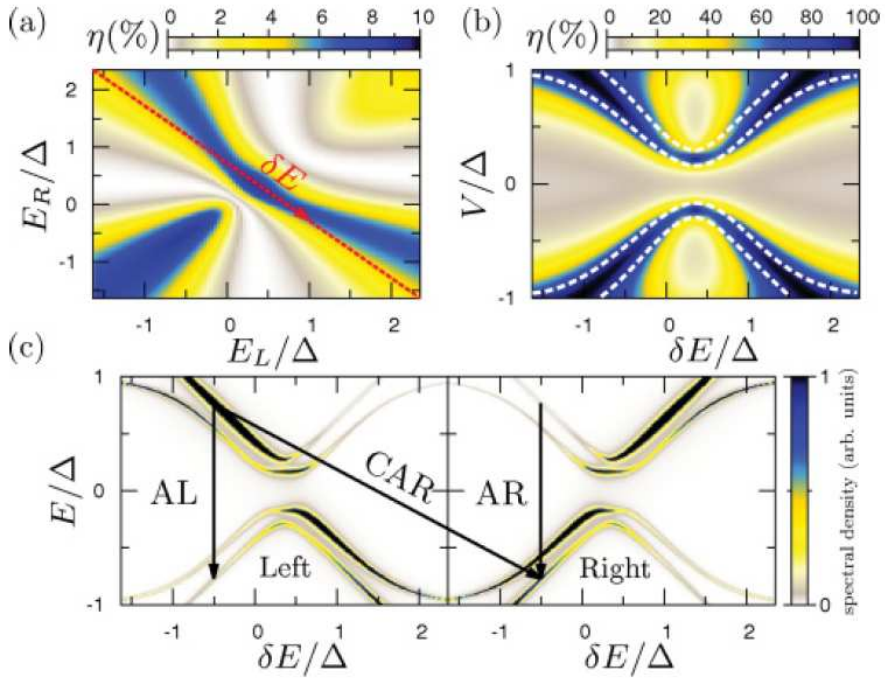

FIGURE 6.6: Color map of the splitting efficiency within the minimal model with parameters corresponding to a semiconducting tube with $W \sim 700nm$ (indicated by the arrow in Figure 6.4) in the linear (a) and non-linear (b) regimes. In the latter case the dot levels are varied along the line $E_L \sim -E_R$ indicated by the dashed red line of (a). The white dashed lines indicate the maxima in the spectral density which is shown in (c) for the two dots along this line. Local and nonlocal Andreev processes at finite V are indicated by the black arrows.

approximation is valid when Kondo and exchange correlations between the dots can be neglected. Further simplification is achieved in the limit $U_\mu \to \infty$ where we find $\hat{G} = \left[\hat{g}^{-1} + i\hat{\Gamma} - \hat{\Sigma}\right]^{-1}$, with $g = (E - \hat{h}_0)^{-1}[1 - \hat{A}_\infty]$ and $(\hat{A}_\infty)_{\mu\nu,\alpha\beta} = n_\mu \delta_{\mu\nu}\delta_{\alpha\beta}$. The evaluation of the mean values $n_\mu = <d^\dagger_{\mu\sigma} d_{\mu\sigma}>$ must be performed self-consistently. The relevant transport coefficients are finally computed as $T_{CAR}(E) = 4\tilde{\Gamma}_L\tilde{\Gamma}_R|G_{LR,12}(E)|^2$ and $R_{AL(R)} = 4\tilde{\Gamma}^2_{L(R)}|G_{LL(RR),12}|^2$.

The main effect of interactions within this approximation is to shift the resonances and to reduce their width, roughly as $(1 - n_\mu)\tilde{\Gamma}_\mu$. Then, the CAR and the local Andreev probabilities are reduced by a factor $(1 - n_1)(1 - n_2)$ and $(1 - n_\mu)^2$ respectively, which therefore does not modify significantly the efficiency at resonance. The color map in Figure 6.6(a) shows the efficiency in the linear regime corresponding to the semiconducting case with $W \sim 700nm$ (arrow in Figure 6.4) and for the region of gate voltages indicated by the circle in the right panel of Figure 6.3. As can be observed, η exhibits maximum values at the crossing point between the resonances of the order of 0.1 which are slightly higher than the values found in the non-interacting case. The efficiency reaches a maximum of the same magnitude along the line $E_L \sim -E_R$ (red dashed line).

What is more remarkable is that the efficiency along this line rises up to $\sim 100\%$ in the non-linear regime $V \neq 0$. This is illustrated in Figure 6.6(b). The high efficiency regions lie within the dot resonances (indicated by the dashed white lines) which are shifted from zero energy due to the presence of an induced minigap and split due to the hybridization between the dots. This last effect is linked to the matrix elements $\Sigma_{LR,\mu\mu}$.

The origin of these high efficiency regions can be understood qualitatively from the spectral density on each dot, which is shown in Figure 6.6(c). As can be observed the electron-hole symmetry in the local spectral density is lost along the line $E_L \sim -E_R$. Crossed Andreev processes like the one sketched as the CAR arrow in Figure 6.6(c) combines electron and hole states on each dot with high spectral density. These inter-dot transitions are then more favorable than the intra-dot electron-hole conversions (arrows AR and AL), in which either the electron or the hole state has low spectral density. As a consequence, local Andreev processes become suppressed while nonlocal CAR processes are enhanced, thus explaining the efficiency increase. It should be stressed that this increase is mainly due to an energy filtering mechanism [133], which is only weakly affected by Coulomb interactions.

6.4 Cooper pair splitters in the nonlinear regime.

The coherence of the emitted states in a Cooper pair splitter device is of capital importance for the implementation of quantum optics-like experiments with electronic states. Since the splitting efficiency is greatly enhanced in the non-linear regime, it is crucial to establish how a Cooper pair splitter behaves when a finite bias is applied to the superconducting electrode.

In a recent experiment, Hofstetter *et al.* [134] extend the study of Cooper pair splitters based on semiconducting nanowires to the nonlinear regime. In this case, one of the QD, say R, is totally grounded, i.e., instead of a single energy level this QD is characterized by a constant density of states. Subsequently, a finite bias difference V was applied to this dot and the conductance through the other QD, $G_L = \mathrm{d}I_L/\mathrm{d}V$ was measured. This finite bias spectroscopy is very useful to identify the nonlocal processes and distinguish the contribution of CAR to the nonlocal conductance. Indeed, nonlocal Andreev states originated from the CAR processes are expected to depend on the single-particle energies of the quasiparticles forming the split Cooper pair [72]. In their findings, a positive nonlocal differential conductance was found on-resonance, i.e. when the gate voltage in L is aligned with the energy level of the QD. This result is interpreted as an enhancement of the contribution from CAR processes. On the other hand, a negative differential conductance was measured off-resonance, consistent with a higher rate of EC processes.

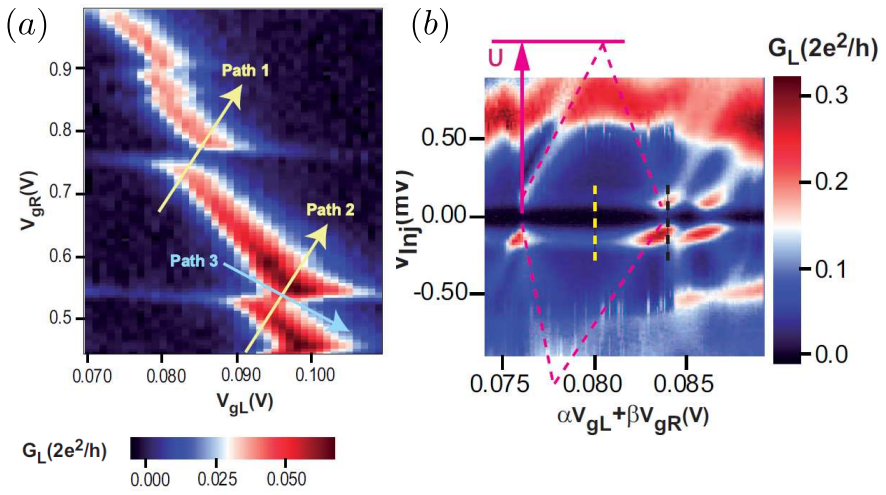

FIGURE 6.7: (*a*): Stability diagram of a SWCN based Cooper pair splitter in the linear regime showing the avoided crossings of levels characteristic of the DQD regime. The paths $1-3$ correspond to the directions for the non-linear spectroscopy. (*b*): Non-linear spectroscopy along path 1 of (*a*) on a wide energy scale showing a Coulomb 'diamond'.

These results imply that the rate of the contribution of the EC and CAR processes to the differential conductance can be tuned by an electric potential. Although the setup for this experiment was not exactly in the double quantum dot regime and a complete theoretical explanation of the data has not yet been obtained [135], these results are promising and call for a deeper understanding of the finite-bias spectroscopy of Cooper pairs.

In a similar way, the experimental setup of Ref. [122] for carbon nanotubes can be taken into the non-linear regime. The case of SWCN allows for a more clear realization of the DQD regime, as it is shown in Figure 6.7(a). In this case, for a temperature of 120 mK, the stability diagram of the conductance for the left arm, G_L, is presented showing a pattern of avoided crossings of energy levels. The non-linear spectroscopy of the Cooper pair splitting is realized injecting a bias voltage V_{inj} between the normal leads and tuning the gate potentials to follow the paths marked in the figure. Paths 1 and 2 correspond to a situation where the energy levels of both dots are moved in the same direction, i.e., $E_L \sim E_R$, while path 3 represents the case where they are moved in opposite directions, $E_L \sim -E_R$. Figure 6.7(b) shows the non-linear spectroscopy following path 1. The range of the applied bias voltage is wide enough to show the average charging energy of the dots $U \approx 1$ eV, shown as the pink diamond. The superconducting gap is the horizontal dark strip at zero bias and can be estimated, outside the resonances, as $\Delta \approx 85\ \mu$V. The resonances correspond to the anti-crossings, where some states penetrating the gap are clearly shown.

The differential conductance G_L far from a resonance displays a clear gap that can be

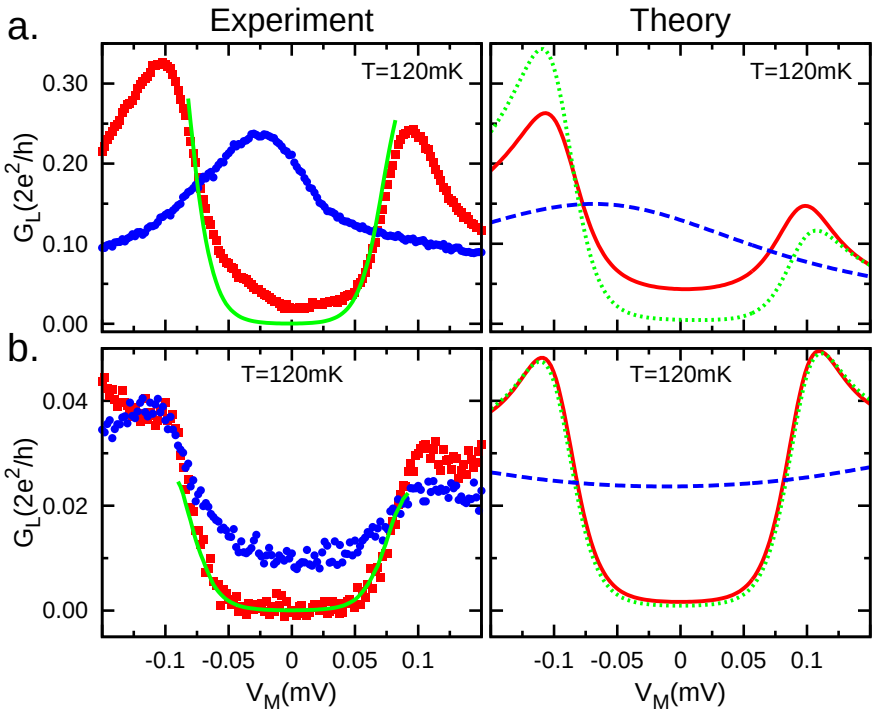

FIGURE 6.8: Differential conductance G_L, measured on-resonance, panel *a*, and off-resonance, panel *b*. The experimental results are taken from the dashed lines of Figure 6.7(b), with the on-resonance corresponding with the black line and the off-resonance to the yellow. The theoretical results are calculated using the TB model described in the main text.

fitted to a BCS curve with a gap of 85 μeV at 120 mK. The experimental data and the fitting are clearly shown in the left panel of Figure 6.8(b) as the red squares and the green solid line, respectively. The blue circles correspond to the differential conductance measured when a magnetic field, perpendicular to the axis of the superconducting finger and with an intensity of $\sim$ 45 mT, was applied. These results are therefore identified with the normal state of the beam splitter [122]. On the other hand, no gap is found on-resonance. Figure 6.8(a) shows the experimental data (red squares) taken along the black dashed line of Figure 6.7(b) together with the results for an applied magnetic field (blue circles). The fitting to a BCS-like curve with the same parameters as before (green solid line) shows a distinctive behavior. Firstly, the quasi-particle peaks at the edges of the BCS gap are clearly enhanced and broadened. Secondly, the gap disappears. Lastly, the change of shape of the differential conductance inside the gap indicates the presence of midgap states. As a consequence, the results seems to indicate the existence of subgap states which arise from the crossed Andreev reflection and the partial confinement in each of the dots.

To confirm these observations and, subsequently, quantify the ratio of CAR processes in the measured conductance, the experimental results are compared with the TB model previously presented. Since the comparison with the experiments is now quantitative,

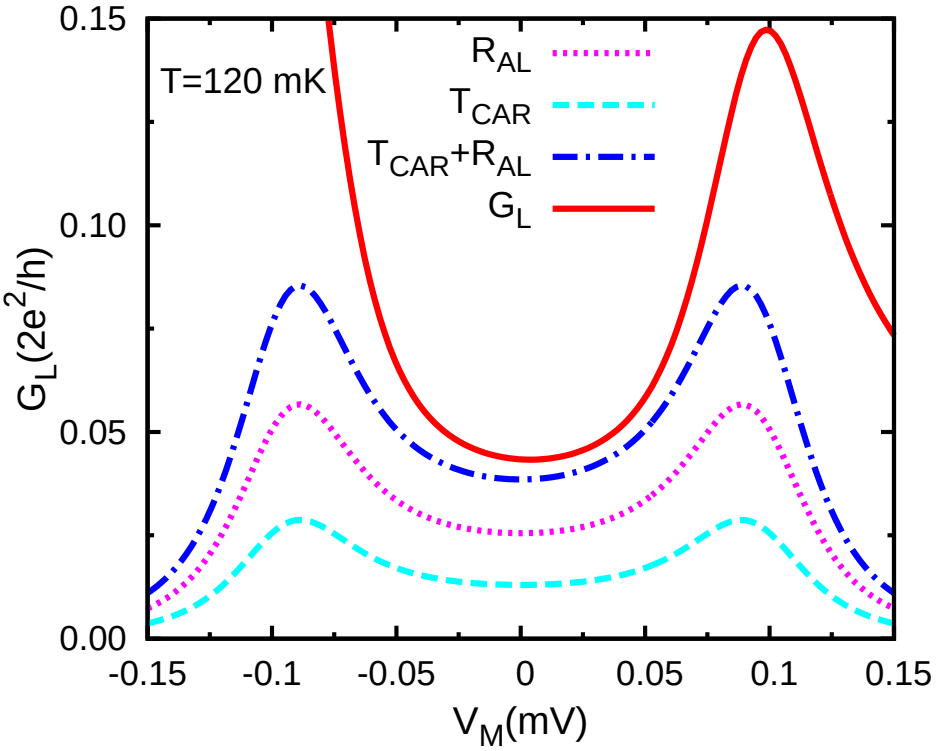

FIGURE 6.9: The solid red line shows the differential conductance G_L from the TB calculations on-resonance [equivalent to the right panel of Figure 6.8(a)]. The dotted and the dashed lines correspond to the local Andreev reflection probability R_{AL} and the CAR probability T_{CAR}, respectively. The dashed-dotted line is the addition of the two.

and not only qualitative as before, a slightly finer tuning of the parameters is needed. We thus describe a metallic zigzag SWCN, with radius ~ 0.5 nm and total length 600 nm, contacted at its ends by normal metallic leads. The central superconducting region has a width of 90 nm, which is slightly smaller than the previously used. The tunneling rates with the normal electrodes are $\Gamma_L \simeq 0.1t_g$ and $\Gamma_R \simeq 0.03t_g$. This asymmetry does not result in a different behavior of the conductances G_L and G_R, but appears essentially as a scale factor between them. Additionally, the induced gap is $\Delta_i \simeq 0.1$ meV and the effective coupling of the resonant levels with the superconducting finger is $\Gamma_S \sim \Delta_i$. Furthermore, the coupling with the central electrode is smooth enough at the atomic scale to neglect inter-valley scattering. However, for small radius, the spin-valley degeneracy is broken by spin-orbit interactions. One can focus in only one the crossings of these spin-valley resonances for each dot.

The right panels of Figure 6.8(a) and Figure 6.8(b) show the numerical calculations for G_L using the described realistic parameters (solid red lines). While in the results presented previously only the contribution of subgap processes (i.e., local and nonlocal Andreev reflections) to the conductance were taken into account, now we include the contribution of single particle processes. These processes are responsible for the

enhancement and broadening of the conductance for $eV > \Delta$. Additionally, the blue dashed lines in the theoretical plots show the results for the normal state conductance. All results have been calculated for a temperature of 120 mK. In order to distinguish the contribution of these quasi-particle processes from the one coming from the Andreev processes, we also plot in Figure 6.8(a) and Figure 6.8(b) the numerical results up to the first order in the coupling with the central superconducting electrode (green dotted line). Both local and nonlocal Andreev processes have a second order contribution in the coupling with the superconductor. The first order results are therefore including only the contribution to the conductance from single quasi-particles, which reduces to the BCS gap out of resonance and is enhanced on the gap edge, but without contribution within the gap, when on-resonance. The differences between the theoretical results in Figure 6.8(a) and Figure 6.8(b) are demonstrating that the Andreev processes only occur on-resonance.

The qualitative agreement between theory and experiment is very good for both the on and off-resonance conductance. Therefore, we can analyze the experimental results from the theoretical simulations. On the one hand, the off-resonance conductance (lower panels of Figure 6.8) is well described by a BCS gap. On the other hand, the on-resonance conductance includes a rich subgap structure. Due to the finite temperature, the single particle processes give a small contribution for $eV \lesssim \Delta$, which is not dominant inside the gap. The subgap structure is therefore due to the local and nonlocal Andreev reflections.

From the numerical calculations we can estimate the contribution from each process to the differential conductance. In Figure 6.9 we plot again the differential conductance on-resonance taken from the right panel of Figure 6.8(a) (solid red line). The CAR probability T_{CAR} and the local Andreev reflection probability R_{AL} are shown as the dashed and the dotted lines, respectively. It is clearly seen that $R_{AL} \approx 2T_{CAR}$. Additionally, the dash-dotted blue line shows the sum of these two contributions which accounts for almost the total contribution to the differential conductance within the gap. Close to the border of the gap and outside it the differential conductance is dominated by the quasi-particle contribution.

When the coupling to the normal electrodes is weak, i.e., smaller than the energy gap Δ of the superconductor, Andreev states can be detected by means of a spectroscopy measurement. In this regime, Andreev bound states have been detected in carbon nanotubes [136] and graphene-based [137] Josephson junctions. For these cases, the Andreev bound states carry a supercurrent between th two superconductors of the Josephson junction. In the present case, in addition to having only one superconductor involved in the Andreev reflection process, the coupling to the normal electrodes is much stronger, relative

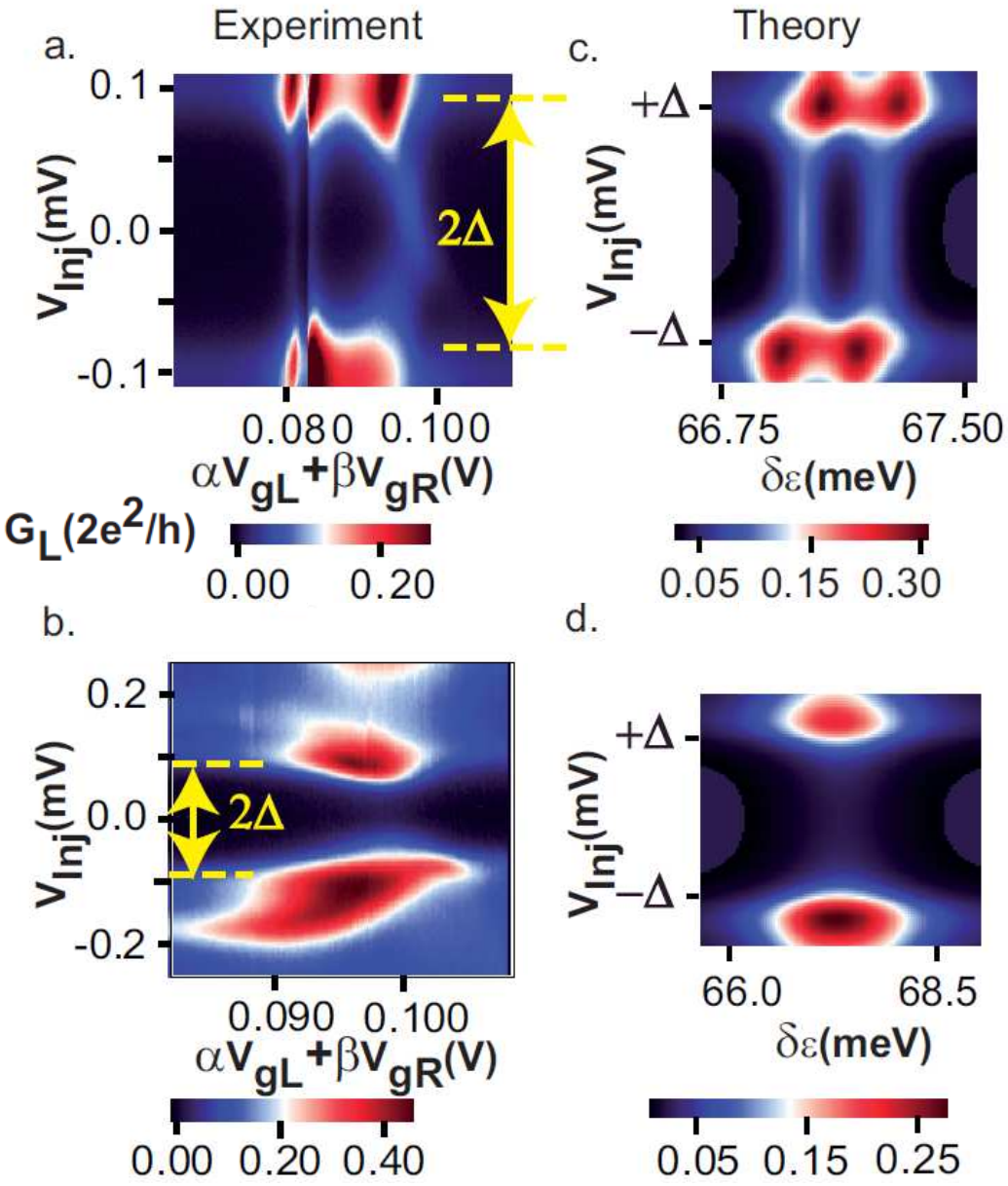

FIGURE 6.10: (*a*): Zoom on the non-linear spectroscopy of the CPS in or scale of G_L along path 2 from Figure 6.7(a). The "egg" shape due to the non-local Andreev levels is observed. (*b*): Zoom on the non-linear spectroscopy of the CPS in or scale of G_L along path 3, with $E_L \sim -E_R$, from Figure 6.7(a). (*c*) and (*d*): Numerical results from the TB model, with the parameters specified in the text, for paths similar to 2 and 3.

to the superconducting energy gap. Subsequently, the Andreev states can not be detected with the exquisite detail of Refs. [136, 137]. Their presence, however, is still revealed qualitatively on a map of the differential conductance as a function of the bias voltage and a definite path for the gate voltages, as it is shown in Figure 6.10(a). This map corresponds to a zoom of the resonance obtained following path 2 of Figure 6.7(a). This experimental results show a clear subgap structure, where a contribution within the gap is found when the gate voltages are on each resonance[1]. Figure 6.10(c) shows the equivalent numerical calculations. The conductance map reveals two broad features within the gap close to the resonances, formed almost entirely by the contribution from Andreev processes (see Figure 6.9). The "egg shaped" area delimited by these contributions presents the off-resonance BCS profile. Due to the qualitative agreement with the experimental results, the theoretical analysis reveals that these subgap contributions are a clear signature of the nonlocal Andreev processes inside the gap. When the temperature is increased, the contribution from the quasi-particle processes to the differential conductance becomes stronger. The "egg" structure is therefore tilted and the subgap contribution to the differential conductance is gradually less pronounced. Additionally, Figure 6.10(b) and Figure 6.10(d) display the experimental and the numerical results taken from path 3 of Figure 6.7(a), respectively. This particular path is taken so it does not cross any resonance and thus the subgap structure is absent, with the exception to the contribution from the quasi-particles close to the gap edges.

6.5 Conclusion, discussion and perspectives.

We have analyzed the splitting efficiency of SWCNT double-quantum-dot devices in terms of material and geometrical parameters. The single-channel character of the connection between the dots in this configuration explains the weak decay of CAR with distance, which is consistent with the experimental observations. Furthermore we have shown how the splitting efficiency can rise to $\sim 100\%$ by working in the nonlinear regime. In this respect, the appearance of recent experimental results by Hofstetter *et al.* [134] is encouraging; they extend the study of Cooper pair splitters based on semiconducting nanowires to the nonlinear regime.

As a consequence, we have also investigated the operation of a Cooper pair splitter, based on a SWCN-DQD, in the nonlinear regime. We have identified the contribution to the differential conductance coming from Andreev processes. This contribution is enhanced at the position of the nonlocal Andreev levels that are partially confined at each dot.

[1] A similar result is shown in Figure 6.7(b), although in a much wider energy scale. For that case, the contribution from each resonance is more clear, where in Figure 6.10(a) one of the resonances show what it seems to be an experimental glitch.

The experimental results were taken in the strong coupling regime, which limits the possibility of having a clear spectroscopy of these levels, since they are broadened by the coupling between the dots and the normal electrodes. The numerical results allow, however, to qualitatively identify these levels, which shows that Cooper pairs can survive once injected in the quantum dot in the nonlinear regime.

Chapter 7

Summary and conclusions.

This thesis has dealt with the study of the superconducting proximity effect in graphene and with the nonlocal transport in carbon based materials with reduced dimensionality. A theoretical analysis of the proximity effect in a graphene-superconductor junction has been presented. We have presented a microscopic description of the interface, considering different experimental setups. We have predicted the behavior of the local density of states of a graphene layer in contact with a superconducting electrode. Additionally, we have predicted the appearance of bound states associated to the graphene-superconductor interface for energies below the superconducting gap. On the other hand, we have proposed and, subsequently, analyzed the possibility of focusing beams of electron and holes in separated spatial region on a graphene-superconductor-graphene junction. Finally, we have analyzed the crossed Andreev reflections that occur in carbon nanotubes coupled with superconducting electrodes. A list of the publications resulted from this work is given in Appendix E. We now provide a detailed enumeration of the results of each chapter.

We have presented in Chapter 3 the extension to carbon based nanostructures of the Green function techniques for both the continuous and the tight-binding model. Specifically, Green function techniques including the presence of superconducting correlations have been adapted to graphene systems. As a result, we have provided "hybrid" models in which the graphene layer is described using a continuous approach based on the Dirac equation and a discrete model is used for the description of the coupling with the superconductor. In particular, analytic expressions for the Green function of the graphene normal-superconductor system are given in Chapter 4. Additionally, a novel method for combining the continuous results using a microscopic Dyson equation, is presented in Chapter 3. The results presented here have been published in Ref. [83] and, partly, in Ref. [82].

In Chapter 4, a microscopic description of a graphene-based NS junction has been presented. Two different models for microscopically describing the superconducting electrodes are provided. On the one hand, a model in which the superconductor induces a finite pairing in the graphene regions underneath has been used. This model maintains the honeycomb structure of graphene at the interface. On the other hand, a graphene layer is directly coupled with a bulk superconducting electrode. The Andreev reflection probability and its channel decomposition have been shown to depend critically on the model used for describing the interface. Moreover, the proximity effect on the local density of states of graphene has been studied. For finite layers, the induced minigap and its dependence on the length of the layer has been analyzed. Additionally, results for the local density of states profiles for finite and semi-infinite layers have been presented, taking into account the orientation of the edges and the transmission of the interface. Finally, it is shown that all the microscopic properties of the graphene-superconductor junctions can be qualitatively explained by the presence of interface bound states which appear due to the interplay of Andreev and normal reflection. A simple analytic model for the formation of these bound states at the graphene-superconductor interface is given. These results have been published in Refs. [82, 83, 87].

The interface bound states provide long-range superconducting correlations on the graphene layer, which may be exploited for the detection of crossed Andreev processes. The possible applications of these results for studying the nonlocal transport in a graphene-superconductor system are developed in the first part of Chapter 5. These results are still unpublished. In the second part of Chapter 5, we have shown that selective focusing of electrons and holes can be produced in a graphene-superconductor-graphene junction. In addition, the geometry can be tuned in order to have a dominance of Crossed Andreev processes over the incoherent transmission of electrons. We have also shown that the focusing is robust against deviations from the ideal conditions. Under these premises, a possible experimental realization of this proposal has been sketched. These properties open an interesting route for the detection of entangled electron pairs over distances of $\sim 1\ \mu$m. These results have been published in Ref. [138].

In conclusion, a microscopic theory has been developed for describing a wide variety of graphene-superconductor hybrid structures. The detailed possibilities of the Green function techniques described in Chapter 3 have been already used in several publications [82, 87, 138], but they can still be used in more sophisticated systems. Specifically, with the use of the model explained in Appendix A, the inclusion of disorder in the graphene-superconductor junction can lead to a new level of detail in the description of such a system. In particular, this model is used in Section 4.4 to study the robustness of the interface bound states to disorder. A more detailed study of the effect of disorder on the graphene-superconductor interface is needed, since the novel specular Andreev

reflection, unique of graphene, is enhanced at the low-doping regime, where the electron-hole puddles play an important role.

On the other hand, the same Green function techniques are easily applied to systems based on carbon nanotubes, as it is explained in detail in Appendix C. A consequence of that is the microscopic theory for the Cooper pair splitters developed in Section 6.3. Additionally, in Chapter 6, we have analyzed the splitting efficiency of single-walled carbon nanotube double-quantum-dot devices in terms of material and geometrical parameters. The single-channel character of the connection between the dots in this configuration explains the weak decay of the Crossed Andreev processes with distance, which is consistent with the experimental observations. Furthermore, we have shown how the splitting efficiency can rise to $\sim 100\%$ by working in the nonlinear regime. These results have been published in Ref. [139]. The theoretical model presented is used for the analysis of experiments for the production of entangled electron pairs using these devices. Specifically, the nonlinear transport in a double quantum dot connected to two normal electrodes and a superconducting finger has been analyzed. A great agreement with the experiments has been reached, providing an unique analytic insight on the experimental results. This latter part is still unpublished. Cooper pair splitters based on double quantum dots in the non-linear regime are an open field where promising experiments are been conducted [134]. The success in the fitting of the experimental results shown in Section 6.3 is encouraging.

Chapter 8

Sumario y conclusiones.

Esta tesis ha versado en el estudio del efecto de proximidad superconductor y el transporte no local en materiales de dimensionalidad reducida basados en carbono. Se ha presentado un análisis teórico del efecto de proximidad en una unión grafeno-superconductor. Se ha presentado, también, una descripción microscópica de la interfase, considerando distintos montajes experimentales. Además, se ha predicho el comportamiento de la densidad local de estados de una lámina de grafeno en contacto con un electrodo superconductor. Finalmente, se ha predicho la aparición de estados ligados asociados a las interfases grafeno-superconductor para energias menores que el gap superconductor. Por otro lado, se ha propuesto y, en consecuencia, analizado la posibilidad de "focalizar" haces de electrones y huecos en distintas regiones de una juntura grafeno-superconductor-grafeno. Finalmente, se han analizado las reflexiones de Andreev cruzadas en nanotubos de carbono acoplados a electrodos superconductores. En el Apéndice E se incluye una lista de las publicaciones derivadas de este trabajo. A continuación se provee una detallada enumeración de los resultados de cada capítulo.

En el Capítulo 3 se ha presentado la extensión para nanoestructuras basadas en carbono de las técnicas basadas en funciones de Green, tanto para modelos continuos como para modelos tipo tight-binding. Principalmente se han desarrollado métodos de funciones de Green adaptados al caso del grafeno en presencia de correlaciones superconductoras. Se han desarrollado modelos "híbridos" en los que se utiliza una descripción continua tipo ecuación de Dirac para el grafeno y un modelo discreto para describir la interfase con el superconductor. En particular, en el Capítulo 4 se muestran las expresiones analíticas para las funciones de Green de una juntura grafeno-superconductor. Además, un nuevo método para combinar los resultados de los modelos continuos mediante una ecuación de Dyson microscópica se detalla en el Capitulo 3. Los resultados aquí presentados se han publicado en la Ref. [83] y, parcialmente, en la Ref. [82].

En el Capítulo 4 se ha presentado una descripción microscópica de una unión grafeno-superconductor. Se han introducido dos modelos para describir microscópicamente los electrodos superconductores. En uno, el superconductor cubre una región de la lámina de grafeno e introduce una correlación de emparejamiento en ella. Este modelo mantiene la estructura hexagonal del grafeno. En el otro, la lámina de grafeno se conecta directamente a un electrodo superconductor. Se ha demostrado que la probabilidad de reflexión Andreev y su descomposición en canales dependen críticamente del modelo usado para describir la interfase. Además, se ha estudiado el efecto de proximidad en la densidad local de estados de una lámina de grafeno. Para láminas finitas, se ha analizado el minigap inducido y su dependencia con la longitud de la lámina. También se han presentado los resultados para láminas semi-infinitas. Se ha tenido en cuenta el tipo de borde de la lámina de grafeno y la transparencia de la interfase con el superconductor. Finalmente, se ha demostrado que las propiedades microscópicas de las junturas grafeno-superconductor se pueden explicar cualitativamente a través de la presencia de estados ligados que aparecen debido a la conexión entre reflexión normal y Andreev. Se ha presentado un modelo analítico simple para la descripción de estos estados ligados. Los resultados presentados en este capítulo se han publicado en las Refs. [82, 83, 87].

Los estados ligados en la interfase son responsables de la aparición de correlaciones superconductoras de largo alcance en la lámina de grafeno. Las posibles aplicaciones de estos resultados en el estudio del transporte no local en un sistema grafeno-superconductor se han desarrollado en la primera parte del Capítulo 5. Estos resultados aún no están publicados. En la segunda parte del Capítulo 5, se ha demostrado la focalización selectiva de electrones y huecos que se produce en una unión grafeno-superconductor-grafeno. Además, la geometría de esta juntura se puede adecuar para obtener un dominio de los procesos cruzados de Andreev sobre la transmisión incoherente de electrones. También se ha demostrado que esta focalización es robusta frente a desviaciones con respecto a las condiciones ideales. Bajo estas condiciones, se ha esquematizado una propuesta experimental. Estas propiedades abren una interesante posibilidad para la detección de pares de electrones entrelazados separados distancias de ~ 1 μm. Estos resultados se han publicado en la Ref. [138].

En conclusión, se ha desarrollado una teoría microscópica para describir una amplia variedad de estructuras híbridas grafeno-superconductor. Las posibilidades de las técnicas de funciones de Green descritas en el Capítulo 3 han sido publicadas en distintos artículos [82, 87, 138], pero todavía se pueden usar en sistemas más sofisticados. En particular, usando el modelo detallado en el Apéndice A, la inclusión de desorden en una juntura grafeno-superconductor permite llegar a un nuevo grado de detalle en la descripción de dicho sistema. Este modelo se ha usado en la Sección 4.4 para estudiar el efecto del desorden en los estados ligados de la interfase. Un estudio más detallado del efecto del

desorden en la interfase grafeno-superconductor es necesario, teniendo en cuenta que la reflexión especular de Andreev, única en grafeno, es dominante en el regimen de bajo dopado, donde las inhomogeneidades de carga juegan un rol muy importante.

Finalmente, en el Capítulo 6, se ha analizado la eficiencia de separado de pares de Cooper en puntos cuánticos dobles basados en nanotubos de carbono. La conexión entre los puntos cuánticos en esta configuración se realiza mediante un único canal, lo cual explica el débil decaimiento de los procesos de Andreev cruzados con la distancia, consistentemente con las observaciones experimentales. Además, se ha demostrado que la eficiencia de separado se puede elevar hasta $\sim 100\%$ trabajando en el régimen no lineal. Estos resultados se han publicado en la Ref. [139]. El modelo teórico presentado se ha usado en el análisis de los resultados experimentales sobre la producción de pares de electrones entrelazados en estos dispositivos. En particular, se ha alcanzado un gran acuerdo con las mediciones realizadas en el régimen no lineal, lo que ha proporcionado una detallada descripción analítica de los experimentos. Estos resultados todavía no están publicados. Los dispositivos divisores de pares de Cooper basados en puntos cuánticos dobles en el régimen no lineal representan un nuevo campo donde experimentos muy prometedores se están realizando [134]. El éxito demostrado en la Sección 6.3, donde se compara la teoria con los resultados experimentales es muy prometedor.

Appendix A

Transport in superlattices on single layer graphene.

This Appendix is devoted to the study of electronic transport in graphene in the presence of superlattice potentials. Such potentials may create a strong anisotropy in the electron velocity around the Dirac point. As a consequence, new Dirac points can be created in the band structure of graphene. The anisotropy introduced by a one-dimensional potential is highly dependent on the direction of the potential. For that motive, transport parallel and perpendicular to the direction of the potential is studied. On the other hand, the case of a two-dimensional potential is also considered. In this case, the study is centered on isotropic superlattice potentials. These potentials leave the conductivity unaltered for a wide range of parameters. This latter case is also the framework for the study of disorder in graphene samples as it is done in Section 4.4 and in Section 5.2.

This Appendix is organized as follows. In Section A.1 we motivate our work in superlattices on graphene, briefly discussing previous works and introducing the main results. Subsequently, in Section A.2 we present the analytical results for the conductivity obtained assuming independent anisotropic Dirac points. In Section A.3 we present numerical results obtained with a microscopic tight-binding Hamiltonian and compare with the analytical expressions. Section A.4 is dedicated to the conclusions.

A.1 Introduction.

The application of electric fields via nano gate geometries makes it possible to subject graphene-based systems to potentials varying on a short length scale. Using these techniques, recently it has been possible to study experimentally transport through *pn*

junctions and *pnp* junctions in graphene [29, 119, 140–142]. Theoretically, there has also been much effort devoted to the study of the spectra and the electronic transport through differently doped regions [18, 42, 143–145] whose behavior differs from that of conventional two-dimensional electron gases.

A superlattice potential on top of graphene opens the possibility of tailoring its band structure and modifying its transport properties [146–149]. In particular in the case of a one dimensional superlattice potential, the properties of the carriers are extremely sensitive to the amplitude V_0 and period d of the superlattice. For a one dimensional superlattice, the velocity of the carriers is highly anisotropic [112, 150, 151] and the number of Dirac points at the Fermi energy can be altered by varying the product $V_0 d$ [152–154]. Moreover, when the potential magnitude of the superlattice varies slowly in space, the electronic spectra develops a Landau level spectrum [155]. The effect of superlattice potentials due to external magnetic fields has also attracted a great deal of attention [156–159].

Several groups have numerically studied electronic transport perpendicular to the superlattice barriers [152, 154, 160–165]. Starting from the theoretical universal value $\sigma_0 = \frac{4}{\pi}\frac{e^2}{h}$ [18], the conductivity increases with the product $V_0 d$ and develops peaks at the critical values of $V_0 d$ for which new Dirac points emerge [152].

In this Appendix we consider electronic transport in graphene in the presence of superlattice potentials that are piecewise constant. In the case of one-dimensional superlattices we study both transport parallel [Figure A.1(a)] and perpendicular [Figure A.1(b)] to the barriers. We also analyze transport in two-dimensional superlattices [Figure A.1(c)]. Analytical expressions for the conductivity are obtained by describing the carriers with the Dirac Hamiltonian and using the Kubo formula. These are compared with numerical results obtained using a tight-binding Hamiltonian for graphene in the presence of a superlattice potential and the Landauer-Büttiker formalism for obtaining the electrical conductivity in the presence of leads.

In the case of a one dimensional superlattice, we find that, as a function of the product $V_0 d$, the conductivity parallel to the superlattice barriers, $\sigma_\parallel$, decreases quadratically from its value in the absence of the potential, σ_0, whereas in the perpendicular direction the conductivity $\sigma_\perp$ increases quadratically. The appearance of new Dirac points produces peaks in $\sigma_\perp$ and minima in $\sigma_\parallel$. For two-dimensional superlattices the conductivity depends on the relative values of the product $V_0 d$ in different directions. Interestingly, for isotropic superlattice potentials, the conductivity is unaffected by the perturbation and remains at the universal value $\sigma_0 = \frac{4}{\pi}\frac{e^2}{h}$. Further insight into the character of transport is obtained from the channel decomposition of the transmission matrix.

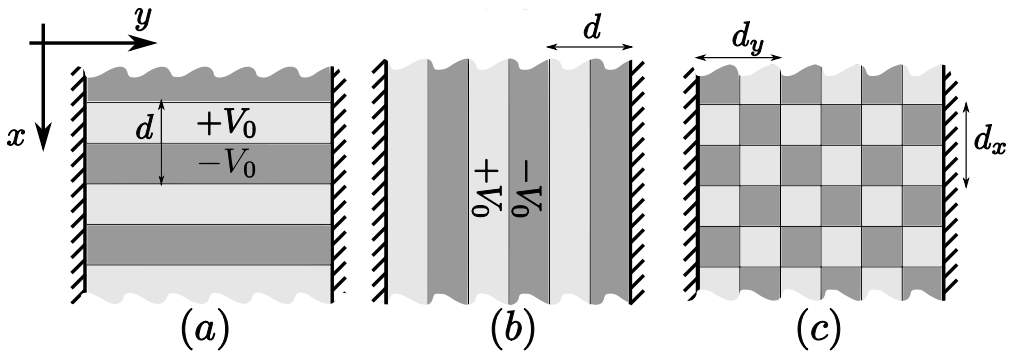

FIGURE A.1: Schematic representation of the superlattice potentials used showing the axis selection. The system is infinite along the x-direction and has a finite length along the y-direction. The dashed patterns on each side of the y-direction indicate the leads for the Landauer conductance calculations. The superlattice barriers can be parallel (a) or perpendicular (b) to the direction of transport. We also consider a chessboard-like two dimensional superlattice potential in which $d_y \simeq d_x$ (c).

A.2 One dimensional superlattice potential

A.2.1 Preliminaries.

The electronic structure of an infinitely large flat graphene flake is described by the Dirac Hamiltonian,

$$H_0 = \hbar v_F \mathbf{k} \cdot \sigma \tag{A.1}$$

where $\hbar\mathbf{k}$ is the momentum operator, σ are the Pauli matrices and $v_F \simeq 10^6 m/s$ is the Fermi velocity. The two entries of the Dirac Hamiltonian correspond to the two carbon atoms in the unit cell in graphene.

The eigenvalues and eigenvectors of this Hamiltonian are $\varepsilon_{k,s}{=}sv_F\hbar k$ and $|s,\mathbf{k}>= \frac{e^{i\mathbf{kr}}}{\sqrt{2}}\begin{pmatrix} 1 \\ se^{i\theta(\mathbf{k})} \end{pmatrix}$, where $s = -1$ and $s = 1$ describe the occupied and empty bands respectively. In the previous expressions $\theta(\mathbf{k})$ is the angle of the vector $\mathbf{k}$ with respect to the $\hat{k}_x$ direction.

A.2.2 Superlattice band structure.

We consider a one-dimensional Kronig-Penney superlattice along the $\hat{x}$-direction (see Figure A.1(a)). The period of the potential is d, $V(x) = V(x+d)$ and $V(x){=}V_0\,\mathrm{sgn}(x)$ for $|x| < d/2$. For this potential it is possible to find an analytical expression for the band structure [145, 154], that in the limit of small wave vector and energies takes the

form

$$\varepsilon(\mathbf{k}) = \pm\hbar v_F \left(k_x^2 + k_y^2 \frac{\sin^2(\tilde{V})}{\tilde{V}^2} \right)^{1/2} \quad , \tag{A.2}$$

where $\tilde{V}=\frac{V_0 d}{2\hbar v_F}$. The group velocity of the state is anisotropically renormalized, and has a strong dependence on the direction of the wave vector $\mathbf{k}$ [150]. At the Dirac point and for directions along the superlattice axis the velocity of the carriers is unaffected by the potentials, $v_x^0=v_F$. However the group velocity along the direction perpendicular to the superlattice direction is strongly renormalized and takes the form

$$v_y^0 \simeq v_F \frac{|\sin(\tilde{V})|}{\tilde{V}} \quad . \tag{A.3}$$

Whenever the superlattice parameters satisfy the condition,

$$\frac{V_0 d}{\hbar v_F} = 2\pi j \quad j = 1, 2, 3, ... \tag{A.4}$$

the group velocity in the $\hat{y}$ direction vanishes and a new pair of Dirac points emerges from the original Dirac point, moving in opposite direction along the $\hat{k}_y$-direction [152, 153]. Near the new Dirac points and at low energy the dispersion is also linear and anisotropic. For the j-th pair of new Dirac points the velocity in the $\hat{x}$ and $\hat{y}$ directions have the expressions [154],

$$\begin{aligned} v_x^j &= \frac{j^2\pi^2}{\tilde{V}^2} v_F \\ v_y^j &= v_F - v_x^j \ . \end{aligned} \tag{A.5}$$

A.2.3 Electrical conductivity.

The conductivity in the collisionless limit has the expression [166, 167]

$$\sigma_{\mu\mu}(\omega) = -i\frac{e^2}{\hbar} g_s g_v \sum_{\mathbf{k},s,s'} \frac{f_{\mathbf{k},s'} - f_{\mathbf{k},s}}{\varepsilon_{\mathbf{k},s'} - \varepsilon_{\mathbf{k},s}} \frac{| < s,k|v_\mu|s',k > |^2}{\varepsilon_{\mathbf{k},s'} - \varepsilon_{\mathbf{k},s} - \hbar\omega - i\delta} \tag{A.6}$$

where s' and s are band indices, $f_{\mathbf{k},s}$ is the Fermi distribution function for the states $|s,\mathbf{k}>$, v_μ is the velocity operator in the $\hat{\mu}$ direction and δ is a positive infinitesimal constant. The conductivity contains a factor $g_s g_v$=4, which takes into account the spin and valley degeneracy. In the case of a single Dirac point with anisotropic velocities v_x and v_y, expressed with a Dirac Hamiltonian of the form

$$H_A = \hbar(v_x k_x \sigma_x + v_y k_y \sigma_y),$$

one may show that the conductivity parallel and perpendicular to the potential barriers of the superlattice may be written in the form

$$\begin{aligned} \sigma^0_{\parallel}(\omega=0) &= \frac{v^0_y}{v^0_x}\sigma_0 = \sigma_0\frac{|\sin(\tilde{V})|}{\tilde{V}}, \\ \sigma^0_{\perp}(\omega=0) &= \frac{v^0_x}{v^0_y}\sigma_0 = \sigma_0\frac{\tilde{V}}{|\sin(\tilde{V})|}, \end{aligned} \tag{A.7}$$

with σ_0 the conductivity of an *isotropic* Dirac Hamiltonian. The value of σ_0 depends on the order in which the zero frequency, zero temperature and vanishing "smearing parameter" δ [167] limits are taken [167, 168]. However the form of the velocity rescaling of the conductivity is independent of the order in which the limits are taken.

In the case of several Dirac points in the spectrum, we assume that each of the points contributes to the conductivity in parallel and using Equation A.5, the conductivity takes the form,

$$\begin{aligned} \sigma_{\parallel} &= \sigma_0\left(\frac{|\sin(\tilde{V})|}{\tilde{V}} + 2\sum_{j=1}^{j_{max}}\frac{\tilde{V}^2-(\pi j)^2}{(\pi j)^2}\right) \\ \sigma_{\perp} &= \sigma_0\left(\frac{\tilde{V}}{|\sin(\tilde{V})|} + 2\sum_{j=1}^{j_{max}}\frac{(\pi j)^2}{\tilde{V}^2-(\pi j)^2}\right) \end{aligned} \tag{A.8}$$

where j_{max}=Integer$(\frac{\tilde{V}}{\pi})$ indicates the number of Dirac point pairs induced by the superlattice. From this expression we see that for small potentials the conductivity perpendicular to the superlattice barriers increases quadratically with $V_0 d$, and each time a new pair of Dirac points emerges the conductivity exhibits a peak. In the direction parallel to the barriers, the conductivity decreases quadratically with $V_0 d$ and dips when new Dirac points emerge.

We remark that in obtaining Equation A.8, we have assumed that each Dirac point contributes as an independent channel to the conductivity and that near each Dirac point the dispersion relation is linear over a wide range of the reciprocal space.

A.2.4 Mode dependent transmission.

The conductivity of a system governed by the Dirac equation with anisotropic velocities, $H = \hbar(v_x k_x \sigma_x + v_y k_y \sigma_y)$, can be also obtained by calculating the transmission probability of modes confined in a stripe of width W and length L connected to heavily doped contacts [16, 28, 36]. For transport along the $\hat{x}$-direction, the transmission probability

for a transverse mode has the form

$$T_n = \frac{1}{\cosh^2(\frac{v_y}{v_x} q_n L)} \,, \tag{A.9}$$

where the transverse momentum q_n depends on the details of the precise boundary condition of the strip [36, 37]. For wide enough strips the conductivity of the system is independent of the boundary conditions and is found by summing over the modes,

$$\begin{aligned} \sigma_{xx} &= g_s g_v \frac{L}{W} \frac{e^2}{h} \sum_n T_n(\hat{x}) = \frac{e^2}{h} \frac{2L}{\pi} \int_{-\infty}^{\infty} \frac{dq}{\cosh^2(\frac{v_y}{v_x} qL)} \\ &= \frac{4}{\pi} \frac{e^2}{h} \frac{v_x}{v_y} \quad \text{for } W >> L \,. \end{aligned} \tag{A.10}$$

The conductivity in the $\hat{y}$ direction is obtained by interchanging x and y in the last equation. The condition for the existence of a well defined -size independent- conductivity is the dependence of the transmission probability on the product qL (Equation A.9) and the linear dispersion of the carriers. The condition $W \gg L$ allows the sum the transmissions over the modes to be written as an integral over q in Equation A.10.

A.2.5 Two dimensional superlattice potential.

The striking result of Equation A.10 is that for symmetric superlattice potentials the conductivity in the $\hat{x}$ and $\hat{y}$ directions are equal and take the value of pristine graphene, $\sigma_{xx}{=}\sigma_{yy}{=}\sigma_0{=}\frac{4}{\pi}\frac{e^2}{h}$.

In the particular situation of a two dimensional superlattice potential on top of a graphene sheet, in second order perturbation theory the group velocity of quasiparticles with momentum $\mathbf{k}$ has the form [150]

$$v_{\mathbf{k}} = v_F - v_F \sum_{\mathbf{G}\neq 0} \frac{2|U(\mathbf{G})|^2}{\hbar^2 v_F^2 |\mathbf{G}|^2} \sin^2 \theta_{\mathbf{k},\mathbf{G}} \,, \tag{A.11}$$

where $\mathbf{G}$ and $U(\mathbf{G})$ are the reciprocal lattice vectors and the corresponding Fourier component of the external potential and $\theta_{\mathbf{k},\mathbf{G}}$ is the angle between $\mathbf{G}$ and $\mathbf{k}$. Using the same approximation as in the previous subsection the conductivity in the $\hat{x}$-direction takes the form

$$\sigma_{xx} = \sigma_0 \frac{\hbar^2 v_F^2 - \sum_{\mathbf{G}\neq 0} 2|U(\mathbf{G})|^2 \frac{G_y^2}{|\mathbf{G}|^4}}{\hbar^2 v_F^2 - \sum_{\mathbf{G}\neq 0} 2|U(\mathbf{G})|^2 \frac{G_x^2}{|\mathbf{G}|^4}} \,. \tag{A.12}$$

The conductivity in the $\hat{y}$-direction is obtained by interchanging G_x and G_y in this expression. The expression Equation A.11 has been obtained in second order perturbation

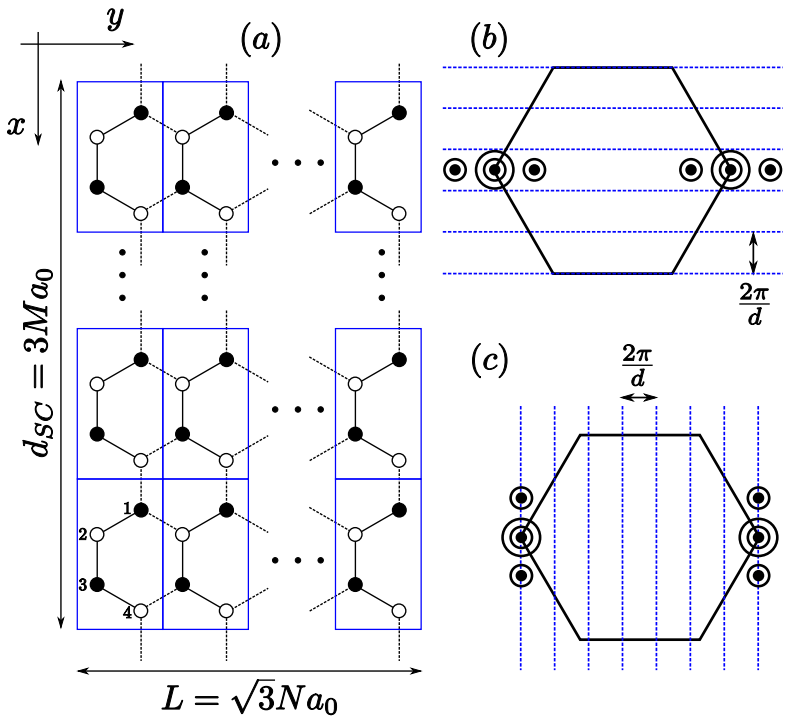

FIGURE A.2: (*a*): Schematic representation of the superlattice used in the tight-binding calculations showing the axis selection. The system is infinite along the x-direction and has a finite length $L = \sqrt{3}Na_0$ along the y-direction. The superlattice has a vertical period $d_{SC} = 3Ma_0$ in which periodic boundary conditions are imposed. We include a sketch of the Brillouin zone with the same axis selection for a potential applied along the x-direction (*b*) and the y-direction (*c*). The length of the reduced Brillouin zone ($2\pi/d_{SC}$) is indicated. The splitting of the Dirac points is also sketched. Note that the new Dirac points always move perpendicularly to the direction of the potential.

theory and it is a good approximation provided that the superlattice potential does not induce new Dirac points. We expect that Equation A.12 will be valid in the same regime.

A.3 Numerical calculations.

In order to compute numerically the transport properties we describe the electronic states of a defect free graphene layer using the tight-binding approximation,

$$\hat{H} = -t_g \sum_{<ij>} \hat{c}_i^\dagger \hat{c}_j + \sum_i V_i \hat{c}_i^\dagger \hat{c}_i \ , \tag{A.13}$$

where $t_g = 2\hbar v_F/3a_0$ denotes the hopping element between nearest carbon atoms on the hexagonal lattice, a_0 is the smallest carbon-carbon distance and V_i is the potential applied to the lattice. The spin degree of freedom has been omitted due to degeneracy.

In order to analyze the different transport situations depicted in Figure A.1 we assume that the central region is a strip with armchair edges along the $\hat{x}$-direction as depicted in Figure A.2. The strip is constructed by repeating a unit cell composed of four atoms N times along the $\hat{y}$-direction and M times along the $\hat{x}$-direction. Thus, the length of the graphene layer is $L = N\sqrt{3}a_0$. For describing the $W \gg L$ limit we impose periodic boundary conditions in the transversal direction $\hat{x}$ and define $q \in [-\pi/d_{SC}, \pi/d_{SC}]$ as the corresponding wave vector, with $d_{SC} = 3Ma_0$ being the vertical length of the supercell.

We connect the armchair edges of the nanoribbon to heavily doped graphene leads, maintaining the graphene sublattice structure at the edges and thus representing the experimental situation in which the electrodes are deposited on top of the graphene layer [82, 87, 95–97]. The corresponding self-energies on the graphene sites at the layer edges are approximated by a $4M \times 4M$ matrix with elements $\Gamma^{L,R}_{ij,\alpha\beta} = \delta_{ij}\gamma^{L,R}_{\alpha\beta}$, where $\alpha, \beta = 1, \ldots, 4$ label the atomic sites within the unit cell and $i, j = 1, \ldots, M$ label the unit cells in the superlattice. Following the geometry depicted in Figure A.2, the elements of the self-energy matrix are explicitly defined as $\gamma^L_{22} = \gamma^L_{33} = \gamma^R_{11} = \gamma^R_{44} = i\sqrt{3}/2$ and $\gamma^L_{23} = \gamma^L_{32} = \gamma^R_{14} = \gamma^R_{41} = -1/2$ [82]. Thus, we calculate the transmission at zero energy, $T(q)$, as

$$T(q) = 4\mathrm{Tr}\left[\hat{\Gamma}_L \hat{G}^r_{LR}(E=0,q)\hat{\Gamma}_R \hat{G}^a_{RL}(E=0,q)\right], \tag{A.14}$$

where $\hat{G}^{r,a}_{LR,RL}(E,q)$ are the $4M \times 4M$ retarded and advanced Green functions between the edges of the layer. Furthermore, for analyzing the transmission distribution it is useful to determine the eigenvalues $\tau_\alpha(q)$ of the transmission matrix $\hat{t}^\dagger\hat{t}$, where $\hat{t} = 2\sqrt{\hat{\Gamma}_L}\hat{G}^r_{LR}(E,q)\sqrt{\hat{\Gamma}_R}$. From these eigenvalues one can determine the probability distribution $P(\tau) = \sum_{\alpha,q}\delta(\tau - \tau_\alpha(q))$ and the Fano factor

$$F = \frac{\sum_{\alpha=1}^{4M}\sum_q \tau_\alpha(q)\left(1-\tau_\alpha(q)\right)}{\sum_{\alpha=1}^{4M}\sum_q \tau_\alpha(q)}. \tag{A.15}$$

By integrating the transmission, the conductance is given by $G = (4e^2/\hbar)\int \mathrm{d}q\mathrm{Tr}\left[\hat{t}\hat{t}^\dagger\right]$, where both the spin and valley degeneracies have been taken into account. The resulting conductivity, within the limit $W \gg L$, is obtained by multiplying by the geometrical factor L.

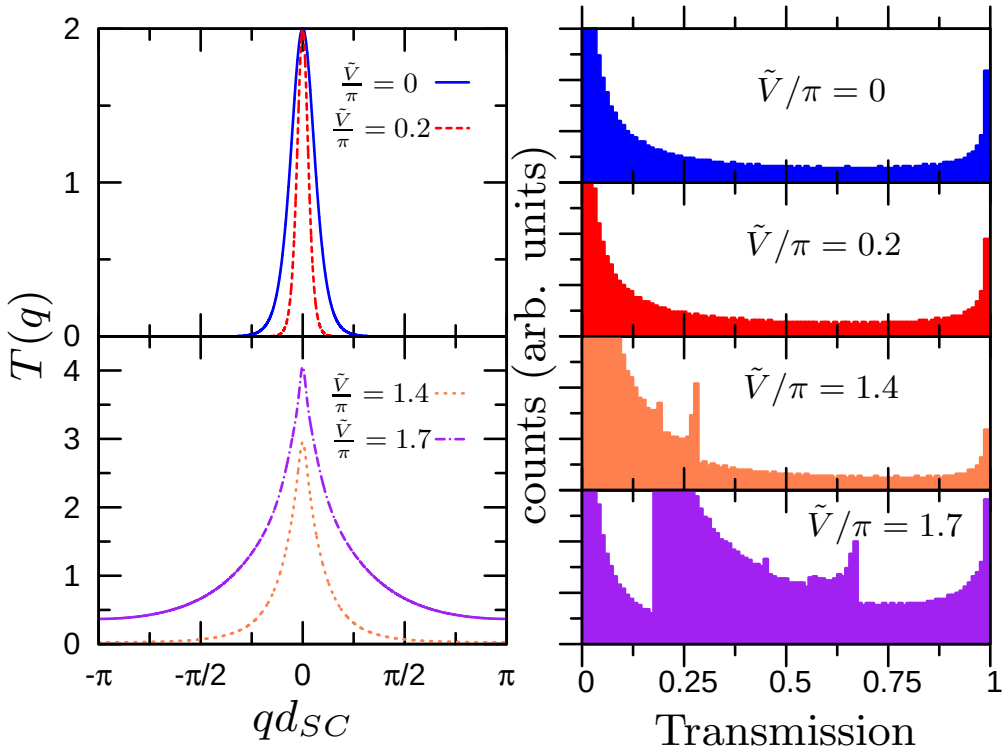

FIGURE A.3: For a potential along the x-direction as depicted in Figure A.1(a), in the left panels we plot the transmission $T(q)$ per spin channel as a function of qd_{SC} for a superlattice of period $d = 42a_0$ and amplitudes $\tilde{V} = \frac{V_0 d}{2\hbar v_F} < \pi$ (top left panel) and for a period $d = 54a_0$ and amplitudes $\tilde{V} > \pi$ (bottom left panel). Note that for this orientation of the potential $d = d_{SC}$. In the right panels we plot the distribution of the eigenvalues of the transmission matrix for the different values of $\tilde{V}$. The length of the stripe is $L = 100\sqrt{3}a_0$.

A.3.1 Transport parallel to the superlattice barriers.

For studying the transport parallel to the superlattice, we consider a periodic one-dimensional potential along the $\hat{x}$-direction within the previous geometry as is schematically depicted in Figure A.1(a). The one-dimensional superlattice potential, V_i, has the piecewise constant form,

$$V_i = \begin{cases} V_0 & , \quad 0 \leq x_i \leq \frac{d}{2} \\ -V_0 & , \quad \frac{d}{2} < x_i \leq d \end{cases} , \tag{A.16}$$

where $d = d_{SC} = 3Ma_0$ is the period of the potential.

In Figure A.3 we plot the transmission $T(q)$ as function of the product qd for a superlattice of period $d = 42a_0$ and amplitudes $V_0 d = 0$ and $V_0 d = 1.4\hbar v_F$ in the top left panel and for a period $d = 54a_0$ and amplitudes $V_0 d = 8.6\hbar v_F$ and $V_0 d = 10.8\hbar v_F$ in the bottom left panel. The horizontal length of the graphene layer is $L = 100\sqrt{3}a_0$.

We also plot in the right panels of Figure A.3 the distribution of the eigenvalues of the transmission matrix.

In Figure A.4 we plot, as function of $V_0 d$, the conductivity and the Fano factor obtained for a system of length $L{=}100\sqrt{3}a_0$ and for different values of the superlattice period, d.

We first discuss the case of potential barriers in the range $V_0 < V_c = \frac{2\pi\hbar v_F}{d}$ [top panels of Figure A.3]. For these superlattices the original Dirac points are the only active transport channels. As a function of q the transmission is peaked at $q{=}0$, and the width of the peak diminishes when $V_0 d$ increases. The transmission fits very well to the functional form [see Equation A.9] $T(q) = 2/\cosh^2(\frac{\tilde{V}}{|\sin\tilde{V}|}qL)$, where the factor 2 accounts for the valley degeneracy and $\tilde{V} = \frac{V_0 d}{2\hbar v_F}$. The corresponding distribution of the eigenvalues of the transmission matrix has the form $P(\tau) \sim 1/\left(\tau\sqrt{1-\tau}\right)$ indicating the pseudo-diffusive character of the transport in this range of potentials. The conductivity obtained by integrating the transmission is well-defined and, in this range of $V_0 d$, has the form $\sigma_{\parallel}^0 = \sigma_0 \frac{|\sin(\tilde{V})|}{\tilde{V}}$ [see Figure A.4]. The Fano factor in this range of potentials is 1/3 in agreement with the pseudo-diffusive character of transport. We thus conclude that in the range of parameters $V_0 d < 2\pi\hbar v_F$ the transport is pseudo-diffusive, the conductivity only depends on the product $V_0 d$ and has the form $\sigma_{\parallel}^0 = \sigma_0 \frac{|\sin(\tilde{V})|}{\tilde{V}}$.

For normalized barrier heights $V_0 d$ larger than $2\pi\hbar v_F$ two new Dirac points per valley appear [152, 153]. These new Dirac points are new transmission channels in the system, that for transport parallel to the superlattice barriers are superimposed in reciprocal space upon the original Dirac points. The resultant transmission exhibits a wider distribution in reciprocal space [see bottom left panel of Figure A.3]. The width of the transmission can reach the edges of the reduced Brillouin zone $\pm\pi/d$ for small values of L/d. The corresponding distribution of the eigenvalues of the transmission matrix is a superposition of the distribution of each mode, and the corresponding Fano factor is different than 1/3. The conductivity should be independent on the system size. We find that the value of L where the conductivity is well defined depends on d and coincides with the value of L in which the transmission is non zero at the edges of the reduced Brillouin zone. In Figure A.4 we see that the general trend of the conductivity for values of $V_0 d$ larger than $2\pi\hbar v_F$ is qualitatively described by the continuum model, Equation A.8. However the analytical model neglects some effects such as the coupling between the modes or the deviation from linear dispersion, so that in this range of superlattice parameters the conductivity depends separately on V_0 and d. The coupling between the modes also leads to a Fano factor with a value larger than 1/3, and the transport is not pseudo-diffusive.

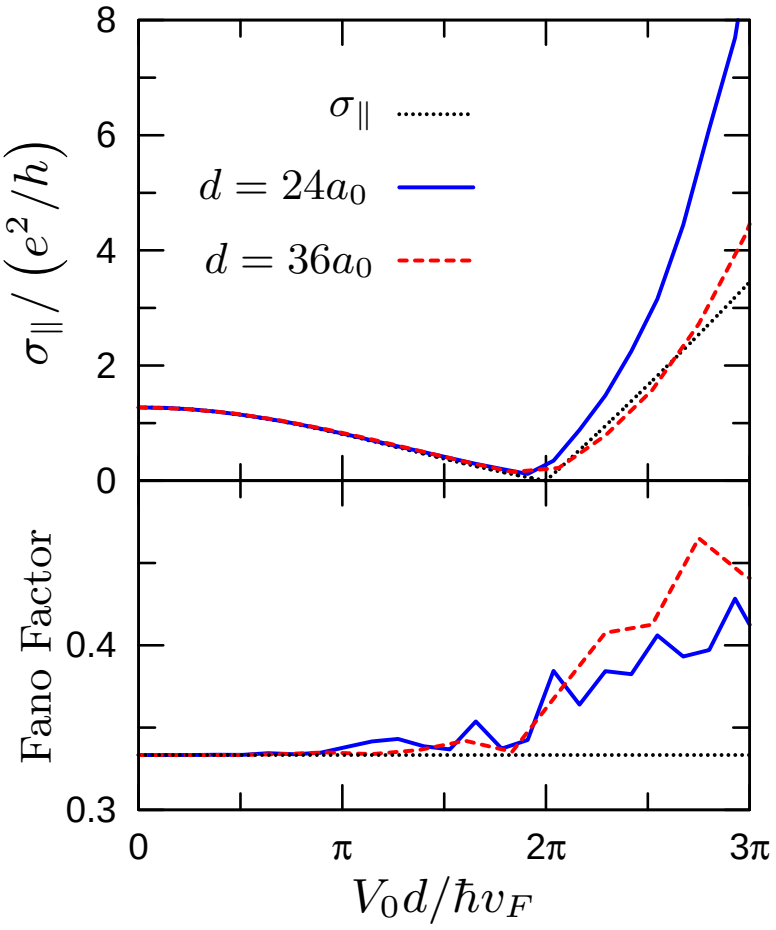

FIGURE A.4: Transport parallel to the superlattice barriers. Top (bottom) panel shows the conductivity (Fano factor) for a graphene sheet with $L = 500\sqrt{3}a_0$ and superlattice period $d = 24a_0$ (solid blue line) and $L = 200\sqrt{3}a_0$ and superlattice period $d = 36a_0$ (dashed red line) as a function of the normalized barrier height $V_0 d$. Dotted line corresponds to the conductivity obtained in the continuum model assuming independent transport channels, Equation A.8, in the top panel and to the pseudo-diffusive value $F = 1/3$ in the bottom panel.

A.3.2 Transport perpendicular to the superlattice barriers.

In this section we consider a potential in the $\hat{y}$-direction and study the transport in the same direction, i.e. perpendicular to the superlattice barriers [see Figure A.1(b)]. Following the same geometry as in the previous section (see details in Figure A.2), we define a one-dimensional piecewise potential along the $\hat{y}$-direction as

$$V_i = \begin{cases} V_0 & , \quad 0 \leq y_i \leq \frac{d}{2} \\ -V_0 & , \quad \frac{d}{2} < y_i \leq d \end{cases} , \tag{A.17}$$

where $d = 2n\sqrt{3}a_0$ is the period of the potential.

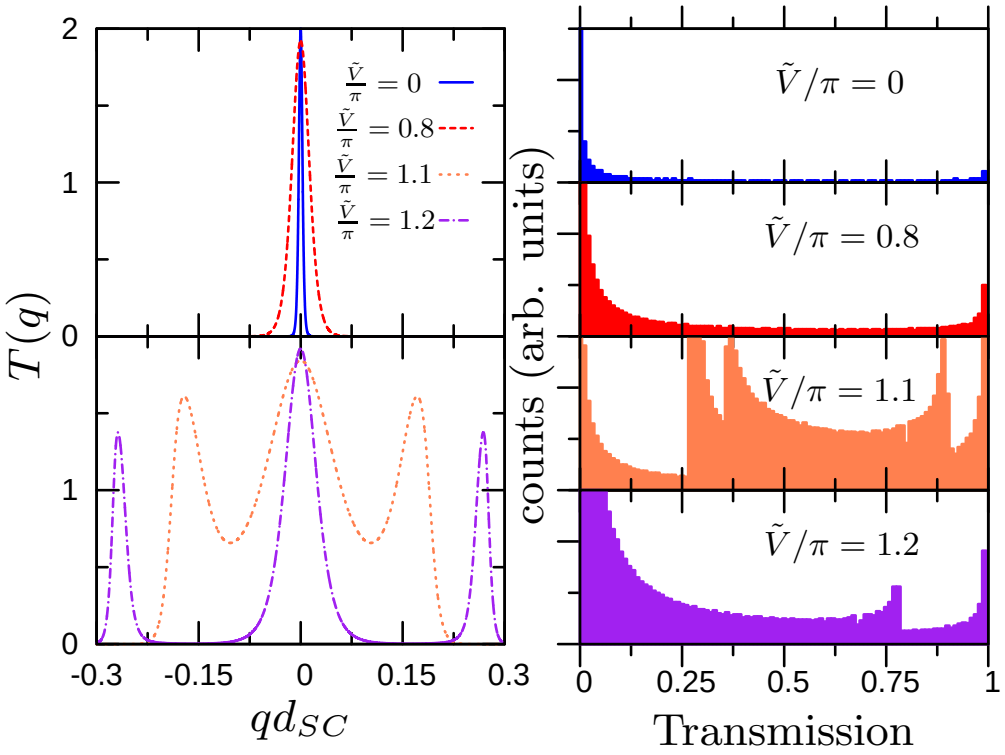

FIGURE A.5: For a potential along the y-direction as depicted in Figure A.1(b), in the left panels we plot the transmission $T(q)$ per spin channel as function of qd_{SC} for a superlattice potential of period $d = 38.1a_0$ and normalized amplitudes $\tilde{V} = \frac{V_0 d}{2\hbar v_F} < \pi$ (top left panel) and $\tilde{V} > \pi$ (bottom left panel). In the right panels we plot the distribution of the eigenvalues of the transmission matrix for the different values of $\tilde{V}$. The length of the stripe is $L = 500\sqrt{3}a_0$.

In the left column of Figure A.5 we plot the transmission $T(q)$ as a function of qd_{SC} for a superlattice with period $d = 38.1a_0$ and amplitudes $V_0 d = 0$, $V_0 d = 5\hbar v_F$ (top left panel), $V_0 d = 6.6\hbar v_F$ and $V_0 d = 7.2\hbar v_F$ (bottom left panel). The horizontal length of the graphene strip is $L = 500\sqrt{3}a_0$. In the right column of Figure A.5 we plot the corresponding distribution of the eigenvalues of the transmission matrix.

In the top panel of Figure A.6 we show, as function of $V_0 d$, the conductivity for horizontal periods of $d = 34.6a_0$ and $d = 76.2a_0$, for a graphene sheet of length L=$500\sqrt{3}a_0$. In the bottom panel of Figure A.6 we plot the Fano factor for the same two values of the period of the superlattice.

In the range of potential barriers before the creation of new Dirac points, i.e. $V_0 < V_c$, the behavior of the transmission is exactly the inverse of the previous case. The contribution to the transmission from each valley is superimposed as a sharp peak at $q = 0$. However, contrary to the previous result, the width of the peak increases with the product $V_0 d$. Following Equation A.9, the transmission is fitted to $T(q) = 2/\cosh^2(\frac{|\sin\tilde{V}|}{\tilde{V}} qL)$. Subsequently, the distribution of the eigenvalues is that of pseudo-diffusive transport.

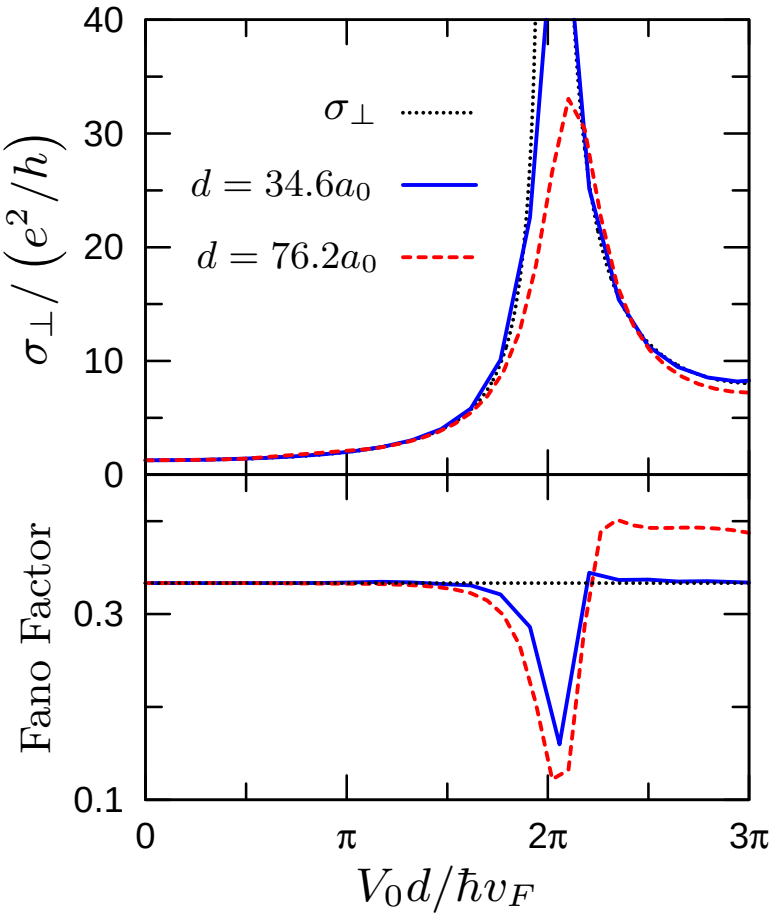

FIGURE A.6: Transport perpendicular to the superlattice barriers. Top (bottom) panel shows the conductivity (Fano factor) for a graphene sheet with $L = 500\sqrt{3}a_0$ and superlattice periods $d = 34.6a_0$ (solid blue line) $d = 74.2a_0$ (dashed red line) as a function of the normalized barrier height $V_0 d$. Dotted line corresponds to the conductivity obtained in the continuous model assuming independent transport channels, Equation A.8, in the top panel and to the pseudo-diffusive value $F = 1/3$ in the bottom panel.

On the other hand, when $V_0 > 2\pi\hbar v_F$, a pair of Dirac points is created for each valley. In the bottom panel of Figure A.5 we show how these new peaks split from the original ones until there are three almost independent contributions to the transmission. In this later case the distribution of eigenvalues for each mode returns to a form of the type $P(\tau) \sim 1/\left(\tau\sqrt{1-\tau}\right)$, indicative of pseudo-diffusive behavior. Before the new Dirac points are completely separated from the original ones, the coupling between modes produces a deviation from the pseudo-diffusive transport.

The behavior of the conductivity perpendicular to the barriers is completely different than the parallel case. The perpendicular conductivity presents peaks at the values of the normalized potential height where new Dirac points appear. The numerical calculated conductivity agrees very well with the analytical one, Equation A.8, even for values of $V_0 d > 2\pi\hbar v_F$. The Fano factor has the value 1/3 for all values of $V_0 d$ except near the

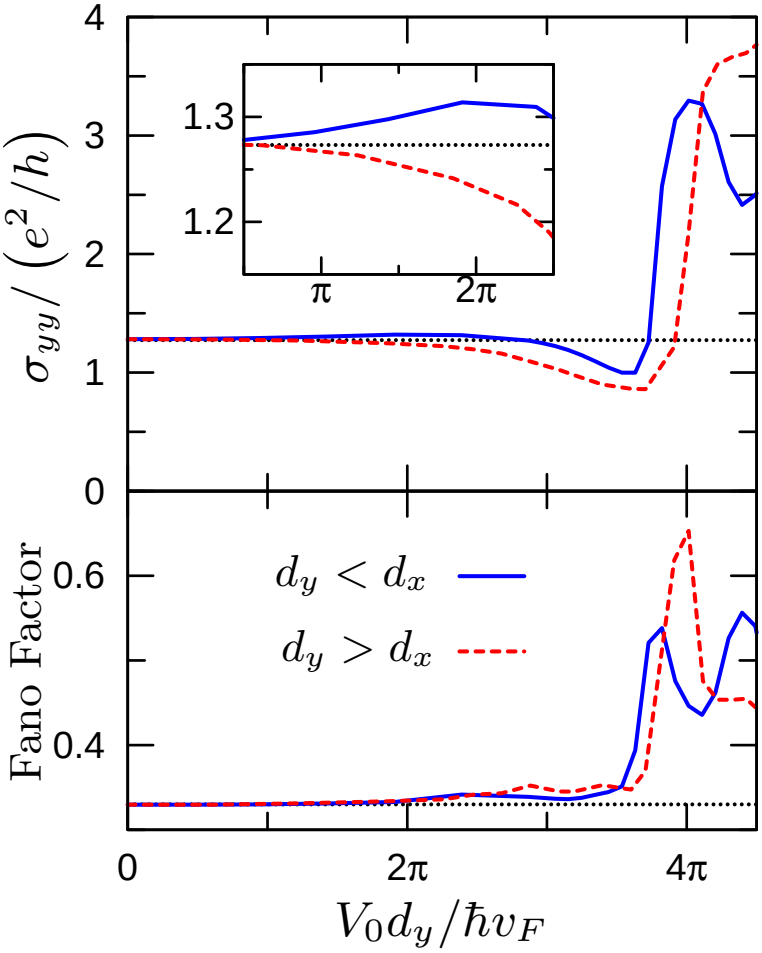

FIGURE A.7: In the top (bottom) panel we plot the conductivity (Fano factor) as a function of the normalized barrier height $V_0 d_y$ for a graphene sheet in presence of a two dimensional superlattice with a fixed vertical period of $d_x = 48a_0$ and different horizontal periods $d_y = 45a_0$ (blue solid line) and $d_y = 48.5a_0$ (red dashed line). The dotted line corresponds to the conductivity of pristine graphene (σ_0) in the top panel and to the pseudo-diffusive limit (1/3) in the bottom panel. The length of the graphene sheet is $L = 200\sqrt{3}a_0$. Inset: the conductivity as a function of the normalized barrier height in the proximity of the critical potential V_c in which a new pair of Dirac points is created.

values of $V_0 d$ for which new Dirac appears. This indicates that, in this geometry, the Dirac points are weakly coupled and the approach of Section A.2 for the conductivity is appropriate.

A.3.3 Transport in a two dimensional superlattice

One of the more striking results presented in Section A.2 is that the conductivity of graphene in the presence of a symmetric two dimensional superlattice potential is $\frac{4}{\pi}\frac{e^2}{\hbar}$ independent of the period and the height of the potential barriers. In order to check

this result we have built a chessboard-like potential combining piecewise potentials in the $\hat{x}$, Equation A.16, and $\hat{y}$, Equation A.17, directions in a way in which a potential barrier is always followed by a well along each direction (see Figure A.1(c)). The length of the period in the $\hat{x}$ and $\hat{y}$ directions is d_x and d_y respectively. Because the underlying triangular lattice of graphene, the period in both directions cannot be exactly equal.

The top panel of Figure A.7 shows the conductivity as a function of the potential height V_0 for a graphene layer with $L = 200\sqrt{3}a_0$ and a fixed vertical period of $d_x = 48a_0$. We plot the conductivity for two different horizontal periods $d_y = 45a_0$ and $d_y = 48.5a_0$. We compare these results with the isotropic conductivity of graphene $\sigma_0 = \frac{4}{\pi}\frac{e^2}{h}$.

A remarkable result is that the conductivity in this potential remains almost constant in the range $V_0 \gtrsim V_c$ where a new pair of Dirac points is created in the previously studied cases. Thus, in this range of potential barriers, Equation A.12 obtained in second order perturbation theory remains a good approximation according to the tight-binding results. Furthermore, the pseudo-diffusive behavior of transport is maintained for a large range of the potential barriers. In the bottom panel of Figure A.7 we show how the Fano factor is stable around the pseudo-diffusive value of 1/3 while $V_0 d_y \lesssim 4\pi\hbar v_F$. When $V_0 d_y \sim 4\pi\hbar v_F$, which for the previous potentials corresponded to the creation of the second pair of Dirac points, the conductivity deviates from σ_0, the Fano factor increases and transport is no longer pseudo-diffusive. The approximation of weakly coupled Dirac points is then no longer applicable.

The small deviations from the conductivity of pristine graphene that occurs when $V_0 d_y \sim 2\pi\hbar v_F$ can be more clearly appreciated in the inset of Figure A.7. Due to the geometry of the graphene layer, the period in both directions is never exactly the same. This affects the validity of Equation A.12 to a small degree. When $d_y \lesssim d_x$ the conductivity slightly increases from σ_0, presenting a positive slope, while if $d_y \gtrsim d_x$ the effect is the opposite. When the difference between both periods becomes larger the conductivity continuously evolves into the corresponding case of the previous sections (Figure A.4 and Figure A.6).

A.4 Conclusions

Superlattice potentials generically induce anisotropy in the dispersions near the Dirac points in graphene, and under certain circumstances may induce extra Dirac points at zero energy. In this work we demonstrated that when the Fermi energy passes through a spectrum with a single anisotropic Dirac point, the resulting conductivity can be

expressed in a very simple way in terms of the velocities along the two principle directions of the anisotropy, and the conductivity for the corresponding isotropic Dirac point. The result can be generalized to the case of several Dirac points when they are sufficiently separated in momentum space so that a conductivity expressed as a sum over those of independent Dirac points is sensible. For a two-dimensional superlattice which induces little anisotropy in the spectrum, a remarkable result is that the conductivity is essentially unchanged from the result for pristine graphene, even if the velocity renormalization is quite large.

Numerical tight-binding calculations generally confirm this simple picture. In particular one finds the conductivity parallel and perpendicular to the superlattice barriers for a one-dimensional potential evolve in opposite directions with increasing $V_0 d$, and that for a spectrum in which no new Dirac points have been generated there is quantitative agreement with the simple analytical model. As new Dirac points are introduced into the spectrum one finds dips in $\sigma_{\parallel}$ and peaks in $\sigma_{\perp}$ as expected, although the results are less quantitatively described by the continuum model, presumably because the wave functions cannot be uniquely associated with single Dirac points. Deviations of the Fano factor from pseudo-diffusive behavior confirm this interpretation.

These studies suggest that more complicated potentials could also yield behaviors in the conductance with simple interpretations. For example, a modulated superlattice potential yields a Landau level spectrum [155], for which $\sigma_{\parallel}$ may have behavior reminiscent of edge state transport. It is also interesting to speculate that for isotropic superlattice potentials, one may sufficiently slow the electron velocity so that electron-electron interaction effects become important [169, 170]. We leave these questions as well as the possible effect of temperature and disorder for future research.

Finally, the two-dimensional superlattice potential is suitable to be used to simulate disorder in a graphene sample. Indeed, the effect of charge puddles in graphene can be simulated by defining an area of dimensions $d_x d_y$ in which the potential takes a random value V_0. This technique is used in Section 4.4 and in Section 5.2 to study the effect of disorder.

Appendix B

Scattering amplitudes at the graphene-superconductor interface.

We consider a normal-superconductor interface along the y-direction in a graphene sheet, with the normal region extended at $x < 0$. An incoming electron into the interface from the normal region can be reflected as an electron or a hole with probability amplitudes r_{ee} and r_{eh} respectively or it can be transmitted into the superconducting region as an electron-like or a hole-like quasiparticle, with probability amplitudes t_{ee} and t_{eh} respectively. The scattering states in both regions are

$$\psi^L(x) = e^{ik_e^L x}\begin{pmatrix}\varphi_{1e}^L\\0\end{pmatrix} + r_{ee}e^{-ik_e^L x}\begin{pmatrix}\varphi_{2e}^L\\0\end{pmatrix} + r_{eh}e^{ik_h^L x}\begin{pmatrix}0\\\varphi_{1h}^L\end{pmatrix}, \tag{B.1}$$

$$\psi^S(x) = t_{ee}e^{ik_e^S x}\begin{pmatrix}u\varphi_{1e}^S\\v\varphi_{1e}^S\end{pmatrix} + t_{eh}e^{-ik_h^S x}\begin{pmatrix}v\varphi_{2h}^S\\u\varphi_{2h}^S\end{pmatrix}, \tag{B.2}$$

where the dependence on y has been omitted because the vertical momentum q is conserved. Following the notation explained in Ref. [83], we have defined the bispinors in sublattice space $\varphi_{1e,1h}^T = (1, e_{e,h}^{\pm i\alpha})$, $\varphi_{2e,2h}^T = (1, -e^{\mp i\alpha_{e,h}})$ and the BCS coherence factors $u^2(v^2) = (E \pm \Omega)/2\Delta$, which are normalized so that $|u|^2 + |v|^2 = 1$. We are interested in the heavily doped regime with $|E_F^L| = |E_F^S| \equiv E_F \gg \Delta, E$, which satisfies the mean-field approach for superconductivity. In this regime $k_{e,h}^L \approx k_{e,h}^S$ and $k_e^{L,S} = k_h^{L,S}$. The angles at each region are thus defined as $\alpha_e^L = \alpha_h^L = \phi$ and $\alpha_e^S = \alpha_h^S = s\phi$ with $\phi = \arcsin \hbar v_F/E_F$ and $s = \text{sign}(E_F^L)\text{sign}(E_F^S)$, which is positive when there is no change in the doping level at the interface and negative otherwise (i.e. for a *np* or a *pn* junction). Matching the scattering states at the interface it is straightforward to obtain the

reflection and transmission amplitudes (a detailed description is given in Ref. [58]), in the energy regime of this work they reduce to

$$r_{ee} = \frac{(e^{i\phi}+e^{is\phi})(e^{-i\phi}+e^{-is\phi})}{e^{-2i\phi}+e^{-2is\phi}}, \tag{B.3}$$

$$r_{eh} = \frac{-2i\cos\phi e^{-is\phi}}{e^{-2i\phi}+e^{-2is\phi}}, \tag{B.4}$$

$$t_{ee} = (1-i)\cos\phi\frac{e^{-i\phi}+e^{-is\phi}}{e^{-2i\phi}+e^{-2is\phi}}, \tag{B.5}$$

$$t_{eh} = -(1+i)\cos\phi\frac{e^{-i\phi}-e^{-is\phi}}{e^{-2i\phi}+e^{-2is\phi}}. \tag{B.6}$$

When the NS interface is equivalent to a perfectly transparent symmetric *nn* junction the incoming electron is transmitted into the superconductor only as an electron-like quasiparticle since $s=1$ and thus $t_{eh}=0$.

On the other hand, we can analogously examine the reflection and transmission amplitudes of an incoming electron-like excitation from the superconductor into the rightmost normal region. The scattering states are thus

$$\psi^S(x) = e^{ik_e^S x}\begin{pmatrix} u\varphi_{1e}^S \\ v\varphi_{1e}^S \end{pmatrix} + r'_{ee}e^{-ik_e^S x}\begin{pmatrix} u\varphi_{2e}^S \\ v\varphi_{2e}^S \end{pmatrix} + r'_{eh}e^{ik_h^S x}\begin{pmatrix} v\varphi_{1h}^S \\ u\varphi_{1h}^S \end{pmatrix}, \tag{B.7}$$

$$\psi^R(x) = t'_{ee}e^{ik_e^R x}\begin{pmatrix} \varphi_{1e}^R \\ 0 \end{pmatrix} + t'_{eh}e^{-ik_h^R x}\begin{pmatrix} 0 \\ \varphi_{2h}^R \end{pmatrix}. \tag{B.8}$$

The resulting amplitudes, in the energy regime used are

$$r'_{ee} = \frac{1-e^{2i\phi}}{e^{-2i\phi}+e^{-2is\phi}}, \tag{B.9}$$

$$r'_{eh} = ie^{i\phi}\frac{(e^{is\phi}+e^{-is\phi})}{e^{-2i\phi}+e^{-2is\phi}}, \tag{B.10}$$

$$t'_{ee} = \frac{(1+i)}{2}\frac{1+e^{-2is\phi}+e^{i\phi}(e^{is\phi}+e^{-is\phi})}{e^{-2i\phi}+e^{-2is\phi}}, \tag{B.11}$$

$$t'_{eh} = \frac{(1-i)}{2}\frac{1+e^{2is\phi}-e^{i\phi}(e^{is\phi}+e^{-is\phi})}{e^{-2i\phi}+e^{-2is\phi}}. \tag{B.12}$$

The incoming electron-like excitation can be reflected inside the superconductor both preserving and changing the particle type. The former is a specular reflection with a change of sign in both components of the velocity while the latter is a retro-reflection in which the new excitation follows back the path of the incident one. Equivalent results are obtained for an incoming hole-like excitation. As in the previous case, for a *nn* junction ($s=1$) there is only transmission into the normal region preserving the particle type since $t'_{eh}=0$.

To summarize, for a *pnp* junction the incident electron from the normal region L splits into electron and hole-like excitations inside the superconductor and this splitting determines the focusing points of each type on the normal region R. On the other hand, for a *nnp* junction only electron-like excitations are created inside the superconductor and thus there is only focusing of electrons in region R. This condition can be relaxed if the transparency of the interface is not perfect or if the junction is not symmetric (i.e. $|E_F^N| \neq |E_F^S|$).

The dependence on the transparency of the interface is studied in Ref. [57] and Ref. [58]. In the limit of interest for this work we obtain the following expression for the creation of hole-like excitations inside the superconductor

$$\begin{aligned} t_{eh} &= -2(1+i)\frac{\cos\theta e^{i\theta}}{d}\left\{\cos\chi(1-e^{i(1+s)\theta}) + i\sin\chi(1-e^{is\theta})\right\}, \qquad \text{(B.13)} \\ d &= (1+\cos\chi)(1+e^{2i(1+s)\theta}) + (1-\cos\chi)e^{2is\theta} + 2e^{2i\theta}(1-\cos^2\chi), \\ t'_{eh} &= \frac{1-i}{d'}\left\{\cos\chi(1-e^{i(1+s)\theta})(1+e^{2is\theta}) + i\sin\chi(1+e^{-2is\theta})(e^{is\theta}-e^{i\theta})\right\}, \qquad \text{(B.14)} \\ d' &= \cos^2\chi(1+e^{2i(1+s)\theta}) - \sin^2\chi e^{2i\theta}, \end{aligned}$$

where $\chi = E_F^I d/\hbar v_F$. The height and width of the barrier are E_F^I and d respectively. We have used the limit of thin barrier taking $E_F^I \to \infty$ and $d \to 0$ such that χ remains constant. The perfect transparency or absence of barrier is recovered when $\chi = n\pi$ for any integer n. Subsequently, when the barrier is not perfectly transparent the transmissions are modified resulting in the possibility of having $t'_{eh} \neq 0$ in a *nn* junction. The price to pay is a reduction of the transmission amplitudes.

Appendix C

Green functions techniques applied to carbon nanotubes.

We include in this Appendix a brief description on how to adapt the Green functions techniques for graphene samples developed in Chapter 3 to carbon nanotubes. We also provide some details on the calculation of the self-energy between the dots and the central superconducting region.

Analogously to the case of graphene, low-energy excitations on carbon nanotubes can be described by a Dirac-Weyl equation [5]. Following Ref. [130] and [129], the normal state effective Hamiltonian corresponding to a quantized momenta q_n around the tube is $H^e_{\tau,s} = -i\hbar v_F \partial_x \cdot \sigma_x + \tau\hbar v_F q_n \sigma_y + \tau\delta_0 s - \tau\delta_1 s\sigma_y + V(x)$. The first two terms form the usual Dirac Hamiltonian while the diagonal terms in δ_0 and δ_1 take into account the spin-orbit (SO) interaction, with $\tau, s = \pm 1$ corresponding to the valley and spin indexes, respectively.

The Bogoliubov-de Gennes-Dirac equations for a superconducting single-walled carbon nanotube (SWCNT) of width W and radius R are written in Nambu space as

$$\begin{pmatrix} H^e_{\tau,s} - E_F & \Delta(x) \\ \Delta(x) & E_F - H^e_{\tau,s} \end{pmatrix} \begin{pmatrix} u_{\tau,s} \\ v_{\tau,s} \end{pmatrix} = E_{\tau,s} \begin{pmatrix} u_{\tau,s} \\ v_{\tau,s} \end{pmatrix} \tag{C.1}$$

Considering that the induced superconducting pairing amplitude $\Delta(x) = \Delta_i$ is uniformly extended along the whole tube, we can apply the method of Chapter 3 to obtain the Green function of the isolated finite superconducting SWCN. Thus, we write the

asymptotic solutions of Equation C.1 as

$$\phi_{<}^{e(h)}(x) = \left\{ e^{\mp ik_{\pm}x}\varphi_{2e(1h)} + r_L^{A,\pm} e^{\pm ik_{\pm}x}\varphi_{1e(2h)} \right\} \otimes \begin{pmatrix} u(v) \\ v(u) \end{pmatrix} \tag{C.2}$$

$$\phi_{>}^{e(h)}(x) = \left\{ e^{\pm ik_{\pm}x}\varphi_{1e(2h)} + r_R^{B,\pm} e^{\pm ik_{\pm}x}\varphi_{1e(2h)} \right\} \otimes \begin{pmatrix} u(v) \\ v(u) \end{pmatrix}, \tag{C.3}$$

where $k_{\pm} = \sqrt{(E_F \pm \Omega)^2/\hbar^2 v_F^2 - q^2}$, with $\Omega = \sqrt{E^2 - \Delta_i^2}$; and the bispinors in sublattice space are $\varphi_{1e,1h}^T = (e^{\mp i\alpha_{\pm}}, e^{\pm i\alpha_{\pm}})$ and $\varphi_{2e,2h}^T = (e^{\pm i\alpha_{\pm}}, -e^{\mp i\alpha_{\pm}})$, with $e^{i\alpha_{\pm}} = (k_{\pm} + iq)/\sqrt{k_{\pm}^2 + q_0^2}$. The reflection amplitude at the left (right) edge formed with atoms that belong to sublattice A (B) is $r_L^{A,\pm} = -e^{\pm i\alpha_{\pm}}$ ($r_R^{B,\pm} = e^{\pm i\alpha_{\pm}} e^{\pm 2ik_{\pm}W}$) and $u^2(v^2) = (1 \pm \sqrt{E^2 - \Delta^2}/E)/2$ are the BCS coherence factors.

The four-dimensional spinors $\Phi_{>}^{e(h)}(x,y) = e^{iqy}\phi_{>}^{e(h)}(x)$ and $\Phi_{<}^{e(h)}(x,y) = e^{iqy}\phi_{<}^{e(h)}(x)$ in Nambu and sublattice space represent an electron-like (hole-like) excitation moving in the positive and negative horizontal direction that are reflected at the edges.

C.1 Self-energy describing the coupling with the superconducting electrode.

In order to obtain the propagator for the finite nanotube region we combine the asymptotic solutions of Equation C.3 following the method described in Chapter 3. This results in

$$g_{S,\mu\nu} = \left(\frac{F_{\mu\nu}^1}{\Omega}(E + \sigma_x \Delta_i) + \sigma_z F_{\mu\nu}^2 \right), \tag{C.4}$$

where the indexes $\mu, \nu = L, R$ denote the two edges of this region and σ_x, σ_z are the Pauli matrices in Nambu space. The functions $F_{\mu\nu}^{1,2}$ depend on the width of the superconducting region W and are of the form

$$F_{LR}^{1,2} = F_{RL}^{1,2} = \frac{\cos\alpha_-}{2\cos(k_-W + \alpha_-)} \mp \frac{\cos\alpha_+}{2\cos(k_+W + \alpha_+)}, \tag{C.5}$$

$$F_{LL}^{1,2} = F_{RR}^{1,2} = \frac{i\sin k_-W}{2\cos(k_-W + \alpha_-)} \mp \frac{i\sin k_+W}{2\cos(k_+W + \alpha_+)}. \tag{C.6}$$

An equivalent expression to Equation C.4 is obtained for a normal finite SWCN in the limit $\Delta_i = 0$. This finite normal region can be coupled to a normal electrode on one edge, leaving the other edge free to be coupled to the superconducting region. The resulting system is shown in Figure 6.1. To study the transport properties of this system in the double quantum dot regime we are only interested in the contributions

due to a single level on each normal region, dubbed $\mu = L, R$. The normal finite tube, including the coupling with the macroscopic electrode on one edge, can be described by the retarded Green function projected to the other edge, i.e. $g_{\mu}^{(0)} = A_{\mu}(E - \epsilon_{\mu} - i\tilde{\Gamma}_{\mu})^{-1}$. This approximation is valid around one of the resonances of the normal tube, with $\tilde{\Gamma}_{\mu} = \Gamma_{\mu} a_0 / W_{\mu}$ being the effective tunneling rate to the normal macroscopic electrode and W_{μ} the length of the tube. The parameter A_{μ} gives the weight of the wave function at the edge and is used to renormalize the contribution to the self-energy of the coupled system.

With this, the self-energy between the dots and the superconductor is given by

$$\Sigma_{\mu\nu} = \sqrt{\tilde{\Gamma}_{S_{\mu}} \tilde{\Gamma}_{S_{\nu}}} \sigma_z g_{S,\mu\nu} \sigma_z \ , \tag{C.7}$$

where $\tilde{\Gamma}_{S_{\mu}}$ are the effective tunneling rates from the central region to the dots, $\tilde{\Gamma}_{S_{\mu}} = t a_0 \left| \sin\left(k_{0\mu} W_{\mu}\right) \cos\alpha_{\mu} \right| / (2W_{\mu})$, $k_{0\mu}$ being the wavevector for the corresponding dot state and $\cos\alpha_{\mu} = k_{0\mu} / \sqrt{k_{0\mu} + q^2}$.

C.2 Spatial evolution of the CAR and EC coefficients.

We use the microscopic insight that Equation C.7 gives to study the spatial dependence of the non-local electron-electron and electron-hole signals. To simplify the analytic results we work in the limit when the coupling between the dots and the superconducting region is in the tunnel regime and the width of the superconducting SWCN, W, is large compared with the electron coherence length. The electron-hole element of the non-local Green function of the coupled system is

$$G_{LR,eh} \simeq \frac{\Sigma_{LR,eh}}{\left(E - \epsilon_L + i\tilde{\Gamma}_L - \Sigma_{LL,ee}\right)\left(E + \epsilon_R + i\tilde{\Gamma}_R - \Sigma_{RR,hh}\right)}, \tag{C.8}$$

with an equivalent expression for $G_{LR,he}$ changing the electron (e) and hole (h) indexes. This yields that the interdot CAR transmission can be expressed as

$$T_{CAR} = |G_{LR,eh}|^2 = \frac{|\Sigma_{LR,eh}|^2}{|i\tilde{\Gamma}_L + \Sigma_{LL,ee}|^2 |i\tilde{\Gamma}_R + \Sigma_{RR,hh}|^2}. \tag{C.9}$$

Within this limit, the local and non-local electron-hole contributions of the self-energy are reduced to

$$\Sigma_{LR,eh} = 2i\Gamma_S \frac{\Delta_i}{\Omega} \cos\alpha \sin\left(k_0 W + \alpha\right) e^{-W/\xi(E)} \tag{C.10}$$

$$\Sigma_{LL,eh} = \Gamma_S \frac{\Delta_i}{\Omega} \cos\alpha. \tag{C.11}$$

The CAR coefficients decay exponentially on the range given by $\xi(E) = \xi_0 \Delta_i / \sqrt{\Delta_i^2 - E^2}$, with $\xi_0 = \hbar v_F / \Delta_i \sqrt{1 - (\hbar v_F q / E_{FS})}$ and $q = q_0 \pm \delta_1 / \hbar v_F$ the lowest-energy mode. The analysis of this decay and the comparison with the well-known result for 3D superconductors is done in Section 6.3.

Appendix D

Equation of motion approach to include interactions

In this Appendix we describe the approximation used to include interactions within the minimal model for the S-DQD system. The dot levels will be indicated by the indexes $\mu = L, R$ (dot), $\sigma = \uparrow, \downarrow$ (spin). The Hamiltonian of the system is

$$\hat{H} = \hat{H}_L + \hat{H}_R + \hat{H}_S + \sum_{\mu,\sigma} E_\mu \hat{n}_{\mu\sigma} + \sum_{\mu} U_\mu \hat{n}_\mu \left(\hat{n}_\mu - 1\right)/2 + \hat{H}_T + \hat{H}_{DS} \,, \tag{D.1}$$

where $d^\dagger_{\mu\sigma}$ creates an electron in dot μ with spin σ, $\hat{n}_{\mu\sigma} = \hat{d}^\dagger_{\mu\sigma} d_{\mu\sigma}$, and $\hat{n}_\mu = \sum_\sigma \hat{n}_{\mu\sigma}$, $\hat{H}_{L,R,S}$ describe the isolated left, right and central superconducting leads respectively. Finally $\hat{H}_T$ corresponds to the tunnel coupling between the dot level and the normal leads while H_{DS} couple the dots to the superconducting electrode.

The transport properties of this model can be adequately described in terms of the DQD retarded Green functions in Nambu space, defined as $\hat{G}(\tau) = -i\theta(\tau)\langle\left[\hat{\psi}(\tau), \hat{\psi}^\dagger(0)\right]_+\rangle$, where $\hat{\psi}_\mu = \left(d_{\mu\uparrow}, d^\dagger_{\mu\downarrow}, d_{\mu\uparrow}, d^\dagger_{\mu\downarrow}\right)$ is a bispinor in Nambu-space. To simplify the notation we shall use hereafter $\hat{G} = << \hat{\psi}; \hat{\psi}^\dagger >>$. To deal with the interaction we rely here on an equation of motion (EOM) approach, with a decoupling at the level of the two-particle Green functions. From the equation of motion for $\hat{G}$, in frequency representation we obtain

$$\left[\omega\hat{I} - \hat{h}_0 + i\hat{\Gamma} - \hat{\Sigma}\right]\hat{G} = \hat{I} + \hat{U}\hat{W} \,, \tag{D.2}$$

where we have defined the matrices in Nambu-dot space $(\hat{h}_0)_{\mu\nu,\alpha\beta} = \delta_{\mu\nu}\delta_{\alpha\beta}(-1)^{\alpha+1}E_\mu$, $(\hat{U})_{\mu\nu,\alpha\beta} = \delta_{\mu\nu}\delta_{\alpha\beta}(-1)^{\alpha+1}U_\mu$ and $\hat{W} = << \hat{\phi}; \hat{\psi}^\dagger >>$; with $(\hat{\phi})_{\mu,\alpha} = \delta_{\alpha,1} d_{\mu\uparrow} n_{\mu\downarrow} + \delta_{\alpha,2} d^\dagger_{\mu\downarrow} n_{\mu\uparrow}$. $\hat{W}$ is a two body Green function generated by the presence of the U-terms in the model Hamiltonian. The tunneling rates $(\hat{\Gamma})_{\mu\nu,\alpha\beta} = \Gamma_\mu a_0 / W_\mu \delta_{\mu\nu}\delta_{\alpha\beta}$ arise from

the coupling to the normal leads, while $\hat{\Sigma}$ is the matrix self-energy described in the previous section. To close the system of equations we analyze the EOM for $\hat{W}$ and we introduce a mean field decoupling scheme for the rest of two-body Green functions which are generated. In this way we obtain

$$\left(\omega\hat{I}-\hat{h}_1\right)\hat{W}=\hat{A}\left[1+\left(\hat{\Sigma}-i\hat{\Gamma}\right)\hat{G}\right]\ , \tag{D.3}$$

where $(\hat{A})_{\mu\nu,\alpha\beta}=\delta_{\mu\nu}\left(\delta_{\alpha\beta}<n_\mu>+(1-\delta_{\alpha\beta})<\hat{d}_{\mu\uparrow}\hat{d}_{\mu\downarrow}>\right)$ and $\hat{h}_1=\hat{h}_0+\hat{U}$.

Extracting $\hat{W}$ from (D.3) and substituting in (D.2) we obtain an expression for $\hat{G}$ which can be evaluated self-consistently

$$\hat{G}=\left[\omega-\hat{h}_0+i\hat{\Gamma}-\hat{\Sigma}-\hat{U}\left(\omega-\hat{h}_1\right)^{-1}\hat{A}\left(-i\hat{\Gamma}+\hat{\Sigma}\right)\right]^{-1}\left[\hat{I}+\hat{U}\left(\omega-\hat{h}_1\right)^{-1}\hat{A}\right]\ . \tag{D.4}$$

This can be written in a more compact way as

$$\hat{G}=\left[\hat{g}^{-1}+i\hat{\Gamma}-\hat{\Sigma}\right]^{-1}\ , \tag{D.5}$$

where

$$\hat{g}=\left(\omega-\hat{h}_0\right)^{-1}\left[\hat{I}+\hat{U}\left(\omega-\hat{h}_1\right)^{-1}\hat{A}\right]\ .$$

Finally, taking the limit $U_\mu\to\infty$ further simplification occurs as one can safely neglect the induced pairing correlations $<\hat{d}_{\mu\uparrow}\hat{d}_{\mu\downarrow}>$ [171, 172]. This allows to write

$$\hat{g}\to\left(\omega-\hat{h}_0\right)^{-1}\left[\hat{I}-\hat{A}_\infty\right], \tag{D.6}$$

where $(\hat{A}_\infty)_{\mu\nu}=\delta_{\mu\nu}<n_\mu>$.

Appendix E

List of Publications

1. S. Gómez, P. Burset, W. J. Herrera, A. Levy Yeyati. Selective focusing of electrons and holes in a graphene-based superconducting lens. Phys. Rev. B 85, 115411 (2012)

2. P. Burset, W. J. Herrera, A. Levy Yeyati. Microscopic theory of Cooper pair beam splitters based on carbon nanotubes. Phys. Rev. B 84, 115448 (2011).

3. P. Burset, A. Levy Yeyati, L. Brey, H. Fertig. Transport in superlattices on single-layer graphene. Phys. Rev. B 83, 195434 (2011).

4. W. J. Herrera, P. Burset, A. Levy Yeyati. A Green function approach to graphene-superconductor junctions with well-defined edges. J. Phys: Condens. Matter 22, 275304 (2010).

5. P. Burset, W. J. Herrera, A. Levy Yeyati. Proximity-induced interface bound states in superconductor-graphene junctions. Phys. Rev. B 80, 041402(R) (2009).

6. P. Burset, A. Levy Yeyati, A. Martn-Rodero. Microscopic theory of the proximity effect in superconductor-graphene nanostructures. Phys. Rev. B 77, 205425 (2008).

7. L.G. Herrmann, P. Burset, W.J. Herrera, F. Portier, P. Roche, C. Strunk, A. Levy Yeyati, T. Kontos. Spectrosocopy of nonlocal Cooper pairs in a double quantum dot. Submitted.

8. H. Soller, P. Burset, L. Hofstetter, A. Baumgartner, K. Kang, C. Schönenberger, A. Komnik, A. Levy Yeyati. Finite bias Cooper pair splitting: theory and experiment. In preparation.

Bibliography

[1] P. R. Wallace, Phys. Rev. **71**, 622 (1947), URL http://link.aps.org/doi/10.1103/PhysRev.71.622. (Cited on sections 2.1 and 2.1.1).

[2] J. C. Slonczewski and P. R. Weiss, Phys. Rev. **109**, 272 (1958). (Cited on section 2.1).

[3] G. W. Semenoff, Phys. Rev. Lett. **53**, 2449 (1984). (Cited on section 2.1).

[4] S. Iijima, Nature (London) **354**, 56 (1991), URL http://dx.doi.org/10.1038/354056a0. (Cited on section 2.1).

[5] T. Ando, Journal of the Physical Society of Japan **74**, 777 (2005), URL http://jpsj.ipap.jp/link?JPSJ/74/777/. (Cited on sections 2.1, 3.3, and C).

[6] H. Boehm, R. Setton, and E. Stumpp, Pure and applied chemistry **66**, 1893 (1994), ISSN 0033-4545. (Cited on section 2.1).

[7] K. Novoselov, A. Geim, S. Mozorov, D. Jiang, Y. Zhang, S. Dubonos, I. Gregorieva, and A. Firsov, Science **306**, 666 (2004). (Cited on sections 2.1 and 2.1.1).

[8] K. Novoselov, D. Jiang, F. Schedin, T. Booth, V. Khotkevich, S. Morozov, and A. Geim, Proceedings of the National Academy of Sciences of the United States of America **102**, 10451 (2005), ISSN 0027-8424. (Cited on sections 2.1 and 2.1.1).

[9] K. Novoselov, A. Geim, S. Morozov, D. Jiang, M. Katsnelson, I. Grigorieva, S. Dubonos, and A. Firsov, Nature **438**, 197 (2005), ISSN 0028-0836. (Cited on sections 2.1 and 2.1.1).

[10] A. K. Geim, Science **324**, 1530 (2009), URL http://www.sciencemag.org/content/324/5934/1530.abstract. (Cited on section 2.1).

[11] H. B. Heersche, P. Jarillo-Herrero, J. B. Oostinga, L. M. K. Vandersypen, and A. F. Morpurgo, Nature (London) **446**, 56 (2007). (Cited on sections 2.1, 4.1, and 5.2.1).

[12] A. Shailos, W. Nativel, A. Kasumov, C. Collet, M. Ferrier, S. Guron, R. Deblock, and H. Bouchiat, EPL (Europhysics Letters) **79**, 57008 (2007). (Cited on sections 4.1 and 5.2.1).

[13] F. Miao, S. Wijeratne, Y. Zhang, U. C. Coskun, W. Bao, and C. N. Lau, Science **317**, 1530 (2007). (Cited on section 5.2.1).

[14] X. Du, I. Skachko, and E. Y. Andrei, Phys. Rev. B **77**, 184507 (2008). (Cited on sections 2.1, 4.1, and 5.2.1).

[15] A. H. Castro Neto, F. Guinea, N. M. R. Peres, K. S. Novoselov, and A. K. Geim, Rev. Mod. Phys. **81**, 109 (2009), URL http://link.aps.org/doi/10.1103/RevModPhys.81.109. (Cited on sections 2.1 and 4.4.3).

[16] S. Das Sarma, S. Adam, E. H. Hwang, and E. Rossi, Rev. Mod. Phys. **83**, 407 (2011), URL http://link.aps.org/doi/10.1103/RevModPhys.83.407. (Cited on sections 2.1, 2.1.1, and A.2.4).

[17] G. V.P., S. S.G., and C. J.P., International Journal of Modern Physics B **21**, 4611 (2007), URL http://www.worldscinet.com/ijmpb/21/2127/S0217979207038022.html. (Cited on sections 2.1, 3.3, and 3.3).

[18] C. W. J. Beenakker, Rev. Mod. Phys. **80**, 1337 (2008), URL http://link.aps.org/doi/10.1103/RevModPhys.80.1337. (Cited on sections 2.1 and A.1).

[19] P. Allain and J. Fuchs, The European Physical Journal B - Condensed Matter and Complex Systems **83**, 301 (2011), ISSN 1434-6028, 10.1140/epjb/e2011-20351-3, URL http://dx.doi.org/10.1140/epjb/e2011-20351-3. (Cited on section 2.1).

[20] F. Molitor, J. Gttinger, C. Stampfer, S. Drscher, A. Jacobsen, T. Ihn, and K. Ensslin, Journal of Physics: Condensed Matter **23**, 243201 (2011), URL http://stacks.iop.org/0953-8984/23/i=24/a=243201. (Cited on sections 2.1 and 2.1.2).

[21] A. Rozhkov, G. Giavaras, Y. P. Bliokh, V. Freilikher, and F. Nori, Physics Reports **503**, 77 (2011), ISSN 0370-1573, URL http://www.sciencedirect.com/science/article/pii/S0370157311000469. (Cited on section 2.1).

[22] P. Recher and B. Trauzettel, Nanotechnology **21**, 302001 (2010), URL http://stacks.iop.org/0957-4484/21/i=30/a=302001. (Cited on sections 2.1 and 2.1.2).

[23] E. R. Mucciolo and C. H. Lewenkopf, Journal of Physics: Condensed Matter **22**, 273201 (2010), URL http://stacks.iop.org/0953-8984/22/i=27/a=273201. (Cited on section 2.1).

[24] N. M. R. Peres, Journal of Physics: Condensed Matter **21**, 323201 (2009), URL http://stacks.iop.org/0953-8984/21/i=32/a=323201. (Cited on section 2.1).

[25] T. Ando and T. Nakanishi, Journal of the Physical Society of Japan **67**, 1704 (1998), URL http://jpsj.ipap.jp/link?JPSJ/67/1704/. (Cited on section 2.1.2).

[26] T. Ando, T. Nakanishi, and R. Saito, Journal of the Physical Society of Japan **67**, 2857 (1998), URL http://jpsj.ipap.jp/link?JPSJ/67/2857/. (Cited on section 2.1.2).

[27] O. Klein, Zeitschrift fr Physik A Hadrons and Nuclei **53**, 157 (1929), ISSN 0939-7922, 10.1007/BF01339716, URL http://dx.doi.org/10.1007/BF01339716. (Cited on section 2.1.2).

[28] M. I. Katsnelson, K. S. Novoselov, and A. K. Geim, Nature Physics **2**, 620 (2006). (Cited on sections 2.1.2 and A.2.4).

[29] B. Huard, J. A. Sulpizio, N. Stander, K. Todd, B. Yang, and D. Goldhaber-Gordon, Phys. Rev. Lett. **98**, 236803 (2007). (Cited on sections 2.1.2 and A.1).

[30] M. Lemme, T. Echtermeyer, M. Baus, and H. Kurz, Electron Device Letters, IEEE **28**, 282 (2007), ISSN 0741-3106. (Cited on section: see previous reference).

[31] B. Özyilmaz, P. Jarillo-Herrero, D. Efetov, D. A. Abanin, L. S. Levitov, and P. Kim, Phys. Rev. Lett. **99**, 166804 (2007). (Cited on section 5.2.1).

[32] J. R. Williams, L. DiCarlo, and C. M. Marcus, Science **317**, 638 (2007), URL http://www.sciencemag.org/content/317/5838/638.abstract. (Cited on section: see previous reference).

[33] E. Rossi, J. H. Bardarson, P. W. Brouwer, and S. Das Sarma, Phys. Rev. B **81**, 121408 (2010). (Cited on section 2.1.2).

[34] V. V. Cheianov and V. I. Fal'ko, Phys. Rev. B **74**, 041403 (2006). (Cited on section 2.1.2).

[35] M. I. Katsnelson, The European Physical Journal B - Condensed Matter and Complex Systems **51**, 157 (2006), ISSN 1434-6028, 10.1140/epjb/e2006-00203-1, URL http://dx.doi.org/10.1140/epjb/e2006-00203-1. (Cited on sections 2.1.2 and 4.2).

[36] J. Tworzydło, B. Trauzettel, M. Titov, A. Rycerz, and C. W. J. Beenakker, Phys. Rev. Lett. **96**, 246802 (2006), URL http://link.aps.org/doi/10.1103/PhysRevLett.96.246802. (Cited on sections 2.1.2, 2.1.2, 4.2, A.2.4, and A.2.4).

[37] L. Brey and H. A. Fertig, Phys. Rev. B **73**, 235411 (2006), URL http://link.aps.org/doi/10.1103/PhysRevB.73.235411. (Cited on sections 2.1.2, 3.2.2, 3.3.1, 3.3.2, 4.3.2, 4.3.4, and A.2.4).

[38] A. R. Akhmerov and C. W. J. Beenakker, Phys. Rev. B **75**, 045426 (2007), URL http://link.aps.org/doi/10.1103/PhysRevB.75.045426. (Cited on sections 2.1.2, 4.1, and 4.3.1).

[39] E. Prada, P. San-Jose, B. Wunsch, and F. Guinea, Phys. Rev. B **75**, 113407 (2007), URL http://link.aps.org/doi/10.1103/PhysRevB.75.113407. (Cited on sections 2.1.2 and 4.1).

[40] J. Martin, N. Akerman, G. Ulbricht, T. Lohmann, J. H. Smet, K. Von Klitzing, and A. Yacoby, Nat. Phys. **4**, 144 (2008). (Cited on sections 2.1.2, 4.4.5, and 5.2.4).

[41] Y. Zhang, V. W. Brar, C. Girit, A. Zettl, and M. F. Crommie, Nature Physics **5**, 722 (2009). (Cited on sections 2.1.2, 4.4.5, 4.4.5, and 5.2.4).

[42] V. V. Cheianov, V. I. Fal'ko, B. L. Altshuler, and I. L. Aleiner, Phys. Rev. Lett. **99**, 176801 (2007), URL http://link.aps.org/doi/10.1103/PhysRevLett.99.176801. (Cited on sections 2.1.2 and A.1).

[43] E. Rossi and S. Das Sarma, Phys. Rev. Lett. **101**, 166803 (2008), URL http://link.aps.org/doi/10.1103/PhysRevLett.101.166803. (Cited on section 2.1.2).

[44] H. Onnes, Leiden Comm. **1206** (1911). (Cited on section 2.2).

[45] W. Meissner and R. Ochsenfeld, Naturwissenschaften **21**, 787 (1933), ISSN 0028-1042, 10.1007/BF01504252, URL http://dx.doi.org/10.1007/BF01504252. (Cited on section 2.2).

[46] F. London and H. London, Proceedings of the Royal Society of London. Series A, Mathematical and Physical Sciences **149**, pp. 71 (1935), ISSN 00804630, URL http://www.jstor.org/stable/96265. (Cited on section 2.2).

[47] V. L. Ginzburg and L. D. Landau, Zh. Eksp. Teor. Fiz. **20** (1950). (Cited on sections 2.2 and 2.2).

[48] J. Bardeen, L. N. Cooper, and J. R. Schrieffer, Phys. Rev. **108**, 1175 (1957), URL http://link.aps.org/doi/10.1103/PhysRev.108.1175. (Cited on section 2.2).

[49] S. Guéron, H. Pothier, N. O. Birge, D. Esteve, and M. H. Devoret, Phys. Rev. Lett. **77**, 3025 (1996), URL http://link.aps.org/doi/10.1103/PhysRevLett.77.3025. (Cited on sections 2.2 and 2.2).

[50] S. Pilgram, W. Belzig, and C. Bruder, Phys. Rev. B **62**, 12462 (2000), URL http://link.aps.org/doi/10.1103/PhysRevB.62.12462. (Cited on section 2.2).

[51] G. E. Blonder, M. Tinkham, and T. M. Klapwijk, Phys. Rev. B **25**, 4515 (1982), URL http://link.aps.org/doi/10.1103/PhysRevB.25.4515. (Cited on sections 2.2, 2.3.2, 4.2.2, and 4.4.1).

[52] A. Andreev, Zh. Eksp. Teor. Fiz. **46** (1968), [Sov. Phys. JETP **19**, 1228 (1964)]. (Cited on section 2.3.1).

[53] N. Ashcroft and N. Mermin, *Solid State Physics* (Harcourt College Publishers, 1976). (Cited on section 5).

[54] C. Kittel, *Introduction to Solid State Physics* (John Wiley and Sons, 1953). (Cited on section 5).

[55] G. E. Blonder and M. Tinkham, Phys. Rev. B **27**, 112 (1983), URL http://link.aps.org/doi/10.1103/PhysRevB.27.112. (Cited on section 2.3.2).

[56] C. W. J. Beenakker, Phys. Rev. Lett. **97**, 067007 (2006). (Cited on sections 2.3.3, 2.3.4, 2.3.4, 4.1, 4.2, 4.2.2, 4.2.2, 4.2.2, 4.2.3, 4.4.1, 4.4.1, 5.1.1, and 5.1.2).

[57] S. Bhattacharjee and K. Sengupta, Phys. Rev. Lett. **97**, 217001 (2006). (Cited on sections 2.3.3, 4.1, 4.4.2, 5.2.3, and B).

[58] J. Linder and A. Sudbø, Phys. Rev. B **77**, 064507 (2008). (Cited on sections 8, 4.1, 5.2.3, B, and B).

[59] G. Deutscher and D. Feinberg, Applied Physics Letters **76**, 487 (2000), ISSN 0003-6951. (Cited on sections 2.3.5, 5.2.1, and 6.1).

[60] G. Falci, D. Feinberg, and F. W. J. Hekking, EPL (Europhysics Letters) **54**, 255 (2001), URL http://stacks.iop.org/0295-5075/54/i=2/a=255. (Cited on sections 2.3.5, 6.1, and 6.3.2).

[61] R. Mélin and D. Feinberg, Phys. Rev. B **70**, 174509 (2004), URL http://link.aps.org/doi/10.1103/PhysRevB.70.174509. (Cited on sections 2.3.5, 6.1, and 6.3.2).

[62] J. P. Morten, A. Brataas, and W. Belzig, Phys. Rev. B **74**, 214510 (2006), URL http://link.aps.org/doi/10.1103/PhysRevB.74.214510. (Cited on sections 2.3.5 and 6.1).

[63] M. S. Kalenkov and A. D. Zaikin, Phys. Rev. B **75**, 172503 (2007), URL http://link.aps.org/doi/10.1103/PhysRevB.75.172503. (Cited on section: see previous reference).

[64] R. Mélin, F. S. Bergeret, and A. L. Yeyati, Phys. Rev. B **79**, 104518 (2009), URL http://link.aps.org/doi/10.1103/PhysRevB.79.104518. (Cited on sections 2.3.5 and 6.1).

[65] A. L. Yeyati, F. S. Bergeret, A. Martín-Rodero, and T. M. Klapwijk, Nat. Phys. **3**, 455 (2007), URL http://www.nature.com/nphys/journal/v3/n7/full/nphys621.html. (Cited on sections 2.3.5 and 6.1).

[66] F. S. Bergeret and A. Levy Yeyati, Phys. Rev. B **80**, 174508 (2009), URL http://link.aps.org/doi/10.1103/PhysRevB.80.174508. (Cited on sections 2.3.5 and 6.1).

[67] D. Beckmann, H. B. Weber, and H. v. Löhneysen, Phys. Rev. Lett. **93**, 197003 (2004), URL http://link.aps.org/doi/10.1103/PhysRevLett.93.197003. (Cited on sections 2.3.5 and 6.1).

[68] S. Russo, M. Kroug, T. M. Klapwijk, and A. F. Morpurgo, Phys. Rev. Lett. **95**, 027002 (2005), URL http://link.aps.org/doi/10.1103/PhysRevLett.95.027002. (Cited on section 2.3.5).

[69] P. Cadden-Zimansky and V. Chandrasekhar, Phys. Rev. Lett. **97**, 237003 (2006), URL http://link.aps.org/doi/10.1103/PhysRevLett.97.237003. (Cited on section 2.3.5).

[70] A. Kleine, A. Baumgartner, J. Trbovic, and C. Schoenenberger, EPL (Europhysics Letters) **87**, 27011 (2009), URL http://stacks.iop.org/0295-5075/87/i=2/a=27011. (Cited on section: see previous reference).

[71] J. Wei and V. Chandrasekhar, Nat. Phys. **6**, 494 (2010), URL http://dx.doi.org/10.1038/nphys1669. (Cited on sections 2.3.5 and 6.1).

[72] P. Recher, E. V. Sukhorukov, and D. Loss, Phys. Rev. B **63**, 165314 (2001), URL http://link.aps.org/doi/10.1103/PhysRevB.63.165314. (Cited on sections 2.3.5, 6.1, 6.2, and 6.4).

[73] N. M. Chtchelkatchev, G. Blatter, G. B. Lesovik, and T. Martin, Phys. Rev. B **66**, 161320 (2002), URL http://link.aps.org/doi/10.1103/PhysRevB.66.161320. (Cited on section 2.3.5).

[74] P. Samuelsson, E. V. Sukhorukov, and M. Büttiker, Phys. Rev. Lett. **91**, 157002 (2003), URL http://link.aps.org/doi/10.1103/PhysRevLett.91.157002. (Cited on section 2.3.5).

[75] C. Bena, S. Vishveshwara, L. Balents, and M. P. A. Fisher, Phys. Rev. Lett. **89**, 037901 (2002), URL http://link.aps.org/doi/10.1103/PhysRevLett.89.037901. (Cited on sections 2.3.5 and 6.1).

[76] P. W. Anderson, Phys. Rev. **112**, 1900 (1958), URL http://link.aps.org/doi/10.1103/PhysRev.112.1900. (Cited on section 2.4.1.3).

[77] Y. Nambu, Phys. Rev. **117**, 648 (1960), URL http://link.aps.org/doi/10.1103/PhysRev.117.648. (Cited on section 2.4.1.3).

[78] J. Rammer and H. Smith, Rev. Mod. Phys. **58**, 323 (1986), URL http://link.aps.org/doi/10.1103/RevModPhys.58.323. (Cited on section 2.4.2).

[79] A. Kamenev and A. Levchenko, ArXiv:0901.3586v2 (2009), (Les Houches lectures). (Cited on section 2.4.2).

[80] L. Keldysh, Zh. Eksp. Teor. Fiz. **47** (1964), [Sov. Phys. JETP **20**,1018 (1965)]. (Cited on section 2.4.2).

[81] C. Caroli, R. Combescot, P. Nozieres, and D. Saint-James, Journal of Physics C: Solid State Physics **4**, 916 (1971), URL http://stacks.iop.org/0022-3719/4/i=8/a=018. (Cited on section 2.4.3).

[82] P. Burset, A. L. Yeyati, and A. Martín-Rodero, Phys. Rev. B **77**, 205425 (2008), URL http://link.aps.org/doi/10.1103/PhysRevB.77.205425. (Cited on sections 3.1, 3.3.1, 3.4.1, 4.3.4, 5.2.2, 5.2.2, 7, 8, and A.3).

[83] W. J. Herrera, P. Burset, and A. L. Yeyati, Journal of Physics: Condensed Matter **22**, 275304 (2010), URL http://stacks.iop.org/0953-8984/22/i=27/a=275304. (Cited on sections 3.1, 5.1.2, 7, 8, and B).

[84] E. Vecino, A. Martín-Rodero, and A. Levy Yeyati, Phys. Rev. B **64**, 184502 (2001), URL http://link.aps.org/doi/10.1103/PhysRevB.64.184502. (Cited on section 3.2.2).

[85] W. L. McMillan, Phys. Rev. **175**, 559 (1968), URL http://link.aps.org/doi/10.1103/PhysRev.175.559. (Cited on section 3.3).

[86] S. Kashiwaya and Y. Tanaka, Reports on Progress in Physics **63**, 1641 (2000), URL http://stacks.iop.org/0034-4885/63/i=10/a=202. (Cited on section 3.3).

[87] P. Burset, W. Herrera, and A. Levy Yeyati, Phys. Rev. B **80**, 041402 (2009), URL http://link.aps.org/doi/10.1103/PhysRevB.80.041402. (Cited on sections 3.4.1, 7, 8, and A.3).

[88] H. B. Heersche, P. Jarillo-Herrero, J. B. Oostinga, L. M. Vandersypen, and A. F. Morpurgo, Solid State Communications **143**, 72 (2007), ISSN 0038-1098, exploring graphene - Recent research advances, URL http://www.sciencedirect.com/science/article/pii/S0038109807003031. (Cited on section 4.1).

[89] M. Titov and C. W. J. Beenakker, Phys. Rev. B **74**, 041401 (2006), URL http://link.aps.org/doi/10.1103/PhysRevB.74.041401. (Cited on sections 4.1 and 4.2).

[90] A. G. Moghaddam and M. Zareyan, Phys. Rev. B **74**, 241403 (2006), URL http://link.aps.org/doi/10.1103/PhysRevB.74.241403. (Cited on section: see previous reference).

[91] J. C. Cuevas and A. L. Yeyati, Phys. Rev. B **74**, 180501 (2006), URL http://link.aps.org/doi/10.1103/PhysRevB.74.180501. (Cited on section 4.1).

[92] J. Linder and A. Sudbø, Phys. Rev. Lett. **99**, 147001 (2007), URL http://link.aps.org/doi/10.1103/PhysRevLett.99.147001. (Cited on section 4.1).

[93] G. Tkachov, Phys. Rev. B **76**, 235409 (2007). (Cited on sections 4.1, 4.3, 4.3.3, 5.2.2, and 5.2.2).

[94] M. Titov, A. Ossipov, and C. W. J. Beenakker, Phys. Rev. B **75**, 045417 (2007), URL http://link.aps.org/doi/10.1103/PhysRevB.75.045417. (Cited on sections 4.1, 4.3, and 4.4).

[95] H. Schomerus, Phys. Rev. B **76**, 045433 (2007), URL http://link.aps.org/doi/10.1103/PhysRevB.76.045433. (Cited on sections 4.2 and A.3).

[96] Y. M. Blanter and I. Martin, Phys. Rev. B **76**, 155433 (2007), URL http://link.aps.org/doi/10.1103/PhysRevB.76.155433. (Cited on section 4.2).

[97] L. Brey and H. A. Fertig, Phys. Rev. B **76**, 205435 (2007), URL http://link.aps.org/doi/10.1103/PhysRevB.76.205435. (Cited on sections 4.2 and A.3).

[98] J. C. Cuevas, A. Martín-Rodero, and A. L. Yeyati, Phys. Rev. B **54**, 7366 (1996), URL http://link.aps.org/doi/10.1103/PhysRevB.54.7366. (Cited on section 4.2.2).

[99] J. C. Cuevas, A. L. Yeyati, and A. Martín-Rodero, Phys. Rev. Lett. **80**, 1066 (1998), URL http://link.aps.org/doi/10.1103/PhysRevLett.80.1066. (Cited on section 4.2.2).

[100] I. O. Kulik and A. N. Omelyanchuk, Sov. Phys. JETP Lett. **21** (1975). (Cited on section 4.3).

[101] A. Altland, B. D. Simons, and D. T. Semchuk, Advances in Physics **49**, 321 (2000), URL http://www.tandfonline.com/doi/abs/10.1080/000187300243354. (Cited on section 4.3).

[102] P. San-Jose, E. Prada, and D. S. Golubev, Phys. Rev. B **76**, 195445 (2007). (Cited on section 4.3.1).

[103] D. L. Bergman and K. Le Hur, Phys. Rev. B **79**, 184520 (2009), URL http://link.aps.org/doi/10.1103/PhysRevB.79.184520. (Cited on section 4.4).

[104] D. Zhang, C. S. Ting, and C.-R. Hu, Phys. Rev. B **70**, 172508 (2004), URL http://link.aps.org/doi/10.1103/PhysRevB.70.172508. (Cited on section 4.4.4).

[105] V. Lukic and E. J. Nicol, Phys. Rev. B **76**, 144508 (2007), URL http://link.aps.org/doi/10.1103/PhysRevB.76.144508. (Cited on section 4.4.4).

[106] N. Nemec, D. Tománek, and G. Cuniberti, Phys. Rev. B **77**, 125420 (2008), URL http://link.aps.org/doi/10.1103/PhysRevB.77.125420. (Cited on section 4.4.4).

[107] J. M. Byers and M. E. Flatté, Phys. Rev. Lett. **74**, 306 (1995), URL http://link.aps.org/doi/10.1103/PhysRevLett.74.306. (Cited on sections 4.4.6 and 5.1.2).

[108] Q. Niu, M. C. Chang, and C. K. Shih, Phys. Rev. B **51**, 5502 (1995), URL http://link.aps.org/doi/10.1103/PhysRevB.51.5502. (Cited on section 5.1.2).

[109] V. V. Cheianov, V. Fal'ko, and B. L. Altshuler, Science **315**, 1252 (2007), URL http://www.sciencemag.org/content/315/5816/1252.abstract. (Cited on sections 5.2.1, 5.2.2, and 5.2.4).

[110] V. G. Veselago, Soviet Physics Uspekhi **10**, 509 (1968), URL http://stacks.iop.org/0038-5670/10/i=4/a=R04. (Cited on section 5.2.1).

[111] J. B. Pendry, Phys. Rev. Lett. **85**, 3966 (2000). (Cited on section 5.2.1).

[112] C.-H. Park, Y.-W. Son, L. Yang, M. L. Cohen, and S. G. Louie, Nano Letters **8**, 2920 (2008), pMID: 18720975, URL http://pubs.acs.org/doi/abs/10.1021/nl801752r. (Cited on sections 5.2.1 and A.1).

[113] J. Cserti, A. Pályi, and C. Péterfalvi, Phys. Rev. Lett. **99**, 246801 (2007). (Cited on sections 5.2.1 and 5.2.4).

[114] Y. Xing, J. Wang, and Q.-f. Sun, Phys. Rev. B **81**, 165425 (2010). (Cited on sections 5.2.1 and 5.2.4).

[115] F. Hassler, A. R. Akhmerov, and C. W. J. Beenakker, Phys. Rev. B **82**, 125423 (2010). (Cited on sections 5.2.1, 5.2.2, and 5.2.4).

[116] A. Matulis, M. R. Masir, and F. M. Peeters, Phys. Rev. B **83**, 115458 (2011). (Cited on section 5.2.1).

[117] A. G. Moghaddam and M. Zareyan, Phys. Rev. Lett. **105**, 146803 (2010). (Cited on section 5.2.1).

[118] R. V. Gorbachev, A. S. Mayorov, A. K. Savchenko, D. W. Horsell, and F. Guinea, Nano Letters **8**, 1995 (2008). (Cited on section 5.2.1).

[119] J. J. Velasco, G. Liu, W. Bao, and C. N. Lau, New Journal of Physics **11**, 095008 (2009). (Cited on section A.1).

[120] H.-Y. Chiu, V. Perebeinos, Y.-M. Lin, and P. Avouris, Nano Letters **10**, 4634 (2010). (Cited on section 5.2.1).

[121] J. Cayssol, Phys. Rev. Lett. **100**, 147001 (2008), URL http://link.aps.org/doi/10.1103/PhysRevLett.100.147001. (Cited on section 5.2.1).

[122] L. G. Herrmann, F. Portier, P. Roche, A. L. Yeyati, T. Kontos, and C. Strunk, Phys. Rev. Lett. **104**, 026801 (2010). (Cited on sections 5.2.1, 6.1, 6.2, 6.3, 6.3.1, 6.4, and 6.4).

[123] L. Hofstetter, S. Csonka, J. Nygard, and C. Schoenenberger, Nature **461**, 960 (2009). (Cited on sections 5.2.1, 6.1, 6.2, 6.3, 6.3.1, and 6.3.2).

[124] A. M. Black-Schaffer and S. Doniach, Phys. Rev. B **78**, 024504 (2008), URL http://link.aps.org/doi/10.1103/PhysRevB.78.024504. (Cited on sections 5.2.2 and 5.2.2).

[125] G. Giovannetti, P. A. Khomyakov, G. Brocks, V. M. Karpan, J. van den Brink, and P. J. Kelly, Phys. Rev. Lett. **101**, 026803 (2008). (Cited on sections 5.2.2 and 6.3.1).

[126] M. L. Shendeleva, Journal of Microscopy **229**, 452 (2008), ISSN 00222720. (Cited on section 5.2.4).

[127] V. Bouchiat, N. Chtchelkatchev, D. Feinberg, G. B. Lesovik, T. Martin, and J. Torrs, Nanotechnology **14**, 77 (2003), URL http://stacks.iop.org/0957-4484/14/i=1/a=318. (Cited on section 6.1).

[128] W. G. van der Wiel, S. De Franceschi, J. M. Elzerman, T. Fujisawa, S. Tarucha, and L. P. Kouwenhoven, Rev. Mod. Phys. **75**, 1 (2002), URL http://link.aps.org/doi/10.1103/RevModPhys.75.1. (Cited on section 6.2).

[129] J.-S. Jeong and H.-W. Lee, Phys. Rev. B **80**, 075409 (2009), URL http://link.aps.org/doi/10.1103/PhysRevB.80.075409. (Cited on sections 6.3 and C).

[130] S. Weiss, E. I. Rashba, F. Kuemmeth, H. O. H. Churchill, and K. Flensberg, Phys. Rev. B **82**, 165427 (2010), URL http://link.aps.org/doi/10.1103/PhysRevB.82.165427. (Cited on sections 6.3 and C).

[131] F. Kuemmeth, S. Ilani, D. C. Ralph, and P. L. McEuen, Nature **452**, 448 (2008). (Cited on section 6.3.1).

[132] S. Barraza-Lopez, M. Vanević, M. Kindermann, and M. Y. Chou, Phys. Rev. Lett. **104**, 076807 (2010), URL http://link.aps.org/doi/10.1103/PhysRevLett.104.076807. (Cited on section 6.3.1).

[133] M. Veldhorst and A. Brinkman, Phys. Rev. Lett. **105**, 107002 (2010), URL http://link.aps.org/doi/10.1103/PhysRevLett.105.107002. (Cited on section 6.3.3).

[134] L. Hofstetter, S. Csonka, A. Baumgartner, G. Fülöp, S. d'Hollosy, J. Nygård, and C. Schönenberger, Phys. Rev. Lett. **107**, 136801 (2011), URL http://link.aps.org/doi/10.1103/PhysRevLett.107.136801. (Cited on sections 6.4, 6.5, 7, and 8).

[135] H. Soller, P. Burset, L. Hofstetter, A. Baumgartner, K. Kang, C. Schönenberger, A. Komnik, and A. Levy Yeyati, In preparation (2012). (Cited on section 6.4).

[136] J.-D. Pillet, C. H. L. Quay, P. Morfin, C. Bena, A. L. Yeyati, and P. Joyez, Nature Physics **6**, 965 (2010), URL http://dx.doi.org/10.1038/nphys1811. (Cited on section 6.4).

[137] T. Dirks, T. L. Hughes, S. Lal, B. Uchoa, Y.-F. Chen, C. Chialvo, P. M. Goldbart, and N. Mason, Nature Physics **7**, 386 (2011), URL http://dx.doi.org/10.1038/nphys1911. (Cited on section 6.4).

[138] S. Gómez, P. Burset, W. J. Herrera, and A. L. Yeyati, Phys. Rev. B **85**, 115411 (2012), URL http://link.aps.org/doi/10.1103/PhysRevB.85.115411. (Cited on sections 7 and 8).

[139] P. Burset, A. L. Yeyati, L. Brey, and H. A. Fertig, Phys. Rev. B **83**, 195434 (2011). (Cited on sections 7 and 8).

[140] A. F. Young and P. Kim, Nature Phys. **5**, 222 (2009). (Cited on section A.1).

[141] N. Stander, B. Huard, and D. Goldhaber-Gordon, Phys. Rev. Lett. **102**, 026807 (2009). (Cited on section: see previous reference).

[142] S. Russo, M. F. Craciun, M. Yamamoto, S. Tarucha, and A. F. Morpurgo, New Journal of Physics **11**, 095018 (2009). (Cited on section A.1).

[143] J. M. Pereira, V. Mlinar, F. M. Peeters, and P. Vasilopoulos, Phys. Rev. B **74**, 045424 (2006). (Cited on section A.1).

[144] L. M. Zhang and M. M. Fogler, Phys. Rev. Lett. **100**, 116804 (2008). (Cited on section: see previous reference).

[145] D. P. Arovas, L. Brey, H. A. Fertig, E.-A. Kim, and K. Ziegler, New Journal of Physics **12**, 123020 (2010). (Cited on sections A.1 and A.2.2).

[146] A. L. Vázquez de Parga, F. Calleja, B. Borca, M. C. G. Passeggi, J. J. Hinarejos, F. Guinea, and R. Miranda, Phys. Rev. Lett. **100**, 056807 (2008). (Cited on section A.1).

[147] I. Pletikosić, M. Kralj, P. Pervan, R. Brako, J. Coraux, A. T. N'Diaye, C. Busse, and T. Michely, Phys. Rev. Lett. **102**, 056808 (2009). (Cited on section: see previous reference).

[148] F. Guinea and T. Low, Philosophical Transactions of the Royal Society A: Mathematical, Physical and Engineering Sciences **368**, 5391 (2010). (Cited on section: see previous reference).

[149] C.-H. Park, L. Yang, Y.-W. Son, M. L. Cohen, and S. G. Louie, Phys. Rev. Lett. **101**, 126804 (2008), URL http://link.aps.org/doi/10.1103/PhysRevLett.101.126804. (Cited on section A.1).

[150] C.-H. Park, L. Yang, Y.-W. Son, M. L. Cohen, and S. G. Louie, Nature Physics **4**, 213 (2008), URL http://www.nature.com/nphys/journal/v4/n3/suppinfo/nphys890_S1.html. (Cited on sections A.1, A.2.2, and A.2.5).

[151] M. Barbier, F. M. Peeters, P. Vasilopoulos, and J. M. Pereira, Phys. Rev. B **77**, 115446 (2008), URL http://link.aps.org/doi/10.1103/PhysRevB.77.115446. (Cited on section A.1).

[152] L. Brey and H. A. Fertig, Phys. Rev. Lett. **103**, 046809 (2009). (Cited on sections A.1, A.2.2, and A.3.1).

[153] C.-H. Park, Y.-W. Son, L. Yang, M. L. Cohen, and S. G. Louie, Phys. Rev. Lett. **103**, 046808 (2009). (Cited on sections A.2.2 and A.3.1).

[154] M. Barbier, P. Vasilopoulos, and F. M. Peeters, Phys. Rev. B **81**, 075438 (2010). (Cited on sections A.1, A.2.2, and A.2.2).

[155] J. Sun, H. A. Fertig, and L. Brey, Phys. Rev. Lett. **105**, 156801 (2010). (Cited on sections A.1 and A.4).

[156] L. Dell'Anna and A. De Martino, Phys. Rev. B **79**, 045420 (2009). (Cited on section A.1).

[157] I. Snyman, Phys. Rev. B **80**, 054303 (2009). (Cited on section: see previous reference).

[158] L. Z. Tan, C.-H. Park, and S. G. Louie, Phys. Rev. B **81**, 195426 (2010). (Cited on section: see previous reference).

[159] L. Dell'Anna and A. De Martino, Phys. Rev. B **83**, 155449 (2011), URL http://link.aps.org/doi/10.1103/PhysRevB.83.155449. (Cited on section A.1).

[160] N. Abedpour, A. Esmailpour, R. Asgari, and M. R. R. Tabar, Phys. Rev. B **79**, 165412 (2009). (Cited on section A.1).

[161] M. Barbier, P. Vasilopoulos, and F. M. Peeters, Phys. Rev. B **80**, 205415 (2009). (Cited on section: see previous reference).

[162] L.-G. Wang and S.-Y. Zhu, Phys. Rev. B **81**, 205444 (2010). (Cited on section: see previous reference).

[163] V. A. Yampol'skii, S. Savel'ev, and F. Nori, New Journal of Physics **10**, 053024 (2008). (Cited on section: see previous reference).

[164] C. Bai and X. Zhang, Phys. Rev. B **76**, 075430 (2007), URL http://link.aps.org/doi/10.1103/PhysRevB.76.075430. (Cited on section: see previous reference).

[165] P. San-Jose, E. Prada, and D. S. Golubev, Phys. Rev. B **76**, 195445 (2007). (Cited on section A.1).

[166] K. Ziegler, Phys. Rev. B **75**, 233407 (2007). (Cited on section A.2.3).

[167] S. Ryu, C. Mudry, A. Furusaki, and A. W. W. Ludwig, Phys. Rev. B **75**, 205344 (2007), URL http://link.aps.org/doi/10.1103/PhysRevB.75.205344. (Cited on sections A.2.3 and A.2.3).

[168] A. W. W. Ludwig, M. P. A. Fisher, R. Shankar, and G. Grinstein, Phys. Rev. B **50**, 7526 (1994), URL http://link.aps.org/doi/10.1103/PhysRevB.50.7526. (Cited on section A.2.3).

[169] J. Wang, H. A. Fertig, and G. Murthy, Phys. Rev. Lett. **104**, 186401 (2010). (Cited on section A.4).

[170] J. Wang, H. A. Fertig, G. Murthy, and L. Brey, Phys. Rev. B **83**, 035404 (2011). (Cited on section A.4).

[171] J. C. Cuevas, A. Levy Yeyati, and A. Martín-Rodero, Phys. Rev. B **63**, 094515 (2001), URL http://link.aps.org/doi/10.1103/PhysRevB.63.094515. (Cited on section D).

[172] Y. Tanaka, N. Kawakami, and O. Oguri, Journal of the Physical Society of Japan **76**, 074701 (2007), URL http://jpsj.ipap.jp/link?JPSJ/76/074701/. (Cited on section D).